



HAL
open science

Nouvelles zéolithes acides obtenues à partir de silico-germanates

Elsy El Hayek

► **To cite this version:**

Elsy El Hayek. Nouvelles zéolithes acides obtenues à partir de silico-germanates. Chemical engineering. Université de Lyon; KU Leuven (1970-..), 2020. English. NNT : 2020LYSE1298 . tel-03892693

HAL Id: tel-03892693

<https://theses.hal.science/tel-03892693v1>

Submitted on 10 Dec 2022

HAL is a multi-disciplinary open access archive for the deposit and dissemination of scientific research documents, whether they are published or not. The documents may come from teaching and research institutions in France or abroad, or from public or private research centers.

L'archive ouverte pluridisciplinaire **HAL**, est destinée au dépôt et à la diffusion de documents scientifiques de niveau recherche, publiés ou non, émanant des établissements d'enseignement et de recherche français ou étrangers, des laboratoires publics ou privés.



N°d'ordre NNT:2020LYSE1298

THESE de DOCTORAT DE L'UNIVERSITE DE LYON ET DE KU LEUVEN UNIVERSITY

opérée au sein de
l'Université Claude Bernard Lyon 1

Ecole Doctorale N° 206
Ecole Doctorale de Chimie, Procédés, Environnement

Spécialité de doctorat : Matériaux et Catalyse
Discipline : Chimie

Et au sein de
KU Leuven University

Arenberg Doctoral School
Faculty of Bioscience Engineering

Spécialité de doctorat : Bioscience Engineering

Soutenue publiquement le 09/12/2020, par :
Elsy EL HAYEK

New acid zeolites obtained from silicogermanates

Devant le jury composé de :

ČEJKA, Jiří	Professeur/ Charles University (Prague)	Rapporteur
VAN SPEYBROECK, Veronique BATS, Nicolas	Professeur/Ghent University Responsable domaine scientifique (Johnson Matthey)	Rapporteuse Examineur
DANIELE, Stéphane KIRSCHHOCK, Christine	Professeur/Université Lyon 1 Professeur/KU Leuven	Examineur Examinatrice
CHIZALLET, Céline MARTENS, Johan HARBUZARU, Bogdan	Ingénieure de recherche/IFPEN Professeur/KU Leuven Ingénieur de recherche/IFPEN	Directrice de thèse Directeur de thèse Invité

Acknowledgements

After three years of PhD thesis at IFP Energies and KU Leuven, I would like to express my gratitude:

To the jury members: Jiří Čejka, Veronique Van Speybroeck, Christine Kirschock, Stéphane Daniele and Nicolas Bats for accepting to read and judge this work.

To IFP Energies Nouvelles, for the opportunity and for the funding of this work, conducted at the department of ‘Génie des matériaux divisés’ within the Catalysis, Biocatalysis and separation division. To Luc Nougier, the director of Catalysis, Biocatalysis and separation division for his welcoming. To Alain Methivier, Head of the department for his motivating words and for giving me the opportunity to participate in different conferences.

To my supervisors: Céline Chizallet, Bogdan Harbuzaru and Johan Martens. I learned a lot during these three years of PhD and it is entirely thanks to them. Their precious advices, discussions and corrections nourished my scientific maturity. The continuous positive mindset of Bogdan, the patience of Céline for teaching me modeling and the pleasant explanations of Johan, combined to their kindness and support assured the best environment for doing my PhD.

To all my department colleagues. To Eric Llido, for training me on all the experimental equipment used during my PhD. To Monique Prigent, Sebastien Aubineau and Raquel Martinez, for assuring a great atmosphere in the laboratories. To the different co-officers starting from Thierry Pousserau, to Gerhard Pirngruber, to Delphine Marti and Clement Mothe. I will always remember the ‘particular French vocabulary idioms’ of Delphine and Clement. To Souad Rafiq Clément for the great moments spent during the EAZC conference. To Bernard Didier for scaling up the procedure of the OSDA synthesis. To Emmanuel Rosati, Sandrine Lazare, Justine Tirapu and Baptiste Cottin for their funny jokes.

To all the colleagues of ‘Physique et analyse’ division who have participated in this PhD. To Mickael Rivallan for our exchanges and his explanations concerning the IR spectroscopy. To Carole Bobin and Sylvain Carbonneau for our discussions about the choice of techniques. To Véronique Lefebvre for training me on the use of the MEB spectroscopy. To Thomas Coquet for forming me on the development and validation of an XRF method. To Nathalie Crozet for our technical discussions. To Emmanuel Soyer and Isabelle Clemenceau for the IR measurements and to Corinne Gajan and Floriane Lovery for the ICP measurements.

To the colleagues of ‘Catalyse Métaux /Solides’ department. To Christophe Bouchy, for our discussions, for all the explanations concerning the hexadecane catalytic test. To Sophie Bailly for forming me on the preparation of the catalysts of this test. To Ana Marta Costa, for her help

with the preparation. To Veronique Delattre and Frederic Portejoie for the hexadecane test experiments.

To all the colleagues of the Center for Surface Chemistry and Catalysis at KU Leuven. I was lucky to work with experts in the NMR and catalysis fields. I would like to address my special thanks to Gina Vanbutsele, for training me on the use of the catalytic reactor but also for all the catalytic tests she made herself after the deconfinement, for her availability, her fast answers to all my questions and for her warm welcoming. To Sambhu Radhakrishnan, Eric Breynaert, Karel Duerinckx and Dirk Dom for all the NMR measurements, fruitful discussions, ideas and explanations. To all my co-officers during my stays in Leuven: Charlotte Lejaegere, Nick Pellens, Maarten Houllberghs, Niels Ostyn and Sreeprasanth Pulinthanathu Sree, for their kind welcoming. To Loes Veheyden, Sam Smet and Ibrahim Khalil for our lunch talks. To Christine Kirschhock and Johan Hofkens for evaluating my work during the supervisory committee evaluations.

To all the PhD students, especially to Laureline Treps, with whom I shared every moment since day one at IFPEN. To Hanane Bouras for being such a great colleague. To Larissa Brito, Damien Dussol, Ana Teresa Fialho Batista, Marisa Duarte, Mayara Azin and Audrey Valette for the funny chats during the ride-shares. To Amit Sahu, Jerome Rey, Sharmin Sharna for the great lunch breaks. To Isabelle Costa, Julie Guillement, Stefan Kocic, Coralie Demaret, Farah El Masri, Sabah El Mohammed, Wassim Ammar, Catarina Simao, Giulia Ferri and all the PhD students for the great moments during the trainings, afterworks, docdays... .

To all the people that impacted my life. To Samar Adham, Antoine Gedeon and Franck Launay, for believing in me and for opening the path for me toward the research adventure. To Nicolas Bats, writer of this PhD Topic, for choosing me as a PhD candidate. Even if we did not work together, the topic itself was the greatest gift.

To all my friends, especially Patrick and Eddy for their presence since high school. To Marieline, Mathilda, Rita, Sally, Rita, Elie, Younes, Oscar, Charbel for making life funnier.

Finally, I express all my recognition to my parents and my siblings, for doing everything possible to offer me the best education and life conditions and for their unconditional support that make me reach my goals.

Abstract

Zeolites are microporous crystalline aluminosilicates composed of three-dimensional arrangements of SiO_4 and AlO_4 tetrahedra. These materials have various applications in the fields of adsorption, catalysis, separation and ion exchange. The introduction of germanium during the synthesis of these zeolites is a strategy for accessing new structures, sometimes with extra-large pores, attractive for the catalytic transformation of bulky molecules. However, a major remaining challenge is the substitution of germanium for aluminum to generate structures with compensation cations assuring the acidic activity. Also, microporous silicogermanates are often unstable in the presence of water after the removal of the organic structure directing agents, which limits their use. To stabilize these silicogermanates, recently, two experimental post-treatment approaches were developed. The first approach allows the initial structure of the parent zeolite to be maintained during the substitution of Ge atoms with other atoms like Al. In the second method elimination of the Ge atoms through hydrolysis leads to substructures that can be connected again creating this way new stable structures having smaller pores due to systematic omission of T-atoms from the original structure. Herein, a combination of theoretical calculations (DFT, Density Functional Theory) and experimental work (synthesis, characterization, catalysis) is used to explore the stabilization of silicogermanates. The *ab initio* study shows that all silicogermanates having structural codes attributed by the International Zeolite Association and their (alumino)silicates analogues are intrinsically stable. It also indicates that substitution of Ge for Si or Al is possible thermodynamically and is favorable using chloride precursors. As a consequence, a silicon tetrachloride treatment unit was used for the first time to substitute Ge for Si experimentally. This treatment led to the stabilization of the crystalline UTL structure of the IM-12 zeolite. Further treatments using polyaluminum chloride or trichloride solutions succeeded in incorporating aluminum in the zeolite framework. Various elemental and physicochemical techniques (XRD, N_2 physisorption, XRF, ICP, FTIR and MAS NMR) were implemented to characterize the materials along the treatment procedure. DFT models of the bulk and the external surfaces of the UTL structure with different elemental composition were build and helped assigning the experimental MAS NMR spectra. Finally, the obtained materials were tested as acid phases in the bi-functional hydroisomerization of n-decane and n-hexadecane, reflecting promising catalytic activity. This work opens perspectives for the catalytic use of stable derivatives of silicogermanate zeolites.

Key-words: zeolite, silicogermanate, IM-12, post-treatment, stabilization, substitution, DFT, NMR, n-alkane conversion.

Résumé

Les zéolithes sont des aluminosilicates cristallins microporeux composés d'arrangements tridimensionnels de tétraèdres SiO_4 et AlO_4 . Ces matériaux ont diverses applications dans les domaines de l'adsorption, de la catalyse, de la séparation et de l'échange d'ions. L'introduction du germanium lors de la synthèse de ces zéolithes est une stratégie pour accéder à de nouvelles structures, parfois avec des pores extra-larges, attractifs pour la transformation catalytique de molécules volumineuses. Cependant, un défi majeur reste la substitution du germanium par l'aluminium pour générer des structures présentant des sites acides. De plus, les silicogermanates microporeux sont souvent instables en présence d'eau après élimination des structurants organiques, ce qui limite leur utilisation. Pour stabiliser ces silicogermanates, récemment, deux approches expérimentales de post-traitement ont été développées. La première approche permet de maintenir la structure initiale de la zéolithe mère tandis que la seconde conduit à la création de nouvelles structures stables mais présentant des pores plus petits. Dans ce travail, une combinaison de calculs théoriques (DFT, Théorie de la fonctionnelle de la densité) et de travaux expérimentaux (synthèse, caractérisation, catalyse) est utilisée pour explorer la stabilisation des silicogermanates. L'étude *ab initio* montre que tous les silicogermanates ayant des codes structuraux attribués par l'Association Internationale des Zéolithes et leurs analogues (alumino)silicates sont intrinsèquement stables. Elle indique également que la substitution du Ge par Si ou Al est possible thermodynamiquement et est favorable en utilisant des chlorures. En conséquence, une unité de traitement au tétrachlorure de silicium a été utilisée pour la première fois pour remplacer le Ge par du Si. Ce traitement a permis la stabilisation de la structure cristalline de la zéolithe IM-12. D'autres traitements utilisant des solutions de chlorure de polyaluminium ou de trichlorure d'aluminium ont permis d'incorporer de l'aluminium dans la charpente de la zéolithe. Différentes techniques élémentaires et physico-chimiques (DRX, physisorption d'azote, FX, ICP, FTIR et RMN du solide) ont été utilisées pour caractériser les matériaux tout au long de la procédure de traitement. Des modèles DFT du bulk et des surfaces externes de la structure UTL, en variant la composition élémentaire, ont été construits et ont contribué à l'attribution des spectres expérimentaux de RMN MAS. Enfin, les matériaux obtenus ont été testés comme phase acide pour l'hydroisomérisation bifonctionnelle du n-décane et du n-hexadécane, reflétant une activité catalytique prometteuse. Ces travaux ouvrent des perspectives pour l'utilisation catalytique de dérivés stables de zéolithes silicogermanates.

Mots-clés: zéolithe, silicogermanate, IM-12, post-traitement, stabilisation, substitution, DFT, RMN, conversion de n-alcane.

Samenvatting

Zeolites zijn microporeuze kristallijne materialen, opgebouwd met SiO_4 en AlO_4 tetrahedra. Ze worden ingezet als adsorbenten, katalysatoren, en ionen wisselaars in tal van toepassingen. Het toevoegen van germanium tijdens het kristallisatieproces van zeolieten leidt tot de vorming van nieuwe structuren met vaak wijdere poriën, wat aantrekkelijk is om grote moleculen toegang te verschaffen tot de poriën waarin de katalytisch actieve plaatsen zich bevinden. Dergelijke silicium germanaten hebben echter twee belangrijke nadelen. Ze zijn onvoldoende zuur voor de zure katalyse, en ze zijn onstabiel wanneer ze, na evacuatie van tijdens de synthese ingebouwde organische moleculen uit hun poriën, aan water worden blootgesteld. Om deze zeolieten bruikbaar te maken voor de katalyse kunnen ze na hun kristallisatie aan een nabehandeling worden onderworpen. Eén benadering bestaat er uit om de in het zeolietrooster ingebouwde germanium atomen te vervangen door andere atomen, zoals aluminium en silicium. Een andere piste is het uitloggen van de germanium atomen en het zeolietrooster zich te laten herstellen door inkrimping tot nieuwe stabiele structuren met nauwere poriën. In dit werk werd de stabiliteit van dergelijke zeolieten geëvalueerd met theoretische berekeningen (DFT, Density Functional Theory) en experimenteel onderzoek van de nabehandelingen en hun invloed op katalytische eigenschappen. Ab initio berekeningen toonden aan dat de silicaat en aluminium silicaat analogen van silicium germanaten uit de zeolieten Atlas van de Internationale Zeoliet Associatie intrinsiek stabiel zijn. Deze berekeningen toonden verder aan dat systematische vervanging van Ge door Si of Al atomen een thermodynamisch gunstig proces is, vooral wanneer chloride precursoren gebruikt worden. Op basis van deze voorspelling werden silicium germanaten behandeld met siliciumtetrachloride om zo de germanium atomen in het rooster te vervangen door silicium atomen. De benadering werd met succes toegepast op een IM-12 zeoliet met structuurcode UTL. Ook aluminium kon worden ingebouwd door de zeolieten te behandelen met aluminiumchloride verbindingen. Het nabehandelingsproces en de bekomen zeolieten werden uitvoering gekarakteriseerd met fysicochemische technieken (X-stralen diffractie, N_2 porosimetrie, X-stralen fluorescentie, Inductively Coupled Plasma (ICP), Fourier Transform IR spectroscopie (FTIR) en Nucleair Magnetische Resonantie spectroscopie onder magische hoek rotatie (MAS NMR). DFT modellen van het oppervlak en het inwendige van de UTL structuren waren handig om de experimentele observaties tijdens de veranderende chemische samenstelling te verklaren. Tenslotte werden de nieuwe zeolieten geëvalueerd voor katalytische toepassingen. Veelbelovende resultaten werden geboekt in de bifunctionele omzetting van n-decaan en hexadecaan. Dit werk opent perspectieven voor tal van praktische toepassingen van met nabehandeling gestabiliseerde varianten van silicium germanaat zeoliten.

Trefwoorden: zeolite, silicium germanaat, IM-12, na de behandeling, stabilisatie, vervanging, DFT, NMR, omzetting van n-alkaan.

Résumé étendu

Les zéolithes sont des aluminosilicates cristallins microporeux impliqués dans diverses applications industrielles telles que l'adsorption, la catalyse, la séparation et l'échange d'ions. L'introduction du germanium dans leur synthèse permet l'obtention de nouvelles structures avec des pores extra-larges ce qui présente un fort intérêt pour la catalyse. Cependant, ces silicogermanates sont d'une part instables en présence d'eau après calcination, ce qui limite leurs applications, et d'une autre part nécessitent l'incorporation de l'Al dans la charpente afin d'introduire des cations de compensation H^+ qui donnent l'activité acide à la zéolithe. L'état de l'art montre que ces silicogermanates peuvent être stabilisés par substitution du Ge par du Si et de l'Al. Ces post-traitements peuvent soit maintenir la structure initiale soit la transformer en de nouvelles structures stables, mais ayant des ouvertures des pores réduites.

L'objectif de la présente thèse est de stabiliser un silicogermanate en maintenant sa structure initiale, tout en introduisant des sites acides, et de tester son activité catalytique. Afin de choisir la structure la plus appropriée pour mettre en œuvre cette démarche, une étude par calcul *ab initio* (en DFT, théorie de la fonctionnelle de la densité) de la stabilité de tous les silicogermanates attribués par l'IZA a été réalisée. Cette étude a montré que tous les silicogermanates et leurs analogues (alumino)silicates sont intrinsèquement stables. Cependant, ces analogues aluminosilicates ne peuvent souvent pas être préparés par synthèse directe mais pourront donc en principe être obtenus par post-traitement des silicogermanates. Les calculs DFT ont également montré que la substitution du Ge par du Si et de l'Al est thermodynamiquement possible et que les sources de type chlorures sont favorisées par rapport aux hydroxydes. Partant de cette conclusion, aucune préférence thermodynamique pour le choix du candidat n'a pu être retenue. Ainsi le choix de ce dernier a été basé sur l'analyse de la littérature. L'IM-12 (UTL) est un silicogermanate possédant des ouvertures de pores de 14 et 12 atomes T (T = Si ou Ge). Le post-traitement de ce silicogermanate a souvent conduit à des nouvelles structures avec des pores plus petits ou au maintien partiel de la structure initiale avec une perte importante de microporosité. Ainsi, stabiliser ce silicogermanate sans diminuer sa microporosité constitue-t-il le défi de cette thèse.

La substitution du Ge par du Si a été pour la première fois assurée par un traitement avec du $SiCl_4$ en phase gaz. Afin d'introduire de l'Al dans la zéolithe, deux modes d'alumination ont été testés : soit avec une solution aqueuse de chlorure de polyaluminium (PAC) soit avec une solution de trichlorure d'aluminium dans de l'éthanol. Différentes techniques de caractérisation élémentaires, physicochimiques et morphologiques ont été utilisées afin de suivre l'évolution du matériau après chaque étape de post-traitement. Après une étude d'optimisation des différents traitements, et pour la première fois à notre connaissance, de l'aluminium a été incorporé dans la zéolithe en utilisant la solution de PAC sans modifications importantes de sa structure initiale ni de son volume microporeux. La RMN MAS (Résonance Magnétique

Nucléaire avec rotation à l'angle magique) du ^{27}Al a mis en évidence la présence d'aluminium tetra et hexa-coordonné. Le traitement par du AlCl_3 a quant à lui permis la conservation de la structure UTL mais l'incorporation de très faibles quantités d'aluminium seulement, inférieures à la limite de détection de la RMN MAS ^{27}Al et de l'infrarouge (FTIR). Ce traitement nécessite plus d'optimisation.

Afin d'étudier la nature des sites acides présents dans l'IM-12 suite aux traitements avec du PAC, les groupements hydroxyles ont été observés par FTIR. Les spectres montrent la présence d'une quantité importante de silanols, et de très faibles quantités de sites acides pontés Si-OH-Al, ainsi que des Al-OH à la surface ou en extra-réseau. Ces distributions reflètent que l'Al n'a pas substitué tous les atomes de Ge extraits du réseau, engendrant cette augmentation de la quantité de silanols. Afin de déterminer si les substitutions se font à la surface externe ou interne de la cristallite de zéolithe, des modèles représentant des orientations possibles de la surface externe ainsi que des défauts ont été construits. Il a été montré que thermodynamiquement, la substitution à la surface externe ou à l'intérieur du cristal de zéolithe correspond à un gain d'énergie similaire. Ces mêmes modèles ont servi pour la prédiction par DFT des déplacements chimiques en RMN MAS. Les spectres expérimentaux en RMN MAS du proton des différents échantillons d'IM-12 ont été attribués en combinant des données de la littérature et les déplacements chimiques simulés. Les attributions ont reflété la présence de silanols, des Al-(H₂O) en liaison avec un oxygène de la charpente et des sites pontés Si-OH-Al. Ces différentes techniques spectroscopiques reflètent ainsi la présence de différents types de groupes hydroxyles liés à de l'Al. Afin de quantifier l'acidité de Brønsted et de Lewis des échantillons, l'adsorption de pyridine comme molécule sonde basique, a été suivie par la FTIR. Cette analyse met en évidence la présence de très faibles quantités de sites acides de Brønsted et Lewis comparé à des zéolithes classiques.

Enfin, ces matériaux ont été engagés dans la préparation de catalyseurs bi-fonctionnels qui ont été évalués pour l'hydro-isomérisation des n-alcane. Deux n-alcane ont été testés : le n-décane et le n-hexadécane. L'hydro-isomérisation du n-décane est une réaction modèle donnant des informations sur la topologie des zéolithes et sur la localisation des sites actifs. En se basant sur les différents critères de cette réaction modèle, il a été démontré que ces catalyseurs présentent des ouvertures de pores larges. Par contre, certains d'entre eux semblent être à l'origine de contraintes de diffusion liées à la distribution de l'acidité à l'intérieur de la porosité des cristaux de zéolithe IM-12, qui sont de grande taille, autour de $7 \times 6 \mu\text{m}$ avec des épaisseurs de l'ordre de 350 nm. Cette distribution peut être différente en fonction des étapes de traitement d'alumination. La deuxième réaction étudiée est celle de l'hydro-isomérisation du n-hexadécane. L'augmentation de la taille de la chaîne carbonée est en effet susceptible de donner des informations sur l'accessibilité des sites acides. L'hydro-isomérisation du n-hexadécane a confirmé certains des résultats obtenus pour le n-décane, mais le classement entre échantillons en termes d'activité n'est pas le même dans les réactions test de transformation du n-décane et

du n-hexadécane. Ces résultats sont interprétés en termes de différences de localisation des sites acides au sein des cristaux. Enfin, ces tests montrent que les zéolithes IM-12 traitées avec du PAC présentent une activité significative (en termes de fréquence de rotation) en comparaison à d'autres zéolithes ayant un contenu en Al plus important. En revanche, les zéolithes traitées avec $AlCl_3$ présentent une activité trop faible pour que cette dernière puisse s'exprimer en catalyse : le catalyseur bifonctionnel correspondant présente essentiellement les caractéristiques d'un catalyseur métallique (hydrogénolyse).

Ces travaux montrent d'un point de vue théorique et expérimental que la stabilisation et la fonctionnalisation de la zéolithe IM-12 pourront être assurées par la substitution du Ge par du Si et de l'Al, ouvrant les perspectives pour l'utilisation en catalyse industrielle des dérivés stables de zéolithes de type silicogermanates.

ACKNOWLEDGEMENTS	III
ABSTRACT	V
RESUME	VI
SAMENVATTING	VII
RESUME ETENDU	IX
INTRODUCTION	1
1. LITERATURE STUDY	5
1.1. ZEOLITES OVERVIEW	5
1.1.1. DEFINITION.....	5
1.1.2. HISTORY AND APPLICATIONS.....	7
1.1.3. ZEOLITES SYNTHESIS MECHANISM.....	8
1.2. GERMANIUM AND ZEOLITES	14
1.2.1. GERMANIUM PROPERTIES.....	14
1.2.2. SILICOGERMANATES.....	15
1.3. POST-TREATMENTS OF SILICOGERMANATES	21
1.3.1. MAINTAINING THE INITIAL STRUCTURES OF INITIAL SILICOGERMANATES	22
1.3.2. CREATING NEW STRUCTURES THROUGH ACID LEACHING.....	37
1.4. BIFUNCTIONAL ZEOLITE CATALYSTS	48
1.4.1 GENERAL MECHANISM OF N-DECANE HYDROISOMERIZATION ON BIFUNCTIONAL ZEOLITES	48
1.4.2 REACTION MECHANISMS INVOLVED IN N-DECANE HYDROCONVERSION.....	50
1.4.3 RELATIONSHIP BETWEEN N-DECANE HYDROCONVERSION AND ZEOLITE TOPOLOGIES (N- DECANE CRITERIA)	54
1.4.4 COMPARISON OF N-DECANE HYDROCONVERSION OVER DIFFERENT BIFUNCTIONAL ZEOLITES	58
1.5. CONCLUSION AND STRATEGY OF THE THESIS	61
2. EXPERIMENTAL AND COMPUTATIONAL METHODS	63
2.1. EXPERIMENTAL PROCEDURES	63
2.1.1. PREPARATION OF (6R,10S)-6,10-DIMETHYL-5-AZONIASPIRO [4,5] DECANE (OSDA) ...	63
2.1.2. IM-12 HYDROTHERMAL SYNTHESIS.....	64
2.1.3. IM-12 CALCINATION	64
2.1.4. POST –TREATMENTS OF IM-12	64
2.1.5. PREPARATION OF BIFUNCTIONAL IM-12 CATALYSTS.....	67
2.1.6. CATALYTIC TESTING.....	67
2.2. CHARACTERIZATION TECHNIQUES	70
2.2.1. X-RAY DIFFRACTION (XRD).....	70

2.2.2.	NITROGEN PHYSISORPTION	71
2.2.3.	THERMOGRAVIMETRIC ANALYSIS (TGA)	71
2.2.4.	SCANNING ELECTRON MICROSCOPY (SEM).....	71
2.2.5.	X-RAY FLUORESCENCE SPECTROMETRY (XRF)	72
2.2.6.	INDUCTIVELY COUPLED PLASMA- OPTICAL EMISSION SPECTROMETRY (ICP-OES)	72
2.2.7.	NUCLEAR MAGNETIC RESONANCE (NMR)	73
2.2.8.	INFRARED SPECTROSCOPY (IR).....	76
2.3.	DENSITY FUNCTIONAL THEORY (DFT) CALCULATIONS	77
2.3.1.	ROLE OF DFT IN THE RESOLUTION OF SCHRÖDINGER EQUATION.....	78
2.3.2.	GEOMETRY OPTIMIZATION AND ENERGIES OF SILICOGERMANATES STRUCTURES	80
2.3.3.	STATISTIC THERMODYNAMIC CALCULATIONS	81
2.3.4.	COMPUTATIONAL METHOD USED IN OUR WORK.....	82
3.	AB INITIO INVESTIGATION OF THE RELATIVE STABILITY OF SILICOGERMANATES AND THEIR (ALUMINO)SILICATES COUNTERPARTS. 87	
3.1.	CHOICE OF GE AND AL DISTRIBUTION.....	89
3.2.	INTRINSIC STABILITY OF SILICOGERMANATES AND THEIR (ALUMINO)SILICATES ANALOGUES.....	90
3.3.	ISOMORPHIC SUBSTITUTION OF GE FOR SI AND AL.....	94
3.4.	CONCLUSION	102
4.	CONSTRUCTION OF EXTERNAL SURFACE AND DEFECT MODELS OF IM-12 ZEOLITE	105
4.1	CONSTRUCTION OF THE EXTERNAL SURFACE MODELS OF IM-12.....	106
4.2	STABILITY OF STUDIED SILICEOUS EXTERNAL SURFACES	108
4.3	STABILITY OF ALUMINOSILICEOUS EXTERNAL SURFACES.....	111
4.3.1	SUBSTITUTION OF SI FOR AL ALONG (100)	111
4.3.2	SUBSTITUTION OF SI FOR AL ALONG (010)	113
4.4	DEHYDRATION OF EXTERNAL SURFACES	114
4.5	THERMODYNAMIC SUBSTITUTION OF GE FOR SI AND AL.....	116
4.6	CONCLUSION	118
5.	EXPERIMENTAL STABILIZATION OF THE IM-12 ZEOLITE.....	121
5.1	SYNTHESIS OF THE IM-12 ZEOLITE.....	122
5.2	POST-TREATMENT OPTIMIZATION	124
5.2.1	OPTIMIZATION OF CALCINATION / SI SUBSTITUTION / AL SUBSTITUTION SEQUENCE....	124
5.2.2	OPTIMIZATION OF THE SiCl ₄ TREATMENT	126
5.2.3	OPTIMIZATION OF POLYALUMINUM CHLORIDE (PAC) TREATMENT.....	131
5.2.4	OPTIMIZATION OF TRICHLORIDE ALUMINUM DISSOLVED IN DRY ETHANOL TREATMENT.....	136
5.3	PREPARATION OF A SERIES OF CATALYSTS BY SUCCESSIVE PAC TREATMENTS	142

5.3.1	STRUCTURAL AND TEXTURAL PROPERTIES	142
5.3.2	COMPOSITION OF THE SOLIDS AND ENVIRONMENT OF THE AL ATOMS	147
5.4	CONCLUSION	152
6.	UNDERSTANDING OF THE ACIDITY OF STABILIZED IM-12 ZEOLITE	155
6.1	IDENTIFICATION OF THE HYDROXYL GROUPS BY FOURIER TRANSFORM INFRARED (FTIR).....	155
6.2	CONSTRUCTION OF BULK MODELS WITH DEFECTS	157
6.3	IDENTIFICATION OF THE HYDROXYL GROUPS BY ¹H MAS NMR	160
6.3.1	ASSIGNMENT OF THE ¹ H MAS NMR SPECTRA	162
6.3.2	STUDY OF THE POST-TREATMENT EFFECT USING ¹ H MAS NMR	163
6.3.3	ASSIGNMENT AND COMPARISON OF ¹ H/ ²⁷ AL TRAPDOR SPECTRA	163
6.4	BRØNSTED AND LEWIS ACIDITIES MEASURED BY PYRIDINE ADSORPTION	164
6.5	CONCLUSION	167
7.	CATALYTIC TESTING OF IM-12 IN THE HYDROISOMERIZATION OF HYDROCARBONS	169
7.1.	HYDROISOMERIZATION OF N-DECANE	169
7.1.1.	HYDROISOMERIZATION OF N-DECANE OVER Pt/IM-12_Si ₃ Ge.....	169
7.1.2.	HYDROISOMERIZATION OF N-DECANE OVER IM-12 BI-FUNCTIONAL CATALYSTS PREPARED BY PAC TREATMENTS	170
7.1.3.	HYDROISOMERIZATION OF N-DECANE OVER IM-12 BI-FUNCTIONAL CATALYSTS PREPARED BY AlCl ₃ TREATMENTS	178
7.2.	HYDROISOMERIZATION OF N-HEXADECANE OVER IM-12 BI-FUNCTIONAL CATALYSTS PREPARED BY PAC OR AlCl₃ TREATMENTS.....	181
7.2.1.	ACTIVITY AND ISOMERIZATION SELECTIVITY	181
7.2.2.	DETAILED ANALYSIS OF THE ISOMER DISTRIBUTION: INSIGHTS TOWARD LOCALIZATION OF THE ACTIVE SITES	183
7.3.	CONCLUSION	187
	CONCLUSIONS AND PERSPECTIVES.....	189
	REFERENCES	193
	APPENDIX CHAPTER 3.....	1
	APPENDIX CHAPTER 4.....	7
	APPENDIX CHAPTER 5.....	10
	APPENDIX CHAPTER 6.....	15
	APPENDIX CHAPTER 7.....	20
	REFERENCES OF APPENDICES.....	24

Introduction

Since the synthesis of the first synthetic zeolite in the 1940s^[1], researchers regularly have succeeded to synthesize new zeolite structure types. These zeolite materials are conventionally obtained by heating under autogenous pressure a hydrogel made of amorphous silica and alumina at high pH in the presence of an inorganic cation (i.e. Na⁺, K⁺, etc.) and/or an organic structuring agent (i.e. quaternary alkylammonium). Other framework elements than Si and Al have also been introduced in the synthesis media, such as phosphorus, titanium or germanium giving rise to so-called zeolite related solids, generally also called zeolites by misuse of language by materials scientists^[2]. While natural zeolites have aluminosilicate composition, synthetic specimen can have any chemical composition, as long as the oxide framework can be described as a four connected network of tetrahedral (called “T sites”). The introduction of hetero elements led to many new structures. For example, the aluminophosphate family was born in the 1980s, giving dozens of original structure types.

Of these hetero-elements introduced into the synthetic gels, germanium has played a special role for about twenty years. The introduction of this element, sometimes coupled with the use of the fluorine element has resulted in many new zeolite structures. In addition, the introduction of Ge allowed the obtaining of very open zeolite structures with large pores. Among these zeolites, one can quote the zeolite ITQ-37 (structural type -ITV)^[3] having pore openings with 30 T- atoms, the zeolite ITQ-33 (structural type ITT)^[4] with pore openings at 18 and 10 T sites or the IM-12 (structural type UTL)^[5] having pore openings with 12 and 14 T sites.

However, the interest of germanium is counterbalanced by a major drawback lying in the ease of hydrolysis of the Ge-O bond. Therefore, these zeolites containing germanium are unstable after calcination if exposed to moisture, and cannot withstand the conventional conditions for preparing an adsorbent or a catalyst^[6]. Indeed, in order to be used in this type of applications, silicogermanates must undergo ion exchange and/or shaping steps which are performed in aqueous medium incompatible with their poor stability^[7].

Two main approaches for silicogermanates post-treatments exist. The first approach developed by Valtchev et al.^[8] consists of stabilizing Ge zeolites by direct substitution of Ge for another structural element such as Aluminum. This approach has been used to stabilize the ITQ-17 zeolite (Polymorph C of zeolite Beta, BEC structural type). The as-synthesized zeolite, containing its structuring organic agent occluded in its porosity, was treated with a solution of hydrated aluminum chloride. An exchange between Ge and Al within the framework occurred leading to an increase of Si/Ge ratio from 3.6 to 5.2, which is sufficient to stabilize the final solid.

A second approach presented in the literature takes advantage of the instability of silicogermanates to transform them into new stable structures. This concept has been studied on the IM-12 zeolite (of UTL structural type) by J. Martens et al. and was called the inverse sigma transformation^[9] and by J. Čejka et al. and was called ADOR (Assembly-Disassembly-Organization-Reassembly) process^[10]. The IM-12 zeolite has a structure that consists of layers interconnected by double four ring (d4r) units containing germanium and silicon. Following the inverse sigma transformation, a treatment in acidic medium extracted a part of these Ge from the framework leading to a structure called Ge-COK-14. By further washing, it was then possible to extract the remaining Ge from the porosity of this structure giving an interrupted structure called -COK-14. A heat treatment dehydrated this structure yielding a new zeolite called COK-14. While following the ADOR process, the UTL zeolite was completely disassembled into layers through acid treatment, then an intercalation agent was added such as diethoxydimethylsilane or octylamine followed by calcination leading to the reassembly into new zeolites IPC-2 (12 and 10 MR) of OKO structural code and IPC-4 (10 and 8 MR) with a PCR structural code. It is then possible to transform an unstable structure (Si-Ge) into a new stable zeolite (Si) but with smaller pores.

Petkov et al.^[11] studied by molecular modeling the stability of the ITQ-44 zeolite when Ge was substituted by different elements such as silicon, aluminum or zinc. These Density Functional Theory (DFT) calculations show that from a thermodynamic point of view, the structure of the zeolite ITQ-44 is stable in the absence of germanium even if it is not possible to date to synthesize this solid without Ge. It has also been shown that the incorporation of aluminum into an ITQ-44 silicic zeolite is favorable, which tends to show that it must be possible to obtain this zeolite in a Si/Al form either by direct synthesis or by post-treatment. These works are interesting because they show that other zeolites than the BEC treated by Valchev et al. must be able to be stabilized by appropriate post-treatments.

The literature describes more than fifty zeolites containing germanium but few articles state their stabilization and/or their use for catalysis applications. The challenging objectives of this work are thus to stabilize a silicogermanate without reducing its microporosity, and to incorporate Al in its framework. The latter requires the presence of compensation cations providing the zeolite an acidic activity.

The strategy followed was to first select a candidate based on a study of the intrinsic stability of known silicogermanate zeolite structures and their silicate and aluminosilicate analogues using periodic density functional theory calculations. Then the thermodynamics of isomorphic substitution of Ge atoms for Si and Al via chemical processes were investigated using different reactants by DFT. Afterwards, the selected candidate was treated using different post treatment procedures. To optimize the treatment conditions, different characterization techniques have been used like XRD, N₂ physisorption, XRF, ICP, FTIR, ¹H, ²⁷Al MAS NMR and adsorption

of pyridine followed by FTIR. In addition, surface models of the selected zeolite and its bulk have been built. They served for modeling the DFT NMR shifts to help assigning the experimental chemical shifts. The latter help understanding the environment of incorporated aluminum and of the active sites. Finally, the obtained materials were tested in the hydroisomerization of n-alkanes with different carbon chain lengths.

A bibliographic review of zeolites, silicogermanates synthesis, their post treatments and the hydroisomerization of alkane principle is presented in chapter 1.

In chapter 2, the experimental procedures of zeolites synthesis, post-treatments and catalytic testing are described. In addition, the different characterization techniques and their protocols are reported. A brief description of the DFT principle and of the used molecular modeling methods is also included.

In chapter 3, an *ab initio* investigation of the relative stability of all silicogermanates that have structural codes attributed by the International Zeolite Association and their (Alumino)Silicates counterparts is discussed. Then, an evaluation of the thermodynamic features of the substitution reactions of Ge for Si and Al is performed. The effect of the topology and the Ge distribution on these substitutions is also discussed.

Chapter 4 discusses the selection of one silicogermanate candidate, namely the IM-12 zeolite. To have an understanding of the surface of this zeolite, different external surface models were constructed. Moreover, the substitution of Ge for Si and Al at the surface of this zeolite was also investigated computationnally.

Chapter 5 presents the characterization of the IM-12 zeolite selected for the experimental investigation and the optimization of the experimental post-treatments, monitored by various characterization techniques, including MAS NMR. A series of substituted IM-12 materials is then selected for the next parts of the study.

Chapter 6 reports a study of the nature of the surface groups, and of the acidity of stabilized IM-12 zeolites, combining IR and MAS NMR. To have a deeper understanding of the obtained results, constructions of defect models inside the bulk of IM-12 crystals and the stability of possible acid sites were undertaken. Moreover, ^1H MAS NMR and $^1\text{H}/^{27}\text{Al}$ TRAPDOR MAS NMR were measured and compared to ^1H NMR chemical shift calculated by DFT. The acidity of post-treated IM-12 zeolites was then quantified using adsorption of pyridine followed by FTIR.

In chapter 7, the catalytic properties of IM-12 as an acid phase for the bifunctional hydroisomerization of n-alkanes are measured. Two n-alkanes were chosen: n-decane and n-

hexadecane. The hydro-conversion of n-decane is a model reaction that gives information on the topology and active sites distribution. Testing an alkane with longer carbon chain such as n-hexadecane might give additional information of the accessibility of the active sites of different IM-12 bi-functional catalysts.

Finally, a general conclusion is provided followed by possible perspectives to the present work.

1. Literature Study

1.1. Zeolites overview

1.1.1. Definition

The term "zeolite" refers to Greek ζέω (zēō), meaning "to boil" and λίθος (líthos), meaning "stone". Zeolites constitute a well-defined class of crystalline aluminosilicates that are frequently found in nature. They have three-dimensional structures formed by the arrangement of tetrahedral $[\text{SiO}_4]^{4-}$ and $[\text{AlO}_4]^{5-}$ linked by bridging oxygen atoms^[12]. This organization generates regular micro-pores giving rise to cages and channels distributed periodically inside the solid, see Figure 1- 1.

These channels allow the diffusion of molecules with compatible diameters. The channels dimensions are conventionally defined by the ring size of the aperture, where, for example, the term "12-members ring" refers to a closed loop that is built from twelve tetrahedral coordinated T sites and twelve oxygen atoms. T sites can be a Si or an Al atom.

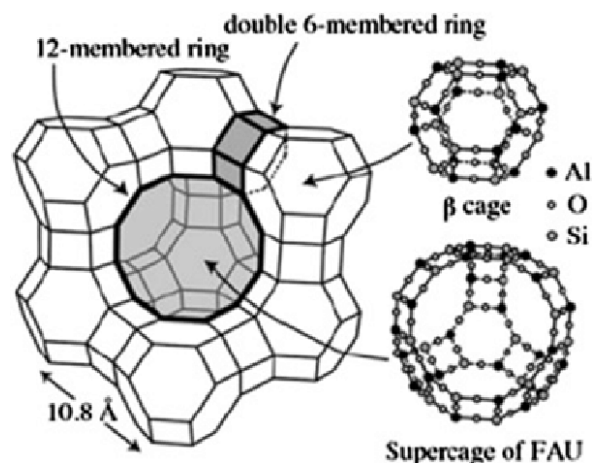


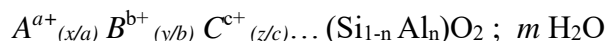
Figure 1- 1: Structure of the Faujasite zeolite^[13].

A zeolite structure can be viewed as an assembly of secondary building units (SBU's). These SBU's, 23 in number, are non-chiral and chosen considering that the entire structure can be described by using only one type of SBU. A number of units, such as double-6-ring (d6r) or Sodalite cages (sod), appear in different structures and may be useful to look for similarities between materials. These units are called Composite Building Units (CBU's), some of them are showed in Figure 1- 2. Unlike SBU's, they do not have to be achiral or to build the entire framework^[14]. A particularly interesting CBU in this thesis work is the unit consisting of a double four ring denoted d4r, to which reference will often be made in the following chapters (Figure 1- 3).

The presence of aluminum in the zeolite induces a charge within the structure. In fact, Aluminum has a degree of oxidation of + III, so when replacing silicon atoms (degree of oxidation + IV) it creates a deficit of charges in the zeolite. With respect to a purely silicic and

electrically neutral zeolite, an aluminosilicate material will therefore be charged overall negatively. This deficit of positive charges is counterbalanced by the compensating cations in the zeolite: alkaline cations (Na^+ , K^+ , etc.), alkali metals cations (Ca^{2+} , Mg^{2+} , etc.) or organic cations for example will assure the electro-neutrality of the material^[15].

The general formula of an aluminosilicate zeolite can be written as follows:



Eq. 1- 1

Where A,B,C... are different compensation cations with a,b,c valencies respectively and $x+y+z = n$ ^[12].

The different topologies of zeolites have a structural code composed of three letters that is attributed by the Committee of Structures of the International Zeolites Association (IZA). This code is related to the name of the material or research team at the origin of its discovery, for example the UTL topology of the IM-12 zeolite derives from Mulhouse twelve^[14]. To date, there are 245 unique structural codes^[16].

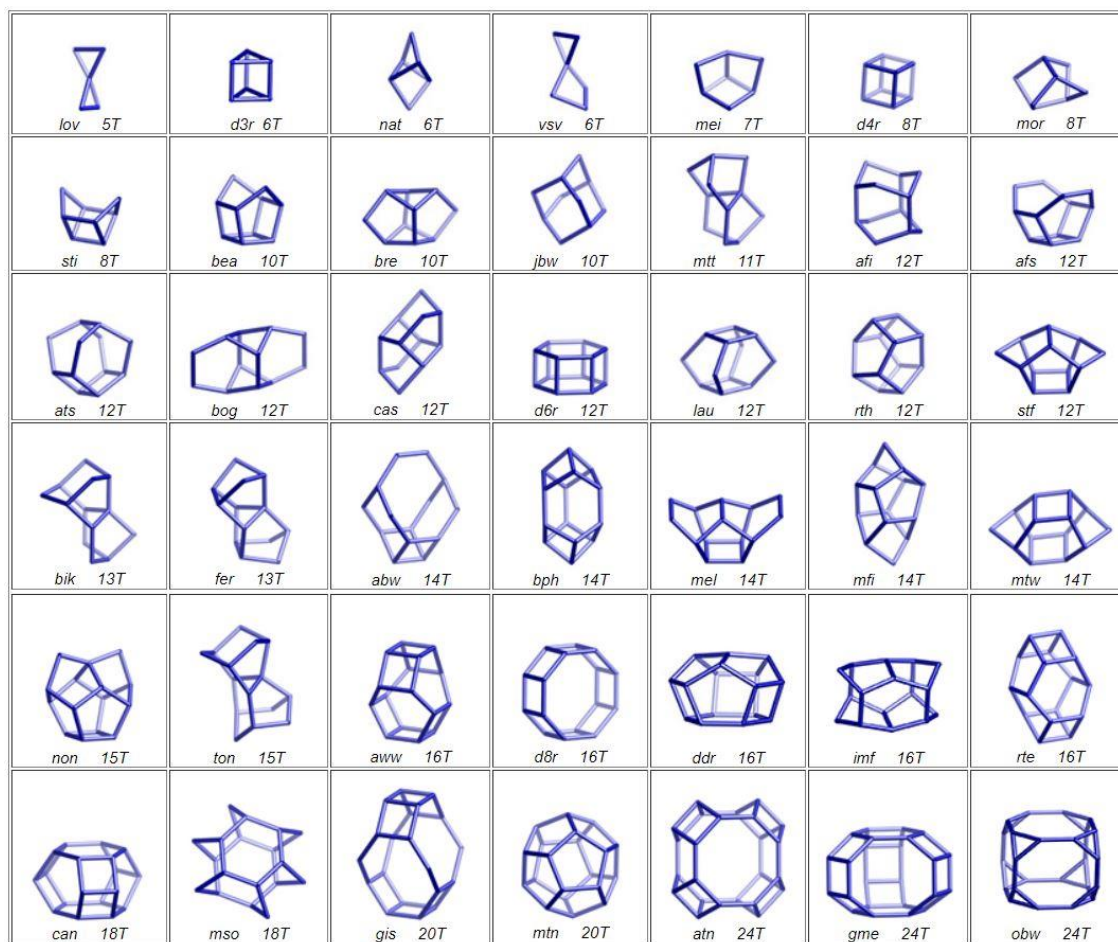


Figure 1- 2: Composite Building Units, their symbols and their T atoms number^[16].

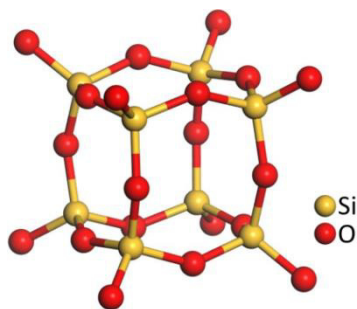


Figure 1- 3: Double four ring (d4r).

1.1.2. History and applications

In 1756, with the discovery of the natural zeolite “stilbite”, by the Swedish mineralogist Cronstedt, the history of zeolites began. He recognized zeolites as hydrated aluminosilicates of the alkaline earths^[17]. In 1840, Damour observed that zeolites dehydration is reversible and does not affect zeolites morphology^[18]. Later in 1845, the synthesis of quartz by heating silica with water in an autoclave was described^[19]. Afterward, in 1850 and 1858 the ion exchange in soils and its reversibility on zeolites respectively were studied^[20]. In 1862, the first hydrothermal synthesis of a zeolite, Levynite (LEV) was reported^[21]. From 1896 to 1930 an important number of studies were made on the ion exchange, adsorption and molecular sieving on zeolites and also on their synthesis and structural properties^[22–25].

Barrer’s work from 1940 to 1948 launched the zeolites industrial synthesis. Considering the molecular size, he defined the first classification of the existing zeolites. He also described the synthetic procedure to obtain a zeolite, e.g. the analogue of Mordenite, a naturally existing zeolite^[26].

In 1954, Union Carbide commercialized synthetic zeolites for separation and purification applications. Then, in 1959 it marketed the first bulk process for normal isoparaffin separation using molecular sieving selectivity and an isomerization catalyst. Later Mobil oil used zeolite X as a cracking catalyst, Henkel introduced zeolites in detergents and Union Carbide launched the use of zeolites for ion exchange^[1].

The 80’s and 90’s period is a blowout of new molecular sieves structures. In the 80’s, the aluminophosphate (AlPO_{4-n}), silicoaluminophosphate (SAPO) and metal aluminophosphate (MeAPO) families were discovered^[27]. Also, metallosilicates were formed through the introduction of metals like Iron, Germanium and others during the synthesis^[28]. Moreover, modification chemistry of zeolites such as prolonged steaming, and treatments with aqueous ammonium fluorosilicate and silicon tetrachloride were reported. In the 90’s and until today, more novel structures have been synthesized and 245 framework type codes have been assigned by the IZA^[1,16].

Note that the worldwide annual market for synthetic zeolites raised from 1.7 in 1998 to 5.2 billion dollars in 2018. The major application was the ion exchange in detergent, followed by catalysis and adsorption applications^[29].

1.1.3. Zeolites synthesis mechanism

Synthetic zeolites are generally obtained by hydrothermal treatment where silica, alumina and a cation source are mixed together in basic or fluoride media. In many cases, an organic compound, known as the structure directing agent is added. The reaction mixture can have either a high pH or a neutral pH when OH⁻ or F⁻ mineralizers are used. This solution is heated at the desired temperature (usually 90-220°C) under autogenous pressure. The reagent mixture amorphous gel will then be transformed into zeolite crystals. Figure 1- 4 illustrates this procedure^[30].

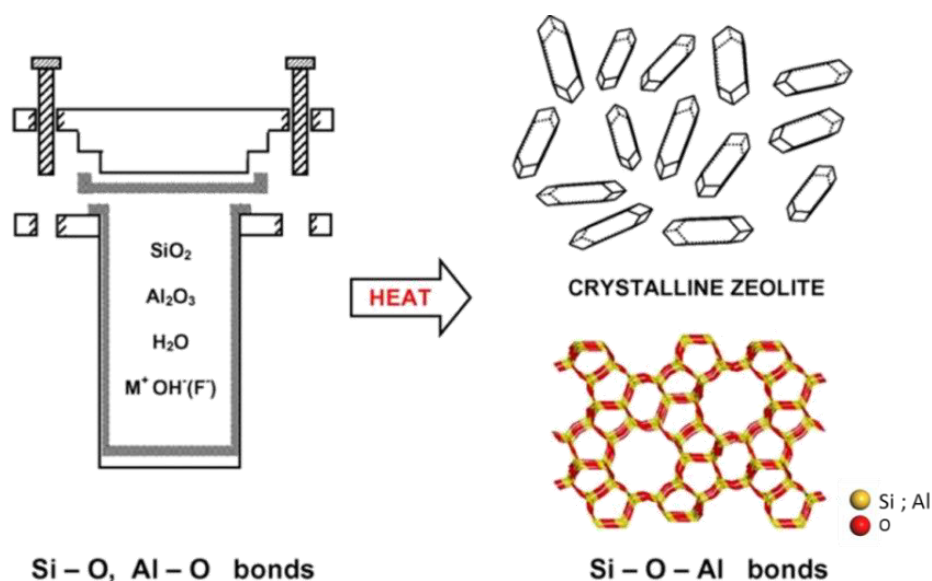


Figure 1- 4: Hydrothermal zeolite synthesis^[30].

Many studies aim to understand the synthesis mechanism. Table 1- 1 presents the different proposed mechanisms. For Barrer et al., zeolite crystallization is a solution mediated process where secondary building units in the form of rings of tetrahedral or polyhedral are connected with different coordination leading to a diversity of aluminosilicates structures^[31]. These authors also proposed that full ionization is not a restriction and oxygen atoms linked to one Al or Si can exist as -OH groups available for condensation/polymerization giving more complex units.

Flanigen and Breck evoked “that growth of the crystal proceed through a type of polymerization and de-polymerization process which involves both the solid and liquid phases”^[32,33]. Later, Breck suggested that hydroxyl ions such as provided by sodium hydroxide depolymerize aluminate and silicate species. The resulting supersaturated gels yield to a large number of nuclei. The growth of these nuclei during the crystallization phase leads to ordered zeolites^[34].

In 1966, Kerr's experiment showed that a sodium hydroxide solution was able to dissolve an amorphous prepared sodium aluminosilicate forming an amorphous substrate. When this solution was in contact with a zeolite Na-A at 100°C for 4h, the mass of zeolite doubled proving that zeolites are formed through the dissolution of the amorphous gel superseded by the combination of these soluble species^[35].

Afterwards, Zhdanov^[36] deduced that temperature increases the rate of crystal growth for a zeolite and that all along the synthesis, this rate is almost stable. He also studied the chemical changes in the solution phase and the nucleation rate during the reaction. All these observations, allowed him to prove that solid and liquid phases of aluminosilicate gels are connected by the solubility equilibrium which means that aluminosilicate and silicate ions are always present in the liquid phase. Once the gel is heated, its solubility increases, hence the concentration of the silicate, aluminate, and aluminosilicate ions rises in the liquid phase. As a result, the probability of condensation reactions between the ions increases, leading to the formation of primary aluminosilicate blocks (4- and 6-membered rings) and crystal nuclei. The formation and growth of crystal nuclei consume silicate, aluminate, and aluminosilicate ions of the liquid phase, and the equilibrium state is reached by permanent dissolving of the solid part of the gel phase. Since zeolite crystals' solubility is much lower than that of the amorphous aluminosilicate skeleton of gels, the crystallization process continues until the complete dissolution of the amorphous phase.

Later, the idea of introducing organic templates into the zeolites synthesis was elaborated and Wadlinger reported the first high silica zeolite beta made using tetraethylammonium cation^[30,37].

Then, Derouane et al. proposed two mechanisms for ZSM-5 crystallization in presence of an organic template^[38]. With low Si/Al ratios few nuclei appear in the liquid phase and grow eventually to large crystallites which may show strongly inhomogeneous aluminum radial distributions. In this case, higher depolymerization rates (higher pH and higher activity of silica) would yield to smaller and more homogeneous crystallites. While with high Si/Al ratios the process takes place in the solid hydrogel phase/surface nucleation, where numerous nuclei are formed giving polycrystalline aggregates. The aluminum distribution is homogeneous if crystallization is terminated as soon as the crystallinity of the solid phase reaches 100%. If, however, longer synthesis times are used, such crystallites are covered by an Al free shell of isostructural silicate.

Chang and Bell^[39] studied the mechanism of ZSM-5 formation by combining XRD, ²⁹Si MAS NMR spectroscopy and ion exchange. The ²⁹Si MAS NMR spectra exhibited two broad features associated with Q³ [-95 to -104 ppm] due to silanol groups, or framework defects, and Q⁴ [-104 to ca. -115 ppm] attributed to Si connected to 4 T-atoms through O-atoms. Therefore the ratio of intensities of Q³/Q⁴ provides an indication of the progress of gel transformation. This is

plotted in Figure 1- 5, along with XRD crystallinity. The Q^3/Q^4 ratio decreases very rapidly compared to the crystallization rate, with the greatest change occurring during the induction period and the early stages of crystallization. In summary, ^{29}Si MAS NMR results suggest that the major changes in gel structure occur during the early stages of reaction. This was confirmed by the demonstration of ion sieve effect indicating that in ZSM-5 synthesis using tetrapropylammonium cation (TPA^+) and a starting composition of $\text{Si}/\text{TPA}^+ = 10$, leads to embryonic structures with $\text{Si}/\text{TPA}^+ = 20-24$ which are formed rapidly upon heating. These embryonic units resemble ZSM-5 channel intersections, 4 per unit cell of 96 tetrahedral atoms each containing essentially one TPA^+ cation providing a possible mechanism for ZSM-5 nucleation. In this mechanism, the hydrophobic effect and the isomorphism between water and silicate structure lead to 1) the formation of clathrate-like water structure around the template, 2) conversion of the clathrate-like hydrate to clathrate-like silicate by isomorphous substitution of silicate for water in the embryonic units, which resemble ZSM-5 channel intersections, 3) progressive ordering of these entities into the final crystal structure through repeated cleavage and recombination of siloxane bonds mediated by hydroxide ion.

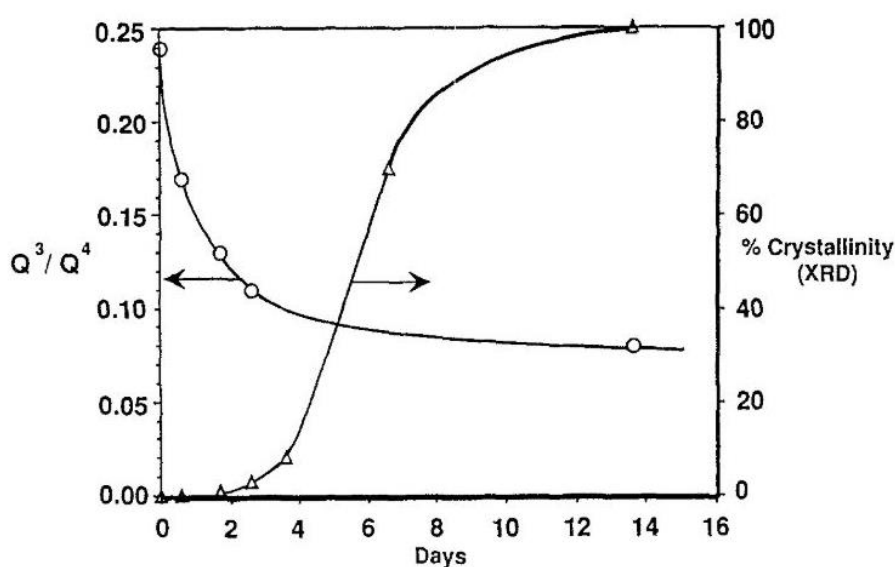


Figure 1- 5: Variation of Q^3/Q^4 with X-ray crystallinity of the zeolite synthesis gel^[39].

Burkett and Davis^[40] extended the principal concept proposed by Chang and Bell. They proved through ^1H - ^{29}Si CP MAS NMR spectroscopy the existence of close interactions between the TPA^+ cations and the silicate species leading to a pre-organized inorganic-organic composite structure where TPA^+ molecules take up a configuration similar to that adopted in the zeolite product. In fact, overlapping of the hydrophobic spheres of organic and inorganic components leads to the formation of these composites. Van der Waals interactions are then established during the heating of the zeolite synthesis gel. These inorganic-organic composite structures are involved in nucleation and subsequent crystal growth through diffusion of these species to the surface of the growing crystallites.

R. Ravishankar et al. studied extensively the mechanism of zeolites formation, particularly that of a silica polymorph: silicalite-1 with MFI topology using different physico-chemical techniques. They proved, from clear solution, that an initial formation of a precursor takes place leading to the formation of nano-slabs with a well-defined size and a specific structure, present before and during the growth of the final crystals^[41,42].

The initial precursor should be formed during the initial contact of the silica source (TEOS) and the template (TPAOH) thus they observed the hydrolysis of TEOS and the poly-condensation process using ²⁹Si liquid NMR and in situ FTIR spectroscopy. After 45 minutes, the IR spectrum resembled to MFI-type zeolite with a displacement of the band corresponding to five ring structures, this shift was due to the small size of the silicate molecule containing the five rings and the lack of connectivity of these rings with a framework. ²⁹Si NMR also pointed at the formation of species containing five and three rings.

The poly-condensation process is presented in Figure 1- 6. Three of the TPAOH propyl are pointed into the TEOS layer, directing the formation of bicyclic pentamer, pentacyclic octamer and the tetracyclic undecamer. At 0°C, a phase boundary between TEOS and TPAOH is present and the tetracyclic undecamer departed to the aqueous layer does not interact with the TPA on its hydrophobic side leading to an internal condensation of the released species. While at room temperature, at the liquid-liquid interface, the TPA mold three tetracyclic undecamers to form the final trimer product containing the MFI framework fragment^[43]. Dilution with water of a concentrated solution of the trimer leads to the formation of subcolloidal particles known as nano-slabs having the MFI framework connectivity occluding TPA molecules and have specific dimensions. X-ray scattering (XRS) and gel permeation chromatography (GPC) show that four nonamers stacked along *b* inevitably conclude in the formation of the nano-slab. After aging, stacking of nano-slabs leads to the formation of intermediates reflecting a cluster growth mechanism^[44]. Finally the aggregation of these intermediates give large particles with Bragg diffraction characteristic of silicalite-1 zeolite^[45].

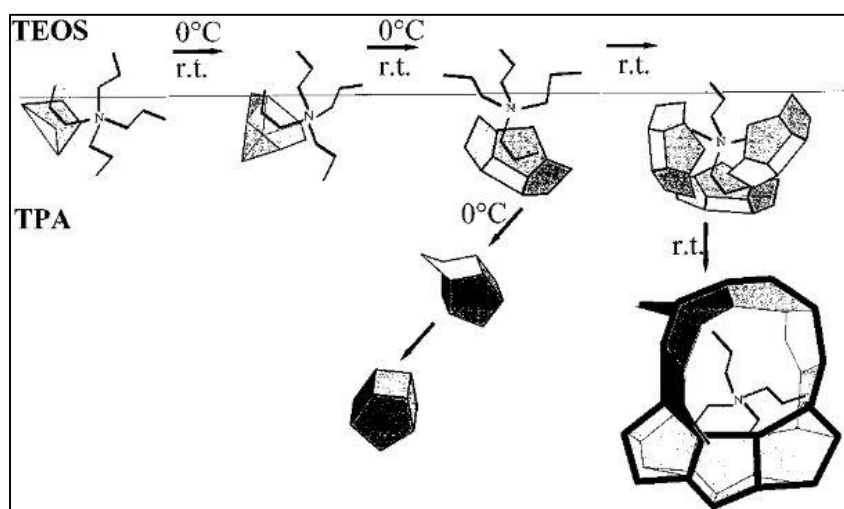


Figure 1- 6: Schematic presentation of the TPA-directed poly-condensation process of TEOS^[43].

Knight and Kinrade criticized the previously described mechanism considering that the proposed structures (pentacyclic octamer, tetracyclic undecamer, 33-mer, double five ring and capped double five ring) were not previously found in solution and that the eighteen known silica species were not considered in the study^[46]. Later, C.E.A Kirschhock et al. replied to this article proving the presence of the proposed silicate oligomers and their transformation through ²⁹Si NMR. They also detected the formation of a new intermediate and showed that temperature affect strongly the intermediates transformation^[47].

After that, Kragten et al. contradicted the previous results suggesting that the extracted particles are amorphous through experimental and simulated XRD pattern. ²⁹Si MAS NMR using simulated annealing showed nanoparticles with open shapes and internal defects meanwhile they questioned if the extraction method of nanoparticles have affected their initial structure in the solution^[48].

Later, Cundy and Cox proposed a global synthesis mechanism^[30] based on all the previously suggested mechanisms. Zeolite formation consists of three steps: induction period, nucleation and crystal growth, see Figure 1- 7.


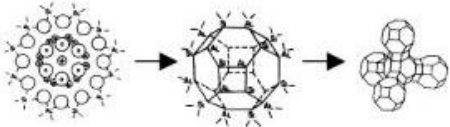
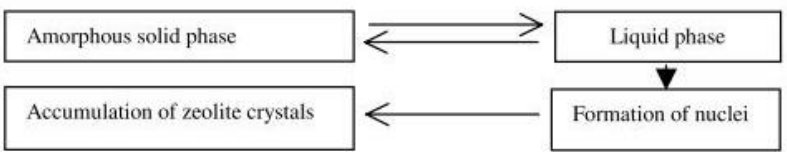
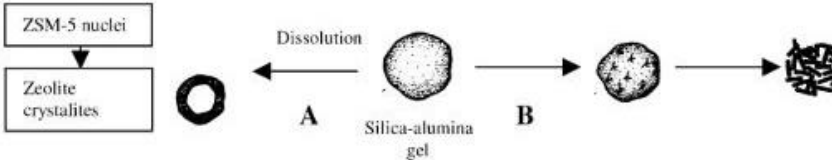
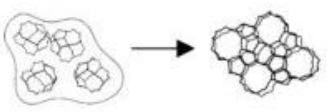


The induction period is the time between the start of the reaction and the time at which the first crystalline product is observed. Once the reactants are mixed, they form a gel referred as the primary amorphous phase, that is heterogeneous and not in equilibrium with the solution. After some time, due to balanced reactions, this phase is transformed into a pseudo steady state called the secondary amorphous phase having a similar chemical composition as the final crystalline product but without the establishment of the periodic zeolite lattice itself. Here cations play a structuring role in the organization of the solid phase.

The next step is the nucleation: the reconstructed areas have reached a critical nuclear size within a statistical distribution of ordered sites that enable such structure to propagate, known as nucleus.

The last step is the crystal growth, which is the successive addition of small particles. The cation is linked up to the surface of an amorphous particle. Monomer from solution units such as silicates attach to the growth site in an ordered way around the cation creating a cyclic unit, a new cation site is then generated so the coordination steps iterate and the cycle continues.

Note that not all the growth units forming the final crystal may have arrived from the solution. In the case where the amorphous phase is the nutrient supplier and host of nucleation sites, some local reconstruction of the gel may occur. Chemical reactions of this growth should be reversible so errors occurred during the process could be corrected and the structure could propagate.

Table 1- 1: Summary of principal proposals for zeolite synthesis mechanism^[30].

Author(s)	Principal system studied	Main features of mechanism	Schematic summary
Barrer	Various low-silica phases	Condensation polymerisation of polygonal and polyhedral anions	
Flanigen and Breck	Na-A, Na-X	Linkage of polyhedra (formed by M ⁺ -assisted arrangement of anions); crystal growth mainly in the solid phase	
Kerr	Na-A	Crystal growth from solution species	Amorphous solid $\xrightarrow{\text{fast}}$ soluble species(S) (S) + nuclei(or zeolite crystals) $\xrightarrow{\text{slow}}$ zeolite A
Zhdanov	Na-A, Na-X	Solid \leftrightarrow liquid solubility equilibrium, nuclei from condensation reactions, crystal growth from solution	
Derouane, Detremmerie, Gabelica and Blom	Na,TPA-ZSM-5	Synthesis "A": liquid phase ion transportation. Synthesis "B": solid hydrogel phase transformation	
Chang and Bell	Na,TPA-Si-ZSM-5	Embryonic clathrate TPA-silicate units, ordered into nuclei through OH ⁻ -mediated Si—O—Si cleavage/recombination	
Burkett and Davis	TPA-Si-ZSM-5	Pre-organised inorganic-organic composites, nucleation through aggregation, crystal growth layer-by-layer	
Leuven Group	TPA-Si-ZSM-5	Oligomers \rightarrow precursor "trimer" (33 Si) \rightarrow $\times 12$ \rightarrow "nanoslabs", growth by aggregation	

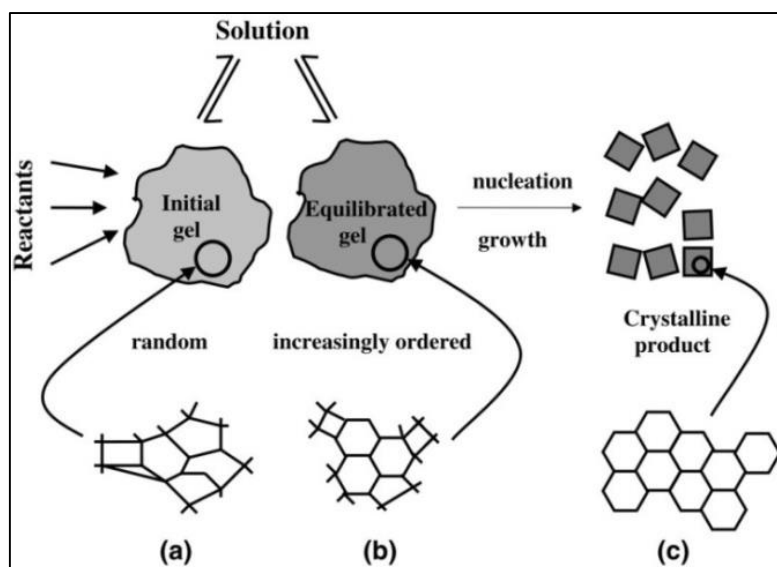


Figure 1- 7: The evolution of order, from the primary amorphous phase (a) through the secondary amorphous phase (b) to the crystalline product (c)^[30].

Summarizing, there are many visions and proposed mechanisms. It could well be that there exist many different mechanisms, depending on the zeolite type and the synthesis conditions. Depending on the research methodology and the experimental techniques, one may arrive at other observations and grasp only part of an overall picture^[49].

1.2. Germanium and zeolites

1.2.1. Germanium Properties

The introduction of hetero-elements into the synthesis medium of zeolites is interesting since it can lead to new structures. During the last decades, Germanium has played a special role as an “inorganic structure director”^[50]. This element has similar properties to silicon, both being members of the 14th column of the periodic table of the elements, e.g. ionization potential and electronegativity are close, 1.90 and 2.01 (Pauling) for Si and Ge respectively, explaining why GeO₂ crystallizes with the same enantiomorphic framework structures as quartz SiO₂.

In the other hand, Ge can exhibit coordination numbers of 4, 5 or 6 while that of Si is usually 4^[51]. Also, Ge-O bond is ~ 0.15 Å longer than the Si-O bond while \widehat{GeOGe} angle is narrower than the \widehat{SiOSi} angle by ~ 15°^[52], (Figure 1- 8).

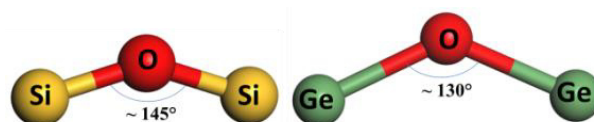


Figure 1- 8: (\widehat{GeOGe}) and (\widehat{SiOSi})^[52].

These differences can be explained by the fact that Ge cation (third row of the periodic table) is intrinsically larger than Si cation (second row) ^[53]. Based on these differences, the presence of Ge during the synthesis makes the formation of smaller polyhedral units easier, it is evident that double rings or double 3 rings are abundant in silicogermanates structures but rarely found in silicates or in aluminosilicates proving the stabilization role of Ge.

1.2.2. Silicogermanates

1.2.2.1. General features

Germanates have recently become an attractive group of the open framework materials. They have extra-large pores, up to 24 member rings such as ASU-16 (1D-24MR)^[54] and FDU-4 (24; 12; 8 MR)^[55] (Figure 1- 9.a and b respectively). Despite these interesting structures, the use of germanates in industrial applications is not affordable due to their high cost compared to silicates. Moreover, some of them have lower thermal stabilities. Silicogermanates can provide a compromise since their cost is reduced while they still have large pores ($\geq 12\text{MR}$). Corma and his group are the pioneers of silicogermanates, from 2001^[56] till today, they reported more than twenty silicogermanates referred to ITQ-n (Instituto de Tecnologia Quimica-n). Zeolite beta is a pure silica or aluminosilicate zeolite formed by an intergrowth of polymorphs A and B and it was predicted that a third polymorph could exist^[57] but was not obtained experimentally. Corma et al. synthesized this predicted polymorph C in the presence of Ge and named it ITQ-17^[56]. It has a 3 dimensional pore topology in which the 12 MR channels are linear (Figure 1- 9.c). It also contains double four ring units (d4r) in its structure which are absent in the polymorphs A and B. They also proved that polymorph C cannot be obtained in the absence of Ge while it can be prepared in the absence of F⁻ and with different structure directing agents indicating the importance of Ge in stabilizing this polymorph.

During the same year, the same team synthesized ITQ-16^[58], which contains the three polymorphs A, B and C of zeolite beta in its structure. The proportion of the three polymorphs is controlled by the choice of the organic structure directing agent and the Ge content in the synthesis gel. The introduction of Al in the framework of this zeolite was possible giving it Brønsted acidity. ITQ-16 can be synthesized in fluoride or alkaline medium, in the latter case the crystallization is longer and a higher concentration of Ge is needed which can suggest an accelerating role of Fluoride anion.

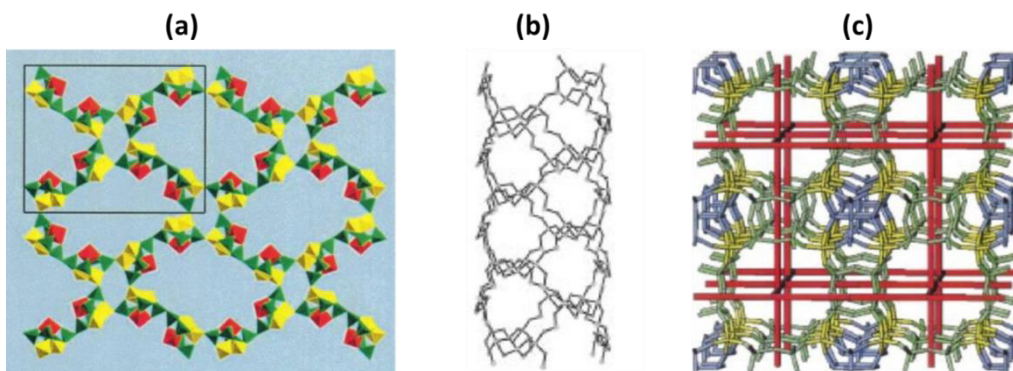


Figure 1- 9: (a): ASU-16 framework with 24 MR^[54]; (b): FDU-4 with 24 MR^[55]; (c): polymorph C of zeolite Beta with 12 MR^[56].

Other groups also worked on silicogermanates, like the LMM Mulhouse (Mulhouse University) and IFPEN with silicogermanates noted IM-n (Institut Français du Pétrole and University of Mulhouse-n) such as IM-7 (10;9;6 MR)^[59] and IM-12 (14;12; MR)^[5]. Another group is the Stockholm University with zeolites named (SU-n) like SU-9^[60] and SU-15^[61]. A team from Peking University (PKU-n) also provided some silicogermanates like PKU-16^[62] and PKU-20^[63]. Nanjing University Du's group zeolite (NUD-n) found two silicogermanates NUD-1^[64] and NUD-2^[65]. Sinopec Composite Material (SCM-n), Standard Oil Synthetic Zeolite (SSZ-n), California Institute of Technology (CIT-n) and Chemistry Jilin University (JU-n) synthesized respectively SCM-14^[66], SSZ-77^[67], CIT-13^[68] and JU-110^[69] silicogermanates. To our knowledge, around 49 silicogermanates exist, among them 26 have structural codes attributed officially by the international zeolite association while the rest do not have structural codes or their codes are assigned in the articles (9 silicogermanates) but not yet by the IZA, see Table 1- 2.

Silicogermanates cover a huge variety of structures with rings sizes varying from 3 in the SU-9^[60] to 28 in the ITQ-43^[70]. Some of them have interrupted structures like the ITQ-53^[71], ITQ-54^[72] with respectively -IFT and -IFU structural codes. Other have disorders like the CIT-13 (Figure 1- 10a)^[68] and NUD-2^[65] with a *CTH structural code and IM-18 (Figure 1- 10b)^[73] with an *UOE structure code.

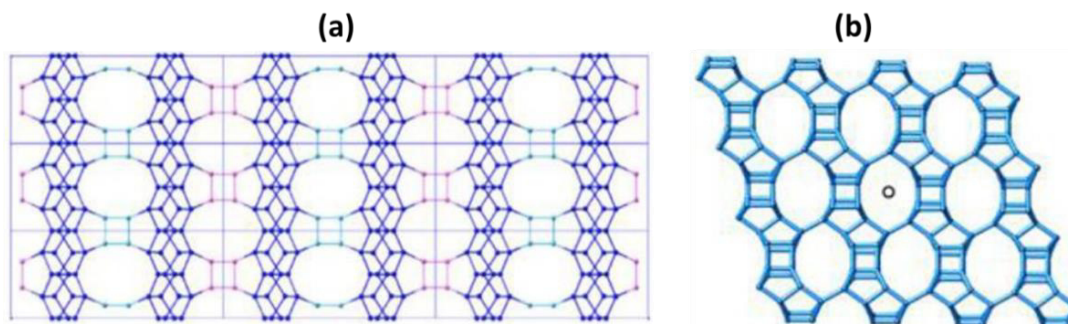


Figure 1- 10: (a) CIT-13 structure^[68]; (b): IM-18 structure^[73].

Table 1- 2: Summary of existing silicogermanates listed by alphabetic structural code order.

Principal Author(s) ^[Ref.]	Zeolite Name	Structural code	Ring sizes
L.Q. Tang ^[60,74] ; Y. Wang ^[74]	SU-9; [Si-Ge-O]-AST	AST	6; 4
L.Q. Tang ^[60]	SU-10	ASV	12; 6
A. Corma ^[56,75] ; L. Shi ^[76] ; K.Jian ^[77]	ITQ-17	BEC	12; 6; 5; 4
A. Corma ^[58]	ITQ-16	Mixture of Beta polymorphs (A, B and C)	12; 6; 5:4
Z. B. Yu ^[78]	SU-78	Intergrown Beta polymorph	12; 12; 12
J. Su ^[79]	PKU-12	-CLO	20; 8; 6; 4
T. Z. Ren ^[80]	SU-57	DFT	8; 6; 4
Y. Yun ^[71]	ITQ-53	-IFT	14; 6; 5; 4; 3
X. Liu ^[81]	ECNU-21	EWO	10; 6; 5
J. Jiang ^[72]	ITQ-54	-IFU	20; 14; 12; 8; 6; 5; 4
M. Hernandez-Rodriguez ^[82]	ITQ-49	IRN	8; 7; 6; 5; 4
J. Jiang ^[83,84] ; K. Qian ^[85] ; R. Bai ^[86]	ITQ-44	IRR	18; 12; 6; 5; 4
A. Corma ^[87]	ITQ-40	-IRY	16; 15; 6; 5; 4; 3
T. Blasco ^[88] ; S. Leiva ^[89]	[Ge-Si-O]-ISV ; [Si-Al-Ge-O]-ISV	ISV	12; 6 ; 5; 4
M. Moliner ^[90]	ITQ-38	ITG	12; 10; 6; 5; 4
T. Boix ^[91] ; A. Corma ^[92,93] ; J. A. Vidal-Moya ^[94] ; R. Castaneda ^[95] ; X. Chen ^[96,97] ; L. Liping ^[98,99] ; X. Liu ^[100] ; Q. Wu ^[101] ; P. Zeng ^[102]	ITQ-13	ITH	10; 9; 6; 5; 4
N. Bats ^[59,59]	IM-7		
A. Corma ^[103,104]	ITQ-34	ITR	10; 9; 6; 5; 4
A. Corma ^[4,105] ; M. Moliner ^[106] ; M. Bjorgen ^[107] ; Q. Kun ^[108] ; L. Liu ^[109] ; L. Wu ^[110] ; Z. Zhang ^[111]	ITQ-33	ITT	18; 10; 6; 5; 4; 3
J. Sun ^[3] ; J. Jiang ^[84] ; K. Qian ^[112] ; F. J. Chen ^[113]	ITQ-37	-ITV	30; 6; 4
R. Castaneda ^[114] ; A. Cantin ^[115] ; W. H. Fu ^[116]	ITQ-24	IWR	12; 10; 6; 5; 4
D. L. Dorset ^[117]	ITQ-26	IWS	12; 6; 5; 4
A. Corma ^[118] ; G. Sastre ^[119] ; X. Liu ^[120] ; R. Yuan ^[121]	ITQ-22	IWW	12; 10; 8; 6; 5; 4
A. Corma ^[122] ;J. E. Schmidt ^[123] ; B. Harbuzaru ^[124]	ITQ-29; Ge-LTA; IM-11	LTA	8; 6; 4
L. Q. Tang ^[60]	SU-11	MFI	10; 6; 5; 4
W. Hua ^[62]	PKU-16	POS	11; 11; 12

L. Tang ^[61]	SU-15	SOF	12; 9; 5; 4
Y. Luo ^[66]	SCM-14	SOR	12; 8; 6; 5; 4
L. Bieseki ^[125]	ITQ-62		
Y. Luo ^[126]	SCM-15	SOV	12; 6; 5; 4
Y. Chen ^[127]	PKU-22a	STI	10; 8; 6; 5; 4
L. Tang ^[61]	SU-32	STW	10; 8; 5; 4
N. Zhang ^[128]	Ge-STW		
D. J. Earl ^[67] ; L. B. McCusker ^[129]	SSZ-77	SVV	6; 5; 4
C. Zhang ^[130]	SYSU-3	-SYT	24; 8; 6; 4
Y. Lorgouilloux ^[131]	IM-16	UOS	10; 8; 6; 5; 4
Y. Lorgouilloux ^[132]	IM-17	UOV	12; 10; 8; 6; 5; 4
Y. Mathieu ^[133]	IM-10	UOZ	6; 4
J. L. Paillaud ^[5] ; O.V. Shvets ^[50,134]	IM-12	UTL	14; 12; 10; 6; 5; 4
A. Corma ^[135]	ITQ-15		
M. Dodin ^[136]	IM-20		
J. H. Kang ^[68] ; B. W. Boal ^[137]	CIT-13	*CTH	14; 10; 6; 5; 4
Z. H. Gao ^[65]	NUD-2		
D. S. Firth ^[138]	SAZ-1		
M. O. Cichocka ^[73]	IM-18	*UOE	10; 8; 6; 5; 4
A. Corma ^[139,140] ; B. B. Schaack ^[141]	ITQ-21	-	12; 6
J. Jiang ^[70,142]	ITQ-43	-	28; 12; 12
F. J. Chen ^[64]	NUD-1	-	18; 12; 10
Y. Wang ^[69]	JU-110	-	10; 9
Y. Chen ^[63]	PKU-20	-	12; 10
L. Tang ^[143]	SU-12	-	24; 12; 10; 8
L. Tang ^[144]	SU-14	-	24; 12; 10; 9
L. Tang ^[145]	SU-21	-	10; 4
L. Tang ^[146]	SU-JU-14	-	24; 12; 10; 9

- means interrupted structure

* means structure with disorders

1.2.2.2. Insight in the Ge distribution

The role of Germanium and its distribution in silicogermanates frameworks have been investigated through ¹⁹F MAS NMR by post incorporation of Fluoride in as prepared zeolites (SDA= HM²⁺Cation)^[120]. When F⁻ anions are in a silicic d4r unit, only one signal is detected at -38 ppm. Meanwhile in the presence of Ge, this signal is divided into different signals, each one characteristic of a certain Ge distribution.

The ¹⁹F MAS NMR spectrum of ITQ-13 synthesized in the presence of HF gave 4 peaks at: -8, -19, -38 and -55 ppm assigned respectively to F⁻ located in dr4 composed as follows: [4Si, 4Ge]^[147], [7Si, 1Ge]^[147], all-silica d4r units^[88] and Ge-containing [4¹5²6²] cages^[94] (Figure 1- 11c).

When ITQ-13 was synthesized in alkaline media and F⁻ anions were post-incorporated, the peak attributed to silicic d4r units (at -38 ppm in the spectrum of solids prepared in the presence of HF)

disappeared. This indicated that all-silica d4r cannot be obtained in OH media (Figure 1- 11a). In addition, the peak at -8 ppm was intense (Figure 1- 11c). Thus they concluded that in absence of F⁻ anions, Ge only crystalizes in Ge rich d4r units particularly in [4Si, 4Ge]- d4r units.

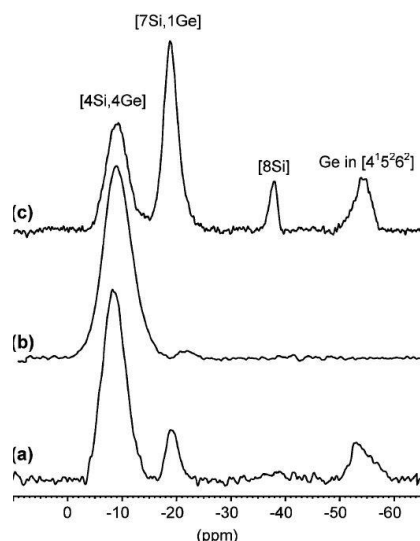


Figure 1- 11: ¹⁹F NMR spectra of (a) ITQ-13 and (b) ITQ-17 prepared under alkaline conditions and treated with NH₄F; (c): ITQ-13 prepared in the presence of HF^[120].

In the same article, ITQ-17 was also studied. Like for the ITQ-13, the ¹⁹F MAS NMR spectrum of the zeolite synthesized in HF medium is different from that of OH media. In the latter, the intense peak at -8 ppm indicates that d4r units contain a high amount of Ge (Figure 1- 11b). Another proof of this distribution is that when considering that Ge in ITQ-13 and ITQ-17 only occupies [4Si, 4Ge]- d4r theoretical Si/Ge ratios (6 and 3 for ITQ-13 and ITQ-17 respectively) are in full agreement with experimental ratios measurements (6.5 and 3 respectively).

They also studied ITQ-24, a zeolite obtained only in basic media and in the presence of Al. The unique signal at 55 ppm in the ²⁷Al MAS NMR spectrum indicates that all aluminum are tetrahedral in the as-made zeolite. After post-incorporation of F⁻ anions, the weakness of the NMR signal at -19 ppm ([7Si, 1Ge]- d4r) in ¹⁹F MAS NMR and the intense signal at -9 ppm indicates that [4Si, 4Ge] d4r units are dominant in the structure, as it is for ITQ-13 and ITQ-17 prepared in the absence of fluoride. Unlike in ITQ-13 and ITQ-17, this signal was broad, which could be due to the presence of Al in the zeolite.

Finally, the same investigation on ITQ-22 was performed. The ¹⁹F MAS NMR spectrum was composed of a major resonance at -8 ppm and a signal at -2 ppm that was not observed before. ITQ-22 has only one type of d4r unit so lines at -2 and -8 ppm cannot be assigned to two nonequivalent crystallographic sites. Thus the authors suggested that the line at -2 ppm can be attributed either to (i): [4Si, 4Ge] d4r units with a specific distribution of Ge atoms, or to (ii) [(8 - n)Si, nGe] units with more or less than 4 Ge atoms (for example, [3Si, 5Ge] or [5Si, 3Ge] d4r).

We presented in Table 1- 2, a list of the existing silicogermanates. In the following paragraph, we are going to describe the IM-12 (UTL structural code) silicogermanate that will be treated in the next chapters.

The IM-12 is a silicogermanate discovered at LMM Mulhouse in collaboration with IFPEN. It has a 2-dimensional channel system with 14 and 12 T member rings with diameters of 9.5 and 8.5 Å^[5,148]. Its framework density is 15.2 T/1000Å³ and the chemical unit cell formula for the as-made silicogermanate is $[(C_{11}H_{22}N)_4(H_2O;OH)_{16}][Ge_xSi_{76-x}O_{152}]$. It has a UTL (Mulhouse Twelve) structural code attributed by the IZA. This material is obtained using organic (6R,10S)-6,10-dimethyl-5-azoniaspiro[4,5]decane hydroxide as SDA in a basic medium. The addition of HF to the synthesis mixture leads to new structures such as MU-31 and MU-26^[149]. The morphology of IM-12 aggregates depends on the synthesis conditions: under static conditions it gives aggregates (150 by 150 by 150 μm) by superposition of thin platelet-like crystals while with stirring it gives gypsum flower-type aggregates (5 by 5 μm and thickness about 300 nm), Figure 1- 12.

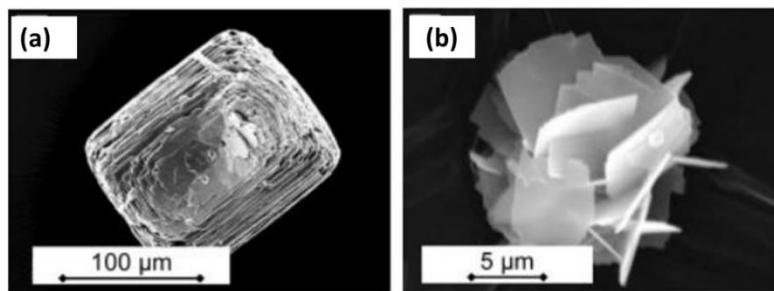


Figure 1- 12: Scanning electron microscopy pictures show two different morphologies of the IM-12 zeolite synthesized under (a) static and (b) stirring conditions^[5].

This zeolite has a particular structure since is formed by layers connected to each other through d4r units (Figure 1- 13).

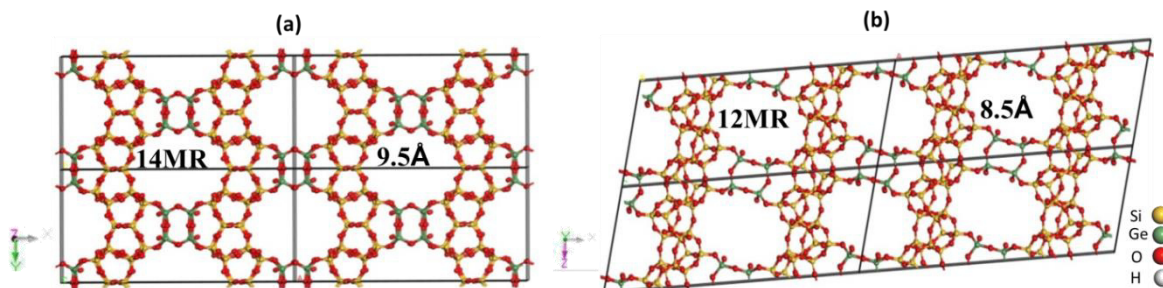


Figure 1- 13: UTL structure viewed along: z axis showing 14 MR (a) and y axis showing 12 MR (b).The represented framework has a Si/Ge molar ratio of 3.75

Shvets et al. optimized the synthesis of pure IM-12 zeolite by studying the kinetic of the reaction and the Si/Ge and (Si+Ge)/SDA ratios effect using (6R,10S)-6,10-dimethyl-5-

azoniaspiro[4,5]decane hydroxide as SDA^[134]. Then these authors tested 25 different OSDA and 13 of them allowed the synthesis of the UTL phase^[50].

Corma et al. synthesized the silicogermanate ITQ-15^[135] with the same UTL structural phase. This zeolite was obtained using 1,3,3-trimethyl-6-azonium-tricyclo-[3.2.1.4^{6,6}] dodecane hydroxide as structure directing agent. They also incorporated aluminum by adding it to the synthesis gel and carried out dealkylation of triisopropylbenzene (TIPB) and diisopropylbenzene (DIPB) and compared the kinetics reaction rate constants to that of UTD-1, a zeolite with unidirectional 14-R channel. The results show that bulkier TIPB has the same rate values for both of zeolites while the rate of DIPB is higher since in ITQ-15, this small molecule can diffuse through bi-dimensional 14- and 12-R pores.

1.3. Post-Treatments of silicogermanates

Two main approaches for silicogermanates post treatments are used in the literature:

The first approach aims to maintain the initial structure of the pristine silicogermanates. These post treatments are either a direct substitution of Ge for other elements (e.g. Al, Ga, Si) or an acid leaching sometimes followed by the incorporation of external T elements to restore the initial structure.

The second approach is to transform the starting zeolite into new stable structures. This time, Ge are eliminated from the framework and the condensation of the resulting interrupted structures leads to stabilized new structures. A list of silicogermanates post treatments is presented in Table 1- 3.

Table 1- 3: Silicogermanates post treatments.

IZA code (name)	Maintaining the initial structure [Ref.]	Creating new structures ^[Ref.]
BEC (ITQ-17)	D.S using PAC ^[150] ; A.L-T ^[7]	✗
ITH (ITQ-13)	D.S using Al(NO ₃) ₃ ^[151] ; A.L ^[152]	✗
ITR (ITQ-34)	A.L	✗
ITT (ITQ-33)	A.L-T ^[153]	✗
IWR (ITQ-24)	D.S using Al(NO ₃) ₃ and Ga(NO ₃) ₃ ^[154] ; A.L-T ^[7]	✗
IWW (ITQ-22)	D.S using Al(NO ₃) ₃ ^[151] ; A.L ^{[155]; [152]}	✗
UOV (IM-17)	D.S using Al(NO ₃) ₃ ^[156]	AL(IPC-12) ^[157]
UTL (IM-12)	A.L-T ^[151] ; A.L ^[7]	A.L (COK-14) ^[9] ; A.L+T (IPC-2) ^[10] ; A.L+Octylamine(IPC-4) ^[10] ; A.L(IPC-6 and IPC-7) ^[158]
UWY (IM-20)	A.L-T ^[7] ; A.L+ recrystallization ^[159]	✗
UOS	A.L+ recrystallization ^[159]	✗

*CTH (CIT-13 or SAZ-1)	x	Air humidity-T (CFI) [160]; A.L+Octylamine (IPC-15)[138]; A.L-T (IPC-16)[138]; A.L/+T(CIT-14)[161,162]; A.L (CIT-15)[161] ; NH ₃ leaching (ECNU-21)[81]
------------------------	---	---

D.S means direct substitution

A.L means acid leaching

A.L-T means acid leaching followed by incorporation of T external elements

1.3.1. Maintaining the initial structures of initial silicogermanates

1.3.1.1. Direct substitution of Ge for other elements

1.3.1.1.1. Direct substitution of Ge for Al or Ga

This approach was developed by Valtchev et al.^[150]. It consists of the direct substitution of Ge for Al. An as-prepared ITQ-17 (Polymorph C of zeolite Beta, BEC structural type) was treated with polyaluminum hydroxide chloride solution (PAC). It is known that successful replacement of framework elements solicits an accessible volume of the zeolite. A benefit of this treatment is that no preliminary elimination of the SDA which risks the collapse of the structure is needed: a one pot SDA extraction and an exchange between Ge and Al in the framework occur. To check the incorporation of Al, different characterization techniques were used. ²⁷Al MAS NMR revealed that extra-framework Al (around 0 ppm) can be eliminated by acid treatment, which is accompanied by the extraction of some framework Al (around 50 ppm), see Figure 1- 14.

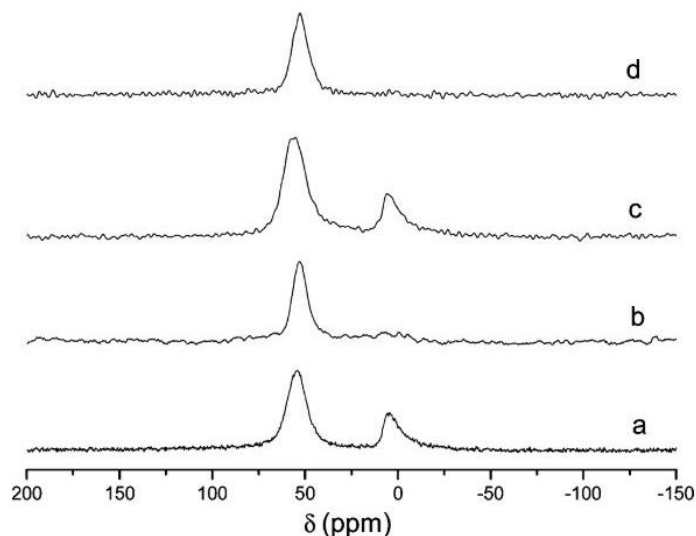


Figure 1- 14: ²⁷Al MAS NMR spectra of the aluminated BEC-type materials. The products obtained after (a) (PAC), (b) (PAC+HCl), (c) (PAC+HCl+PAC), and (d) (PAC+HCl+PAC+HCl)^[150].

In the other hand, ¹H MAS NMR (Figure 1- 15.I) showed the presence of Brønsted acid sites (SiOHAl) with resonance at 6.8 and 8.5 ppm. Peaks at 2.1 and 2.8 ppm correspond to silanol nests

(SiOH) and protons connected to extra framework aluminum (EF-AlOH), respectively. NH₃-TPD experiments were in agreement with ¹H MAS NMR analysis.

In addition, potassium ion exchange proved the existence of cation exchange sites. After calcination 94% of Al was counterbalanced by potassium cations.

The Si/Ge ratio of the treated material raised from 3.6 to 5.2 which appeared to be enough to stabilize the BEC final solid. The later showed a good thermal stability after calcination for 5 h at 600°C. The calcined material was then exposed to 77% humidity at room temperature for 30 days. No difference among the XRD patterns of parent and moisture-exposed materials was observed (Figure 1- 15.II).

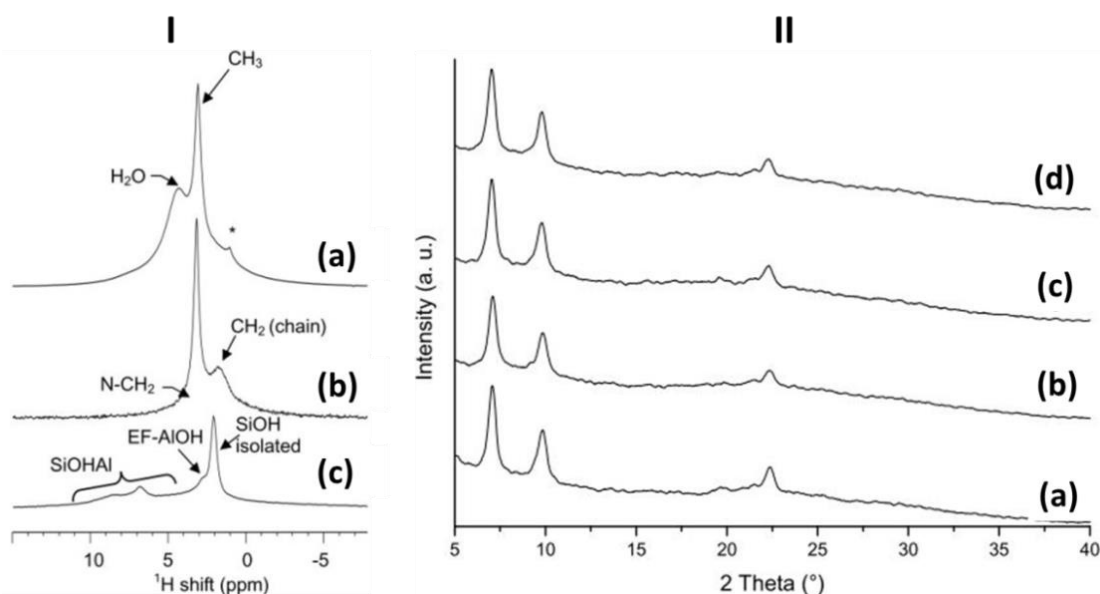


Figure 1- 15: (I):¹H MAS NMR spectra of material subjected (PAC+HCl+PAC+HCl) (a) and the same material subjected to dehydration (b) and calcination (c); (*impurities). (II): XRD patterns of the modified then calcined BEC-type material prior to (a) and after being exposed to 77% atmosphere humidity at room temperature for 18 (b), 24 (c) and 30 (c) days. Adapted from ^[150].

Shamzy et al. undertook the galliation and alumination of an IWR-borogermanosilicate using aluminum or gallium nitrate solutions^[154]. Usually, calcination of silicogermanates leads to the collapse of the structure while this borogermanosilicate, maintained its initial structure with a loss of peak intensities. On the other hand, treatment of the zeolite with 0.01 M HNO₃ (pH = 2) led to the collapse of the structure (Figure 1- 16.I), while it was conserved with treatments in acidic conditions in the presence of Al, (Figure 1- 16.II) which indicates that Al prevented the destruction.

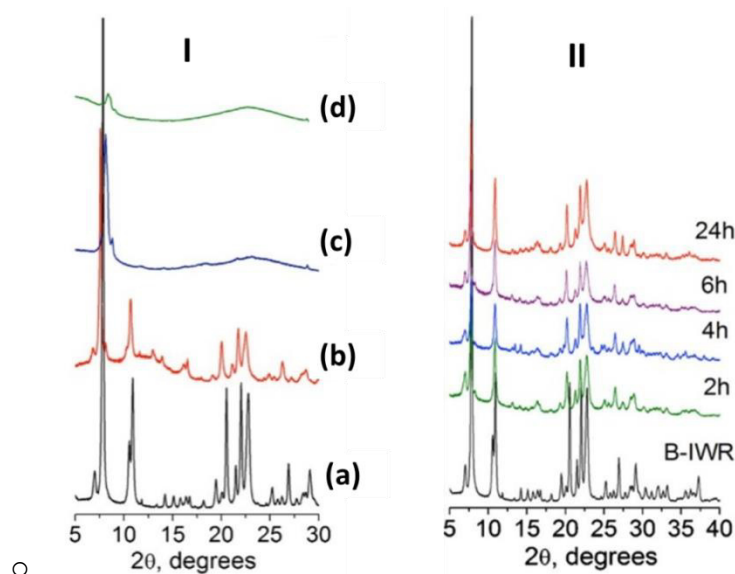


Figure 1- 16: XRD patterns of (I): as-synthesized (a), calcined B-IWR zeolite (b), and calcined B-IWR treated with 0.01 M HNO₃ for 2h (c) and 24h (d). (II): duration effect of ([Al(NO₃)₃] = 1M; pH = 2, T = 80°C treatment. Adapted from [154].

Unlike aluminated, treating B-IWR with Fe(NO₃)₃ led to the collapse of the structure. Higher ionic radius of Fe³⁺ (r = 0.47Å) vs. Al³⁺ (r = 0.39Å) didn't allowed the incorporation of iron in the framework. Also octahedral coordinated Fe³⁺ are highly stable and compete with tetrahedral forms. In the opposite side, no structural changes were detected when the sample was treated with Ga(NO₃)₃.

FTIR spectroscopy of aluminated samples showed an increase of the band intensity attributed to silanol groups (3745 cm⁻¹) compared to parent zeolites (Figure 1- 17). These additional SiOH groups are due to the breaking of Si-O-Ge and Si-O-B linkages. Appearance of a band at 3623 cm⁻¹ indicates the presence of Si-(OH)-Al hydroxyl groups. The weak band at 3678 cm⁻¹ was attributed to OH groups located on extra-framework aluminum.

Pyridine adsorption allowed the identification of the nature of acid sites. The band assigned to bridging hydroxyl groups disappeared indicating the accessibility of Brønsted acid centers for pyridine. The appearance of the band at 1545 cm⁻¹ (pyridinium ion) indicates that these are strong acid sites. Thus the latter can be attributed to framework Si-(OH)-Al. Bands at 1455 and 1445 cm⁻¹ are attributed to pyridine interacting with silanols groups and Lewis acids respectively. The desorption of pyridine showed an increase in the amount of Brønsted acid centers in the following order: B < Ga < Al.

B-, Ga- and Al-IWR zeolites were tested in benzoylation of p-xylene. Al and Ga-substituted IWR showed a remarkably increased conversion and selectivity compared to parent B-IWR. Although Ga-IWR had lower amounts of Lewis and Brønsted sites, it showed higher yield and selectivity to Ketone than Al-IWR. Strong adsorption of the targeted product which poison active centers was more pronounced for Al.

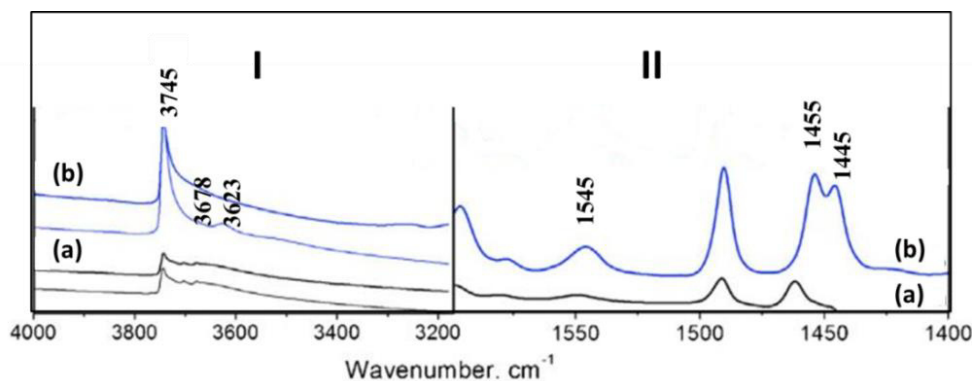


Figure 1- 17: IR spectra of IWR: (I) region of hydroxyl vibrations; (II) region of pyridine vibrations before (down thin spectra) and after adsorption (top/bold spectra) of pyridine: (a) B-IWR; (b) IWR treated with $[Al(NO_3)_3] = 1M$; $pH = 2$, $T = 80^\circ C$ for 24h. Adapted from ^[154].

Later, Shamzy et al. undertook the substitution of Ge for Al by treatment with aluminum nitrate $Al(NO_3)_3$ on calcined ITH and IWW structures^[151]. Samples with high and poor Ge content were treated. Ge rich zeolites collapsed in acid treatments meanwhile when treated with aluminum nitrate ($pH=2$), Ge concentration decreased with maintain of structure ordering proving again that Al prevented the destruction.

For poor-Ge zeolites, incorporated amounts of Al were equal to extracted Ge while for rich Ge-zeolites the eliminated Ge were much higher leading to the formation of micro-mesoporous aluminosilicates. ^{27}Al MAS NMR showed a dominating peak assigned to tetrahedral AlO_4 and a smaller peak related to octahedral extra-framework AlO_6 . The aluminated zeolites were tested in the tetrahydropyranlylation of 1-propanol. Ether yields were 5 and 10% for Ge-rich and Ge-poor ITH respectively, and 45% for both Ge-rich and poor IWW.

Kasneryk et al. post treated two UOV type silicogermanates, one with $Si/Ge = 1.5$ and a second with $Si/Ge= 0.5$ noted UOV-1.5 and UOV-0.5 respectively^[156]. When the parent zeolite was treated with $Al(NO_3)_3$, the initial structure was maintained. Meanwhile with acidic treatments in absence of Al an IPC-12 zeolite was formed. This suggest that Al heals the defects created by fast hydrolysis of Ge-O-Si bonds. The kinetics of alumination were studied by XRD. After 5 min of alumination the interlayer peak (7.08°) shifted to high angle region. XRD patterns after 5 min, 30 min and 3 hours showed additional peaks (16.56 and 24.38°) corresponding to lamellar precursors. While the prolongation of the alumination step to 24 h led to the reformation of the UOV structure (Figure 1-18.a and b). These results are in agreement with ICP/OES analysis, increasing the time of alumination to 24h led to further decrease of Ge content from 24.7 to 5.95% for UOV-1.5 and from 29.7 to 6.48% for UOV-0.5. In parallel, an increase of Al content (from 0.73 to 2.66% and from 2.08 to 2.97 % for UOV-1.5 and UOV-0.5 respectively) was detected. Prolonging the treatment to 7-15 days led to the partial destruction of the structure and a decrease of Al content while that of Ge remained constant. ^{29}Si MAS NMR showed that the signal of silanol groups (Q^3 at $-100ppm$) decreased with increasing treatment from 5 min to 96 h (Figure 1- 18.c). ^{27}Al MAS NMR of treated

UOV-0.5 indicated that after 5 min most Al were octahedral (0.8 ppm) while after 96 h most Al are tetrahedral (dominant peak at 55 ppm) confirming Al incorporation into the framework, see Figure 1- 18.d. Note that UOV-1.5 had higher extraframework Al compared to UOV-0.5 and the directly synthesized Al-UOV by introducing Al into the synthetic gel had lower Al content compared to post aluminated UOV.

The nature and concentration of acid centers in Al containing UOV was investigated using FTIR spectroscopy. The parent zeolites had two adsorption bands, one at 3745 cm^{-1} attributed to silanol groups and one at 3685-3630 cm^{-1} corresponding to Ge-OH groups. After treatment the band corresponding to silanol groups was more intense. Meanwhile the prolongation of alumination time and the increase of temperature led to an increase of the band at 3620 cm^{-1} (Si-OH-Al) and the decrease of silanol band which indicated the healing of silanol defects by Al incorporation, Figure 1- 19.a.

Pyridine adsorption led to the disappearance of Si-(OH)-Al groups (3620 cm^{-1}) revealing the accessibility of Brønsted sites. The appearance of bands at 1455 and 1545 cm^{-1} were attributed to coordinately bonded pyridine and to pyridinium ions adsorbed on Brønsted acid sites respectively (Figure 1- 19.b).

This work shows that alumination is a two-step process: degermanation forming silanol groups followed by healing through Al incorporation. In addition, post treatment alumination allows higher framework-Al amounts, higher Lewis and Brønsted acidity as well as additional mesoporosity compared to Al-directly synthesized samples.

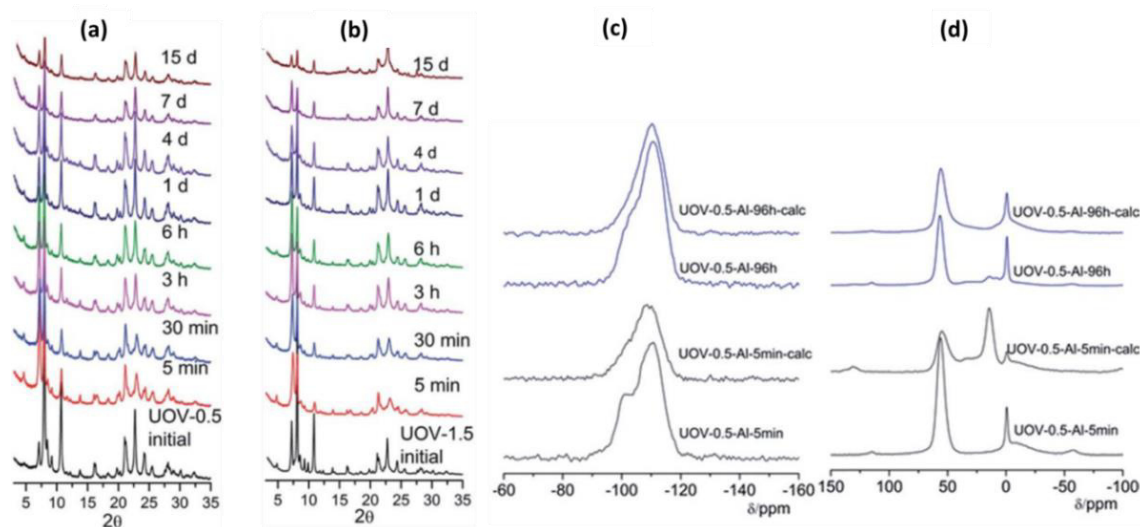


Figure 1- 18: XRD patterns of UOV-0.5 and (a) and UOV-1.5 (b). ^{29}Si MAS NMR (c) and (d): ^{27}Al MAS NMR spectra of UOV-0.5 aluminated at 80°C for 5 min and 96 h before and after calcination^[156].

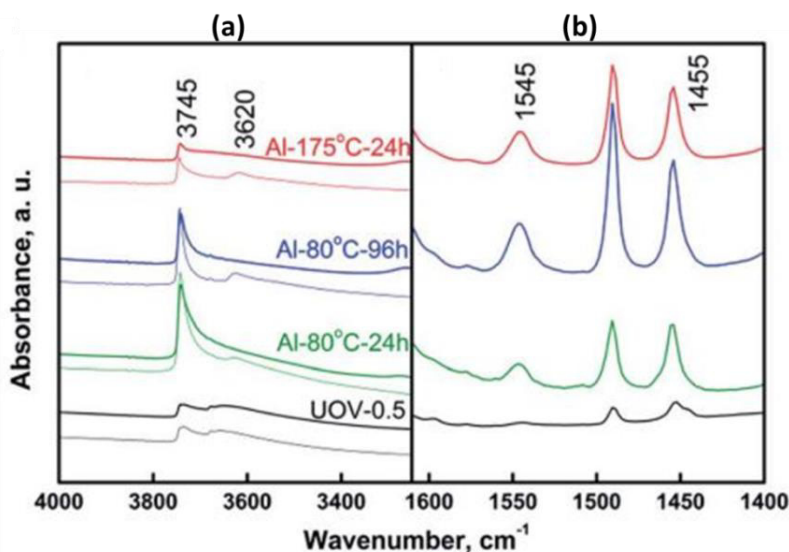


Figure 1- 19: IR spectra of UOV-0.5: parent samples (black), UOV-n-Al-80-24h (green), UOV-n-80-96h (blue), and UOV-n-175-24h (red). (a) Regions of hydroxyl vibrations; (b) region of pyridine vibrations: bottom line and top line spectra show the spectra before and after adsorption of pyridine^[156].

1.3.1.1.2. Direct substitution of Ge for Si

Kots et al.^[6] studied the silylation of a BEC-germanosilicate using synchrotron XRD and MAS NMR. The zeolite was prepared using a different SDA: 1-benzyl-1,4-diazabicyclo[2.2.2]octane which make it more resistant to calcination than other BEC type zeolites. The synchrotron XRD showed that Ge occupies T1, T2 and T3 positions with respectively 53, 20 and 6% relative fraction, see Figure 1- 20.

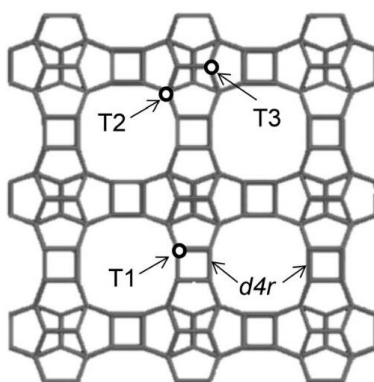


Figure 1- 20: BEC structure with d4r unit and highlighted T positions.

These occupancies are similar to the zeolites prepared by Corma's group and different from that of Smeets. In addition, the reaction between the calcined zeolite and ammonium hexafluorosilicate $(\text{NH}_4)_2\text{SiF}_6$ led to the redistribution of Ge in the framework. ^{19}F MAS NMR shows that fluoride is incorporated inside the d4r, signals at -5.3 and -16.8 ppm were attributed respectively to high Ge in d4r and to 7 or 8 Si inside the d4r unit. Rietveld refinement suggested that Ge was substituted

for Si in T2 and T3 positions but not in T1. This drove the formation of Ge-rich or Si-rich d4r units without a modification of the initial Si/Ge ratio. So in this article, there is not a stabilization of Ge-BEC zeolite but it shows that SDA affects the Ge distribution in the silicogermanate and that Ge in d4r are more stable than in other SBUs.

1.3.1.2. Acid leaching /followed by adding external T source

1.3.1.2.1. Acid leaching

Xu et al. stabilized the IM-12 by acid leaching^[7]. Since this zeolite has a high Si/Ge ratio, treatment of the as prepared silicogermanate using 1M HNO₃ was enough to stabilize its structure. It is suggested that Si debris dissolved form the dense layer substituted Ge atoms.

The first treatment (1M HNO₃ at high temperature 463K) allowed the extraction of 57.6% of OSDA and an increase of Si/Ge ratio from 4.7 to 59.4. While the second treatment led to a Si/Ge ratio of 233. The XRD are represented in Figure 1- 21.I. The IR spectra of the pristine and the treated IM-12 (Figure 1- 21.II) indicates the disappearance of Si-O-Ge framework band (1000 cm⁻¹). Meanwhile the band around 598 cm⁻¹ attributed to vibrations of d4r units had a shift to 621 cm⁻¹. This shift is in agreement with the theoretical calculations for replacing Ge with Si. ²⁹Si MAS NMR of treated IM-12 (Figure 1- 21.III) showed a resonance signal at -107.9 ppm which was assigned to the Si atoms in d4r units (compared to Si in Q⁴ groups, appearing mainly in the range of -107.7/-109.4 ppm).

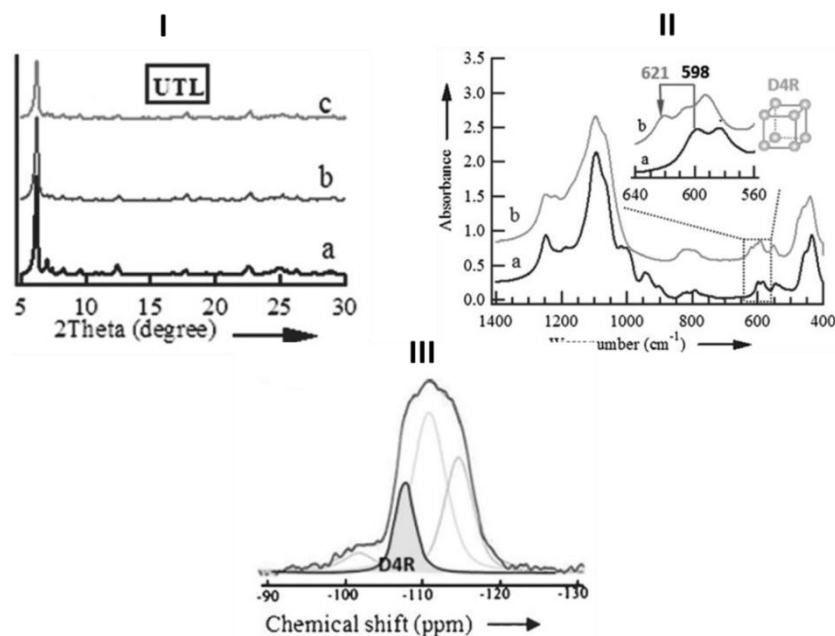


Figure 1- 21: (I): XRD patterns of IM-12, as-synthesized (a), stabilized by Si substitution (b), and further autoclaved in 65% HNO₃ aqueous solution (423K, 24h) and calcination (823K, 6h) (c). (II): IR spectra of a) IM-12 and b) treated sample. (III): ²⁹Si NMR spectra of treated IM-12. Adapted from^[7].

Liu et al. investigated the degermanation of ITQ-17 with different Si/Ge ratios and different SDAs^[163]. Many treatment parameters have been optimized to prevent the loss of crystallinity such as temperature (80°C), mild acidity (10⁻²M HCl) and number of treatments (3 before collapse). The Ge content decreased by 42%. They also indicated through TGA that when the amount of TEA species was significantly reduced (fourth treatment) the zeolite structure started to collapse (Figure 1- 22.I and II). In addition, the silanol peak (-100 ppm) in ¹H-²⁹Si CP/NMR spectra of the treated samples increased with the number of treatments and had a maximum intensity at 3 treatments before the collapsing of the structure (Figure 1- 22.III).

Treatment with alkaline solutions (NH₄OH) showed similar results to acid solutions which indicates that degermanation is not affected by pH conditions but by Ge distribution. In the other hand, the treatment of samples prepared with different SDAs (BD⁺ and HM²⁺) revealed that SDA affect the kinetics of degermanation. For example, the crystallinity of ITQ-17 prepared with BD⁺ decreased by ca. 50% after 3 treatments in HCl, while this value was obtained after 4 treatments for zeolite prepared using TEA⁺ cations.

To check the stability of the treated material, the later was calcined and compared to the XRD patterns of a calcined non-treated sample. In the latter, after 7 days in ambient conditions, some BEC characteristic peaks with low intensities were still detected but the GeO₂ phase was dominant. However, in the treated sample, the GeO₂ phase was present but were much lower than in the non-treated sample reflecting that degermanation stabilizes the BEC type zeolite.

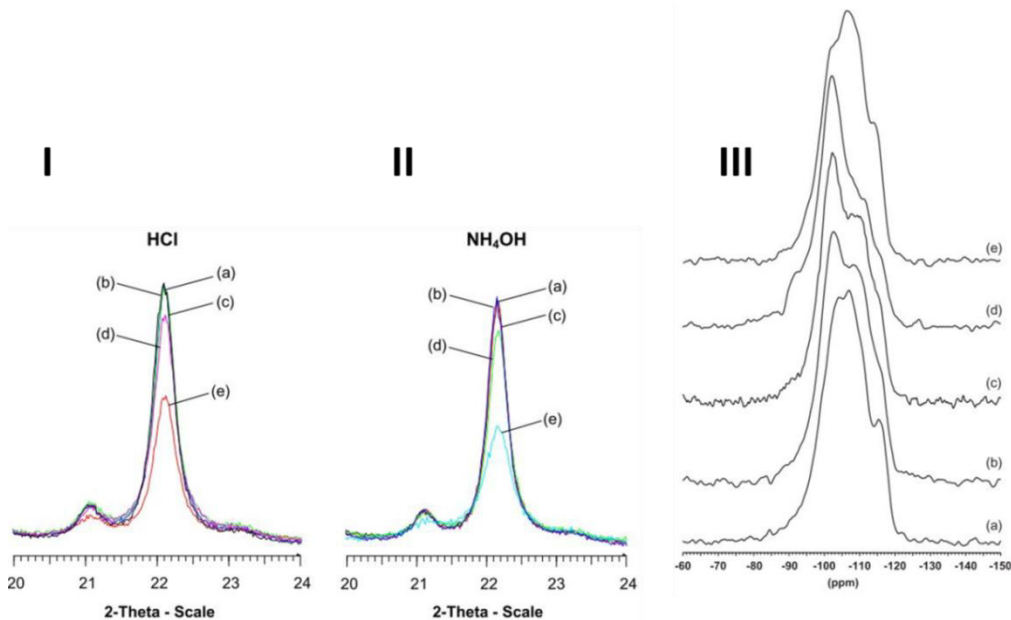


Figure 1- 22: Evolution of the (301) reflection of XRD patterns of ITQ-17 zeolites treated in HCl (I) and NH₄OH (II) solutions. Pattern (a) corresponds to the as-made form of the zeolite and patterns (b)–(e) to the same zeolite after 1–4 treatments, respectively. (III): ¹H-²⁹Si MAS NMR treated in HCl solutions; (a): as made; (b)-(d) 1-3 times treatment respectively and (e) 3 HCl treatment followed by one NH₄F treatment. Adapted from ^[163].

1.3.1.2.2. Acid leaching followed by addition of an external Al source

Burel et al. treated an as prepared ITQ-22 (IWW zeolite) under strong acidic conditions^[155]. Chemical analysis indicated a decrease of Ge content from 17 Ge/u.c to 0.66 Ge/u.c after 2 treatments. XRD results not only showed that the structure was maintained but that the treated sample patterns were in agreement with those of theoretical all-silica IWW zeolite (Figure 1- 23.I).

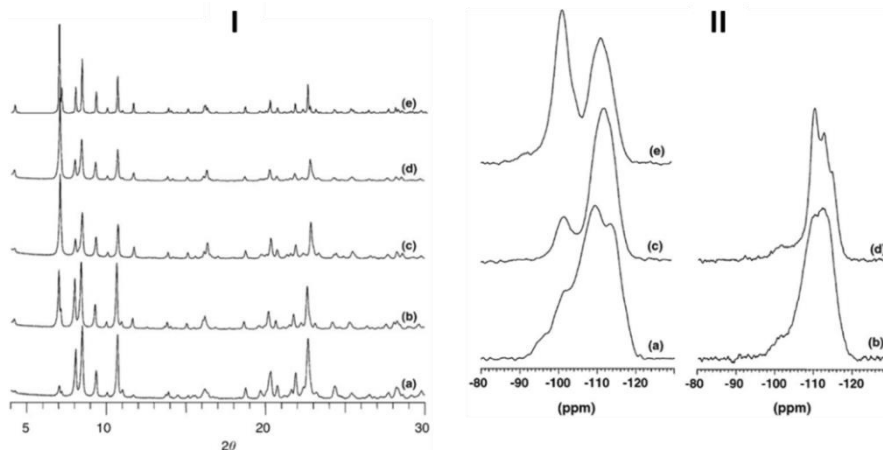


Figure 1- 23: (I): XRD patterns of ITQ-22 and (II) ²⁹Si MAS NMR spectrum of: as-made (a), calcined (b), treated 2 times with 37 wt.% HCl (c), and calcined after HCl treatment (d). I-e pattern was simulated assuming a pure silica framework; II-e correspond to ¹H-²⁹Si CP/MAS NMR spectrum of treated zeolite. Adapted from ^[155].

N₂ adsorption indicated that after HCl treatments, the OSDA was extracted from the zeolite pores (calcined sample vs. treated sample had similar pore volumes, 0.20 mL.g⁻¹ in the calcined vs. 0.17-0.185 mL.g⁻¹ in the treated samples). In addition, the type I isotherm had a hysteresis loop characteristic of mesopores. TEM also confirmed the presence of mesopores oriented along one of the directions of the crystals. This mesopores can result from partial dissolution of the framework. Meanwhile, since the zeolite weight loss corresponded only to the removal of Ge species and organic molecules, it is suggested that dissolved Si species were reincorporated in the framework. Generally, in ²⁹Si MAS NMR spectrum, chemical shifts between -100 and -110 ppm are assigned to silanol groups. Those between -100 and -110 ppm could be assigned to Q⁴ Si atoms with at least one surrounding Ge and those between -110 and -120 ppm correspond to Q⁴ Si atoms surrounded by 4 Si atoms^[88]. The treated sample had only two signals at -100 and -115 ppm (Figure 1- 23.II) assigned respectively to silanol groups and Si(OSi)₄ silicon framework atoms. This also means that Ge atoms were extracted from the structure.

After heating the solid in air at 550°C, no structural changes were detected reflecting the thermal stability of the material. To incorporate Al, the treated zeolite was dispersed in an acidic solution (HCl, pH = 2) of aluminum sulfate. XRD revealed that the crystallinity of the zeolite was not affected. Chemical analysis and ²⁷Al MAS NMR indicated that Al was present in the zeolite and it

is tetrahedral coordinated (single signal at 52 ppm). This treatment allowed the preparation of Al-IWW zeolite.

When Shamzy et al. tried to do a direct substitution of Ge for Al in a calcined UTL type zeolite (same OSDA of IM-12) using aluminum nitrate, the structure collapsed while this treatment was feasible for ITH and IWW structure^[151]. This was explained by either a lower rate of diffusion of $\text{Al}(\text{H}_2\text{O})_6^{3+}$ vs. degermanation along the b-c plane (2D channel system vs. 3D in the two other zeolites) or to the distribution of Ge in the d4r units (Ge-pure s4r). So UTL containing its SDA was post treated. The proposed post treatments are represented in Figure 1- 24.

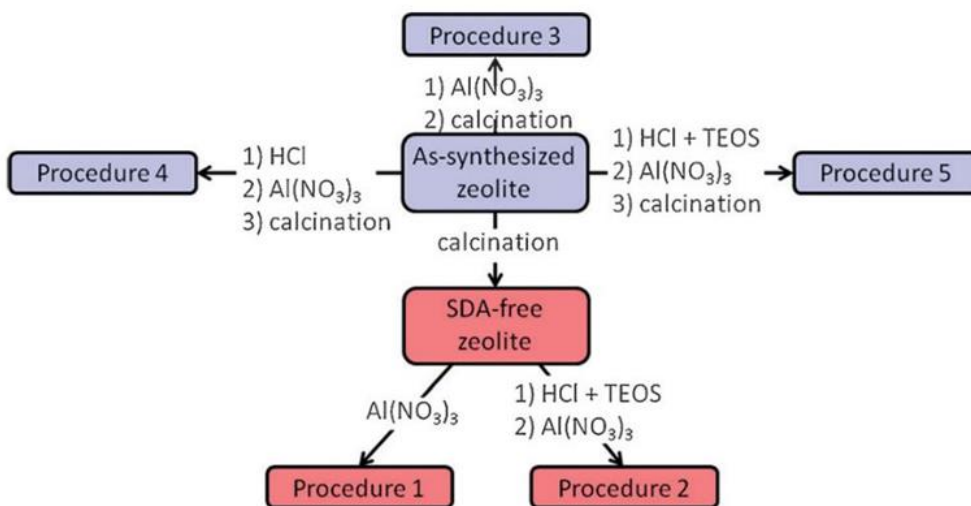


Figure 1- 24: Procedures for UTL post treatments reported in ref.^[151].

If the as prepared UTL is treated with $\text{Al}(\text{NO}_3)_3$, Al is not incorporated and a tiny amount of Ge is eliminated (procedure 3). When procedure 4 is followed, the Ge-rich UTL ($\text{Si}/\text{Ge}=3.8$) collapsed while the Ge poor zeolite ($\text{Si}/\text{Ge}=6$) maintained its structure with a two fold increase of the Si/Ge ratio. An increase of silanol band was also detected (3745 cm^{-1} in the FTIR spectra). Introducing an external Si source during the acid treatment (procedure 5) allowed the maintaining of the structure in the Ge-rich UTL. But for zeolites treated with TEOS, the further treatment using $\text{Al}(\text{NO}_3)_3$ didn't allow any incorporation of Al. While for the zeolites treated only with acids, a very small amount of Al was detected.

To increase the accessible volume and allow the Ge substitution for Al, the degermanation followed by alumination process was applied on calcined samples (procedure 2). The Ge-rich zeolites collapsed while for Ge-poor parent zeolite, the structure was partially maintained, see Figure 1- 25. ^{27}Al MAS NMR indicated an incorporation of Al in the framework and Ar adsorption indicates an important decrease in the microporous volume (from 0.21 to $0.14\text{ cm}^3\cdot\text{g}^{-1}$) and the appearance of meso/macropores. The latter zeolite was tested for the tetrahydropyranylation of 1-propanol and had a ether yield of 15%.

Similarly to UTL, the treatment of as-prepared ITH and IWW had no effect on the zeolites and their Si/Ge ratios remained the same.

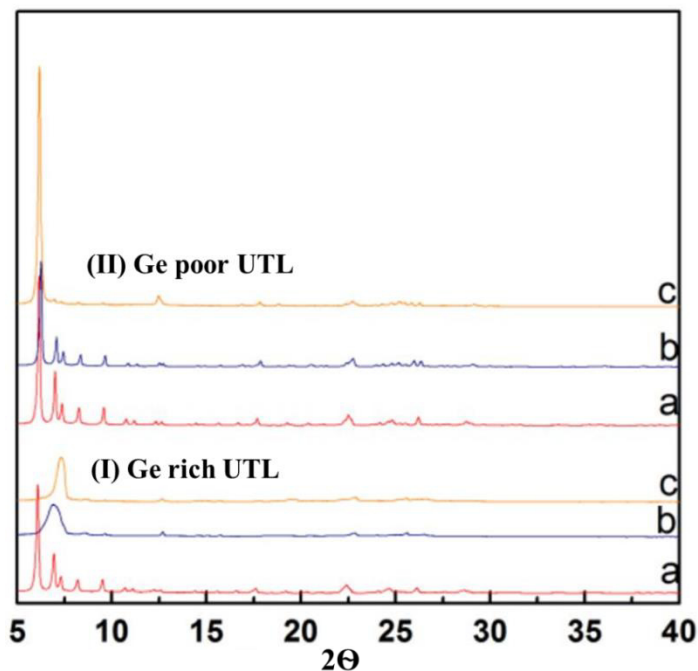


Figure 1- 25: XRD pattern of UTL samples: calcined zeolites (a), calcined UTL zeolite treated with HCl and TEOS (b), calcined UTL zeolite treated with HCl and TEOS then $\text{Al}(\text{NO}_3)_3$ of (I) Ge rich UTL and (II) Ge poor UTL^[151].

Chlubna-Eliasova et al. investigated the hydrolysis of two IWW zeolite samples: a Ge-rich ($[\text{6Ge},2\text{Si}]\text{-d4r}$) and a Ge-poor IWW ($[\text{4Ge},4\text{Si}]\text{-d4r}$)^[164]. When treated with acid, the Ge-rich zeolite was disassembled into a layered material (IPC-5P) which is reassembled into a quasi-pure silica IWW by adding diethoxydimethylsilane.

While treating Ge-poor sample, led to a partial hydrolysis of the structure and Al incorporation using AlCl_3 in 0.05M HCl filled the defects to form an Al-IWW zeolite. The treatment procedure is represented in Figure 1- 26.

It is worth mentioning that incorporating Al into the Ge-rich zeolite gave XRD peaks of low intensity meaning that IWW structure was not completely restored. An explanation is that, for Ge-rich material, in which d4r were hydrolyzed, Al cannot rebuild completely the interlayer connections due to the Löwenstein rule. Meanwhile with Ge-poor sample, hydrolysis led to some defects in d4r that can be filled with Al allowing the restoration of the structure. Thus Ge content and distribution directly affect the post treatments.

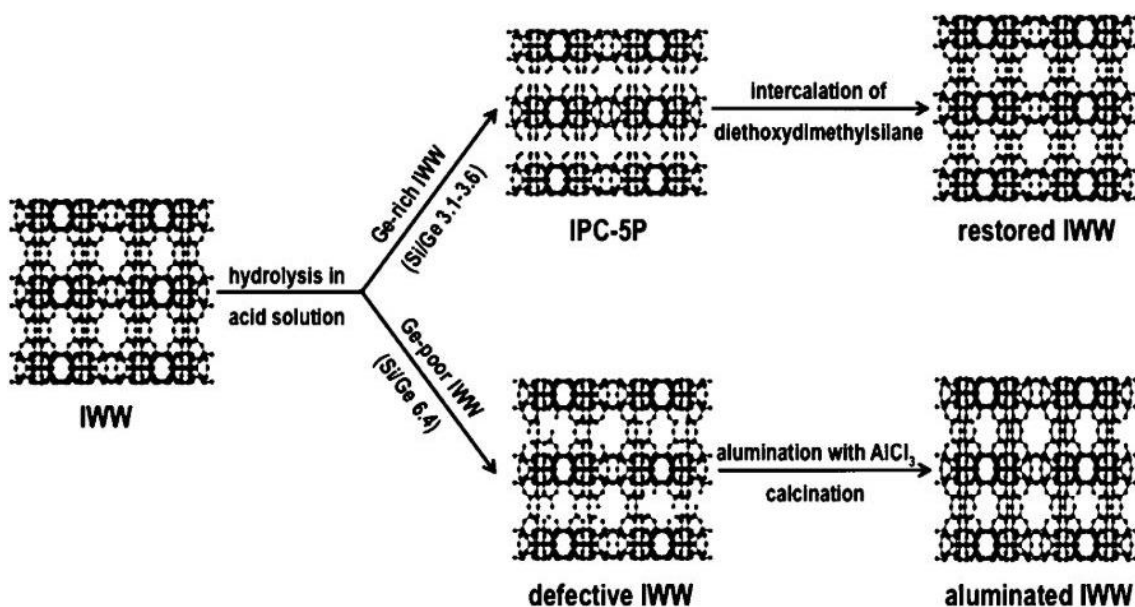


Figure 1- 26: Hydrolysis of IWW with different germanium content and post-synthesis treatments leading to restored IWW frameworks with different chemical composition^[164].

1.3.1.2.3. Acid leaching followed by adding external Si source

Xu et al. stabilized different silicogermanates by isomorphous substitution of Ge for Si giving high silica zeolites^[7].

For ITQ-24, ITQ-17 and IM-20 having low Si/Ge ratios, a treatment with 1M HCl followed by adding tetraethyl orthosilicate (TEOS) as external Si source is needed. The XRD results are presented in Figure 1- 27, a decrease of crystallinity is observed but the materials didn't collapse. The Si/Ge ratios increased to the high-silica region, 15.1 for ITQ-24, 100 for IM-20, and 208 for ITQ-17 with a decrease of microporous volume around 10%.

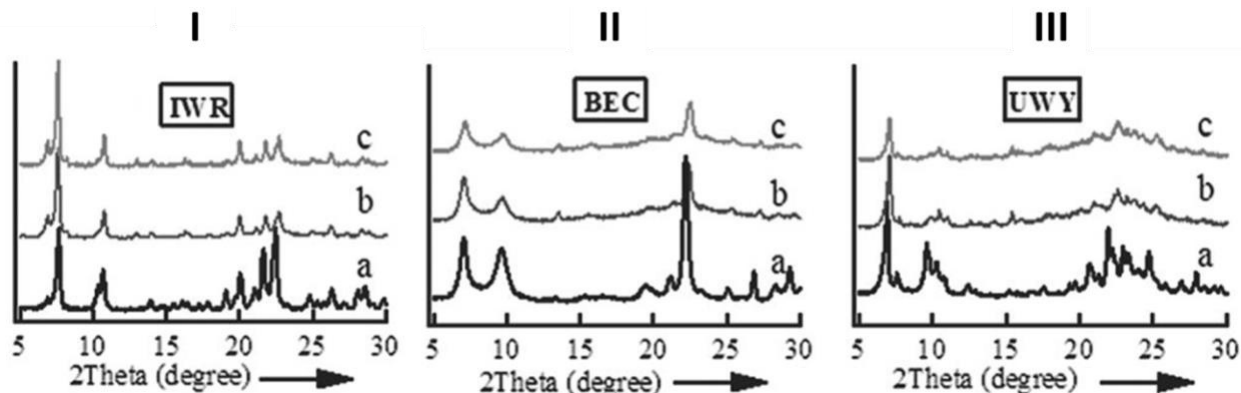


Figure 1- 27: XRD patterns of ITQ-24 (I), ITQ-17 (II) and IM-20 (III). As-synthesized (a), stabilized by Si substitution (b), and further autoclaved in 65% HNO₃ aqueous solution (423K, 24h) and calcination (823 K, 6 h) (c).

Recently Rodriguez-Fernandez et al. optimized the HCl treatment of an as prepared ITQ-33 using TEOS as external Si source^[153]. The treatment with 1M HCl led to the appearance of a peak at 26°

on the XRD pattern characteristic of quartz. The latter indicates that severe conditions led to phase transformation. Treating the sample with lower temperature and acid concentration, prevents its formation (Figure 1- 28.I). ICP analysis showed an increase of the Si/Ge ratio from 2.2 to 3.2, while Al content remained the same. In addition, ^{27}Al MAS NMR spectrum of treated ITQ-33 with 1M HCl solution at 150°C showed the exclusive presence of tetrahedral coordinated Al species (single peak centered at ~ 55 ppm). After three successive treatment, Si/Ge molar ratio increased to 7.4 but some Al was extracted (from $\text{T}^{\text{IV}}/\text{Al} \sim 20$ to $\text{T}^{\text{IV}}/\text{Al} \sim 26$).

^{29}Si MAS NMR spectrum of the three-times treated ITQ-33 showed an increase in the intensity of the peaks associated to Si(4Si) (-110 and -116 ppm), and a decrease of the peaks attributed to Si(2Ge, 2Si) in the range -102 and -105 ppm, (see Figure 1- 28.II). This indicates the selective isomorphous substitution of Ge by Si. N_2 adsorption characterization shows a decrease of micropore volume from 0.28 to of ~ 0.19 cm^3/g after three treatments. This decrease could be explained either by the partial collapse of the crystalline structure or by the incorporation of low-polymerized silicon species within the pores.

The treated sample was tested in the catalytic cracking of a vacuum gasoil. The “degermanized” ITQ-33 zeolite, presented a lower VGO conversion than the fresh parent ITQ-33 zeolite. This can be due to lower Al content and/or micropore volume of the treated ITQ-33. However, despite its initially lower activity, the treated ITQ-33 didn’t deactivate after being tested for three consecutive reaction-regeneration cycles.

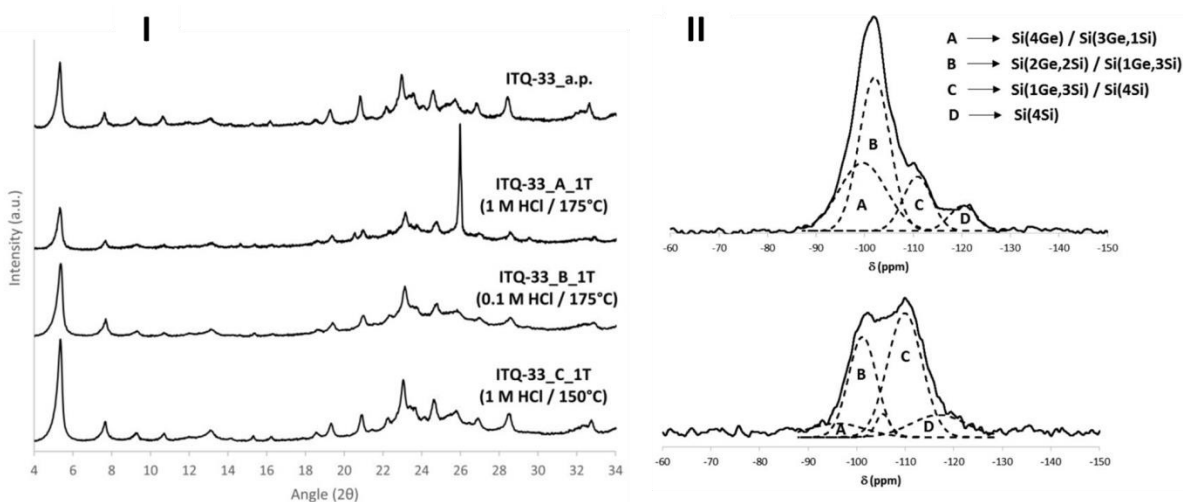


Figure 1- 28: (I) XRD patterns of the as-prepared ITQ-33, and after being treated with an acid solution under different conditions. (II): ^{29}Si MAS NMR of as prepared ITQ-33 (top) and after three times treatments with 1M HCl at 150°C (bottom). Adapted from^[153].

1.3.1.2.4. Acid leaching followed by recrystallization

Peng et al. proposed a new mechanism to form high silica ECNU-24 (UOS) and IM-20 (UWY)^[159]. The concept consist on treating the calcined silicogermanates with 2M HNO_3 leading to the amorphization and structural degradation of the samples and an increasing of the Si/Ge ratios above

10. After that, the leached materials were crystallized in suitable conditions (in presence of NH_4F and OSDA) to form high silica well crystallized zeolites (Figure 1- 29). The disappearance of Si-O-Ge band (1023 cm^{-1}) from the IR spectra confirmed the reduction of the Ge content. The bands assigned to Ge rich content in parent zeolite (525 ; 551 and 567 cm^{-1}) had a blueshift to (542 ; 563 ; 588 and 620 cm^{-1}), this blueshift was in agreement with IR bands assigned using DFT calculations when considering the rearrangement of d4r with decrease of Ge content.

When treated IM-20 was recrystallized in absence of F^- anions, a material with low crystallinity was formed. Since TGA confirmed the participation of OSDA in the recrystallization, it is then suggested that F^- anions are crucial for the construction of high-silica zeolite.

^{19}F MAS NMR showed one resonance for parent IM-20 at -9.1 ppm . Meanwhile recrystallized IM-20 had three additional peaks at -20.4 , -37.8 and -39.5 ppm . Chemical shifts of -38 , -20 and -9 ppm correspond to F^- ions located at the center of d4r with (8Si), (7Si,1Ge) and (4Si, 4Ge) respectively^[88]. It was thus concluded that high silica IM-20 zeolites had d4r composed of 8Si.

To incorporate Al, the acid treatment in presence of aluminum isopropoxide was tried. ^{27}Al MAS NMR confirmed that Al was tetra-coordinated. The final solid was tested in the tetrahydropropyranlation of alcohols. Considering the Si/Al ratios, recrystallized IM-20 had higher catalytic activity compared to ZSM-5 and zeolite beta.

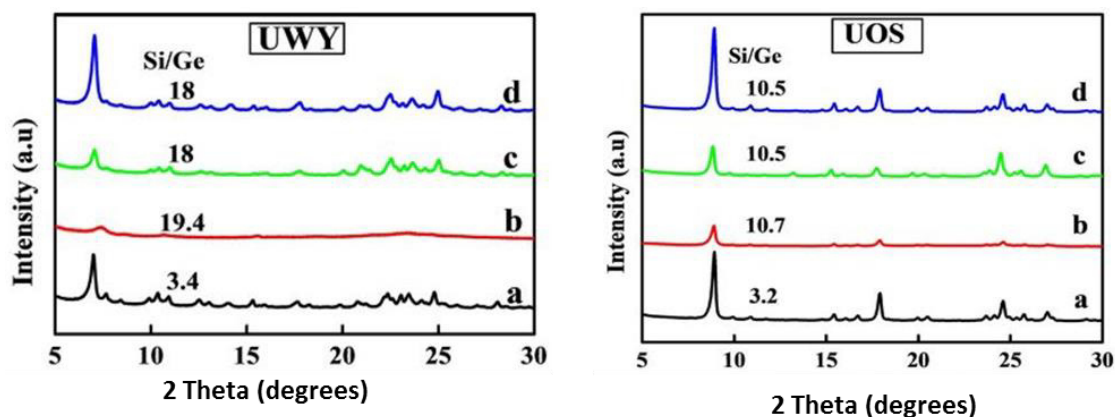


Figure 1- 29: XRD patterns of various UWY-type IM-20 and UOS-type ECNU-24 zeolites. Ge-rich pristine zeolite, calcined (823 K, 6h; a) and after treatment in 2M HNO_3 solution (443 K, 0.5 h and 443 K, 5 h, respectively; b). High-silica materials, as-prepared (c) and after further calcination (823 K, 6 h; d)^[159].

Petkov et al. studied computationally the relative stabilities of (Si, Ge, Al, Ti and Zn)-ITQ-44 within IRR topology by performing periodic density functional theory calculations^[11]. This zeolite has a particular structure containing d4r and d3r. They modeled a pure silica form (Figure 1- 30a) and a representative silicogermanate form following the experimental crystallographic distribution of Ge (Figure 1- 30b)^[83].

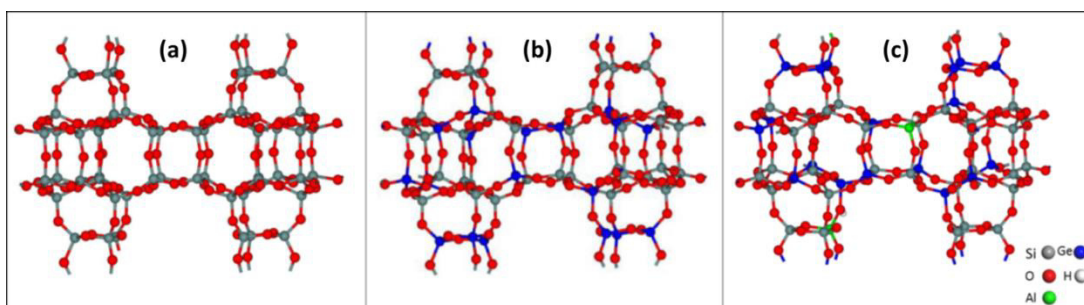
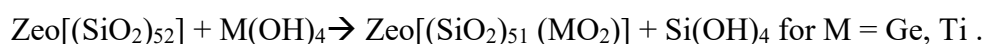


Figure 1- 30: Optimized structures of IRR with different framework composition: (a) $(\text{SiO}_2)_{52}$, (b) $(\text{SiO}_2)_{34}(\text{GeO}_2)_{18}$, and (c) $(\text{SiO}_2)_{32}(\text{GeO}_2)_{18}(\text{AlO}_2\text{H})_2$ ^[11].

In addition, they calculated the relative energy (ΔE) for the substitution of a Si center in the four different crystallographic T-atom positions of the IRR framework by Ge, Ti, or Al from the reaction energy of the following reactions:



Eq. 1- 2



Eq. 1- 3

To check the preferential Ge position, the structure was modeled with different Ge content: increasing Ge content decreased the stability of the zeolite (Figure 1- 31.a). The calculated substitution energy of Ge by Si is 15 kJ/mol per Ge, and the entire silicogermanate structure is 276 kJ/mol less stable than the corresponding Si form. The preferential incorporation of Al was studied on the pure silica zeolite and on the silicogermanate (Figure 1- 30c). Increasing Al content increased the relative stabilities of the structures, e.g. from 276 kJ/mol in the silicogermanate form to 76 kJ/mol after introducing 10 Al atoms, Figure 1- 31b.

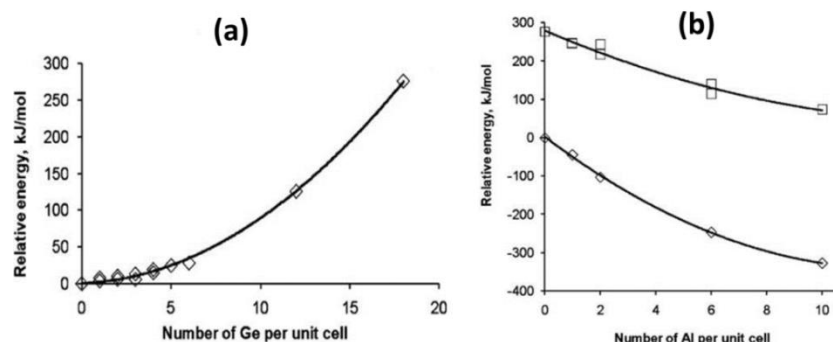


Figure 1- 31: DFT calculated relative energies (in kJ/mol) of (a) IRR structure with increasing amount of Ge atoms in the unit cell and (b) silica structure (rhombus, ◇) and the structure with 18 Ge T-atoms (squares, □) with increasing amount of Al atoms in the unit cell^[11].

To understand the stabilization of silicogermanates by post-treatments, the authors suggested that substitution requires the formation of a framework vacancy followed by the incorporation of a substituting atom. To define the preference in the substitution of Ge and Si, they removed T-atoms from the framework, creating a silanol nest on the removed positions and then calculated the

relative stability of T-atom vacancies, $V_{(Si)}$ or $V_{(Ge)}$. In the all-silica form of ITQ-44, the most preferable position for formation of a Si vacancy is T2 (Figure 1- 32.a). In the ITQ-44 structure containing Si and Ge T-atoms, the most preferable positions for the formation of T-atom vacancies were Si in T2 (in d3r), Figure 1- 32.b and Ge in T1. On the other hand, preference for formation of T-atom vacancies changed when Al was present in the structures. Ge vacancies were favorable over the Si vacancies at all crystallographic positions (Figure 1- 32.c).

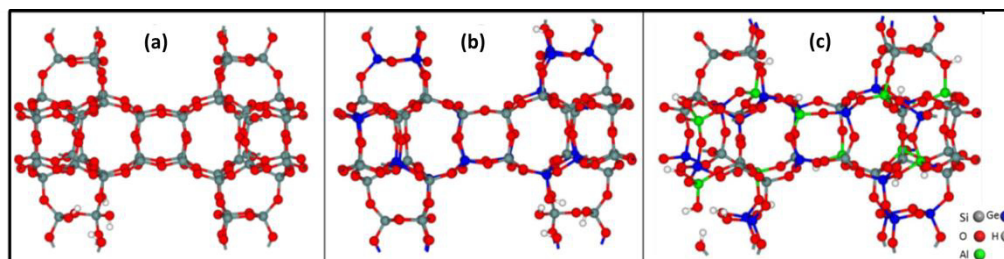


Figure 1- 32: Some of the optimized structures with T-atom vacancy in IRR with different framework composition: (A): $(SiO_2)_{52}-V_{(Si)}/T_2$, (B): $(SiO_2)_{34}(GeO_2)_{18}-V_{(Si)}/T_2$, (C): $(SiO_2)_{24}(GeO_2)_{18}(AlO_2H)_{10}-V_{(Ge)}/T_2$ ^[111].

1.3.2. Creating new structures through acid leaching

In the following paragraph, we present how hydrolysis of a parent silicogermanate can lead to different new structures. Usually, this treatment was applicable on zeolites within frameworks having layers connectivity assured by d4r units (mostly occupied by Ge). The concept consists on leaching Ge from the framework. This partial or full leaching followed by framework rearrangements create new structures. Here we will see how departing from one parent UTL type zeolite, many new structures have been obtained like IPC-2, IPC-4, COK-14, IPC-6, IPC-7, etc. This treatment had different nominations (inverse sigma transformation, ADOR) but the general principle was the same. Later, this treatment was extended to other silicogermanates permitting the enrichment of zeolites topologies.

1.3.2.1. Inverse sigma transformation

In zeolites, systematic insertion and elimination of T atoms is called sigma and inverse sigma transformation respectively^[165]. Verheyen et al. proposed a systematic removal of T-atoms layers followed by the framework reconnection giving a new structure (inverse sigma transformation)^[9]. In fact, the treatment in strong acidic medium (12M HCl) of IM-12 (UTL) extracted a part of Ge located in d4r units leading to a structure called Ge-COK-14. By further washing, it was then possible to extract the remaining Ge from the porosity of this structure giving an interrupted structure called -COK-14. A heat treatment at 550°C dehydrated this structure yielding a new zeolite called COK-14. It is then possible to transform an unstable structure (Si-Ge) with 14 and 12 MR into a new stable zeolite (Si) with 12 and 10 MR (Figure 1- 33). ICP and EDX indicated an increase of Si/Ge ratio from 5.3 for the parent zeolite to 110 for -COK-14.

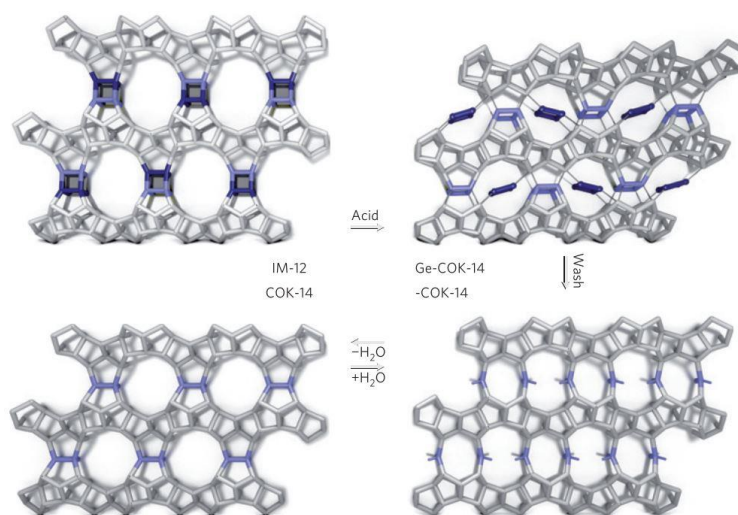


Figure 1- 33: Acid leaching of IM-12 zeolite. Ge-4Rs, dark blue. Si-atoms in layers are presented in grey, Si-atoms in layer-connecting Si-4Rs in light blue^[9].

²⁹Si MAS NMR of the parent IM-12 showed 3 signals, Figure 1- 34: the first is assigned to 3 siloxane bridges and one hydroxyl (Q³ Si) between -90 and -102 ppm, the second to Q⁴ silicon atoms with at least one link to a Ge atom as a direct neighbour (Q⁴-nGe) with a chemical shift in the range of -100 to -110 ppm and the third to Q⁴ silicon atoms surrounded by silicon atoms which only appears between -110 ppm to -120 ppm. The important decrease of the peak attributed to (Q⁴-nGe) in COK-14 confirms the Ge extraction from the framework. The large band of Q³ environments in -COK-14 indicates that some tetrahedral sites are not fully connected. -COK-14 has an idealized unit cell composition of T₆₈O₁₃₂(OH)₈ and an OKO structural type.

Alumination of silicic COK-14 was achieved by atomic layer deposition (ALD) through alternating exposure to trimethylaluminum and water vapors^[166]. The Al-ALD sample was treated with NH₄Cl to obtain the ammonium exchanged form. The treatment of ammonium exchanged sample to obtain the acidic form revealed the transformation of the interrupted structure into a fully connected OKO structure. In addition, after hydration the obtained OKO didn't collapse while the parent pure silica OKO returned to its interrupted form after hydration. Aluminosilicate COK-14 was stable for 6 months in ambient conditions.

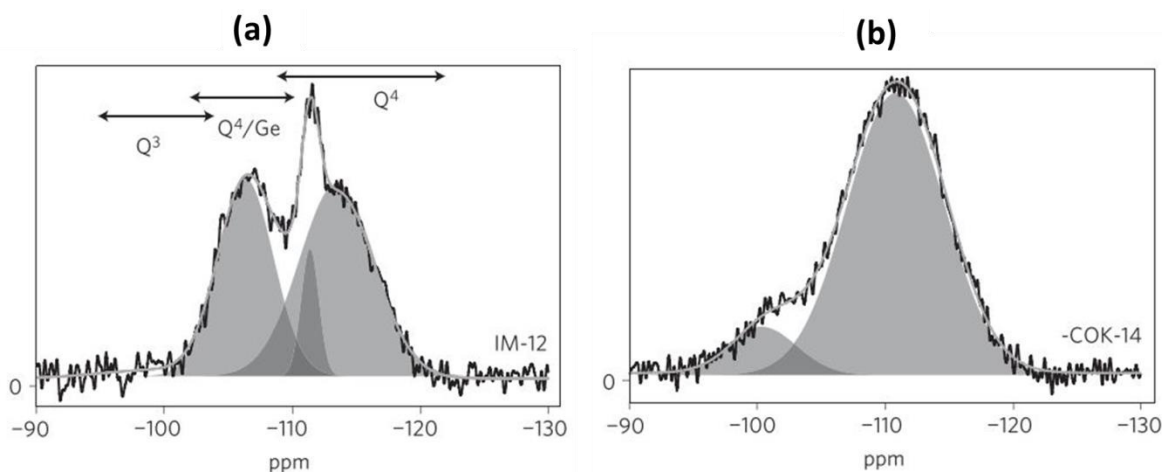


Figure 1- 34: ^{29}Si -NMR spectra of IM-12 (a) and -COK-14 (b)^[9].

^{27}Al MAS NMR revealed the incorporation of tetrahedral aluminum (21%), pentacoordinated or distorted tetrahedral Al (19%) and 60% extra-framework octahedral Al, see Figure 1- 35a. FTIR spectroscopy after adsorption of pyridine (Figure 1- 35b) showed that the total amount of Brønsted acid sites (retaining pyridine) is 6.5 mmol.kg^{-1} at 150°C and 5 mmol.kg^{-1} at 200°C indicating that external Al can be responsible of this low concentration when compared to tetrahedral proportion detected with ^{27}Al MAS NMR.

To prepare a bifunctional catalyst, Pt was impregnated into the ammonium exchanged aluminosilicate –COK-14 using $\text{Pt}(\text{NH}_3)_4\text{Cl}_2$. Pretreatment with oxygen and reduction in hydrogen at 400°C allowed the transformation into fully connected OKO.

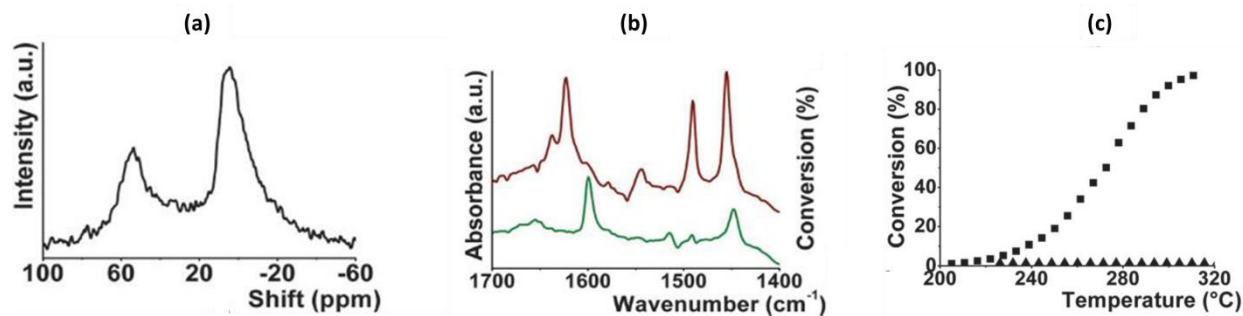


Figure 1- 35: (a) ^{27}Al MAS NMR of aluminosilicate COK-14; (b): FTIR spectra after adsorption of pyridine on all silica –COK-14 (green) and aluminosilicate COK-14 after evacuation at 150°C ; (c) conversion of n-decane against reaction temperature on Pt-loaded all-silica COK-14 (▲) and Pt-loaded aluminosilicate COK-14 (■) (reaction conditions: $P_{\text{H}_2/\text{PC}_{10}} = 214$, $W/F^0 = 980 \text{ kg.s.mol}^{-1}$, $P = 0.45 \text{ MPa}$).^[166]

Hydroconversion of n-decane were tested on Pt-loaded silica and Pt-loaded aluminosilicate COK-14. The latter led to a full conversion of n-decane at 310°C while the non-aluminated sample was completely inactive (Figure 1- 35.c). The same test was repeated a second time on the same sample 4 months later proving the stability and non-deactivation of this aluminated catalyst.

1.3.2.2. Hydrolysis of IM-12 into layers, IPC-1

Roth et al. proposed that treating a borogermanosilicate IM-12 zeolite can lead to the formation of dense lamellas, which can further give new structures^[167]. As mentioned earlier, IM-12 zeolite structure consists of layers interconnected by d4r units. The mild treatment of calcined IM-12 extracts Ge logged in d4r giving a dense lamellar called IPC-1 that look like FER Layer, see Figure 1- 36.a. The hydrolysis depends on different parameters e.g. boron content, use of water or acid solution, and to a large extent the temperature of the treatment. It was noticed that calcination of IPC-1 reveals a small XRD reflection at ca. 7.8° (1.13 nm), consistent with the (001) intralayer reflection in parent UTL (Figure 1- 36b).

They also treated the uncalcined IPC-1 with a silylating agent in nitric acid solution followed by calcination. This treatment gave a new product called IPC-2. While the swallow of an uncalcined IPC-1 with a mixture of cetyltrimethylammonium chloride (CTMA-Cl) and tetrapropylammonium hydroxide (TPA-OH) followed by calcination gave an XRD very similar to that of calcined hydrolyzed UTL. Chemical analysis indicated that Ge and B were eliminated from IPC-1 and IPC-2 solids.

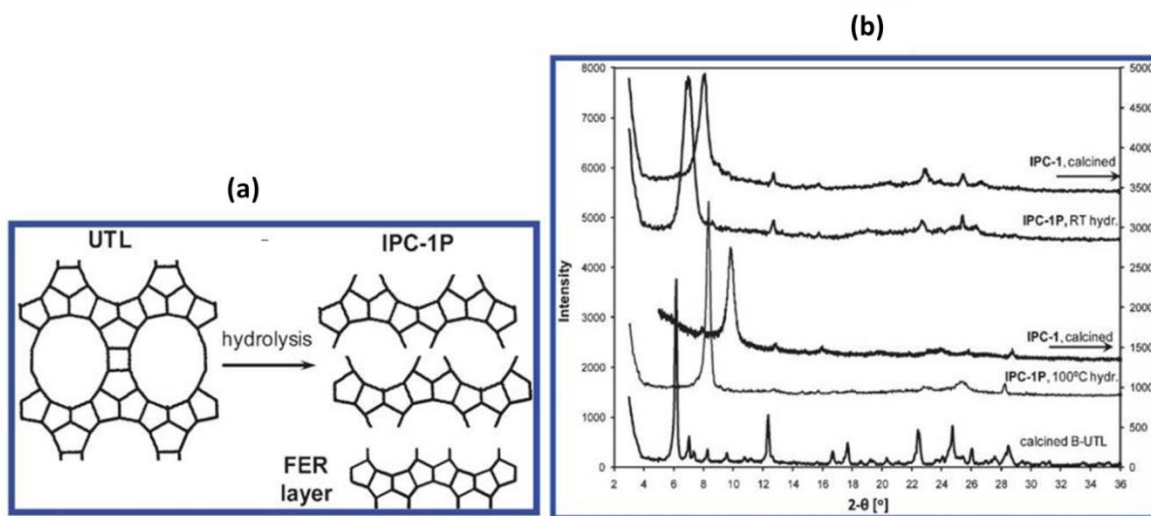


Figure 1- 36: (a) Transformation of UTL into layered zeolite; the included FER layer shows similarity with the UTL layer projection. (b): XRD patterns of UTL zeolite and the products obtained after treatments (IPC-1) ^[167].

1.3.2.3. General features of the ADOR method

Later, Roth et al. described the top down principle known as ADOR method: Assembly, disassembly, organization and reassembly process^[10]. One of the examples is the disassembly of the UTL zeolite into layers and its reassembly into new zeolites IPC-2 (12 and 10 MR) of OKO structural code and IPC-4 (10 and 8 MR) with a PCR structural type. The three zeolites have only one difference which is the linker type of the dense layers. While IM-12 is connected through d4r units, IPC-2 is connected through s4r and IPC-4 through oxygen linkers only, see Figure 1- 37.

Calcined IM-12 was treated with 1M HNO₃ at high temperatures giving IPC-1. Further treatments of uncalcined IPC-1 leads to the formation of new structures. The type of layers linkers is directly related to the intercalating agent added through the treatment.

For IPC-2, diethoxydimethylsilane is added followed by calcination. Methyl groups on silicon atoms are close enough during the condensation of the diethoxysilyl units with silanol layers, making the formation of the Si–O–Si bonds in the s4r unit easier.

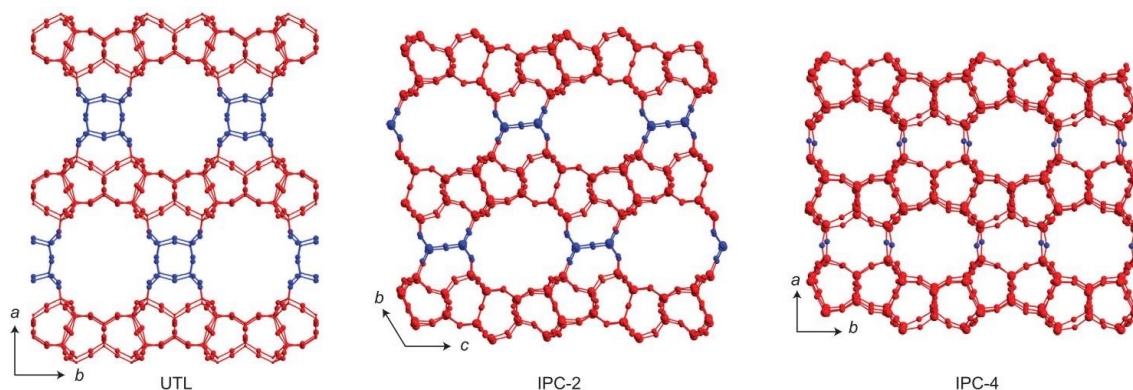


Figure 1- 37: The structures of zeolites UTL, IPC-2 and IPC-4. Layer topology common to all three materials (in red) together with the differently sized linkers (blue) that lead to the different pore sizes in the materials^[10].

For IPC-4, the hydrolyzed UTL was treated with neat octylamine then calcined. In absence of octylamine, hydrolysis of IM-12 led to the formation of non-ordered IPC-1 indicating the importance of the presence of an organic agent. The final Si/Ge ratios were in the ranges 28–32 and 25–30 for IPC-2 and IPC-4, respectively meaning that these new zeolites are stable.

1.3.2.3.1. Intercalating agents

Rearrangement of IPC-1 by intercalating different organic molecules have been investigated^[168]. Intercalated IPC-1 are noted as IPC-1P (organic). All amines gave a PCR type structure which indicates that this rearrangement is the favorable (Figure 1- 38). It can also indicates that amines are not good for obtaining the three remaining possible rearrangements. Calcination of intercalated IPC-1P (organic) with large spacing distance of the intercalated precursor didn't give ordered materials suggesting that long interlayer distance makes the organization of layers more difficult. Another explication is that layers organization in a way allowing OH condensations should happen before the elimination of organic compounds. If the distance between layers is too large, organics are eliminated too fast even before the organization.

After that, some intercalated IPC-1P (organics) were pillared in TEOS, hydrolyzed in water then calcined. Results show that increasing of the alkyl chain of intercalated organics, provides higher d spacing, higher BET area and pore volumes (200, 250 and 300 cm³/g for octyl-, dodecyl- and hexadecyl-chained considered as mesopores.

Another proposed stabilization for IPC-1P (organics) is the treatment with 1M HNO₃ in the presence of alkoxy silanes, followed by calcination. The majority of candidates gave IPC-2 (layers connected with s4r).

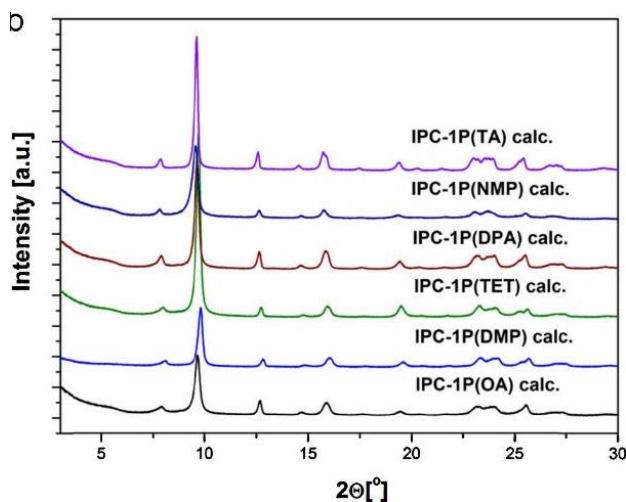


Figure 1- 38: XRD patterns for IPC-1P intercalated with amines, after calcination^[168].

1.3.2.3.2. Treatment conditions

Changing ADOR treatment conditions, e.g. reaction time and acidity led to the formation of two new structures: IPC-6 and IPC-7 starting from IM-12^[158]. Indeed high acidity led before to the formation of IPC-2 by rearrangement of silica from the layers to interlayers sites. And since neutral/very mildly acidic conditions gave IPC-4 by de-intercalation of remaining species from between the layers, varying acidity between these conditions could lead to new structures. Treating sample 1PC-1P with [HCl] = 1.5 M gave the IPC-6 zeolite. Its structure is formed from 50% of the material with a de-intercalation to form IPC-4 and 50% of rearrangement to form IPC-2 (Figure 1- 39.a). Each unit cell have the two types of connections. Rietveld refinement and synchrotron X-ray indicated that the structure is a combination of the two settings and not an intergrowth. IPC-7 having 14 MR consists of a combination of 50% d4r and 50% s4r units connecting the layers (Figure 1- 39.b). In the other hand, both materials are disordered.

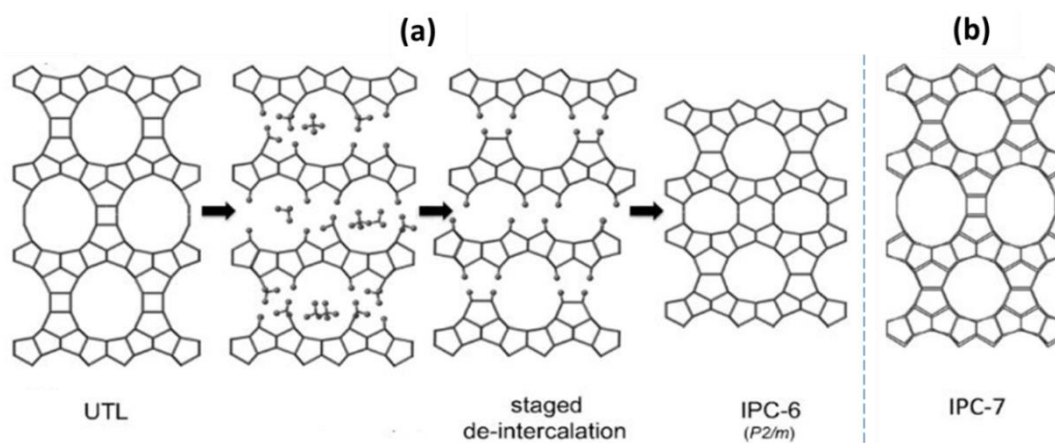


Figure 1- 39: Staged structure of IPC-6. (a) Formation of IPC-6 based on a staged deintercalation mechanism; (b): Structure of IPC-7^[158].

1.3.2.3.3. *Template effect*

Asakura et al. prepared a macroporous UTL using acetylene black as a macropore template. Hydrolysis of UTL parent zeolite followed by intercalation of tetrabutylammonium ions gave a hierarchically micro- and macroporous PCR type material, see Figure 1- 40^[169].

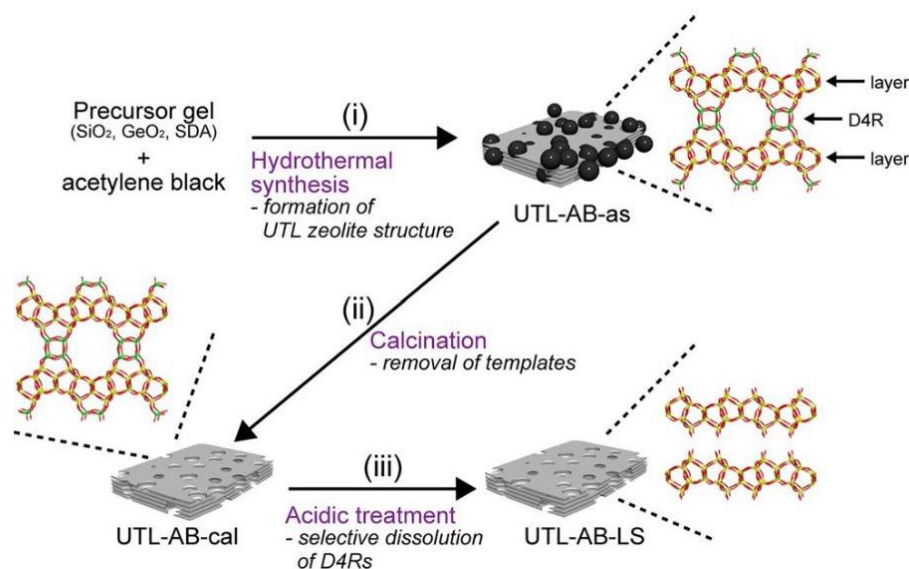


Figure 1- 40: Synthetic procedure of a macroporous layered silicate through (i) hydrothermal synthesis of UTL-type zeolite under the presence of acetylene black, (ii) calcination for elimination of templates, and (iii) acidic treatment for the structural alteration^[169].

Shamzy et al. showed that with optimized acid treatment conditions such as concentration of hydrochloric acid, temperature, duration, etc. the ADOR process can be extended to other silicogermanates possessing layers connected with d4r like ITH, ITR and IWR zeolites^[170].

Kasneryk et al. used this strategy to transform a UOV zeolite (12;10;8 MR) into a new stable IPC-12 zeolite (12; 8 and 6 MR)^[157]. The process is summarized in Figure 1- 41.

Microwave assisted ADOR process allowed the obtaining of novel IPC-5 zeolite from IWW and a variant of IPC-6 from UTL. It was shown that microwave heating allowed the acceleration of the process^[171].

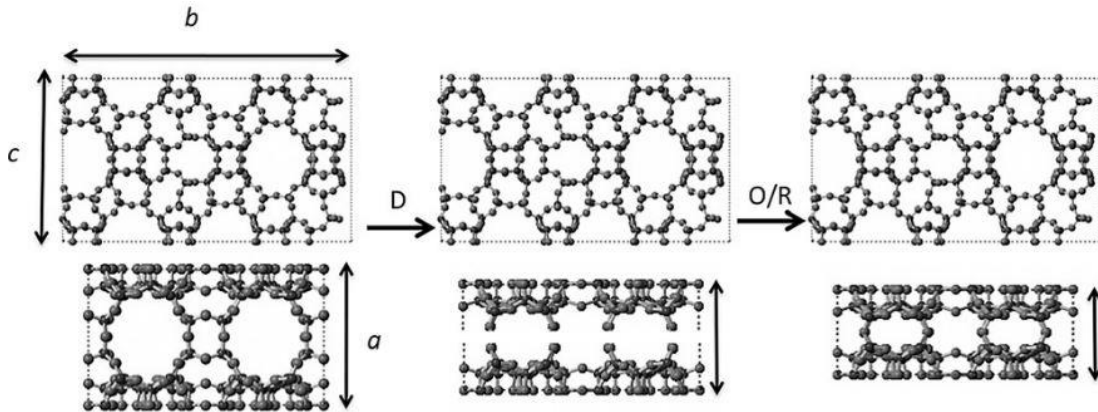


Figure 1- 41: The predicted ADOR process starting with the disassembly (D) of a parent UOV zeolite into layered intermediates by removal of the d4r units, followed by the organization and reassembly steps (O/ R) into the final material^[157].

Hun Kang et al. transformed a CIT-13 zeolite (*CTH) into a CIT-5 germanosilicate (CFI) passing from a 14- and 10 MR to a 14 MR zeolite. The transformation occurs by exposing the calcined CIT-13 to humid atmospheric conditions, without any additional treatment. The sorption of water leads to the rearrangement of Ge-rich d4r, see Figure 1- 42. The obtained Ge-CIT-5 was then treated with an acidic aluminium nitrate solution giving an Al-CIT-5 with Si/Al ratios varying from 14 to 230 and Si/Ge ratios varying from 13 to 38 depending on the treatments conditions^[160].

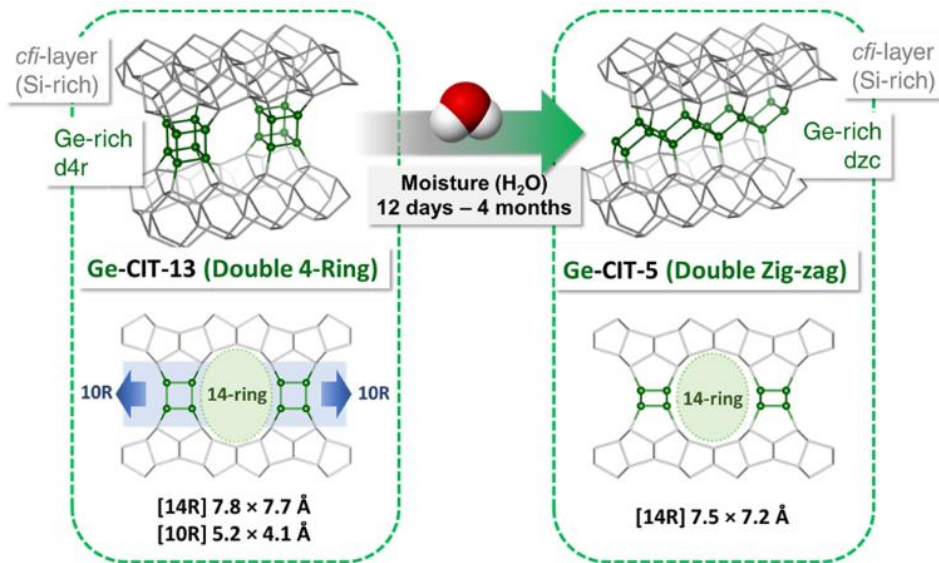


Figure 1- 42: Schematic illustration of the transformation from Ge-CIT-13 to Ge-CIT-5 mediated by water. Dsz denotes double-zigzag chains^[160].

The SAZ-1 zeolite has the same framework topology (*CTH) than the CIT-13. Firth et al. treated the SAZ-1 zeolite through the ADOR process and obtained two new zeolites. At First, SAZ-1 was

hydrolyzed using HCl into layers SAZ-1P. When the latter was treated with octylamine, the IPC-15 zeolite was obtained while the treatment with HNO₃ and diethoxydimethylsilane gave the IPC-16^[138]. Applying the ADOR process on CIT-13 gave CIT-14 (12x8MR) and CIT-15 (10MR) isostructural to IPC-16 et IPC-15 respectively^[161,162]. While the treatment of CIT-13 using aqueous ammonia solution as a delamination agent gave the high silica ECNU-21 zeolite isostructural to CIT-15 and IPC-15. The germanium-related Lewis acid sites served as catalytic sites for the shape-selective hydration of ethylene oxide (EO) to ethylene glycol (EG).^[81]

Trachta et al. predicted computationally the structures that could be obtained by applying the ADOR process on zeolites containing d4r units as interlayer pillars: UTL, IWW, IWV, IWR, ITR, and ITH^[172]. Since each layered material can lead to several new zeolite structures, they adopted a two-step procedure to explore the possible re-arrangements of the layers: 1) minimizing the O-O distance between overlapping silanol groups that undergo topotactic condensation, and 2) optimizing the structural parameters of the condensed 3D zeolite framework using periodic DFT calculations and a program written using MATLAB .

Following this approach, 20 new silicic structures were identified. UTL and ITR can give 4 new zeolites each while other parent zeolites can give 3 structures each due to symmetry reasons, see Table 1- 4.

In addition, all the new zeolite structures reported in Table 1- 4 appear to be thermodynamically accessible (they are within 30 kJ/mol per SiO₂ with respect to α -quartz). Hypothetical zeolites, IWW-d4r (Pbam) and IWV-d4r (Fmmm) are the most promising candidates for experimental research based on their relative thermodynamic stability.

A further investigation on UTL, IWW, IWV, IWR, ITR, and ITH zeolites considered this time two species with distinct interlamellar linkers, denoted as -d4r and -s4r zeolites^[173]. The -d4r materials contain lamellae connected by oxygen (T-O-T) linkers corresponding to a complete removal of the d4r building units from the parent zeolite. The -s4r materials contain single four-membered rings (s4rs) instead of the dissolved d4r units (not necessarily in the same position), see Figure 1- 43.

Table 1- 4 : Relative stabilities, framework densities, and channel characteristics of parent and new zeolites^[172].

Zeolite ^[a]	E_{rel} ^[b]	Channel architecture	FD ^[c]	V_{micro} ^[d]	SA ^[e]
UTL	12.0	2D: 14R×12R	15.1	0.265	779
-D4R(C2/m)	9.1	2D: 10R×8R	18.1	0.137	209
-D4R(Pm)	11.7	2D: 8R×8R	19.0	0.049	43
-D4R(P1)	12.5	1D: 10R	18.7	0.059	76
-D4R(Pm')	14.7	1D: 8R	19.3	0.044	5
IWW	11.7	3D:12R + 8R×10R×10R	15.9	0.21	577
-D4R(Pbam)	11.0	3D: 12R + 8R×8R	17.9	0.137	206
-D4R(C2/c)	19.0	0D	19.9	0.157	210
-D4R(Aba2)	22.3	0D	20.7	0.133	136
IWV	13.3	2D: 14R×12R	14.7	0.299	789
-D4R(Fmmm)	11.1	2D: 10R×8R	18.0	0.175	134
-D4R(Cmm2)	16.8	2D: 8R×8R	18.9	0.149	61
-D4R(C2/m)	21.2	1D: 8R	20.2	0.061	16
IWR	12.1	3D: 12R×10R×10R	15.2	0.262	774
-D4R(P1 _{Cmmm})	11.3	3D: 12R×8R×8R	17.1	0.173	423
-D4R(C2/m)	11.5	2D: 8R×8R	17.8	0.126	222
-D4R(Cmmm)	12.3	3D: 12R×8R×8R	17.1	0.175	411
-D4R(Fmmm)	13.3	3D: 8R×8R×8R	18.0	0.168	376
ITH	10.4	3D: 10R×9R×10R	16.8	0.174	426
-D4R(P1 _{Amm2})	8.9	3D: 9R×8R×8R	19.1	0.090	73
-D4R(Cm)	9.7	1D: 8R	19.3	0.056	7
-D4R(Amm2)	9.9	3D: 9R×8R×8R	19.0	0.094	71
-D4R(Cm')	11.2	0D	19.5	0.130	27
ITR	10.4	3D: 10R×10R×9R	16.8	0.176	432
-D4R(P21/m)	8.3	3D: 9R×8R×8R	19.3	0.084	23
-D4R(P-1)	8.3	3D: 9R×8R×8R	19.4	0.069	10
-D4R(C2/m)	8.4	3D: 9R×8R×8R	19.4	0.073	8
-D4R(C2/m')	8.7	3D: 9R×8R×8R	19.4	0.083	35

[a] d4r-containing parent zeolites (bold) and hypothetical zeolites derived from the parent zeolites by the in silico ADOR procedure.

[b] Relative energies with respect to Si- α -quartz in kJ/mol.

[c] Framework density in Si per 1000Å³.

[d] Microporous volume in cm³/g. [e] Surface area in m²/g.

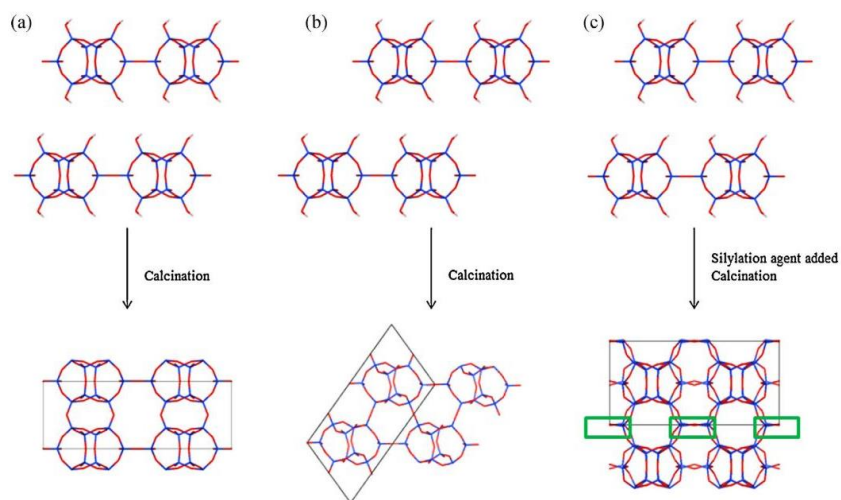


Figure 1- 43: Theoretical construction of the ADOR process leading to (a) - d4r material with lamellae in the fundamental arrangement, (b) - d4r material with shifted arrangement in one or both directions, and (c) -s4r material with s4r linkers marked by green rectangles^[173].

Table 1- 5: Framework energies (FE, in kJ/mol) and densities (FD, in $10^{-3}/\text{\AA}^3$) of (right) - d4r materials and (left) -s4r evaluated at the DFT and FF (force-field) levels of theory.

Zeolite	FE _{DFT}	FE _{FF}	FD _{DFT}	FD _{FF}	Zeolite	FE _{DFT}	FE _{FF}	FD _{DFT}	FD _{FF}
UTL	12.0	15.3	15.1	15.8	UTL	12.0	15.3	15.1	15.8
-D4R(C2/m)	9.1	10.4	18.1	19.3	-S4R(C2)	11.2	13.8	17.0	17.8
-D4R(Pm)	11.7	12.5	19.0	20.2	-S4R(P1)	18.8	22.2	18.0	18.9
-D4R(P1)	12.5	14.0	18.7	19.8	-S4R(Pm)	18.8	23.3	18.5	19.3
-D4R(Pm')	14.7	15.6	19.3	20.6	-S4R(P1')	21.0	24.1	18.8	19.7
IWW	11.7	13.8	15.9	16.8	IWW	11.7	13.8	15.9	16.8
-D4R(Pbam)	11.0	12.3	17.9	19.1	-S4R(P1)	11.6	13.5	18.2	19.1
-D4R(C2/c)	19.0	21.9	19.9	21.0	-S4R(C2/c)	16.1	19.2	18.5	19.3
-D4R(Aba2)	22.3	25.1	20.7	21.8	IWV	13.3	14.6	14.7	15.8
IWV	13.3	14.6	14.7	15.8	-S4R(P1)	10.3	12.5	16.9	17.8
-D4R(Fmmm)	11.1	10.6	18.0	19.9	IWR	12.1	15.5	15.2	15.9
-D4R(Cmm2)	16.8	16.6	18.9	20.6	-S4R(C2/m)	12.3	16.2	17.4	18.0
-D4R(C2/m)	21.2	24.1	20.2	21.6	-S4R(Cmcm)	14.8	18.4	18.5	19.6
IWR	12.1	15.5	15.2	15.9	-S4R(Immm)	17.1	21.1	18.3	19.3
-D4R(P1 _{Cmmm})	11.3	15.0	17.1	18.0	ITH	10.4	12.4	16.8	17.8
-D4R(C2/m)	11.5	14.1	17.8	18.8	-S4R(Cmc21)	9.3	11.2	18.7	19.8
-D4R(Cmmm)	12.3	15.0	17.1	18.8	-S4R(Cm)	9.4	11.4	18.7	19.7
-D4R(Fmmm)	13.3	17.8	18.0	18.9	-S4R(P1)	9.5	11.1	19.2	20.2
ITH	10.4	12.4	16.8	17.8	-S4R(Cm')	9.6	12.0	18.7	19.7
-D4R(P1 _{Amm2})	8.9	11.2	19.1	20.4	-S4R(Imm2)	10.3	12.4	18.6	19.7
-D4R(Cm)	9.4	11.7	19.4	20.6	-S4R(Cm'')	10.7	13.6	18.9	19.8
-D4R(Cm')	9.7	10.5	19.3	20.6	-S4R(Cm''')	11.3	14.0	18.8	19.8
-D4R(Amm2)	9.9	11.2	19.0	20.4	-S4R(Cm''')	12.3	14.7	19.1	20.1
ITR	10.4	12.5	16.8	17.7	ITR	10.4	12.5	16.8	17.7
-D4R(P21/m)	8.3	10.0	19.3	20.5	-S4R(Pnmm)	9.3	11.3	18.8	19.8
-D4R(P-1)	8.3	10.0	19.4	20.8	-S4R(C2/c)	9.3	10.7	19.1	20.2
-D4R(C2/m)	8.4	10.1	19.4	20.7	-S4R(C2)	9.4	11.3	18.8	19.9
-D4R(C2/m')	8.7	10.6	19.4	20.8	-S4R(P-1)	9.5	11.3	18.9	19.9
					-S4R(Cm)	9.5	11.4	18.8	19.9
					-S4R(P1)	9.5	11.6	18.9	19.8
					-S4R(P21)	9.7	11.6	18.7	19.7
					-S4R(P-1')	9.7	11.6	18.7	19.8
					-S4R(P-1'')	9.7	11.6	18.9	20.0

The computed results are represented in Table 1- 5. In summary, each of UTL, IWW and IWR families have one energetically preferred structure for both -s4r and -d4r materials. While IWR family has a single energetically preferred IWR-s4r structure and several structures with similar

framework energies among IWR- d4r zeolites. ITH and ITR materials have many energetically favorable structures independently of the inter-layer linker.

1.4. Bifunctional zeolite catalysts

Acidic solid catalysts such as silica-alumina and zeolites are known for their high activity concerning the conversion of olefins into their skeletal isomers. Combining these catalysts to a (de-)hydrogenative catalyst can lead to paraffin isomerization: paraffin are dehydrogenated into olefin intermediates, the latter skeletal rearrangements are then enhanced by the acid sites^[174-176]. A bifunctional catalyst for hydroisomerization contains an acidic catalyst (typically: the zeolite, thanks to its Brønsted sites) and a metallic phase, that may be a highly dispersed noble metal deposits such as platinum or palladium. Bifunctional zeolites are widely used for the hydrocracking and hydroisomerisation of long paraffin, of renewable hydrocarbons^[177] and for the oligocracking. During the hydroisomerisation of alkanes, the metal sites assure the dehydrogenation of paraffin and the hydrogenation of olefins while the acid sites catalyze the skeletal isomerization of olefins giving isomerized and cracked products. The products of the hydroconversion of alkanes are dependent of the hydrogenation versus acid activities. When hydrogenation activity is higher than that of acidity, the amounts of isomers in the products are higher, in the opposite case splitting predominates and reduces the production of isomers^[178]. Several methods are used to introduce metal sites in acid catalysts like impregnation, homogeneous deposition-precipitation, ion exchange and electrostatic adsorption^[179]. For zeolites, impregnation is the most common process, it is divided into two types depending on the added volume of solution. When the volume of the solution containing the metal precursor is equal to the pore volume of the dried zeolite, the process is called capillary or dry or incipient wetness impregnation. In this type, the capillary suction drives the solution inside the pores. When a water filled zeolite is immersed in the precursor solution and the latter migrates to the pores by diffusion the process is called wet impregnation.

The hydroisomerization of n-decane is a model reaction that defines very finely the relationship between the pore topology of the zeolite and the isomers selectivity. This relationship is presented in the following section. Notably, the mechanisms presented in the following remain valid for longer alkanes such as n-hexadecane.

1.4.1 General mechanism of n-decane hydroisomerization on bifunctional zeolites

The mechanism of hydroisomerization of n-decane without steric constraints is representative of that of long chain alkanes and is represented in Figure 1- 44. At low conversion, n-decane are dehydrogenated on the metal site giving n-decene. The latter desorb from the Pt sites and migrate to the Brønsted acid sites of the zeolite, where they are protonated into secondary n-decyl cations. These carbenium ions can be skeletally rearranged or splitted by carbon-carbon bond rupture via

β -scission producing a smaller alkylcarbenium ion and an alkene. Since the β -scission of n-decene gives primary unstable carbenium ions, only skeletal rearrangements occur first, leading to the formation of monobranched iso-decyl cations. The latter may then be deprotonated by framework deprotonated oxygen atoms and the formed monobranched iso-decene diffuse to metal sites where they are hydrogenated to monobranched isodecane. When the conversion increases, consecutive reactions take place on the acid sites like a second then a third branching rearrangement of the carbenium ions, leading to dibranched and tribranched isodecyl cations. These cations are desorbed as iso-decene and are hydrogenated by the metal sites giving dibranched and tribranched iso-decane. Since the β -scission rate increases with the degree of branching, the tri-branched decyl cation usually do not desorb from the acid sites but instead go through a β -scission giving an alkylcarbenium ion and a alkene. The produced alkylcarbenium ions are either deprotonated then desorbed as alkenes from the acid site and hydrogenated by metal sites to form primary cracked alkanes with a carbon number varying from 3 to 7. Or if the desorption is not fast enough the primary cracked products are submitted to a secondary β -scission giving light alkanes. It is worth mentioning that primary carbenium ions like CH_3^+ and C_2H_5^+ are not stable thus cannot be formed by β -scission explaining the quasi-absence of C_1 and C_2 products in the hydroisomerisation of n-decane^[180]. Hence the presence of these products reflects the presence of hydrogenolysis over the metallic phase.

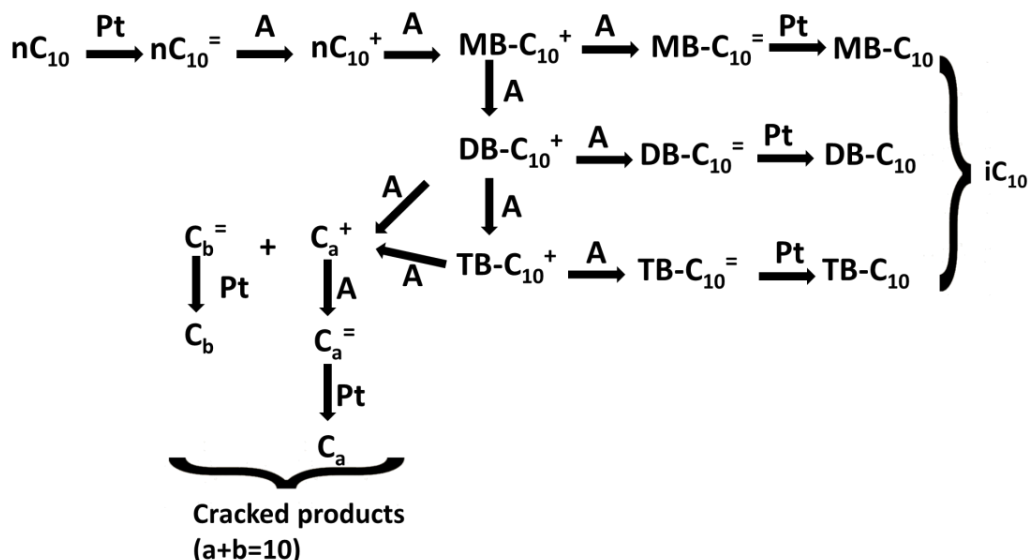


Figure 1- 44: The classical reaction scheme of n-decane ($n\text{C}_{10}$) on a Pt/USY zeolite. The metal sites (M), platinum in this case, are responsible for (de)hydrogenation. The Brønsted acid sites (A) are responsible for (de)protonation. Superscripts “=” and “+” indicate alkenes and alkylcarbenium ions respectively. Prefixes “MB-“, “DB-“ and “TB-“ denote monobranched, dibranched and tribranched skeletal isomers respectively. C_a and C_b represent the cracked products formed, which means that $a + b = 10$. Adapted from ^[181].

The reactions involved in the hydroisomerization of n-decane and their rates control the final products selectivity. They are also indicative of the structural properties of the zeolite, of the active sites distribution (microporosity vs. external surface) and lead to the selection of different criteria specific to the n-decane catalytic test. In the following two paragraphs, we will present the reactions occurring during the hydroisomerisation then the n-decane test criteria.

1.4.2 Reaction mechanisms involved in n-decane hydroconversion

1.4.2.1 Isomerization reactions

Alkanes are dehydrogenated by the metal sites, then the protons of the acid zeolite attack the π electrons of the alkene giving acyclic alkylcarbenium ions that can be rearranged on the same acid sites. The skeletal rearrangement happens following type A (no change in the branching degree) or type B (change in branching degree) isomerizations. Isomerization of acyclic carbenium ions occur via substituted protonated cycloalkanes. The smallest ring of these alkylcarbonium ions are the substituted protonated cyclopropanes (PCP). The three different forms of PCP are represented in Figure 1- 45. Molecular orbital calculations showed that CPCP is more stable than EPCP and both are much more stable than FPCP^[182,183].

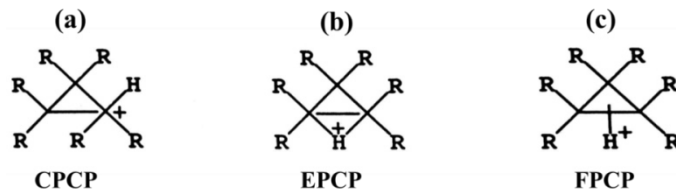


Figure 1- 45: a) Corner protonated cyclopropane (CPCP), b) Edge protonated cyclopropane (EPCP) and c) Face protonated cyclopropane (FPCP)^[180].

In type A isomerization, only the positions of the branching change while their number remains constant. In type B isomerization, the degree of branching is increased or reduced. Type A isomerization occurs via hydride and alkyl shifts. Based on superacid chemistry, the alkyl shift proceeds through the cyclization of the alkylcarbenium ion to form a CPCP followed by reopening of the cycle. An example of type A isomerization of 2-methyl-2-pentyl into a 3-methyl-3-pentyl cation is represented in Figure 1- 46.

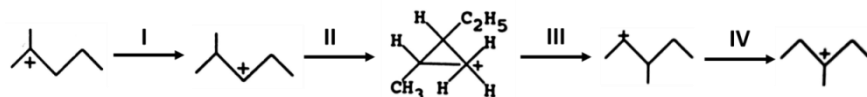


Figure 1- 46 : Possible type A isomerization of 2-methyl-2-pentyl into a 3-methyl-3-pentyl cation consisting of 1,2-hydride shift (I), followed by a cyclization into an intermediate CPCP (II), a reopening of the cyclopropane ring (III) and a 1,2-hydride shift (IV). Adapted from ref^[180].

Type B isomerization involves the formation of a CPCP, followed by a corner to corner proton jump and then the reopening of the cycle. To increase the degree of branching the corner to corner

jump is in a way that the positive charge will be located on the carbon of the PCP free of alkyl substituents while for decreasing the branching the proton moves from the non-substituted corner carbon to a substituted corner carbon. Figure 1- 47 illustrates an example of type B isomerization. Note that type B is slower than type A isomerization due to the additional proton jump step^[180]. Moreover, it was recently demonstrated using molecular dynamics and blue moon ensemble approach that type B isomerisation is slower than type A because of enthalpic and entropic criteria^[183]. The transition state of type B isomerization is a tight EPCP while that of type A isomerization is a loose CPCP. Indeed the more flexible the structure is, the higher are the entropy and the stability.

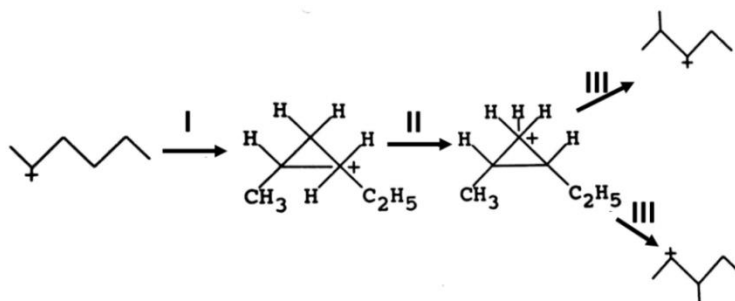


Figure 1- 47: Possible type B isomerization of 3-hexyl cation consisting of a cyclization into an intermediate CPCP (I), a corner to corner proton jump (II) and a reopening of the cyclopropane ring (III). Adapted from^[180].

In the hydroisomerization of n-decane, methylbranched skeletal isomers are formed via PCP intermediates. This PCP mechanism leads to the formation of four positional isomers. Considering identical reaction rates for their transformation, it is noticed that two reaction pathways give 3-methylnonane and 4-methylnonane while only one pathway lead to the formation of 2-methylnonane and 5-methylnonane thus methylbranching at positions 3 and 4 occurs twice as fast as at positions 2 and 5, Figure 1- 48.

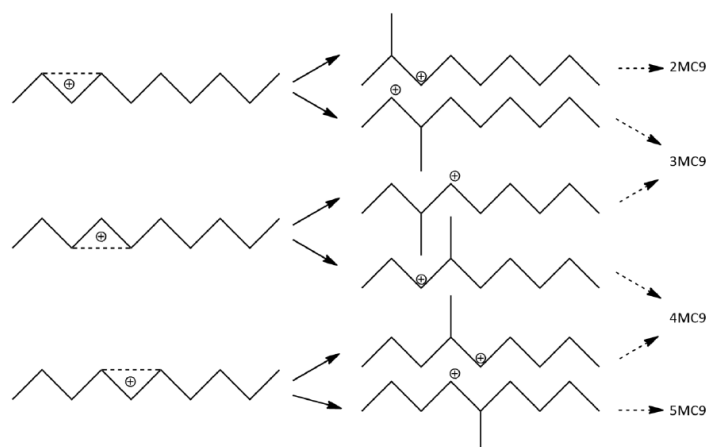


Figure 1- 48 : Formation of methylbranched n-decane skeletal isomers via protonated cyclopropane (PCP) structures. Adapted from^[184].

Longer side chains like ethyl and propylbranches can be formed similarly to the methylbranching mechanism involving CPCP. For the formation of ethyloctanes and propylheptane substituted corner protonated cyclobutanes CPCB and cyclopentanes (CPCPe) are involved. Like the branching mechanism via CPCP type B isomerization, a proton jump can occur with CPCB and CPCPe mechanisms, the only difference is that in the latter cases there is only one possible way of the ring opening to avoid the formation of primary alkylcarbenium ions.

Ethyl and propylbranches can also be formed by side-chain elongation via type A isomerization. It consists of consecutive shifts of ethyl and bulkier alkyl groups on methylbranched cations. A methyl side chain is transformed into an ethylbranched chain which can be converted to a propylbranching. This elongations occur through the 1,2-shift of an alkyl group larger than a methyl group. An example of the elongation of 5-methyl-5-nonyl cation via this mechanism is illustrated in Figure 1- 49.

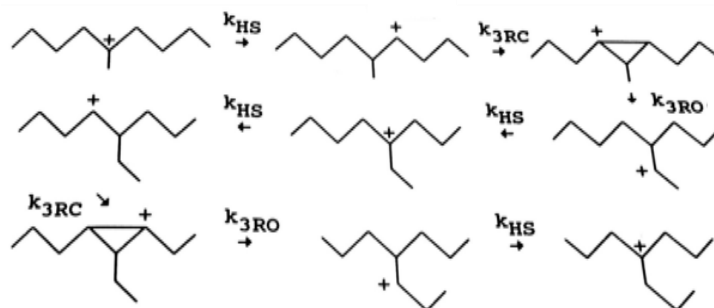


Figure 1- 49 : 1,2-Methyl shift and one-carbon-at-a-time elongation of the methyl side chain in 5-methyl-5-nonyl cation via CPCP intermediates. HS; RC and RO refers to 1,2-hydride shift, ring closure and ring opening respectively [180].

In the case of decane, the formation of ethyloctane and propylheptane via the side chain expansion is as follows^[180]:

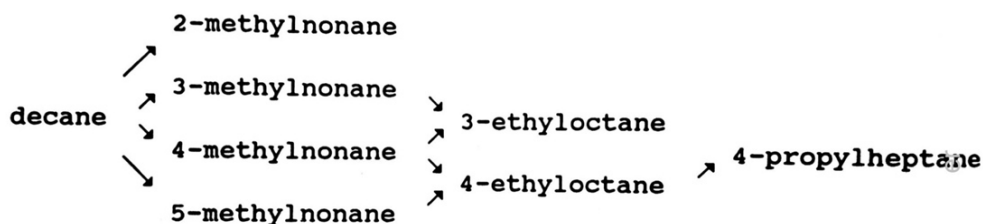


Figure 1- 50 : Formation of ethyloctane and propylheptane via the side chain expansion^[180].

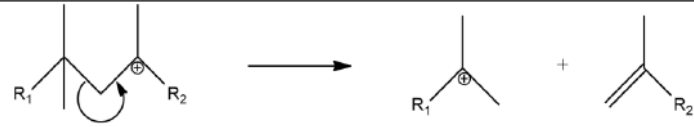
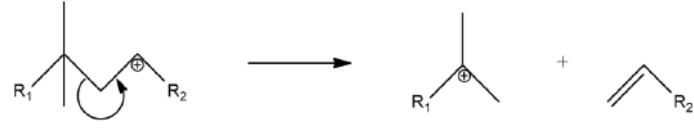
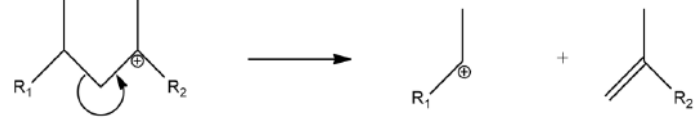
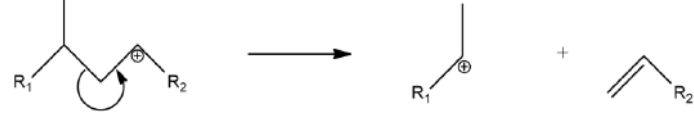
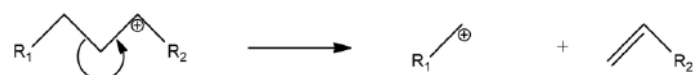
Thus through side-chain elongation via type A isomerization, 3-ethyloctanes, 4-ethyloctanes and 4-propylheptanes are of secondary nature and the larger the side chain of the monobranched isomer, the later the isomer is formed. Meanwhile through type B isomerization, all the monobranched isomers are of primary nature but their rate of formation depends on the ring size of the protonated cycloalkane: formation rate of CPCP > formation rate CPCB > formation rate CPCPe > Rate of CPCH, etc.^[180].

Mono-, di- and multibranched decane isomers are formed by successive methylbranching via PCP intermediates. After skeletal rearrangements of n-decane, hydrocracking can follow via different β -scission mechanisms.

1.4.2.2 Cracking reactions

During the β -scission, the two electrons of the C-C bond in the β position of the initial alkylcarbenium ion move towards the C-C bond in α position^[185]. After the scission, the latter bond becomes olefinic and the C in the γ position becomes electron deficient, as a result a smaller alkylcarbenium ion is formed. The different modes of β -scission are represented in Table 1- 6. In the experimental conditions of hydroisomerization of decane, the formation of primary carbenium ions is not probable thus methane, ethane and their complementary nonane and octane are not expected to be formed. The cracking products are normal or branched paraffins with a carbon number from 3 to 7^[184,186]. The molar distribution of the cracked products per carbon number are also indicative of the primary cracking. The latter is evidenced by the symmetrical product distribution. In addition, as 100 moles of n-decane feed are expected to give 200 moles of primary cracked products, any deviation of this value reflects a secondary cracking or hydrogenolysis^[186].

Table 1- 6 : β -scission modes acting on skeletal isomers of decane. (T) stands for tertiary, (S) for secondary and (P) for primary alkylcarbenium ions. R_1 and R_2 are alkyl substituents. Adapted from^[180].

β -scission mechanism	C ⁺ involved	Reaction type
Type A	T -> T	
Type B ₁	S -> T	
Type B ₂	T -> S	
Type C	S -> S	
Type D	S -> P	

To conclude, the bifunctional conversion of n-decane gives methylnonanes, ethyloctanes, propylheptane, dimethyloctanes and trimethylheptanes as isomeric products. The cracked products are normal or branched paraffin with a carbon number from 3 to 7^[184].

1.4.3 Relationship between n-decane hydroconversion and zeolite topologies (n-decane criteria)

The hydroconversion of n-decane on metal-loaded acid zeolites gives information on the pore structure of a bifunctional catalyst based on different criteria described by J. Martens et al.^[184]:

- Overall distribution of the feed isomers according to their degree of branching and the relative contribution of the ethyl-isomers to the monobranched isomers at low isomerization conversion:

The methylbranched isodecane are formed via protonated cyclopropane (PCP) intermediates. Mono-, di- and multibranched decane isomers are formed by the successive methylbranching via PCP. Since isomerization is followed by hydrocracking, when plotted against conversion it reaches a maximum, see Figure 1- 51. In open pores, the equilibrium between mono and dibranched isomers is reached at this maximum. Thus any deviation indicates having steric constraints. For example, a 10-MR zeolite will desorb minor amounts of dibranched isomers than a 12-MR zeolite which can be seen in Figure 1- 52a.

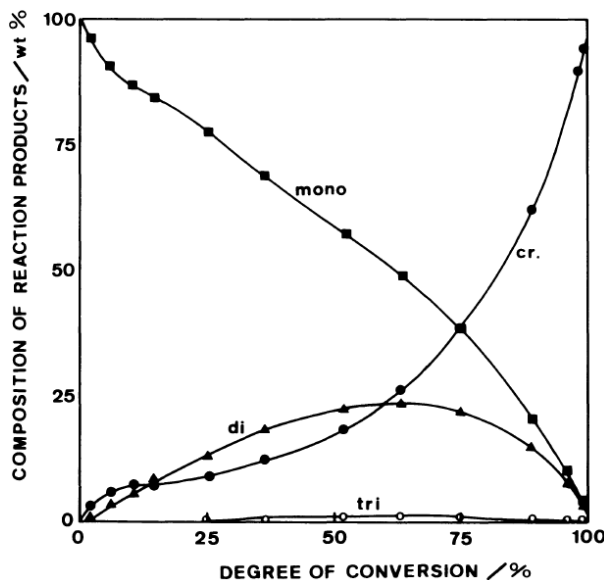


Figure 1- 51 : Distribution of mono-, di-, and tribranched isomers and cracked products (in weight%) from decane against its degree of conversion (%) using a Pt/USY catalyst. The total reaction pressure was 0.35MPa, the H₂/decane molar ratio was 100, the molar flow rate at the reactor inlet (F₀/ W) was 0.4 mmol kg⁻¹.s⁻¹. The conversion was changed by increasing the reaction temperature from 400 to 500 K^[180].

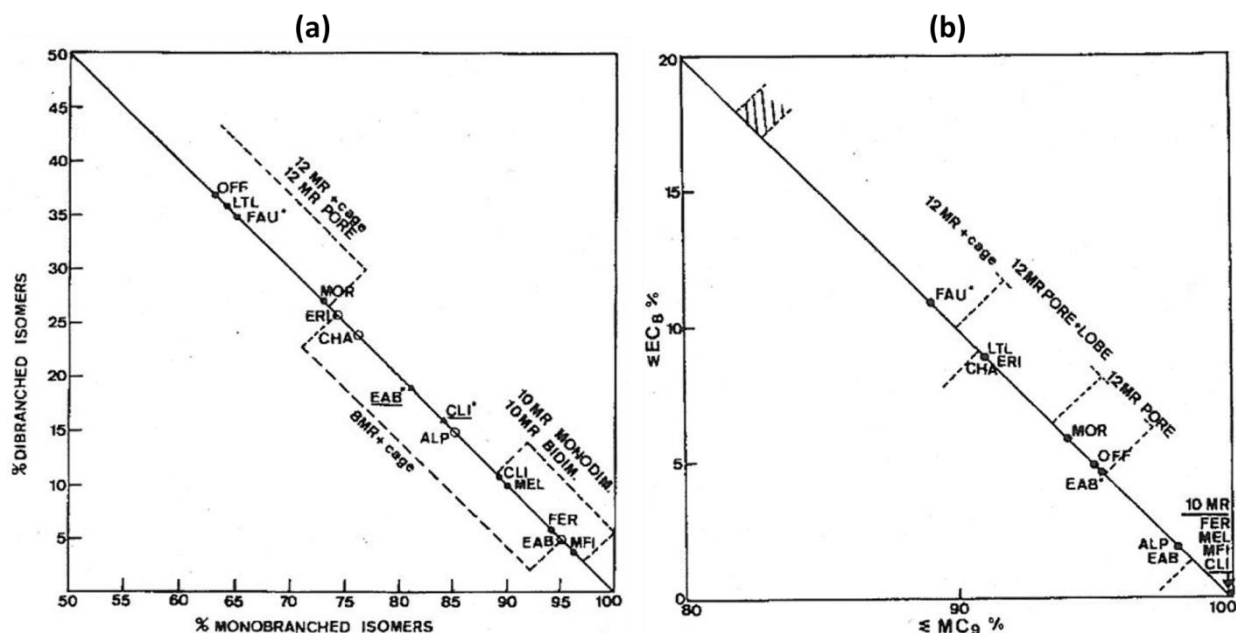


Figure 1- 52: (a) relative distribution of di-against monobranched isomers for n-decane on different known zeolite structures obtained at the maximum isomerization conversion. (b) Yield of ethyloctane (EC8) against methylnonane (MC9) isomers from n-decane on zeolites of known structure, obtained at 5% isomerization conversion; the shaded-area represents thermodynamic composition in the temperature range from 400 to 523K. Adapted from^[184].

However at maximum conversion, the secondary isomerization and consecutive hydrocracking could interfere with these results. To avoid this perturbation, it is better to work at low isomerization conversion such as 5%, giving a criterion that is very sensitive to structural differences.

In fact, the equilibration of methylbranched isomers is reached via classical methyl or alkyl shifts. The latter leads to the formation of ethyloctanes having larger effective kinetic diameter than their corresponding methylnonanes, hence their rate of formation and their diffusion will be prevented sterically in smaller pores. As seen in Figure 1- 52b, zeolites with 10 MR- hinder the formation of ethyloctanes, straight 12MR pores allow their minor formation and 12MR pores with large cages allow the formation of higher ethyloctane amounts.

- Ratio of 3-ethyl- to 4-ethyloctane

3-ethyloctane is obtained via ethyl shift on a 3-methyl-4-nonyl cation or from a pentyl shift on a 4-methyl-3-nonyl cation thus the formation of 3-ethyloctane is obviously more probable via ethyl shift. However, the formation of 4-ethyloctane requires the shift of bulkier alkyls. It is formed from a propyl shift or a butyl-shift on a 4-methyl-5-nonyl and a 5-methyl-4-nonyl cation respectively. It can also be obtained by secondary isomerization through an ethyl shift of 3-ethyloctane, Figure 1- 53.

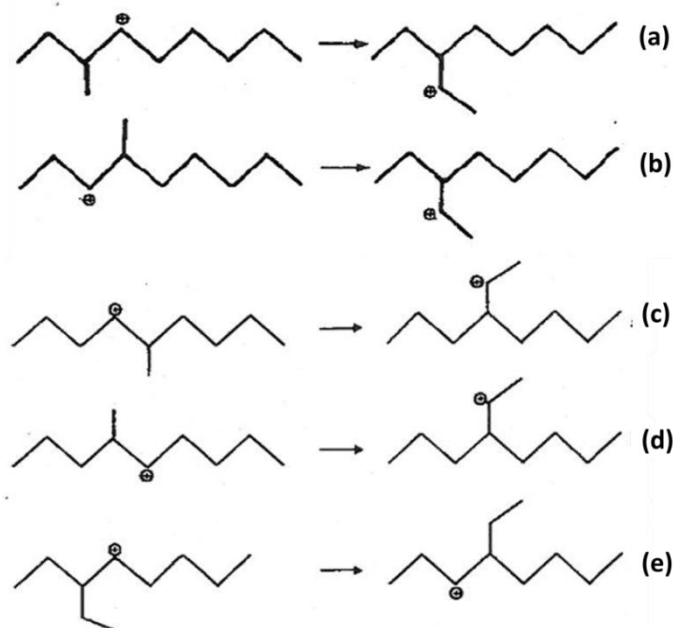


Figure 1- 53 : Formation of 3-Ethyloctane (a,b) and of 4-Ethyloctane (c,d) from methylnonanes via alkylshifts. Interconversion of 3- and 4-ethyloctane via ethyl shift (e). Adapted from^[184]

At low isomerization conversion, the ratio of 3-ethyl- to 4-ethyloctane is not at equilibrium, it always decreases with the increase of temperature, Figure 1- 54. However the line representing this ratio against reaction temperature is structure dependent. For example, as seen in Figure 1- 54, FAU is the most open structure. Zeolite Beta has characteristics similar to LTL, zeolite PHI is similar to MOR zeolite, etc.

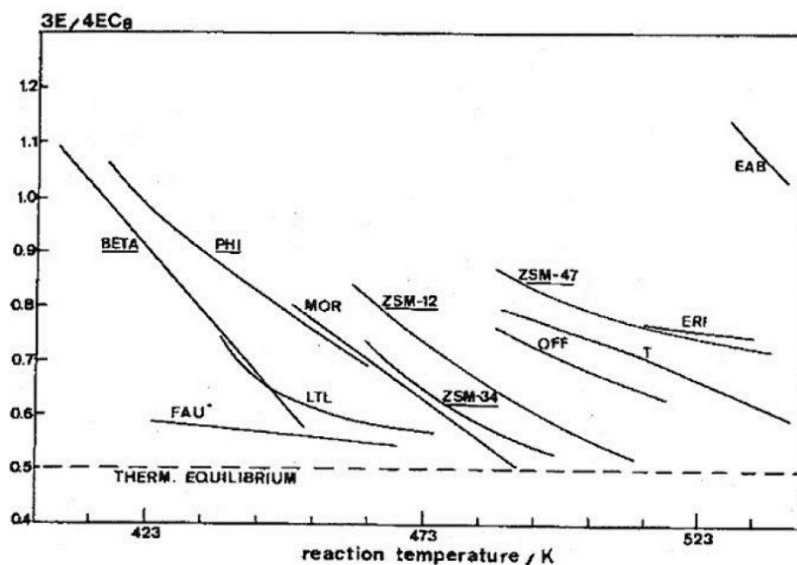


Figure 1- 54 : Ratio of 3-ethyloctane against 4-ethyloctane from n-decane at different reaction temperatures over 1 Pt/H-zeolites^[184].

- Relative distribution of the individual monomethylbranched isomers at low isomerization conversion

As seen in Figure 1- 48, two reaction pathways lead to formation of 3-methylnonane and 4-methylnonane, compared to only one pathway leading to 2-methylnonane and 5-methylnonane. At low conversion, the formation of 2-methylnonane in Y-type zeolites is two times slower than 3- or 4-methylnonane. This is caused by the lower number of PCP structures obtained from decane and giving 2-methyl isomers compared to 3- and 4-methyl isomers. At medium conversion, thermodynamic equilibrium is seen between the different methylnonanes.

Meanwhile, in a ZSM-5 zeolite, in comparison to 4- and 5-MC9 (bulky isomers) the rate of 2-MC9 (smaller isomer) is enhanced for all the conversion range. This reflects that the relative distribution of methylnonanes is dependent of the pore size and structure at low isomerization conversion where no secondary isomerization exists. Thus for the quantification of shape selectivity, the differences in size and geometry of the transition state or differences in the diffusion of olefins from acid sites to metals, a refined constraint index (CI°) can be defined. It is the ratio of the yield of 2-methylnonane to 5-methylnonane at 5% isomerization yield. Based on the thermodynamic equilibrium, the value of this index is between 1 and 2.2 for open structures. A higher value reflects the presence of steric constraints^[186].

- Absolute yield of isopentane in the hydrocracked products at low hydrocracking conversions

The absolute yield of isopentane produced from decane is a criterion sensitive to structural effects without being affected by secondary reactions. Secondary cracking of iC5 is negligible at low cracking conversions since it requires primary carbenium ions. In addition, the C5 yield is independent of C6 and C7 secondary cracking, giving C3+C3 and C4+C3 respectively.

The higher the branching of C10 is, the higher will be the probability for central β -scission giving an increased amount of iC5. Since, in larger pores, isomerization via PCP gives higher degree of branching, then higher amounts of iC5 will then be desorbed. Figure 1- 55 shows that 12-MR zeolites gave the highest yields of iC5, again due to lower steric constraints with respect to smaller pore zeolites.

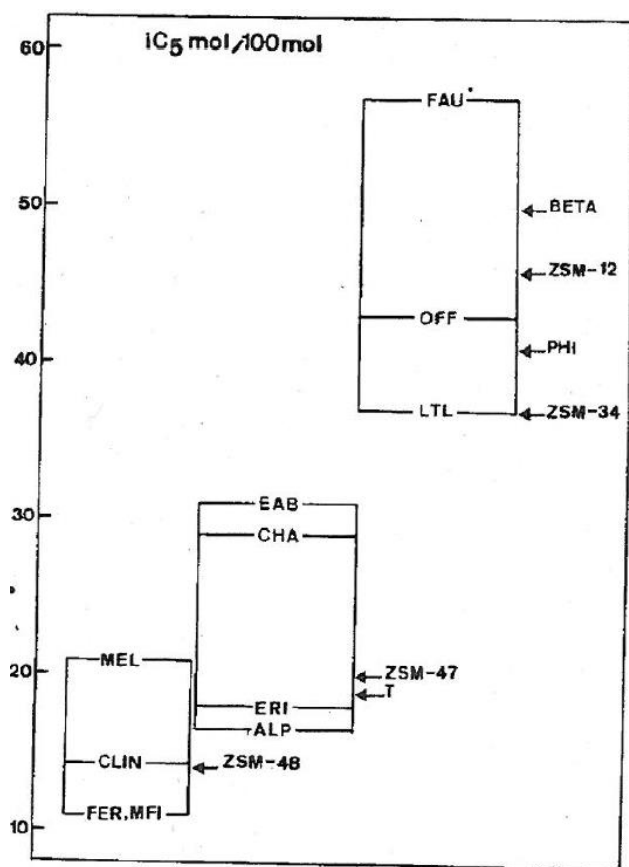


Figure 1- 55: Absolute yield of iC5 formed over different zeolite structures through hydrocracking of n-decane at 5% cracking conversion^[184].

Some criteria alone do not give unique information on the pore structures, however the combination of all these criteria allows making assignments of the pore structure.

1.4.4 Comparison of n-decane hydroconversion over different bifunctional zeolites

Based on the criteria described in the previous paragraph, we can see that the shape selectivity of a bifunctional catalyst can be detected through the conversion of n-decane. Bifunctional catalysts containing ten member ring zeolites such as Pt/ZSM-5 and Pt/ZSM-11 are known for their shape selectivity: no formation of di- and tribranched isomers is detected, Figure 1- 56.a. Their refined constraint index CI° is usually above 2.7 and the carbon number of the cracked products shows a minimum for central cracking^[181].

The products of n-decane conversion on Pt-ZSM-22 reflected a particular high CI° of 14.4 and are particularly rich in 2,7 dimethyloctane suggesting that the reactions are only occurring on pore mouth with absence of hydrocracking making this zeolite very selective for the isomerization of decane.^[181]

Pt/USY having 12 MR had mono-, di- and tri-branched isodecanes in the products, Figure 1- 56.a. As expected, EC-8 are of primary nature in Pt/USY (obtained via PCB) and of secondary nature for 10 MR zeolites (obtained only at high conversion levels), Figure 1- 56.b.

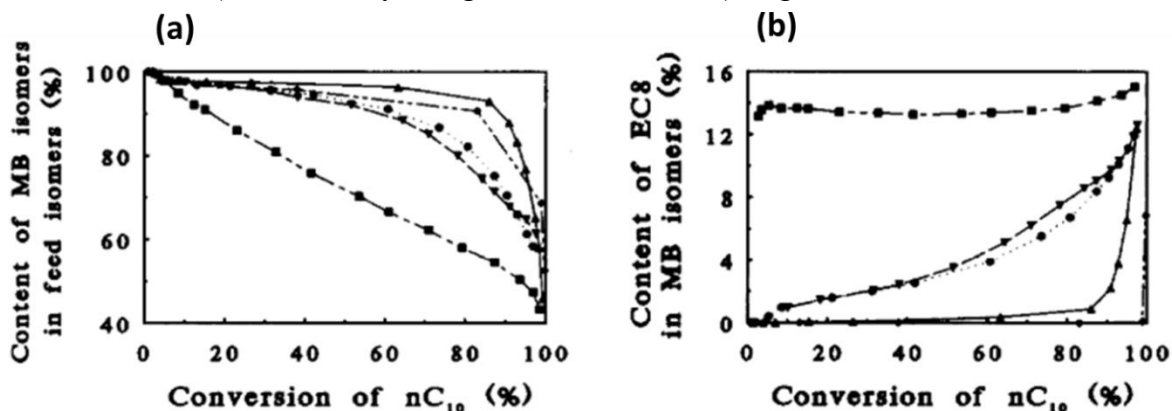


Figure 1- 56: (a) Content of monobranched isomers in the C₁₀ isomers versus degree of conversion. (b) Content of ethyloctanes in the monobranched C₁₀ isomers versus degree of conversion. The experiment numbers are in brackets (see further Appendix chap-1-Table 1- 1). ▲, ZSM-22 (1); ●, ZSM-22 (2); ▼, ZSM-22 (3); ◆, ZSM-5 (4); ■, USY (5)^[181].

The cracked products of Pt/USY are rich in C₅ fragments, Figure 1- 57. 69% of decane cracking on Pt/USY is obtained via type A β -scission not producing propane but only branched fragments. The remaining 31% products are formed via type B₁, B₂ and C β -scission.

On Pt/ZSM-5, the preferential formation of 2-MC₉ isomers lead to preferential type C β -scission. In fact, C₃ and C₇ are formed from 2-MC₉ β -scission while C₅ are obtained from 4-MC₉, this is reflected by the minimum C₅ fragments (Figure 1- 57). Moreover, the content of linear cracked products is higher than that of Pt/USY (Type C gives only linear fragments).

However, even if the isomer feed of Pt/ZSM-22 is rich in 2-MC₉, the C₅ fragments are present in the cracked products (Figure 1- 57), thus type C mechanism is not occurring. The low content of branched fragments at medium conversion excludes type B₁ and B₂ β -scission (Type B₁ and B₂ give equal amounts of linear and branched fragments). This implies the occurrence of type D hydrocracking or hydrogenolysis of the carbon-carbon bond on the Pt sites evidenced by the presence of methane and ethane. In type D mechanism, the secondary carbenium ion is cracked into a linear alkene and a smaller n-alkylcarbenium ion. The longer the latter is, the more it is stable and if it has a carbon number >3, stabilization can occur through hydride shift giving a more stable secondary n-alkylcarbenium ion. Therefore the product pattern of type D hydrocracking are: C₁+C₉ << C₂+C₈ << C₃+C₇ << C₄+C₆ << C₅+C₅. Secondary n-alkylcarbenium with the same carbon number have the same stability thus scission of 2-decyl cation is suppressed with respect to that of the more centrally charged decyl cations. This type D mechanism justifies the amount of C₅ and of the linear fragments. The remaining branched products can be obtained through type D β -scission of methylonyl cations. An alternative explanation is that 2-MC₉ are desorbed while

centrally branched methylnonanes cannot desorb due to sterical constraints of Pt/ZSM-22 and are instead cracked. However since energetically, these mechanisms are less favorable than bifunctional isomerization, the preferential desorption of 2MC-9 does not explain the high isomer selectivity but suggests occurrence of the reactions on pore mouth.^[181]

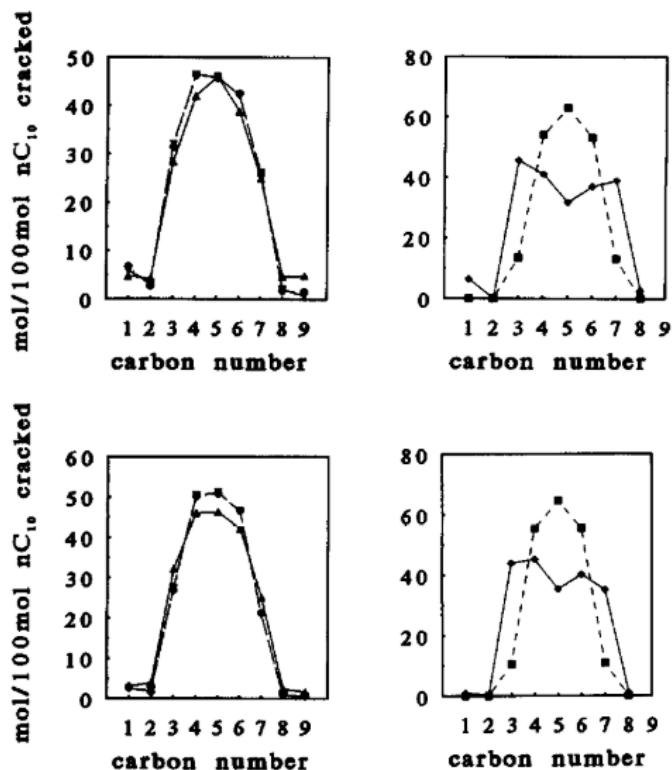


Figure 1- 57 : Selectivity for the C1 to C9 carbon number fractions of the cracked products from decane at cracking yields of 5% (top) and 50% (bottom). The experiment numbers are in brackets (see further Appendix chap-1-Table 1- 1). ▲, ZSM-22 (1); ●, ZSM-22 (2); ▼, ZSM-22 (3); ◆, ZSM-5 (4); ■, USY (5) ^[181].

The hydroisomerization of decane also gives insights for the distribution of active sites in zeolites. The EUO zeolites crystallized using different structure directing agent and possessing the same framework topology had different shape selectivity. The products showed that for EUO prepared with hexamethonium (HM), the active sites are located in the wide side-pockets and also inside the constrained 10MR while for EUO prepared with dibenzyltrimethylammonium (DDMDA), the active sites are only located on the side pockets^[187].

Silicogermanates are known for their extra-large pores thus using them in the hydroisomerization of long carbon chain alkanes is one of their interesting applications. The n-hexadecane is a good example. This test can give information about the accessibility of large pores. The mechanism and the involved reactions are similar to those of n-decane hydroisomerization. Indeed a larger number of different isomers is obtained but overall the families are identical^[188,189].

Note that at this stage we do not have any data on the behavior of the 14MRs in the hydroisomerisation of alkane, which is of great interest for silicogermanates with extra-large pores such as IM-12 zeolite.

1.5. Conclusion and strategy of the thesis

Zeolites containing Ge have not found applications to date despite the interest of their topology. Their post-stabilization into silicate or alumino-silicate solids has been the subject of several developments, sometimes with success for specific zeolite polymorphs, and sometimes it opened the door to the discovery of new zeolites. However so far, maintaining the zeolite structure while obtaining an active catalyst has been limited to few frameworks.

Our aim is to stabilize silicogermanates allowing their industrial valorization based on the described post-treatments. Our priority is to maintain the silicogermanate structure without a loss of its microporous volume.

It is necessary first of all to select one zeolite candidate to be studied. This selection was made based on the results of DFT calculations, in the spirit of Petkov's^[11] work, to study the potential stability of the existing silicogermanates, and their thermodynamic ability to be converted into silicates and silico-aluminates. The second criterion is the previous work available from the literature.

Once the candidate is selected, we proposed to study its post-treatment experimentally with one of the approaches described in this chapter: direct substitution of Ge for Si and Al. To this purpose, we will use new SiCl_4 and AlCl_3 treatments and a PAC treatment following the procedure of Valtchev et al^[150]. In parallel, characterization techniques such as XRD, XRF, nitrogen physisorption, FTIR spectroscopy and multi-nuclear (^1H ; ^{27}Al) MAS NMR are used to determine the success of the substitution and better define the environment of the sites (Ge, Al). In addition, an investigation of the stability of some possible external surfaces of the chosen candidate were constructed. These models may help in discriminating the localization of substitution (bulk vs. external surface). DFT (^1H ; ^{27}Al) MAS NMR chemical shifts of these models and of the zeolite bulk with different elemental composition and defects were also simulated to help attributing the experimental MAS NMR spectra.

The obtained acid solids were impregnated with Pt to prepare bifunctional catalysts. The latter are evaluated in the model reaction of hydroisomerization of n-decane in the aim of gaining information about the topology and the active sites distribution (surface vs. microporosity). At the end, the bifunctional catalysts were tested in the hydroisomerization of n-hexadecane having longer carbon chain length to get information about the accessibility of the active sites.

2. Experimental and Computational Methods

This chapter is divided in three sections. In the first one, a description of the experimental protocols for the preparation of the IM-12 catalyst (OSDA, IM-12 zeolite synthesis and post- treatments, preparation of metal-acid bifunctional catalysts) and the catalytic tests are presented. The second section lists the used characterization techniques with their brief working principle and data acquisition methodology. The third section is dedicated to the computational methodology.

2.1. Experimental procedures

2.1.1. Preparation of (6R,10S)-6,10-dimethyl-5-azoniaspiro [4,5] decane (OSDA)

The organic structure directing agent used for the synthesis of IM-12 zeolite, is the (6R,10S)-6,10-dimethyl-5-azoniaspiro [4,5] decane hydroxide. Figure 2- 1 shows its chemical representation.

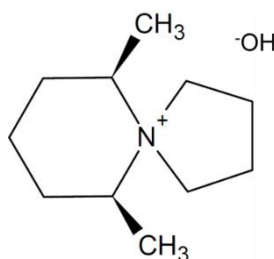


Figure 2- 1: Chemical representation of (6R,10S)-6,10-dimethyl-5-azoniaspiro[4,5] decane hydroxide.

To prepare this OSDA, 420 mL of distilled water, 17.04 g of sodium hydroxide (Sigma Aldrich, >97%) and 91.98 g of 1,4-dibromobutane (Sigma Aldrich, 99%) were mixed in a flask. Then, 48.21g of (2R,6S)-2,6-dimethylpiperidine(TCI, 99%) were added drop by drop over a period of 30 min under reflux. The mixture was refluxed for 12 hours then cooled with ice bath. 210 mL of ice-cooled sodium hydroxide solution (40 wt.%) was added. The mixture was placed in a freezer for 12 hours. The produced solid was then filtered and extracted three times using 600 mL of chloroform (Sigma Aldrich, 99%). After that, 60 g of anhydrous magnesium sulfate (Sigma Aldrich, 99,5%). were added. The mixture was then filtered and washed with 150 mL of chloroform. The organic fractions were evaporated at 40°C until reaching a volume of 300 mL using a rotary evaporator. The ammonium salt was precipitated and washed with ethyl ether (Sigma Aldrich, 99%). The yield of the reaction was 80%. The obtained OSDA is in its bromide form, thus it was exchanged before its use in zeolites synthesis to its hydroxide form. This procedure was performed on ion exchange resin (Dowex Mariathon OH⁻ Anion exchange Resin) or using silver oxide (Sigma Aldrich, 99,9%).

2.1.2. IM-12 hydrothermal synthesis

A gel with the following molar composition: 0.7 SiO₂: 0.3 GeO₂: 0.25 ROH: 25 H₂O was prepared by dissolving 32,622 g of amorphous germanium oxide (ABCR, 99.9%) in 300,534 g of a 16.02 wt.% (6R,10S)-6,10-dimethyl-5-azoniaspiro [4,5] decane hydroxide (ROH) solution (2.1.1). Then, 153.090 g of the silicon source (tetraethyl orthosilicate, TEOS, sigma Aldrich, 99%) and 213,755 mL of distilled water were added to the solution. The mixture was stirred at room temperature until complete hydrolysis of TEOS. The resulting fluid gel was charged into a reactor and heated at 170°C for 18 days under stirring (100 rpm). The solids were recovered by filtration, washed with distilled water and dried overnight at 100°C.

It is worth mentioning that at the beginning of the PhD, the germanium oxide source was bought as amorphous oxide but was actually crystallized and led to the presence of some impurities in the IM-12 zeolite discussed in chapter 4. Thus the sample obtained from this synthesis is called IM-12i. Another pure IM-12 sample was prepared using amorphous GeO₂ and was named IM-12. To get rid of the impurities in IM-12i, the as prepared silicogermanate was treated with 1M HNO₃ at room temperature for 24 h. The solid: acid ratio is 1:50.

Table 2- 1: List of IM-12 samples

Sample name	GeO ₂ source	Zeolite Phase
IM-12i	crystalline	UTL+ impurity
IM-12	amorphous	UTL

2.1.3. IM-12 calcination

When required, the IM-12 zeolite was calcined under dry air with a flow rate of 1.5NL/g/h in a tubular reactor (fluidized bed) following the calcination program shown in Figure 2-2.

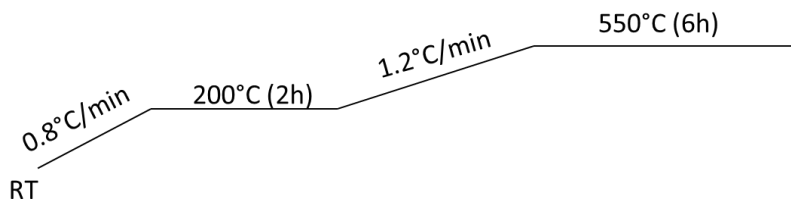


Figure 2- 2: Calcination program of IM-12 zeolite.

2.1.4. Post –treatments of IM-12

2.1.4.1. The Silicon tetrachloride treatment

In the literature, a silicon tetrachloride treatment in gaseous form was used for dealumination of aluminosilicates^[190–193]. In our work, we adapted this unit in the aim of substituting Ge for Si^[194].

This unit is made up of different elements presented in Figure 2- 3:

- an inlet for an inert gas like nitrogen controlled using a flowmeter
- a dry air inlet controlled using a flowmeter
- a container of silica gel to assure further drying of the gas flow
- a container of liquid SiCl_4 equipped with a thermostatically controlled system
- a tubular treatment reactor (fluidized bed)
- distilled water to neutralize the outlet of gases leaving the reactor during the treatment with SiCl_4 to recover the released germanium and SiCl_4 excess
- a vent

The treatment with gaseous SiCl_4 can be carried either on a as prepared or on a calcined microporous silicogermanate. In the latter case, the calcination is carried out directly in the tubular-bed reactor before the SiCl_4 treatment to avoid the contact of the sample with air humidity.

The treatment occurs as follow: 3g of the as prepared silicogermanate are loaded into the tubular-bed reactor. Valves 1 to 5 are closed and valve 6 is open between the tubular-bed reactor and the vent. Then the valves 2 and 4 are opened and the reactor is heated under a dry air flow at a flow rate of 1.5 NL/h/g of zeolite following the calcination program presented in 2.1.3. After that, valve 2 is closed and valve 1 is opened. The reactor is heated or cooled to the temperature desired for the SiCl_4 treatment. The valve 6 is then opened between the tubular-bed reactor and the flask containing the water. Valves 3 and 5 are open and valve 4 is closed. Since the vapor pressure of SiCl_4 is very low, it is evaporated at ambient temperature. The nitrogen flow saturated with SiCl_4 vapors enters then the reactor containing the IM-12. When the desired duration of substitution is reached (full evaporation of SiCl_4 then waiting for 1h), valve 4 is opened and valves 3 and 5 are closed. The reactor is left for 1 hour under a nitrogen flow of 1.5 NL/h/g at the temperature of the treatment before allowing it to cool. Several parameters were studied to optimize this treatment like sample pre-calcination, amount of SiCl_4 and temperature. These parameters are discussed in chap.4.

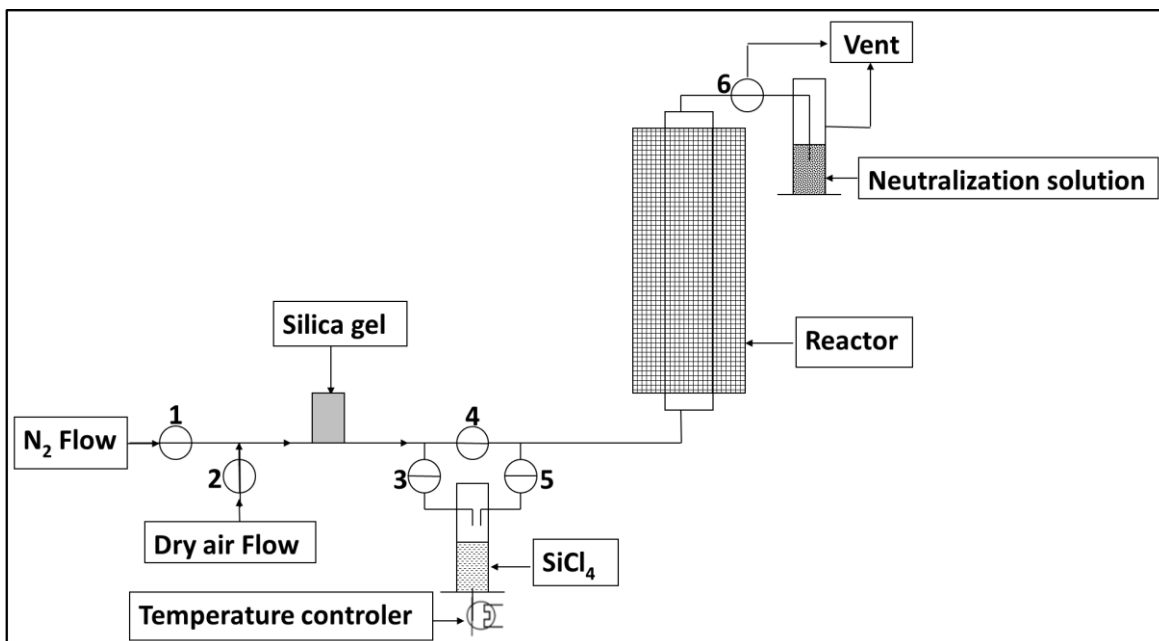


Figure 2- 3: Silicon tetrachloride treatment unit. Adapted from^[194]. (1 to 5) are 2-way valves and (6) is a three-way valve.

2.1.4.2. Alumination using polyaluminum hydroxide solution (PAC)

2.1.4.2.1. PAC treatment

The alumination of IM-12 using aqueous solution of polyaluminum chloride (Pluspac 1340, 7% Al) is carried out with a solid: liquid ratio of 1:50. Thus 150 mL of PAC solution are added to 3g zeolite. The mixture is stirred in a round-bottom flask under reflux system at 80°C. The obtained sample is purified by high speed centrifugation, filtration and washing with distilled water. The sample is then left for drying over night at 100°C.

The optimization of the duration of the treatment is discussed in chapter 4.

2.1.4.2.2. HCl treatment

After the PAC treatment, a treatment with an aqueous solution of HCl (0.1 M) at room temperature is made to reduce the amounts of extra framework aluminum under stirring for 3h with a solid: liquid ratio of 1:30. Typically, 2g of zeolite treated with PAC are mixed to 60 mL of HCl (0.1 M). After the treatment, the sample is thoroughly washed with distilled water and dried at 100°C overnight.

2.1.4.3. Alumination using polyaluminum trichloride aluminum solution

The desired amount of aluminum trichloride (Sigma Aldrich, 99.9999%) is dissolved in dry ethanol (sigma aldrich, 99.8%) in the glove box. The zeolite is then added with a solid: liquid ratio of 1:20. The mixture is then stirred in a round-bottom flask under reflux system. The obtained sample is

purified by filtration and washing with ethanol/water. The temperature, amount of aluminum trichloride and the duration of the treatment are discussed in chapter 4.

2.1.5. Preparation of bifunctional IM-12 catalysts

After the alumination of IM-12 using PAC or AlCl_3 solutions, two groups of bifunctional catalysts were prepared through the incipient wetness impregnation of aluminated IM-12 with platinum or through the mechanical mixture of the IM-12 zeolite with alumina impregnated with platinum.

2.1.5.1. Incipient Wetness impregnation of aluminated IM-12 with 0.3% of Pt

100 mg of aluminated IM-12 zeolite are impregnated with 1 mL of an aqueous solution containing 0.052 g of $[\text{Pt}(\text{NH}_3)_4]\text{Cl}_2 \cdot \text{H}_2\text{O}$ (in the aim of obtaining a catalyst with a platinum loading of 0.3% wt.). The suspension is then dried for 24 hours at 65°C . The powder obtained is pelletized, crushed and sieved between 125 and 250 μm .

2.1.5.2. Mechanical mixture of the aluminated IM-12 with alumina impregnated with platinum

The bifunctional catalyst were obtained by mechanical mixture of 5% of IM-12 zeolite and 95% of Gamma alumina impregnated with 1 or 2% with platinum. The Gamma alumina (calcination of commercial boehmite God 200) was previously impregnated with Pt following this procedure. 500g of gamma alumina is treated for 2h with 50.26 g of HCl (35.8%) then filtered and dried. Then impregnation is performed, with 2.25 L of aqueous solution containing 14.55 or 27.77g of Pt chloroplatinic acid hexahydrate (in the aim of obtaining gamma alumina with a platinum loading of 1 and 2% wt. respectively) at 20°C for 24 hours. The mixture is then filtered, washed 3 times with distilled water and left for drying at 110°C for one night. The obtained solid is then calcined under an oxygen flow of 1mL/h/g with a ramp of $5^\circ\text{C}/\text{min}$ following this program: 150°C (1h), 250°C (1h), 350°C (1h) and 520°C (2h).

The mechanical mixture of 5% of IM-12 zeolite and 95% of impregnated Gamma alumina was kneaded at 300 rpm during 2 min in a Fischer Scientific MM20 mixer. Then, the mechanical mixture was pelletized in an hydraulic press Carver C (4 bar), crushed and sieved at the desired size (250-500 μm).

2.1.6. Catalytic testing

The obtained bifunctional catalysts were then tested for the hydroisomerization of two alkanes with different chain lengths: n-decane and n-hexadecane. For the n-decane testing, samples prepared following the incipient wetness impregnation in section 2.1.5.1 were used. While for the hydroisomerization of n-hexadecane, samples prepared by mechanical mixture of the IM-12 with alumina impregnated with Pt (section 2.1.5.2) were used.

2.1.6.1. Hydroisomerization of n-decane

A high-throughput vapor reactor with 16 parallel tubes is used for the hydroconversion of n-decane (Figure 2- 4). The reactor has two parts: the first part carries 16 open quartz microreactors tubes (internal diameter of 2 mm) equipped with a sintered bed to support the catalyst. The second part of the reactor serves to control the preheating of the n-decane feed, thermal decoupling of the reactors from the sealing o-ring and the equal distribution of the gas flow over the 16 microreactors. The feed inlet of decane is at the bottom of this part. The reactor can be fed with three different gases: hydrogen, oxygen and nitrogen. Hydrogen and oxygen are used for catalyst pre-treatment and for the reduction and oxidation of the noble metal in the catalyst, respectively. Nitrogen is used for purging, especially when switching from oxygen to hydrogen. The n-decane vapor is generated by flowing hydrogen gas through a thermostatic saturator. The microreactors outlets are connected downstream with capillaries. The latter are connected to a GC sampling valve through a 16-way selection valve.

The pre-treatment and consecutive catalytic tests are automatically conducted by Camille process control software from Argonaut. This software regulates gas selection, gas flows, reactor temperature, valve selection and GC operation. After changing the reaction temperature or flow, the reactor is given one hour for stabilization. The different microreactors are sampled sequentially.

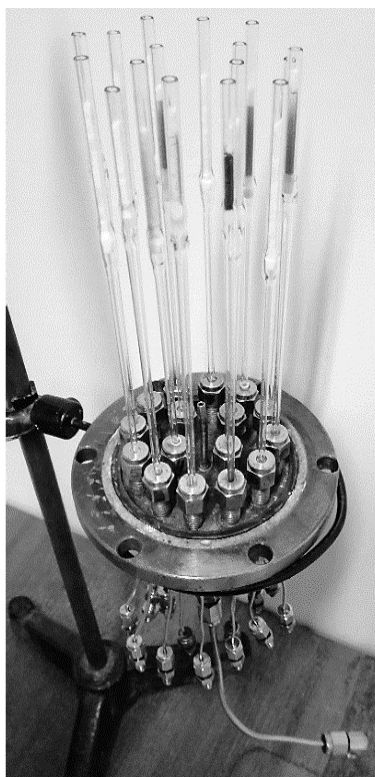


Figure 2- 4: High-throughput vapor reactor with 16 parallel tubes used for the hydroconversion of n-decane.

During the experiments, 50 mg of catalyst pellets with a size between 125 and 250 μm were loaded in each microreactor. The catalyst pre-treatment procedure comprised an oxidation with oxygen and afterwards a reduction with hydrogen. During the oxidation the catalysts in the microreactors were heated to 400°C at 5°C/min with an oxygen flow of 4.7 mL/min per microreactor. After one hour at 400°C under oxygen, the microreactors are flushed with nitrogen for approximately 10 minutes at the same flow. Then the catalysts are reduced under hydrogen for one hour at 400°C with a hydrogen flow of 12.5 mL/min. Finally, the reactors were cooled down to the reaction temperature. The reactor unit is operated at a total pressure of 0.45 MPa and at a hydrogen to n-decane molar ratio of 214. The weight hour space velocity (WHSV) is 0.37 g/g.h. The temperature is then increased by 5°C with a ramp of 5°C/min. Several temperatures are then tested, for each new one, a stabilization time of 1 hour is required before starting the analyses in the GC.

2.1.6.2. Hydroisomerization of n-hexadecane

This test is performed using a Flowrence parallel reactor system. This unit has 4 sections: electrical, reactor, gas feed and liquid feed. All controller loops and indicators are monitored and operated by the Flowrence™ control software.

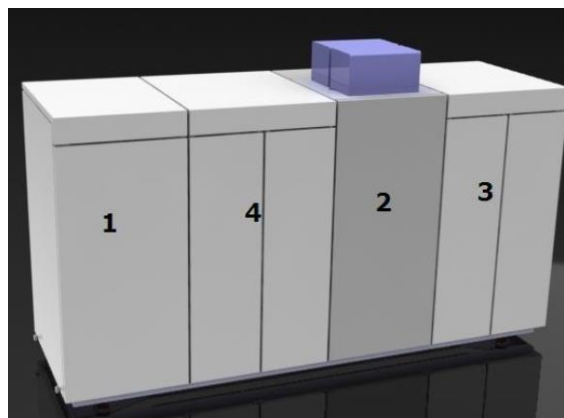


Figure 2- 5: Flowrence reactor.

The online GC is connected directly to the Flowrence™ unit by a sample line. The sampling, start of an analysis run and data acquisition is controlled by the software and needs no intervention of the operator.

To charge the microreactor (2mm internal diameter), 50 mm of Zirblast B120, approximately equivalent to 200 μL was loaded, then 300 mg of catalyst are added followed by fiberglass.

The catalyst is dried at 150°C for 30 min with a nitrogen flow rate of 10 mL/min per reactor at atmospheric pressure. It is then reduced at 450°C for 1 hour with a hydrogen flow rate of 0.08 mL.min⁻¹.mg⁻¹ of catalyst in the reactor under a hydrogen pressure of 10 bar. The reactors are then cooled to the test temperature. The charge is then injected at a total pressure equal to 10 bar and at

a hydrogen to hexadecane molar ratio of 10. After 2 hours, the analyses start for the first temperature level. Two analyzes per reactor are performed.

The temperature is then increased by 5°C with a ramp of 300°C h⁻¹.

Several temperatures are then tested, for each new one, a stabilization time of 1 hour and 15 min is required before starting the analyses in the GC.

2.2.Characterization Techniques

2.2.1. X-ray Diffraction (XRD)

XRD is a technique used for phase identification of crystalline materials. It is based on constructive interference of monochromatic X-rays and a crystalline sample. The X-rays are generated by a cathode ray tube, filtered to produce monochromatic radiation, collimated to concentrate, and directed toward the sample. The interaction of the incident rays with the sample produces constructive interference (and diffracted rays) when conditions satisfy Bragg's Law:

$$n \lambda = 2d \sin \theta$$

Eq. 2- 1

With λ : wavelength of electromagnetic radiation; n: order; d: lattice spacing in a crystalline sample and θ : diffraction angle.

The characteristic x-ray diffraction pattern generated in a typical XRD analysis provides a unique “fingerprint” of the crystals presented in the sample. When properly interpreted, by comparison with standard reference patterns and measurements, this fingerprint allows the identification of the crystalline form.

XRD is used in our work to verify if the UTL structural phase of the IM-12 is obtained and maintained during the post-treatments.

Powder samples are compacted in a sample carrier. X-ray diffractions were collected on a Bruker D4 Endeavor diffractometer with Cu K α radiation ($\lambda = 1.5406 \text{ \AA}$) and a Bragg-Brentano geometry. Two different programs were used:

- for the optimization of the treatments (5.2), the step size was 0.01°. The scanned angles range is from 2 to 70° with a time/step of 9.8 s and a LYNXEYE XE detector.
- for the prepared IM-12 catalysts (5.3), this program is used to increase the resolution: step size of 0.006°. The scanned angles range is from 2 to 40° with a time/step of 49.01s and a Braun Lynx Eye OD detector.

Note that the TOPAS software was used to check the space group of the zeolites.

EVA software was used to calculate the degree of crystallinity. The degree of crystallinity of a peak x is calculated following Eq. 2- 2. x refers to different peaks between 22.5 and 25°. Indeed, to avoid the background, only peaks between 22.5 and 25° are considered. The net and gross surface areas

are measured using Eva software. “ref” correspond to a reference material. In our case the latter was either the calcined zeolite or the SiCl₄ treated zeolite.

$$\text{Degree of cristallinity}_x = \left[\left(\frac{\text{Net area}_x}{\text{Gross area}_x} \right) / \left(\frac{\text{Net area}_{ref}}{\text{Gross area}_{ref}} \right) \right] * 100$$

Eq. 2- 2

The degree of cristallinity of one sample is the average of the degrees of cristallinity of the peaks between 22.5 and 25°.

2.2.2. Nitrogen physisorption

N₂ physisorption is a textural analysis method based on the physical adsorption of N₂ at normal boiling point (77 K) on the surface of the sample. It can be used to measure micro, mesoporosity and surface areas superior to 1 m²/g. It is used to determine the microporous volume following the t-plot method, the total volume and the surface area S_{BET} of studied silicogermanates.

The samples were pre-treated at 200°C for 2 h then at 550°C for 6 h under vacuum. Measurements done with a Micromeritics ASAP 2420 equipment.

2.2.3. Thermogravimetric Analysis (TGA)

TGA is based on the direct measurement of a material mass over time as temperature changes. Coupled with differential thermal analysis, thermogravimetric analysis allows quantification of water and organic species in the analyzed material. It is also used to define the minimum temperature of calcination. TGA-DSC Mettler equipment was used with a temperature range from room temperature to 1000°C (10°C/min).

2.2.4. Scanning Electron Microscopy (SEM)

The general principle of SEM consists of an electron beam (probe) that is focused into the sample. The interaction between the electron probe and the sample generates secondary electrons of low energy. These electrons are accelerated to a secondary electron detector that amplifies the signal. Every impact point is an electrical signal that will be transmitted to a detector. The number of secondary electrons that can be detected depends, among other things, on specimen topography. Thus by scanning the sample, an image of the surface of the crystals is obtained. This technique was used to study the morphology of zeolites.

Sample preparation: The samples were diluted in ethanol under ultrasound. A drop of the suspension was then deposited on an aluminum pad previously polished with SiC granulo paper of 2500 then 4000, then left to dry.

SEM: samples were observed in topographic contrast mode (secondary electrons) using the SE2 detector at 2kV and with a beam size of 20 μm .

2.2.5. X-ray Fluorescence Spectrometry (XRF)

This elemental analysis technique can be applied on both solids and liquids. An atom is excited by an X-ray photon, leading to an expulsion of an electron from its core shell and creating a vacancy. The latter is filled by another electron of a higher energy shell, by releasing energy in the form of X-ray photons. This phenomenon is called fluorescence. The energy of the emitted X-rays is characteristic for each element, allowing for its identification, and the intensity of the peak measured by wavelength dispersive spectrometry (WDS) permits quantification down to some ppm, using a calibration curve.

This analysis is used to determine Si, Ge and Al content in the samples.

To determine the amount of Ge, Si and Al in the zeolites. We prepared and validate a method giving the uncertainties presented in Table 2- 2.

Table 2- 2 : relative uncertainty for Si; Al; Ge.

Element	Concentration range (%)	Relative uncertainty (%)
Si	2-5	± 5
	5-45	± 3
Al	0.49-2	± 15.5
	1-2	± 14
	2-12	± 9
Ge	0.3-1	± 15
	1-5	± 5
	5-62	± 4

Sample preparation: 1 g of dry sample (after loss of ignition) is mixed with 9 g of the eutectic flux 66:34 (Tetraborate de lithium 66% / Metaborate de lithium 34%). The mixture is then heated to 1000°C in a platinum crucible. The sample is dissolved in the flux, then is cast into a mold.

2.2.6. Inductively Coupled Plasma- Optical Emission Spectrometry (ICP-OES)

Inductively coupled plasma optical emission spectroscopy (ICP-OES) is a technique used for a wide range of sample types such as aqueous and organic liquids and solids. Some of these sample types need specific sample preparation techniques or the use of specific accessories.

The advantages of using ICP-OES over other elemental analysis techniques include its wide linear dynamic range, high matrix tolerance, and the enhanced speed of analysis that can be achieved.

To generate plasma, argon gas is supplied to torch coil, and high frequency electric current is applied to the work coil at the tip of the torch tube. Using the electromagnetic field created in the

torch tube by the high frequency current, argon gas is ionized and plasma is generated. This plasma has high electron density and temperature (10 000K) and this energy is used in the excitation-emission of the sample. Emission rays that correspond to the photon wavelength are measured. The element type is determined based on the position of the photon rays, and the content of each element is determined based on the rays' intensity.

This technique was used to quantify Si, Ge, Al contents in samples when the amounts of Al are under the limit of detection of XRF. The relative uncertainty of this technique is 5%.

2.2.7. Nuclear Magnetic Resonance (NMR)

(NMR) is a technique that gives information about the environment of an element indicating arrangement of atoms.

An atomic nucleus whose number of spin $I \neq 0$ has the properties of a magnetic dipole and therefore has a magnetic moment. In the presence of an external static magnetic field B_0 , the magnetic moments randomly oriented, take particular orientations. The resultant of these moments, noted M , is a vector parallel to B_0 .

A second coil then creates an alternating magnetic field of frequency ν_0 according to an axis perpendicular to the initial field B_0 . This deviates M from the axis parallel to B_0 . The duration of perturbation, also called impulse, determines the gap between the two vectors.

To return to its initial position, the resulting vector M , makes a movement of precession around the axis of the vector B_0 : this oscillation, called relaxation, is a signal of resonance whose frequency is again ν_0 and constitutes the NMR signal.

The frequency ν_0 , called resonance frequency or Larmor frequency, is characteristic of each isotope of a nucleus and depends on the intensity of the B_0 field applied according to the relation:

$$\nu_0 = \gamma \cdot B_0 / 2\pi \tag{Eq. 2- 3}$$

where γ is a characteristic gyromagnetic ratio of each isotope, expressed in rad / T / s.

In practice, the environment of the nucleus constitutes a magnetic screen compared to the applied external field B_0 , and the effective field felt by the nucleus is therefore lower than B_0 .

$$B_{\text{eff}} = B_0 \cdot (1 - \sigma) \tag{Eq. 2- 4}$$

where σ is a positive constant called the screening constant and depends of the nucleus environment.

Thus, the frequency of the electromagnetic wave necessary to pass a nucleus from one energy state to another is no longer ν_0 , but ν_{eff} and is slightly weaker than ν_0 . The difference between these two values allow the characterization of the environment of the studied nuclei: each spin I nuclei having a different environment gives a different ν_{eff} .

Since the values of ν_{eff} depend on B_0 , the NMR spectrum is plotted as a function of another scale, the chemical shift, noted δ and defined by the relation:

$$\delta = [(\nu_{\text{eff}} - \nu_{\text{ref}}) / \nu_{\text{ref}}] \cdot 10^6$$

Eq. 2- 5

where ν_{ref} is the resonance frequency of the nucleus considered in a reference product.

The chemical environment of the different nuclei is at the origin of interactions affecting NMR spectra (dipolar interactions, chemical shift interactions, quadrupole interactions, etc.).

In liquids, the Brownian motion of the molecules (rotation, translation) is enough to average the anisotropic part of the interactions.

2.2.7.1. Liquid NMR

The OSDAs synthesized during the thesis were characterized by ^1H and ^{13}C NMR. NMR spectra were recorded on a Bruker Avance III NMR spectrometer with a Broadband probe (BBFO) using a 5 mm o.d glass NMR tubes at 300K. The frequencies used were respectively 300.13 and 75.47 MHz for ^1H and ^{13}C nuclei. 1D proton decoupled ^{13}C spectra were recorded with the following parameters: acquisition time of 1.66 s, pulse duration of 8 μs , relaxation delay of 2 s and a sweeping range 19736.8 Hz in a zgdc30 pulse program. As a proton spectra, these parameters are respectively 3.4 s, 9.2 μs , 2 s and 4807.7 Hz in a zg30 pulse program. The analyses are carried out in the presence of deuterium oxide (D_2O) as solvent.

This technique has also been used to measure the percentage of the structure directing agent present in the aqueous solution after ion exchange, in the presence of dioxane as internal standard.

The peak intensity of the NMR spectrum of a given molecule is proportional to the quantity of this molecule present in solution and to the number of equivalent hydrogen atoms to which the resonance corresponds. For example, for dioxane, the 8 hydrogen atoms are equivalents and the spectrum of this molecule therefore only has a resonance (of $I_{\text{reference}}$ intensity) corresponding to $N(\text{H}_{\text{res}})$ intensity = 8.

If we consider an OSDA with a resonance of I_R intensity corresponding to $N(\text{H}_{\text{res}})_R$ hydrogen atoms, then the following relation is verified:

$$\frac{I_R}{I_{\text{reference}}} = \frac{N(\text{H}_{\text{res}})_R * n_R}{N(\text{H}_{\text{res}})_{\text{reference}} * n_{\text{reference}}}$$

Eq. 2- 6

where n_R and $n_{\text{reference}}$ are respectively the quantity of molecules of OSDA and reference in solution. I_R and $I_{\text{reference}}$ are determined using the spectrum and $n_{\text{reference}}$, $N(\text{H}_{\text{res}})_{\text{reference}}$ and $N(\text{H}_{\text{res}})_R$ are known (for example, $N(\text{H}_{\text{res}})_R = 3$ for a methyl group). We can thus deduce n_R .

2.2.7.2. Solid state MAS NMR

- *General features*

In solid state NMR, an enlargement of the resonance lines due to dipoles couplings between the magnetic moments of the nuclei, and due the anisotropy of crystals causes anisotropy of chemical shifts. It is therefore necessary to minimize the effect of these interactions on the spectrum. The widening of the lines can be decreased by a fast rotation of the sample according to a inclined axis of an angle $\theta = 54^\circ 44'$ with respect to the external magnetic field direction B_0 (called Magic Angle Spinning, MAS). The two terms, dipolar couplings and crystal anisotropy, have an angular dependence of $(3\cos 2\theta - 1)$ type. These dependencies are eliminated if θ is equal to $54^\circ 44'$.

^1H , ^{27}Al MAS NMR are used to identify the defects of zeolites frameworks (e.g. silanols groups), the incorporation of Aluminum (tetrahedral or octahedral coordination) and their quantifications.

- $^1\text{H}/^{27}\text{Al}$ TRAPDOR NMR

TRAPDOR (transfer of polarization in Table 2- resonance) NMR is a solid state NMR technique used to study the dipolar coupling between spin I and spin S that are involved in strong quadrupolar interactions, Figure 2- 6. The comparison of spectra by spin-echoes with and without irradiation of the spin S system shows whether spins I are with and without dipolar coupling to spin S.

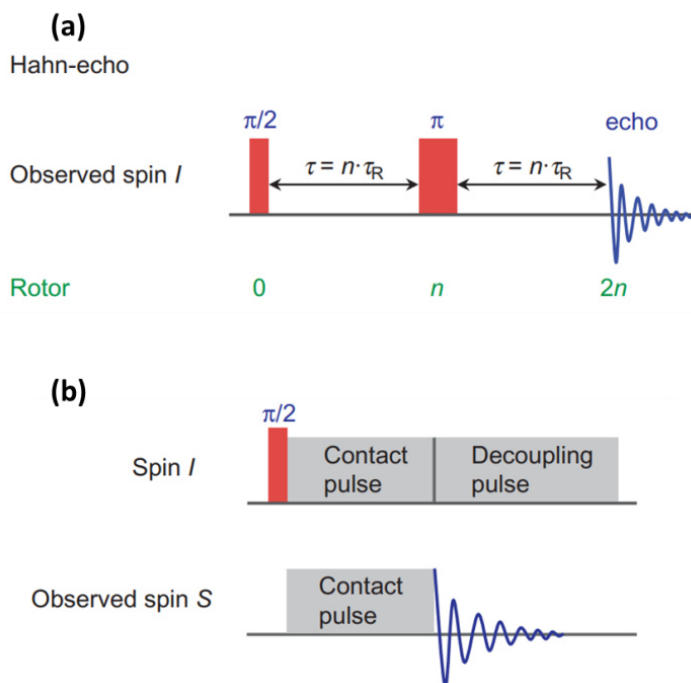


Figure 2- 6: Pulse sequence for Hahn-echo (a) and TRAPDOR (b) spectroscopy experiments. The long S spin pulse produces a rotor-driven modulation of the quadrupolar eigenstates, reintroducing the I–S dipolar coupling. Adapted from^[195].

In our study, this technique is used to define which OH groups are vicinal to aluminum atoms and which are not.

- **MAS NMR experimental part**

^1H and ^{27}Al measurements were performed in a Bruker 500 MHz Avance III spectrometer equipped with a 4 mm H/X/Y triple resonance probe. Samples were filled in a 4 mm ZrO_2 rotor and subjected to magic angle spinning (MAS) at 15 kHz. ^{27}Al spectra were acquired with 170 kHz radio frequency (RF) pulse (solid, CT), relaxation delay of 1s and 73728 transients with spinal 64^[196] ^1H decoupling (50 kHz RF). ^{27}Al spectra were referenced to 1.1M $\text{Al}(\text{NO}_3)_3$ in D_2O solution. ^1H spectra were acquired with an RF pulse of 83 kHz, relaxation delay of 2s and 8 transients. ^1H Hahn-echo and $^1\text{H}/^{27}\text{Al}$ TRAPDOR measurements were done with 15 kHz MAS. T_2 evolution (Hahn-echo) and continuous wave irradiation (120 kHz RF) on ^{27}Al (TRAPDOR) were done for 1 (66.67 μs)/ 3 (200 μs)/ 5 (333 μs) rotor cycles. The ^1H spectra were referenced to secondary reference, adamantane, which was further referenced to primary reference, TMS. Spectral decomposition was performed with DMFIT software^[197].

^1H and $^1\text{H}/^{27}\text{Al}$ TRAPDOR MAS NMR were measured on dry samples pretreated at 200°C under vacuum for 16h.

^{27}Al measurements were performed on hydrated samples. Hydration was made by equilibrating a packed 4 mm rotor in an atmosphere with controlled 77% relative humidity for 48h.

The Al quantification was performed using an external reference (LTA with Si/Al=1). To avoid the variability of the instrumental response between the different samples, following the procedure of Houllberghs et al.^[198] two factors have to be fixed: same coil filling factor (sample volume) and the tuning of the probe to obtain same quality-factors (Q-factor). Once these conditions are assured, comparing the areas of the measured samples to those of the Na-LTA reference sample gives the amount of Al and the Si/Al ratios in the catalysts.

2.2.8. Infrared spectroscopy (IR)

The IR spectroscopy consists on applying an infrared radiation on the sample leading to vibration between the atoms. When the applied IR frequency is equal to the natural frequency of vibration of a functional group, the IR radiation is absorbed giving a characteristic peak value.

- **ATR-IR (Attenuated Total Reflectance Infrared spectroscopy):**

The mono-reflection ATR-IR technique allows the analysis of solid, liquid or viscous samples. This technique is used for the characterization of samples with high extinction coefficients since the penetration of IR radiation in the samples is low.

The crystal used in the Gold Gate accessory is the diamond. Thus, it is not possible to obtain information for wave numbers below 500 cm^{-1} . The IR spectra obtained give qualitative information on the presence (or absence) of functional groups.

The ATR-IR measurements are made on a Nexus spectrometer (ThermoOptek Nicolet) with a resolution of 4 cm^{-1} , 64 scans and a DTGS detector without any preparation of the sample (powder).

- **Transmission FTIR (Fourier Transform Infrared spectroscopy):**

Transmission FTIR spectroscopy is used to characterize the nature of hydroxyls and the acidity of zeolites. The hydroxyls group of the Brønsted acid sites are directly visible in the infrared spectrum due to their OH stretching vibration band. However, Lewis acid sites are not directly detectable thus a probe molecule must be used. The pyridine can easily diffuse inside the large pores of zeolites and its spectral response (intensity of the bands and position of the vibration frequency) is well known in the literature. Moreover, the pyridine is stable on the surface of the catalyst, and is able to easily adsorb on the solids in its vapor phase thus this probe was chosen for our study.

In situ transmission IR monitoring of adsorption / thermodesorption of pyridine are made in transmission on a Nexus spectrometer (ThermoOptek Nicolet) with a resolution of 4 cm^{-1} , 64 scans and a DTGS detector. Before contact with pyridine, the samples are pelletized (disc of 16 mm in diameter and mass of about 20 mg) then pretreated under secondary vacuum for 10 h at $450\text{ }^{\circ}\text{C}$. When the sample is activated, a first spectrum is recorded. The pyridine is then in contact with the sample at room temperature for 10 min at 150°C . Once the adsorption equilibrium is reached (followed by IR), different spectra at different thermodesorption are measured: after 2 hours at $150\text{ }^{\circ}\text{C}$, 1 hour at 250 , 350°C and 450°C . By subtracting the spectrum of the activated sample from the thermodesorption spectra, it is possible to quantify the concentrations of Brønsted (pyridinium concentration from the contribution at ca. 1545 cm^{-1}) and Lewis acid sites interacting with pyridine (from the contribution at ca. 1455 cm^{-1}).

The concentrations initially obtained in $\text{a.u.}\cdot\text{g}^{-1}$ of sample can be recalculated in $\mu\text{mol}\cdot\text{g}^{-1}$ following (Eq. 2- 7) with molar extinction coefficients defined from the literature:

$$\text{Acid sites concentration } (\mu\text{mol}\cdot\text{g}^{-1}) = \frac{\text{IR signal} * \text{disc area}}{\text{disc weight} * \text{molar extinction coefficient}}$$

Eq. 2- 7

2.3.Density Functional Theory (DFT) calculations

Molecular modeling was used in this work to study the intrinsic stability of different silicogermanates and their (alumino)silicates counterparts. This study also considered the external surfaces of IM-12 zeolite (UTL). In addition, the DFT calculations were used to study the possibility of substitution of Ge for other elements, upon thermodynamic considerations. Finally, the theoretical calculation of ^{27}Al and ^1H NMR feature helped attributing the experimental MAS

NMR measurements. All the calculations were performed using ab initio methods (no fitting with any external data such as experiments will be performed).

2.3.1. Role of DFT in the resolution of Schrödinger equation

The aim of quantum chemistry is to find an approximate solution for the non-relativistic time-independent Schrödinger equation. Solving this equation gives various molecular properties such as the geometry, relative stability, vibrational spectra, dipolar and quadripolar moments, electronic spectra and reactivity functions. The Schrödinger equation is presented in Eq. 2- 8.

$$H\psi = E\psi \tag{Eq. 2- 8}$$

With H the Hamiltonian operator, ψ the wavefunction of the multielectronic system that depends on the atom position and on the spin of each electron, and E the energy of the system composed of M nuclei and N electrons.

The Hamiltonian operator, Eq. 2- 9, is composed of two kinetic energy operators, one for the electrons and the other for the nuclei. The third term represents the Coulombian interaction of each electron with each nuclei, the fourth term is for the electron-electron repulsion and the last one is the nuclei-nuclei repulsion.

$$H = -\sum_{i=1}^N \frac{\hbar}{2m_e} \nabla_i^2 - \sum_{k=1}^M \frac{\hbar}{2M_k} \nabla_K^2 - \sum_{i=1}^N \sum_{k=1}^M \frac{e^2}{4\pi\epsilon_0} \cdot \frac{Z_k}{R_{ik}} + \sum_{i=1}^N \sum_{j>i}^N \frac{e^2}{4\pi\epsilon_0 \cdot r_{ij}} + \sum_{k=1}^M \sum_{l>k}^M \frac{e^2}{4\pi\epsilon_0} \cdot \frac{Z_k Z_l}{R_{kl}} \tag{Eq. 2- 9}$$

With \hbar the Planck constant h divided by 2π , m_e the electronic mass, e the electronic charge, M_k the masse of the nucleus k, r_{ij} the distance between the electrons i and j, R_{ik} is the distance between the electron i and the nucleus k and ∇_i^2 is the laplacian of the i^{th} electron.

To simplify this equation, since we know that any nuclei mass is much more important than that of the electron (at least 2000 higher), we can consider that the motion of the nuclei R_k is negligible. This approximation is called the Born-Oppenheimer approximation. Since the nuclei are considered as fixed, the nuclei kinetic energy is equal to 0 and their repulsion is constant. As a result, only the electronic contributions have to be solved:

$$H_{elec}\psi_{elec} = E_{elec}\psi_{elec} \tag{Eq. 2- 10}$$

In the atomic unit system: $m_e=1$, $\hbar=1$, $e=1$ and $4\pi\epsilon_0=1$ thus H_{el} becomes:

$$H_{elec} = \sum_{i=1}^N -\frac{1}{2} \frac{\nabla_i^2}{r_i} - \sum_{i=1}^N \sum_{k=1}^M \frac{Z_k}{R_{ik}} + \sum_{i>j>1}^N \frac{1}{r_{ij}}$$

Eq. 2- 11

For fixed nuclei, the total energy is equal to the sum of electronic energy and the repulsion energy of the nuclei:

$$E_{tot} = E_{elec} + \sum_{k=1}^M \sum_{l>k}^M \frac{Z_k Z_l}{R_{kl}}$$

Eq. 2- 12

However, the electron-electron repulsion poses a major difficulty in solving the Schrödinger equation of the many-body problem.

The Density Functional Theory (DFT) was established by Hohenberg and Kohn^[199] based on two theorems.

The first theorem indicate that H_{elec} and ψ_{elec} are expressed as a function of the electron density (ρ), defined by:

$$\rho(\mathbf{r}) = N \int \dots \int |\psi_{elec}(\mathbf{r}, r_2, \dots, r_n, \sigma_1, \sigma_2, \dots, \sigma_N)|^2 dr_2, \dots, dr_N, \dots, d\sigma_N$$

Eq. 2- 13

With r_n and σ_n the position and the spin state of the electron respectively and

$$N = \int \rho(\mathbf{r}) d\mathbf{r}$$

Eq. 2- 14

As a consequence, E_{elec} can be written as a functional of the electron density:

$$E_{elec}[\rho] = \hat{T}[\rho] + \hat{V}_{ne}[\rho] + \hat{V}_{ee}[\rho] = \int v_{ext}(\mathbf{r})\rho(\mathbf{r})d\mathbf{r} + F_{HK}[\rho]$$

Eq. 2- 15

With $\int v_{ext}(\mathbf{r})$ the external potential, \hat{V}_{ne} and \hat{V}_{ee} nuclei-electron and electron-electron potentials. F_{HK} is a universal functional equal to $\hat{T}[\rho] + \hat{V}_{ne}[\rho]$.

The second theorem states that $E_{elec}[\rho]$ is minimal when the electron density is equal to that of the density of the ground state, as a result, the ground state is found by minimizing E_{elec} .

There is no exact expression for $F_{HK}(\rho)$ thus Kohn and Sham^[200] proposed a mono-electronic formalism consisting of solving the problem through two sections: in the first part, $E_{elec}[\rho]$ is expressed as if the electrons are not interacting while the second one corrects all the approximations made by the first part. Based on this formalism, $E_{elec}[\rho]$ can be written as:

$$E_{elec}[\rho] = \hat{T}_{ni}[\rho] + \hat{V}_{ee,classical}[\rho] + \int v_{ext}(r)\rho(r)dr + E_{xc}[\rho]$$

Eq. 2- 16

With \hat{T}_{ni} the kinetic energy of non-interacting electrons, $\hat{V}_{ee,classical}$ the classical component of Coulombian interaction. E_{xc} is the exchange-correlation energy. It contains corrections for both, the kinetic energy and the non-classical part of \hat{V}_{ee} .

Different types of exchange-correlation functionals exist and are still under investigation to assure a compromise between the computational cost and the accuracy. The Generalized Gradient Approximations (GGA) exchange-correlation functionals consider that real electron systems are not homogeneous and are widely used for large systems. In our study, a GGA exchange-correlation functional is used. It introduced a dependence of the functional by ρ and its gradient. The PBE (Perdew, Burke and Ernzerhof) functional^[201] is used in our study. However these functional underestimate the dispersion interactions that form a part of the van der Waals interactions, thus the PBE-dDsC functional^[202] is used to overcome this underestimation.

The last step is to define the wavefunction. When bulk solid systems and surfaces are being studied, the periodic approach is the most adequate. In this case, an elementary cell is periodically replicated in two or three directions. In the case of the Vienna Ab initio Simulation Package (VASP) used in this work, a plane-wave basis set is used. The wavefunction is expressed as the sum of plane-waves expanded out to a chosen cut off energy. Increasing the cut off energy increases the accuracy by allowing a more expansive wavefunction. The system is described in reciprocal space where the first Brillouin zone is divided and described by a number of K-points that describe the sampling of the wavefunction. The plane-wave basis is efficient if used together with the pseudopotential approach, in which the core electrons are substituted with a pseudopotential that acts upon the valence electrons. In this work projector-augmented wave (PAW) pseudopotentials^[203] were used.

2.3.2. Geometry optimization and energies of silicogermanates structures

As mentioned earlier, the total energy includes the Coulomb interaction between nuclei. The total energy correspond to the lowest energy among all possible configurations. To find this lowest energy, the geometry optimization starts from an initial geometry then calculates its total energy. A point on the surface is associated to this energy ‘single point energy’. From this initial geometry and its energy, the forces applied on the atoms are calculated resulting in the movement of the atoms and the calculation of the new configuration with respect to the positions of the nuclei. This process is repeated until the energy variation is lower that a value defined by the user. The final geometry is considered as the optimized configuration. The temperature is not included in the optimization, the energy obtained is the intern energy at 0 K of the system.

2.3.3. Statistic thermodynamic calculations

For geometry optimization, systems are considered at 0 K. Substitution reactions occur at well-defined temperatures. Thus to obtain a more realistic description of experimental substitutions, statistic thermodynamics of these substitution reactions have been calculated (Gibbs free energy, $\Delta G_{\text{sub, Ge} \rightarrow \text{Si/Al}}$ (kJ)). Gibbs free energy is calculated by considering the rotational, translational, and vibrational degrees of freedom for isolated (gas-phase) molecules.

$$G = H - T.S$$

Eq. 2- 17

The enthalpy is calculated from the free energy U and the product of the pressure and molecular volume:

$$H_m = U_{\text{elec.}} + U_{\text{vib,m}} + U_{\text{trans,m}} + U_{\text{rot,m}} + (P.V_m)$$

Eq. 2- 18

Where $U_{\text{elec.}}$, $U_{\text{vib,m}}$, $U_{\text{trans,m}}$, $U_{\text{rot,m}}$ and V_m are the internal electronic energy, vibrational energy, translational energy, rotational energy and the molar volume respectively.

The first term is the result given by DFT calculations as described in 2.3.1 whereas the other terms are calculated by using statistical thermodynamics.

The vibrational energy is calculated from the natural vibration modes ν_i of the system:

$$U_{\text{vib,m}}(T) = N_A \left[\sum_i \frac{1}{2} h c \nu_i + \sum_i \frac{h c \nu_i \times \exp\left(-\frac{h \nu_i}{k_B T}\right)}{1 - \exp\left(-\frac{h \nu_i}{k_B T}\right)} \right]$$

Eq. 2- 19

With h as Planck constant, k_B as Boltzmann constant and T as Temperature. The first term of this formula “Zero Point Energy, ZPE” corresponds to the vibrational term at 0 K of the system. The rotational and translational terms for ideal gas are:

$$U_{\text{trans.}}(T) = U_{\text{rot,m}}(T) = 3/2(N_A k_B T)$$

Eq. 2- 20

The entropy is calculated from the molecular vibrational entropy, translational entropy and rotational entropy:

$$S_m = S_{\text{vib,m}} + S_{\text{trans,m}} + S_{\text{rot,m}}$$

Eq. 2- 21

$S_{\text{vib,m}}$, $S_{\text{trans,m}}$ and $S_{\text{rot,m}}(T)$ are calculated following:

$$S_{vib,m}(T) = N_A k_B \left[\sum_i \frac{h\nu_i \exp\left(-\frac{h\nu_i}{k_B T}\right)}{1 - \exp\left(-\frac{h\nu_i}{k_B T}\right)} - \sum_i \ln\left(1 - \exp\left(-\frac{h\nu_i}{k_B T}\right)\right) \right]$$

Eq. 2- 22

$$S_{trans}(T) = N k_B (5/2 \ln(T) - \ln(P) + 5/2 \ln(M) - 1,165)$$

Eq. 2- 23

$$S_{rot,m(T)} = N k_B \left[\frac{\sqrt{\pi}}{\sigma} \left(\frac{8\pi^2 k_B}{h^2} \right)^{3/2} \sqrt{A_e \cdot B_e \cdot C_e} \right]$$

Eq. 2- 24

With P the partial pressure of the ideal gas, M is the molar weight, σ is the number of symmetry and A_e , B_e and C_e are rotational constants of the molecule.

The chemical reaction of aA_i with an α_i stoichiometric coefficient is $\sum \alpha_i A_i = 0$

Based on this reaction, the enthalpy, entropy and Gibb's free energy at the temperature T are calculated from:

$$\Delta_r H^\circ(T) = \sum_i \alpha_i H_{i,m}^\circ(T)$$

$$\Delta_r S^\circ(T) = \sum_i \alpha_i S_{i,m}^\circ(T)$$

$$\Delta_r G^\circ(T) = \sum_i \alpha_i G_{i,m}^\circ(T) + \sum_i \alpha_i [H_{i,m}^\circ(T) - T S_{i,m}^\circ(T)]$$

Where the terms $X_{i,m}^\circ(T)$ are the molar values of the compound i in its standard state at the temperature T.

In practice, the website <http://www.colby.edu/chemistry/PChem/scripts/ABC.html> was used to calculate the translational and rotational terms for the entropy of any compound in its gaseous phase (SiCl_4 , GeCl_4). Moreover, we neglected the thermal corrections for condensed phases (silicates, aluminosilicates and silicogermanates).

2.3.4. Computational method used in our work

In practice, periodic DFT calculations were performed using the Vienna ab initio simulation package (VASP) code^[204,205] with the Perdew, Burke and Ernzerhof^[201] (PBE, GGA family) exchange-correlation functional and a density dependent dispersion correction (dDsC) for the dispersion interactions^[202]. The projected augmented wave (PAW) method^[203] was used to describe

the core electron interactions with a cut-off energy of 800 eV and of 400 eV for the geometry optimization of zeolites structures, with or without relaxation of the cell parameters respectively.

All initial zeolites structures were taken from the International Zeolite Association website^[206]. Unit cell parameters were relaxed according to the following procedure:

- Step 1: Cell parameters are fixed while atoms are free (cutoff: 400 eV)
- Step 2: Atoms and cell parameters are free (cutoff: 800 eV)
- Step 3: Cell parameters are fixed while atoms are free (cutoff: 400 eV)

Geometry optimizations were continued until forces were lower than 0.02 eV/Å for steps 1 and 3 and until the energy difference between two consecutive optimization steps was lower than 10⁻⁴ eV for step 2. The break condition for the electronic self-consistent field (SCF loop) was fixed to 10⁻⁵ eV for all calculations. Gaussian smearing was set with a width of 0.05 eV. Table 2- 3 reports all the investigated structures with the K-points mesh used for energy calculations. This approach was also applied on materials used as references: 2x2x2 supercells were used for an accurate estimation of the energy of silica quartz (K-points mesh: 3x3x3), germanium oxide rutile (3x3x4) and α -alumina (3x3x1). The electronic energies of water used as reference for interrupted structures and those of several sets of references: molecular hydroxides e.g. Si(OH)₄, Ge(OH)₄ and Al(OH)₃(H₂O) or chlorides such as SiCl₄, GeCl₄ and AlCl₃ were evaluated by placing each molecule (1x1x1) in a 25x25x25 Å³ cell.

Table 2- 3: List of structure types investigated in the present work. The names correspond to zeolites in their silicogermanate forms.

IZA Structural code	Name	K-points mesh
Regular		
ASV ^[60]	SU-10	3x3x1
BEC ^[56,75-77]	ITQ-17	Γ point
IRN ^[82]	ITQ-49	Γ point
IRR ^[83-86]	ITQ-44	Γ point
ITG ^[90]	ITQ-38	Γ point
ITR ^[103,104]	ITQ-34	Γ point
ITT ^[4,105,107-111]	ITQ-33	Γ point
IWR ^[114-116]	ITQ-24	Γ point
IWS ^[117]	ITQ-26	Γ point
IWW ^[118-121]	ITQ-22	Γ point

POS ^[62]	PKU-16	Γ point
SOF ^[61]	SU-15	1x1x2
SOR ^[66,125]	SCM-14;ITQ-62	1x1x11
STW ^[61,128]	SU-32 ;Ge-STW	Γ point
SOV ^[126]	SCM-15	Γ point
SVV ^[67,129]	SSZ-77	Γ point
UOS ^[131]	IM-16	1x4x4
UOV ^[132]	IM-17	Γ point
UOZ ^[133]	IM-10	4x4x1
UTL ^[5,50,134,135]	IM-12 ;ITQ-15	Γ point
UWY ^[136]	IM-20	Γ point
Interrupted		
-IFT ^[71]	ITQ-53	Γ point
-IFU ^[72]	ITQ-54	Γ point
-IRY ^[87]	ITQ-40	Γ point
-ITV ^[3,84,112,113]	ITQ-37	Γ point
Partially Disordered		
*CTH ^[65,68,137,138]	CIT-13 ;NUD-2; SAZ-1	Γ point
*UOE ^[73]	IM-18	3x3x1

(-) for interrupted, (*) for partially disordered structures.

Substitution energies and free energies of Ge atoms for Si or Al were quantified with respect to several sets of references: molecular hydroxides e.g. Si(OH)₄, Ge(OH)₄ and Al(OH)₃(H₂O) or chlorides such as SiCl₄, GeCl₄ and AlCl₃. The energies of these molecules were evaluated by placing each molecule (1x1x1) in a 25x25x25 Å³ cell.

Substitution reactions occur at finite temperatures. Thus to obtain a more realistic description of experimental substitutions, statistical thermodynamics of these substitution reactions have been used to estimate the Gibbs free energy, $\Delta G_{\text{sub,Ge}\rightarrow\text{Si/Al}}$ (kJ/mol) by considering the rotational, translational, and vibrational degrees of freedom of isolated gas-phase molecules^[207]. Vibrational properties of these molecules were determined by finite difference, with a displacement of ± 0.005 Å of each atom starting from the equilibrium position. The thermal contributions for condensed phases (silicates, aluminosilicates and silicogermanates) were neglected.

For NMR calculations, the linear response and GIAO (gauge-invariant atomic orbital) methods^[208,209] were employed to calculate screening constants for ^1H , ^{27}Al , with the VASP code. Chemical shifts can then be deduced by referencing screening constants to reference compounds (Tetramethylsilane for ^1H and $\alpha\text{-Al}_2\text{O}_3$ was used as a secondary reference for ^{27}Al).

3. Ab Initio Investigation of the Relative Stability of Silicogermanates and Their (Alumino)Silicates Counterparts

The results presented in this chapter are published in the following article:

Ab Initio Investigation of the Relative Stability of Silicogermanates and Their (Alumino)Silicates Counterparts, E. El Hayek, B. Harbuzaru, J. Martens, C. Chizallet, *Microporous Mesoporous Mater.*, 306, 110425, 2020. <https://doi.org/10.1016/j.micromeso.2020.110425>

The text of the chapter is adapted from this article.

As discussed in chapter 1, the diversity of synthetic zeolites with silicogermanate composition has grown significantly. The incorporation of germanium in the zeolite framework favors the formation of smaller polyhedra such as double 4-rings d4r of tetradedra [6,7,9,50,84,210,211]. Many of these zeolites have large pores, thanks to the double 4-ring (d4r) structural subunits occupied by Ge atoms. The wide pores make them potentially interesting for catalytic transformation of bulky molecules, but the thermal and hydrothermal stability after calcination and the acidity are insufficient for practical applications [6,7,150,151,212].

In the present chapter, we studied using periodic density functional theory calculations, the stability of all reported silicogermanate zeolite framework types as a basis of selection of candidates for future experimental studies on isomorphic substitution of Ge atoms by Al and Si. To this aim we investigated the intrinsic stability of silicogermanate zeolite types having structural codes attributed by the international zeolite association. Some silicogermanates already exist in aluminosilicate or silicate forms reflecting the stability of these structures such as AST [60,74,213,214], BEC [56,215,216,216], ISV [88,89,217,218], LTA [122,219,220], MFI [60,221,222] and STI [127,223], therefore we selected one of these structures, the BEC, while the rest have been excluded from the present study. The BEC zeolite was synthesized as a germanate [224], as an overgrown silicate crystal [215], as a pure silicate [216], as a silicogermanate [56] and the post-treatment of the pure BEC silicogermanate allowed successfully the partial substitution of Ge by Al [150]. Moreover, the -CLO and -SYT structures are constructed exclusively by connected d4r units, while BEA, DFT, EWO, MFI and STI structures do not contain d4r units, as a consequence the strategy followed in this work (described in section 3.1) is not applicable and the seven structures were excluded. Thus 20 regular structures [4,5,50,56,60,61,61,62,66,67,75-77,82-86,90,103-105,107-111,114-121,125,128,129,131-136], 4 interrupted [3,71,72,84,87,112,113] and 2 partially disordered [65,68,137,138] structures were studied. Note that the term 'regular' is used for fully ordered type materials, 'interrupted' is related to fully ordered type materials with systematic interruption in the framework such that not all T atoms are 4-connected

to other T atoms. ‘Partially disordered’ refers to materials with disorders in terms of specific building units. The studied samples are represented in Table 3- 1 .

Our calculations were performed using the procedure explained in section 2.3.4.

First we investigated whether the topologies are stable in silicate or aluminosilicate composition. Then we inspected the possibility of substituting Ge for another structural element such as Si or Al to verify which candidates can be stabilized by post-treatment.

Table 3- 1: List of structure types investigated in the present work. The names correspond to zeolites in their silicogermanate forms.

IZA Structural code	Name	K-points mesh
Regular		
ASV ^[60]	SU-10	3x3x1
BEC ^[56,75–77]	ITQ-17	Γ point
IRN ^[82]	ITQ-49	Γ point
IRR ^[83–86]	ITQ-44	Γ point
ITG ^[90]	ITQ-38	Γ point
ITR ^[103,104]	ITQ-34	Γ point
ITT ^[4,105,107–111]	ITQ-33	Γ point
IWR ^[114–116]	ITQ-24	Γ point
IWS ^[117]	ITQ-26	Γ point
IWW ^[118–121]	ITQ-22	Γ point
POS ^[62]	PKU-16	Γ point
SOF ^[61]	SU-15	1x1x2
SOR ^[66,125]	SCM-14;ITQ-62	1x1x11
STW ^[61,128]	SU-32 ; Ge-STW	Γ point
SOV ^[126]	SCM-15	Γ point
SVV ^[67,129]	SSZ-77	Γ point
UOS ^[131]	IM-16	1x4x4
UOV ^[132]	IM-17	Γ point
UOZ ^[133]	IM-10	4x4x1
UTL ^[5,50,134,135]	IM-12 ; ITQ-15	Γ point
UWY ^[136]	IM-20	Γ point
Interrupted		
-IFT ^[71]	ITQ-53	Γ point
-IFU ^[72]	ITQ-54	Γ point
-IRY ^[87]	ITQ-40	Γ point
-ITV ^[3,84,112,113]	ITQ-37	Γ point
Partially Disordered		
*CTH ^[65,68,137,138]	CIT-13 ;NUD-2; SAZ-1	Γ point
*UOE ^[73]	IM-18	3x3x1

(-) for interrupted, (*) for partially disordered structures.

3.1. Choice of Ge and Al distribution

The Ge distribution in silicogermanate zeolite frameworks is not well defined. It is known that high \widehat{SiOSi} angle values lead to more stable solids than their corresponding \widehat{GeOSi} and \widehat{GeOGe} [52,225]. However, when it comes to narrower angles such as in d4rs, germanium assures the stabilization of these units by reducing their strain. Only after reaching a certain amount of Ge, the Ge starts to be located in sites corresponding to sufficient low angles, outside of the d4r [52]. Thus we limited our study to Ge occupying d4r units only. Based on experimental observations in literature, Ge atoms occupy mostly all T sites of the d4r, or half of these [120]. Thus to model silicogermanates structures, we have considered three possibilities: Ge occupying all the T sites of the d4r (Figure 3- 1.a), Ge occupying half of the T sites of the d4r respecting alternation with Si (Figure 3- 1.b) and Ge occupying half of the T sites of the d4r in the same s4r (Figure 3- 1.c).

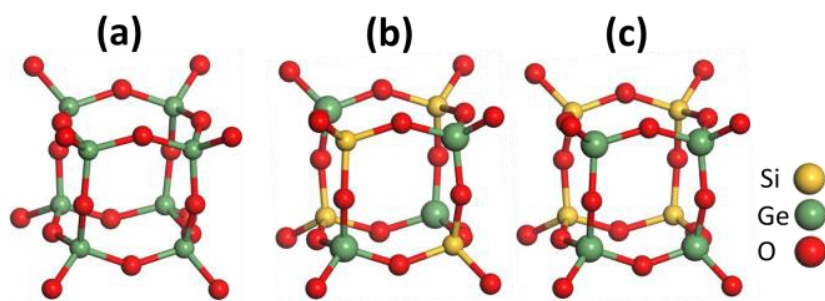


Figure 3- 1: Ge and Si siting in d4r units: (a) Ge occupying all d4r, (b) Ge occupying half of the d4r with alternation with Si and (c) Ge occupying half of the d4r in a same s4r. The d4r part of the structures only are shown, the other parts of the structure (with T sites occupied by Si only) are omitted for the sake of clarity and for generalization purposes.

For aluminosilicates, respecting the Löwenstein rule [226] imposes that Al alternates with Si in the d4r. To compensate the negative charge induced by Al, one hydrogen atom is added for each Al (Figure 3- 2).

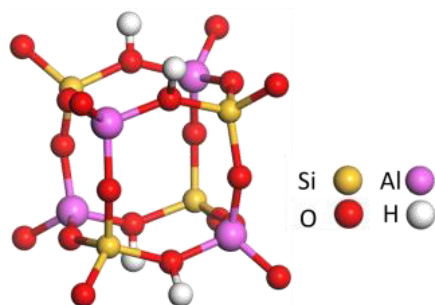


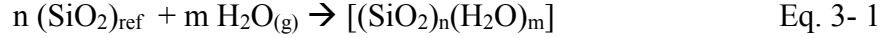
Figure 3- 2: Al and Si siting in aluminosilicate d4r units.

The lattice parameters after geometry optimization of the different structures are reported in Table S3-1.

3.2. Intrinsic stability of silicogermanates and their (alumino)silicates analogues

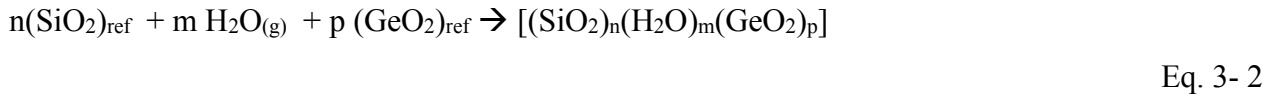
The intrinsic stabilities of the structures were evaluated through their energies of formation. Silica quartz, germanium oxide rutile and α -alumina were chosen as reference structures in our calculations. The energies of formation (ΔE_{form}) per T sites were calculated from the reaction energy of the following reactions:

❖ Silicates:



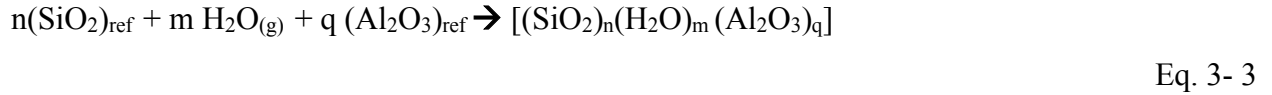
with $T = n$ (T being the total number of T sites),

❖ Silicogermanates with Ge occupying all the corners of d4r:



with $T = n+p$,

❖ Aluminosilicates:



with $T = n+2q$.

Note that water is necessary ($m \neq 0$) only in the chemical reactions involving the formation of interrupted structures.

ΔE_{form} (kJ/mol) per T site for different structures is presented in Figure 3- 3 and Table S3-3. These energies are all positive (with the exception of interrupted structures, see below), confirming that quartz, corundum and rutile are more stable polymorphs, as expected, whereas zeolites are metastable. Interestingly, it was shown that all silicates and aluminosilicates frameworks are more stable than the corresponding silicogermanates.

This result is in accordance with the experimental measurements of the enthalpies of formation per T sites of BEC materials free of connectivity defects where an increase from 17.79 ± 0.72 kJ/mol for the pure silica form ^[110] to 19.74 ± 0.32 and 21.04 ± 0.24 for silicogermanates with Si/Ge ratio of 3.5 and 1.4 respectively was detected ^[211]. The experimental enthalpies were calculated based on a high temperature oxide melt solution calorimetry from 298 to 973K using silica and germania quartz as references. In our calculations, the (electronic) energies of formation per T sites of BEC increase from 14 kJ/mol for pure silica, to 27 and to 37 kJ/mol for silicogermanate forms with Si/Ge of 3 and 1 respectively, considering the transformation in solid forms departing from silica quartz and germanium oxide rutile as reference structures at 0 K (Eq. 3-1, 2 and 3).

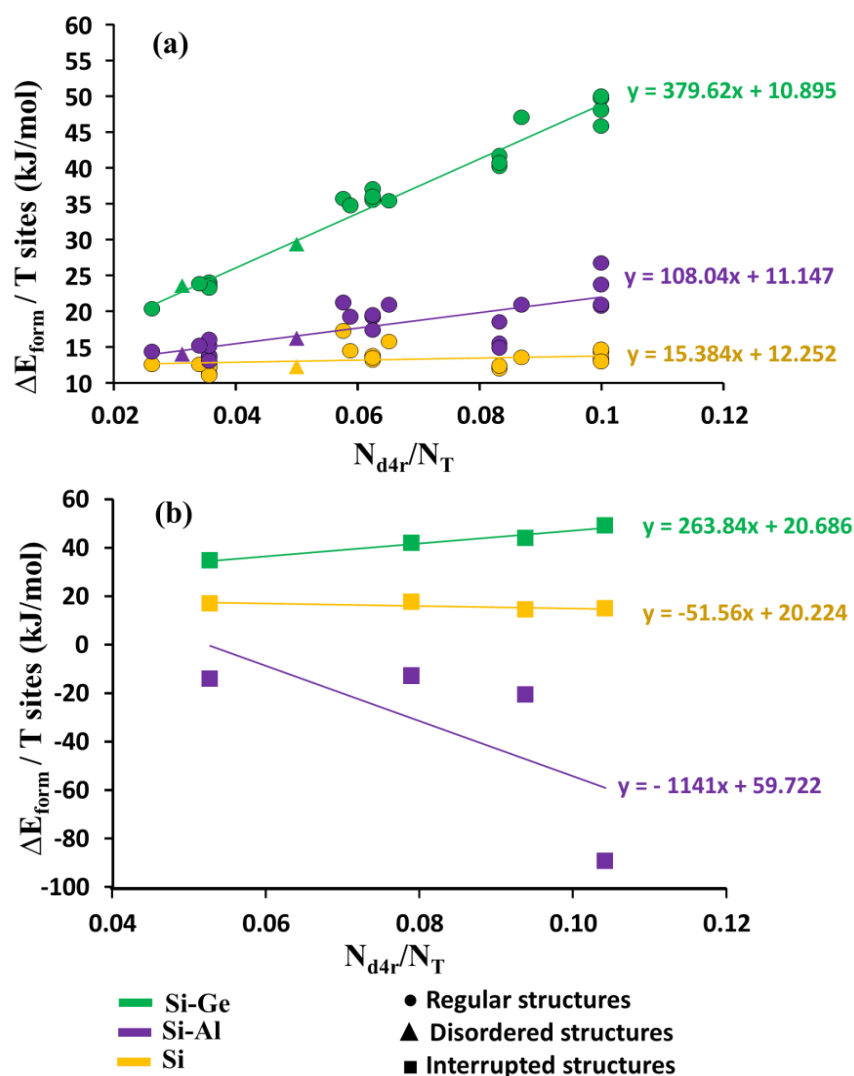


Figure 3- 3: Energies of formation per T site ($\Delta E_{\text{form}} / \text{T sites}$) of silicates (yellow), silicogermanates with Ge occupying the full d4r (green) and aluminosilicates (purple) of (a) regular (circles), partially disordered (triangles) and (b) interrupted (squares) zeolite structures. $N_{\text{d4r}}/N_{\text{T}}$ correspond to the number of d4r of the structure over the total number of T sites.

Note that the germanium oxide rutile was chosen over the α -quartz because of its higher stability [227], by 30 kJ/mol. Using α -quartz Germania as a reference, similar to experiments, the energies of formation of BEC per T sites increase from 14 kJ/mol for pure silica, to 20 and to 22 kJ/mol for silicogermanate forms with Si/Ge of 3 and 1 respectively. This is in excellent agreement with experimental results. Moreover, previous measurements of the enthalpies of formation of ITQ-21 and ITQ-22 after varying the Ge amount, confirmed that silicogermanates forms are less stable than silicate zeolites [228]. This indicates that Ge is destabilizing the structure. The role of this element in the formation of large pore structures is thus of kinetic nature, providing more stable crystal growth intermediates in solution during the synthesis and in orienting the crystallization

process to a specific structure. For example, increasing the Ge content favors the formation of ITQ-22 over the EU-1 zeolite [119].

The energies of formation of normal and disordered structures are correlated with the d4r content of the structure (Figure 3- 3.a). This result is congruent with earlier work by Wu et al [110] showing that the enthalpy of formation increased with increasing number of d4r in a series of zeolites, viz. ITQ-7, -17, -21, -22, and -33.

Interrupted aluminosilicates do not follow the general trend and have higher intrinsic stabilities compared to normal and disordered structures, with negative formation energies (Figure 3- 3.b). This may result from interactions between hydroxyls of interrupted frameworks and compensation hydrogen atoms, see Figure S3.1.a. It can also be due to the reference state of water (gas phase) chosen for the calculation of the formation energy. Furthermore, the particular stability of the –ITV structure ($\Delta E_{\text{form}}/ \text{T sites} = -89 \text{ kJ/mol}$) can be related to the location of all the interrupted sites on the d4r units (Figure S3-1.b) while the –IFU, -IFT and -IRY structures have their interrupted sites on other rings (Figure S3-1.a).

A trend between the framework density and the stability of zeolites was established by force field calculations performed on a large array of solids [229], indicating that zeolites with higher densities tend to be more stable. However, other force field and quantum calculations, [230,231] dealing with a lower number of structures, and experimental measurements [232] suggested a quasi-invariance of the stability with respect to the density, and that the only factor affecting the stability is the presence of 3-membered rings due to its strain. Above this size, the rings seem to be unstrained and to have similar stability.

Our results (Figure S3-2) support the independence of the intrinsic stability of silicogermanates and their densities. This independence is still valid for their aluminosilicate analogues. For silicates, the correlation is of better quality with respect to silicogermanates and aluminosilicates. As a consequence, we suggest that the intrinsic stability of all silicogermanates is rather independent of the framework density but is directly related to the Ge content. The latter element orients the crystallization process to new structures [147]. For instance, the competition between the growth of BEC, ISV and BEA type zeolites can be explained by relative stability changes depending on the Si/Ge ratio [233].

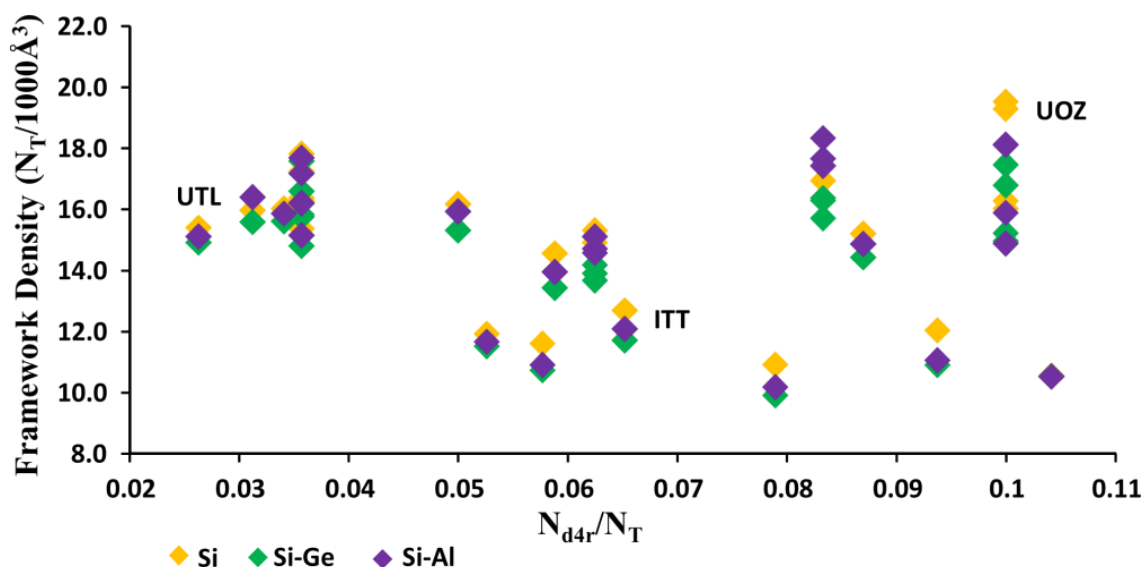


Figure 3- 4: Variation of the framework density against the ratio of the number of d4r units in the structure over the total T sites (N_{d4r}/N_T). The studied framework types are represented in Table 3- 1.

Another interesting aspect is the influence of the content and distribution of d4r units in the framework on its density. Figure 3- 4 points out that the density is not directly related to the content of d4r. Even structures with the same number of d4r have different densities. This is quite pronounced for structures with $N_{d4r}/N_T = 0.1$ (Figure 3- 4). In some cases, increasing the number of d4r in the framework reduces the density of the structure, for example the IM-12 silicogermanate having a UTL framework has a framework density of 14.9 ($T/1000 \text{ \AA}^3$) and two d4r per unit cell, while the ITT structure with 3 d4r per unit cell has a lower framework density of 11.7 ($T/1000 \text{ \AA}^3$). The high framework density of UOZ of 17.45 ($T/1000 \text{ \AA}^3$) is in line with its high d4r content in the framework (4 d4r units per unit cell). Figure 3- 5 sketches how the distribution of d4r in the structure affects the density: in UTL, the d4r are separating the layers and creating a spacious framework with reduced density while the UOZ structure, composed mainly of interconnected d4r, has a higher framework density. In consequence, one can say that density is affected by the arrangement of the d4rs and not by their amount in the framework. This reconfirms that the stability of silicogermanates is not directly related to the framework density.

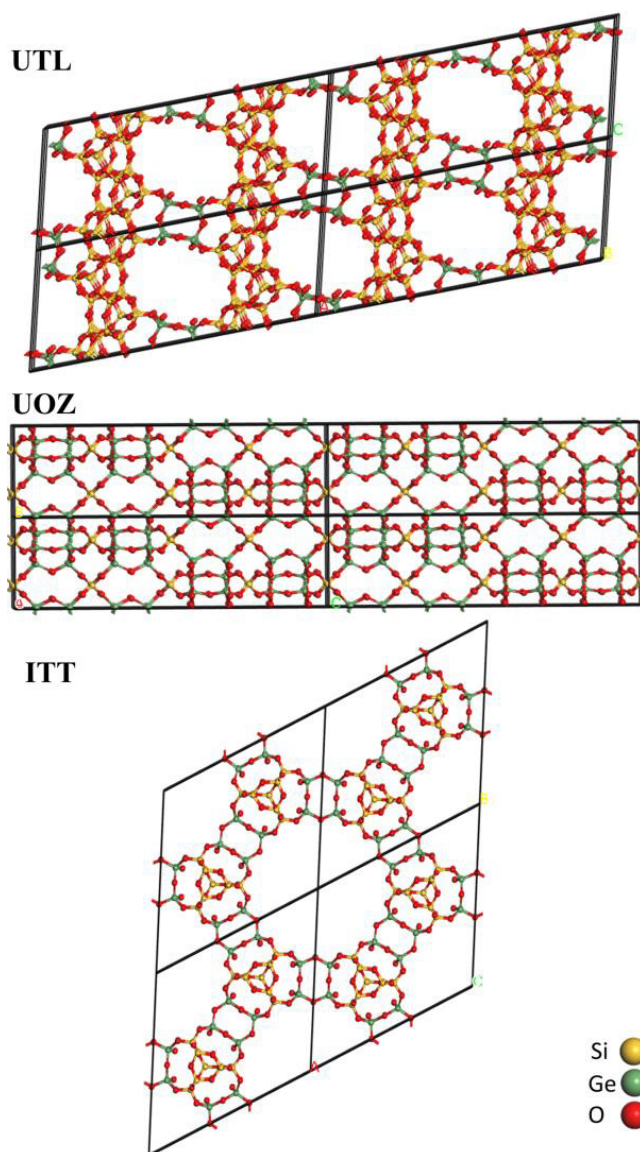


Figure 3- 5: Positioning of d4r in UTL, UOZ and ITT framework structures. For UTL and ITT, only single 4-rings of the d4r units occupied by Ge atoms are shown for clarity.

Based on these results, silicate and aluminosilicate counterparts of silicogermanate zeolites are stable. However, most of these zeolites cannot be obtained by direct synthesis. They may be obtained by post-treatments. To estimate the possibility of these transformations, we have calculated the energies of substitution of Ge for Si and Al, considering various substitution agents.

3.3. Isomorphic substitution of Ge for Si and Al

To investigate the possibility of substitution of Ge for Si and Al, hydroxide and chloride reactant molecules were used in the calculations. In the case of chlorides, the studied substitutions are represented in Figure 3- 6.

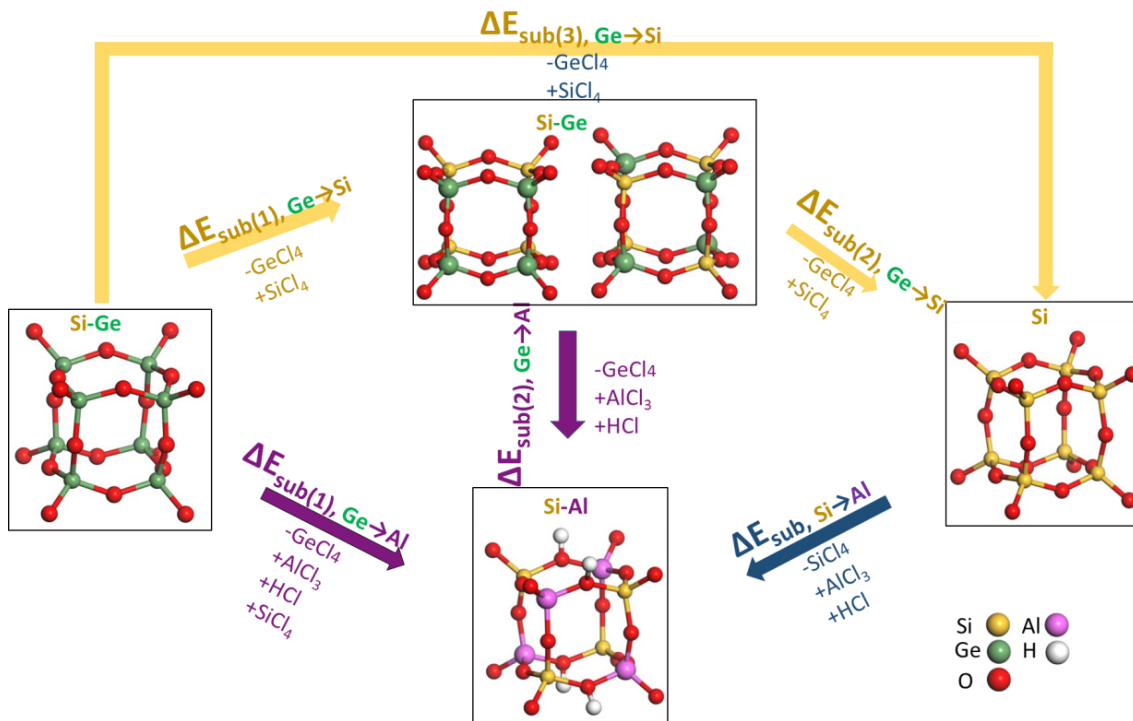


Figure 3- 6 : Substitution scheme of Ge for Si and Al using chlorides. The d4r part of the structures only are shown, the other parts of the structure (with T sites occupied by Si only) are omitted for the sake of clarity and for generalization purposes.

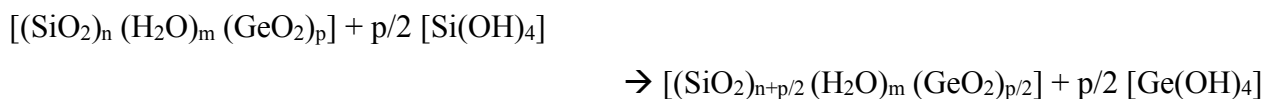
Starting from parent silicogermanates with full-Ge-d4r, we calculated the energies of substitution of Ge for Si to obtain half-Ge-d4r silicogermanates (alternated /same s4r) or full silicate analogues ($\Delta E_{\text{sub}(1/2/3), \text{Ge} \rightarrow \text{Si}}$, represented with yellow arrows). Substitution of Ge by Al was evaluated starting either from full-Ge-d4r or both half-Ge-d4r ($\Delta E_{\text{sub}(1/2), \text{Ge} \rightarrow \text{Al}}$) respecting the Löwenstein rule. Finally, substitution of Si for Al was also evaluated ($\Delta E_{\text{sub}, \text{Si} \rightarrow \text{Al}}$).

The various substitution energies were calculated following the reactions given in equations 4-15 below.

Using hydroxides:

❖ Ge \rightarrow Si:

$\Delta E_{\text{sub}(1), \text{Ge} \rightarrow \text{Si}}$:



Eq. 3- 4

$\Delta E_{\text{sub}(2), \text{Ge} \rightarrow \text{Si}}$:



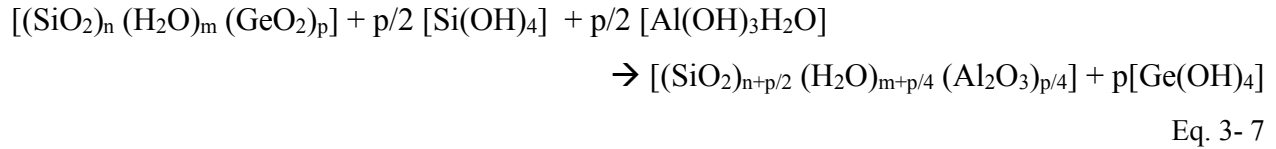
Eq. 3- 5

$\Delta E_{\text{sub (3), Ge} \rightarrow \text{Si}}$:

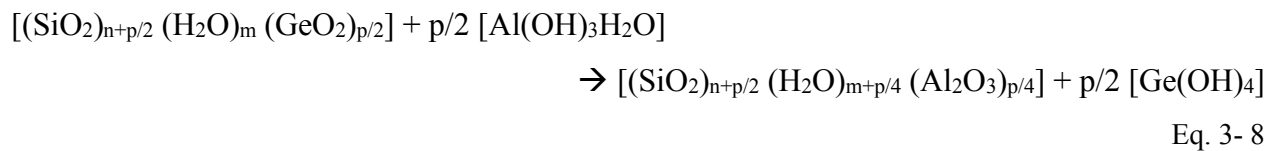


❖ Ge → Al:

$\Delta E_{\text{sub (1), Ge} \rightarrow \text{Al}}$:

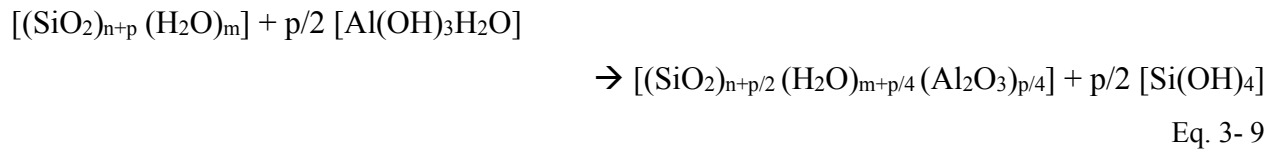


$\Delta E_{\text{sub (2), Ge} \rightarrow \text{Al}}$:



❖ Si → Al:

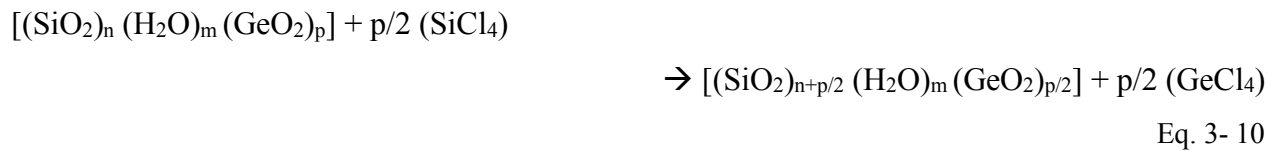
$\Delta E_{\text{sub, Si} \rightarrow \text{Al}}$:



Using chlorides:

❖ Ge → Si:

$\Delta E_{\text{sub (1), Ge} \rightarrow \text{Si}}$:



$\Delta E_{\text{sub (2), Ge} \rightarrow \text{Si}}$:

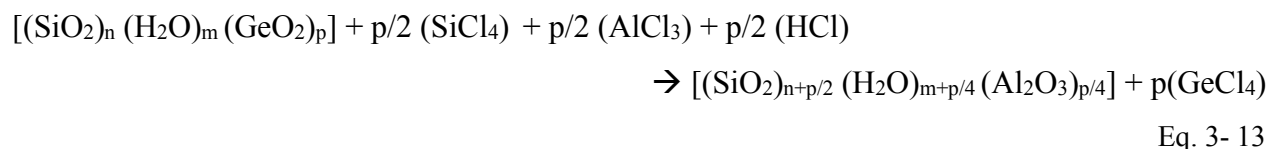


$\Delta E_{\text{sub (3), Ge} \rightarrow \text{Si}}$:

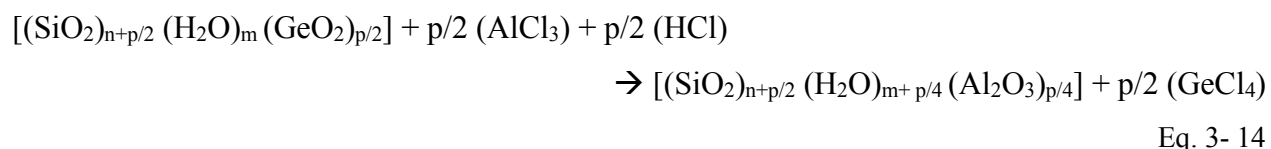


❖ Ge→Al:

$\Delta E_{\text{sub (1), Ge}\rightarrow\text{Al}}$:

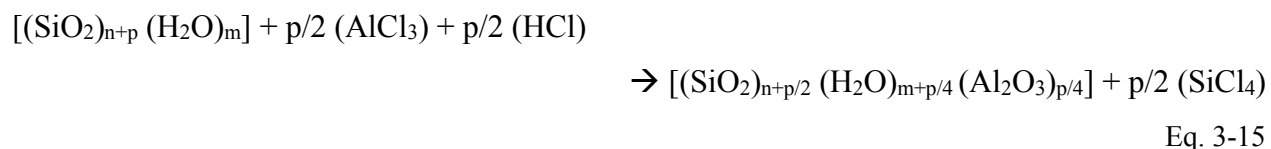


$\Delta E_{\text{sub (2), Ge}\rightarrow\text{Al}}$:



❖ Si→Al:

$\Delta E_{\text{sub, Si}\rightarrow\text{Al}}$:



The values of $\Delta E_{\text{sub (3), Ge}\rightarrow\text{Si}}$ departing from a silicogermanate with Ge occupying the full d4r and $\Delta E_{\text{sub (2), Ge}\rightarrow\text{Al}}$ departing from Ge occupying half of the d4r with alternation are represented in Figure 3- 7 (full removal of Ge). Both families of data follow a similar trend. All the energies of substitutions are negative, this means that thermodynamically the substitution of Ge for Si and Al should be possible using hydroxides or chlorides. In addition, almost no dependence between the substitution and the studied parameters nor the different zeolite structures exists. The results moreover indicate that substitution using chlorides is easier than using hydroxides.

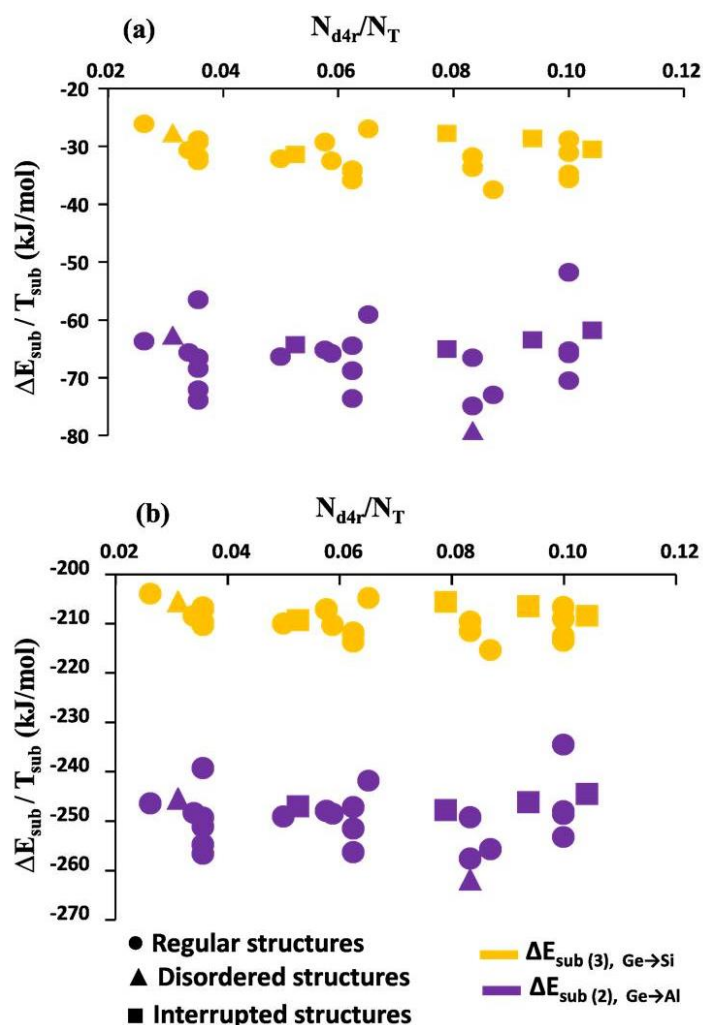


Figure 3- 7: Energies of full substitution of Ge for Si ($\Delta E_{sub}(3), Ge \rightarrow Si$) departing from Ge occupying the full d4r (yellow) and of Ge for Al ($\Delta E_{sub}(2), Ge \rightarrow Al$) departing from Ge occupying half of the d4r with alternation (purple), normalized to the number of substituted T sites, using (a) hydroxides and (b) chlorides against the number of d4r in the structures over the total T sites (N_{d4r}/N_T). Spheres, triangles and squares correspond to regular, partially disordered and interrupted zeolite structures, respectively.

The energetics of substitution were investigated on structures with Ge occupying entire d4r units, Ge occupying half of the d4r with alternation with Si or in s4r composing d4r, $\Delta E_{sub}(1, 2 \text{ and } 3), Ge \rightarrow Si$ and $\Delta E_{sub}(1 \text{ and } 2), Ge \rightarrow Al$. Changing the Ge organization was found not affecting the substitution energy since the energies of substitutions are almost overlapped (red and green, Figure 3- 8).

The energies of substitution of Ge for Si or Al and even the energies of substitution of Si for Al per substituted atom indicate that these substitutions are almost independent of the population with the different atoms of the d4r of silicogermanates. In fact, the difference of these energies between all silicogermanates did not exceed 30 kJ/mol (Figure 3- 8).

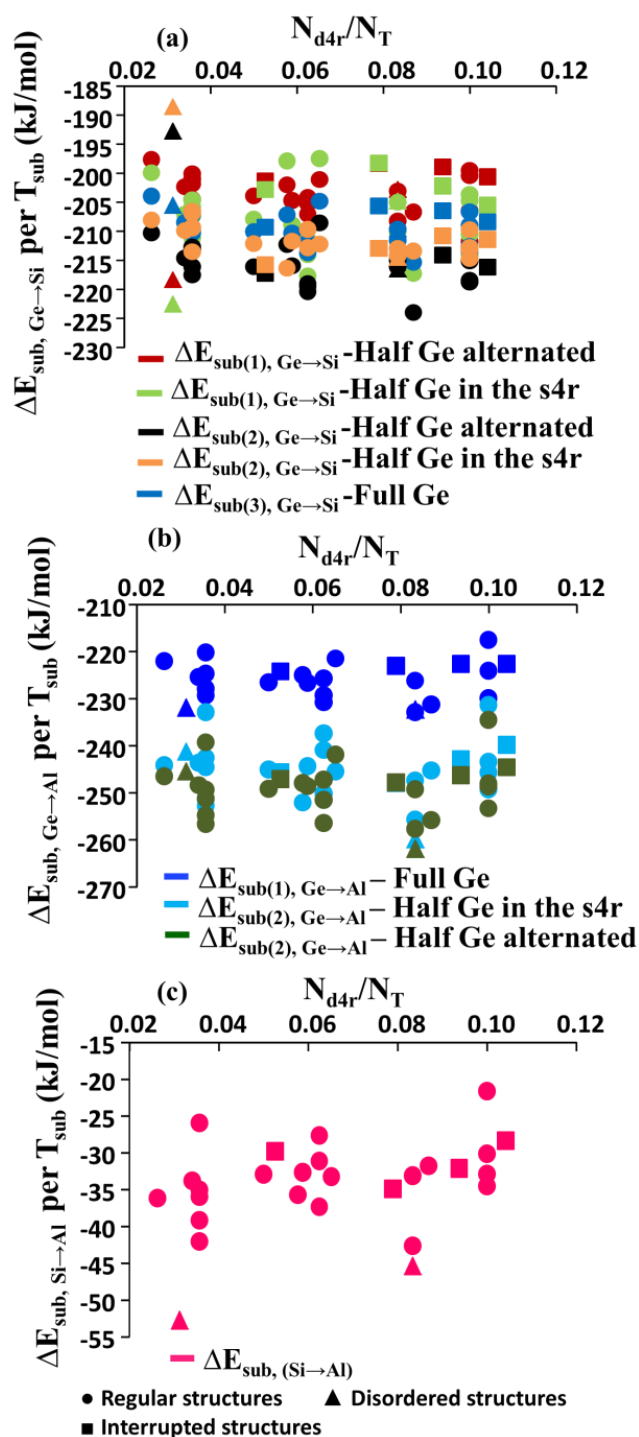


Figure 3- 8: Energies of partial substitution of Ge for Si $\Delta E_{\text{sub}(1), \text{Ge} \rightarrow \text{Si}}$ departing from full occupation of d4r with Ge and full substitution $\Delta E_{\text{sub}(2,3), \text{Ge} \rightarrow \text{Si}}$ departing from Ge occupying half/same s4r and fully in the d4r respectively(a). Energies of partial substitution of Ge for Al $\Delta E_{\text{sub}(1), \text{Ge} \rightarrow \text{Al}}$ departing from Ge occupying the full d4r and full substitution $\Delta E_{\text{sub}(2), \text{Ge} \rightarrow \text{Al}}$ departing from Ge occupying half of the d4r with alternation or in the same s4r (b). Energies of full substitution of Si for Al $\Delta E_{\text{sub, Si} \rightarrow \text{Al}}$ departing from Al occupying half of the d4r (c). All the energies are normalized to the number of substituted T sites against the number of d4r in the structures over the total T sites ($N_{\text{d4r}}/N_{\text{T}}$). Spheres, triangles and squares correspond to regular, partially disordered and interrupted structures respectively.

Moreover, it was found that the framework density does not differentiate zeolites with the same amount of d4rs. This is illustrated for zeolites with N_{d4r}/N_T equal to 0.036 and 0.1 in Figure S3-3. In addition, in the latter zeolites, only small variations of the \widehat{OTO} angles in the d4r depending on chemical composition were noticed. The \widehat{OAlO} angles lie between 108 and 110° and the \widehat{OSiO} between 109 and 111°. This implies that the d4r units are uniform inside the different structures and are unconstrained by the density and the detailed framework structure of the zeolite.

Sastre et al. predicted the feasibility of obtaining pure silica and germania zeolites by calculating an energetic penalty associated with \widehat{TOT} angles [52]. Based on that work, we measured the \widehat{TOT} (T= Si, Ge, Al) angles inside the d4r of the studied structures. The average \widehat{GeOGe} angle varied from 128 to 141°, that of \widehat{SiOGe} from 135 to 145°, the \widehat{SiOAl} ranges from 141 to 147° and \widehat{SiOSi} from 144 to 148°. As known, the ideal angles are 145 and 130° for \widehat{SiOSi} and \widehat{GeOGe} , respectively [234]. This indicates that Ge is crucial for the construction of the d4r having narrow angles. Once the framework is formed, its relaxation in the presence of other elements such as Al or Si is possible by the broadening of the \widehat{TOT} in the d4r. However, the stability of the structure is not directly related to the d4r angles, Figure 3- 9. Furthermore, when the energy of substitution is reported against the difference of \widehat{TOT} angles between the initial and the substituted zeolite no correlation is noticed, Figure 3- S4. These results indicate that the d4r itself is not responsible of the zeolite stability and its suitability for isomorphic substitution. The \widehat{TOT} effect can be related to the entire framework. Additionally, the average of the angles in the d4r does not correlate with the content of d4r of a structure (Figure 3- 9). In other words, the intrinsic stability of the structures is not dependent of the characteristics of the d4r but of their number. In fact, the d4r units could create a tension on the surrounding angles. It is then possible that their number affects the strains exerted elsewhere in the network. These results are in agreement with the experimental enthalpies of high silica zeolites where the enthalpies were not correlated to the average \widehat{SiOSi} angle but were critically dependent of the presence of an important amount of low \widehat{SiOSi} angles ($< 140^\circ$) [232].

Hence, an important conclusion from this theoretical study is that all reported silicogermanate zeolites are suited for isomorphic substitution of Ge with Si or Al atoms without significant distinction.

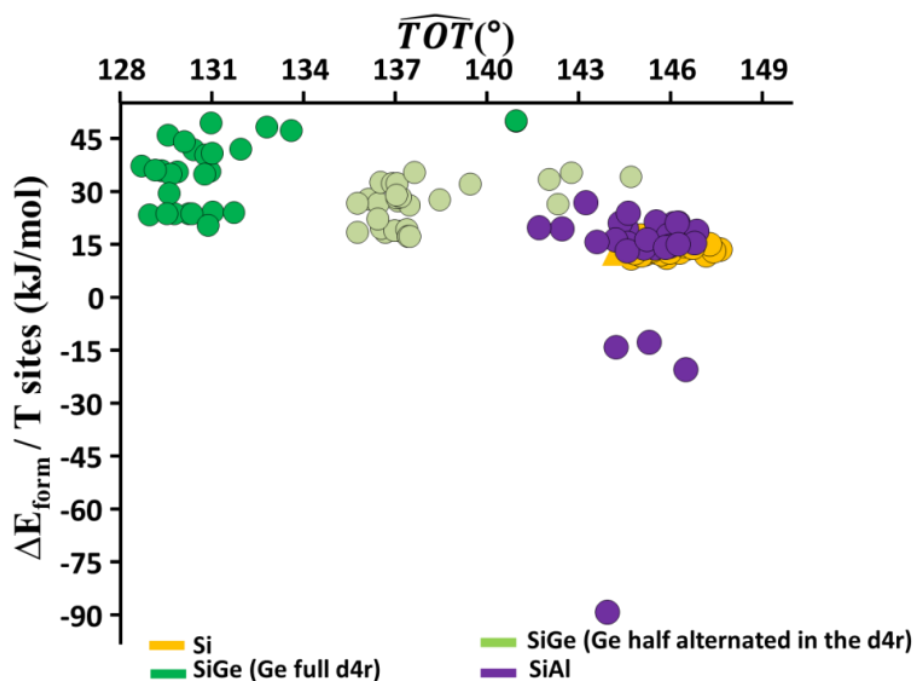


Figure 3- 9: Energies of formation per T sites ($\Delta E_{\text{form}} / \text{T sites}$) of silicates (yellow), silicogermanates with Ge occupying the full d4r (dark green)/ Ge occupying half of the d4r with alternation (light green) and aluminosilicates (purple) of all studied structures. \widehat{TOT} corresponds to angles in the d4r respectively \widehat{SiOSi} , \widehat{GeOGe} , \widehat{SiOGe} and \widehat{SiOAl} .

On the other hand, it is worth mentioning, that the average of $\Delta E_{\text{sub, Si} \rightarrow \text{Al}}$ per T substituted atom is -38 kJ/mol while that of $\Delta E_{\text{sub, Ge} \rightarrow \text{Al}}$ is -248 kJ/mol which highlights that substituting Ge for Al is energetically much more favorable than Si for Al (Figure 3- 8). This suggests a preferential reactivity order during the isomorphic substitution post-treatment. For example, one could start by substituting partially Ge for Si to favor the conditions of respecting the Löwenstein rule in the next step of alumination. Then a treatment to substitute the remaining Ge for Al could follow. These treatments will then insure the stabilization of the material and the introduction of catalytic activity due to the presence of a newly introduced bridging OH groups.

The above energies are computed at 0 K. To obtain a more realistic description of experimental substitutions the Gibbs free energies (ΔG_{sub}) have also been calculated at temperatures varying from 298 K to 1000 K. The difference between these energies for normal and disordered structures does not exceed 20 kJ/mol so the temperature effect is small, Figure 3- 10. Interestingly, substitution of Ge for Si becomes easier by increasing the temperature meanwhile working at lower temperature is preferable to substitute Ge for Al. Indeed, during the substitution of Ge for Al, adding an HCl molecule, Eq. 3- (13-14), leads to a loss of entropy. During the substitution of Ge for Si, the entropies of SiCl_4 and GeCl_4 are close hence the thermal effect is less pronounced.

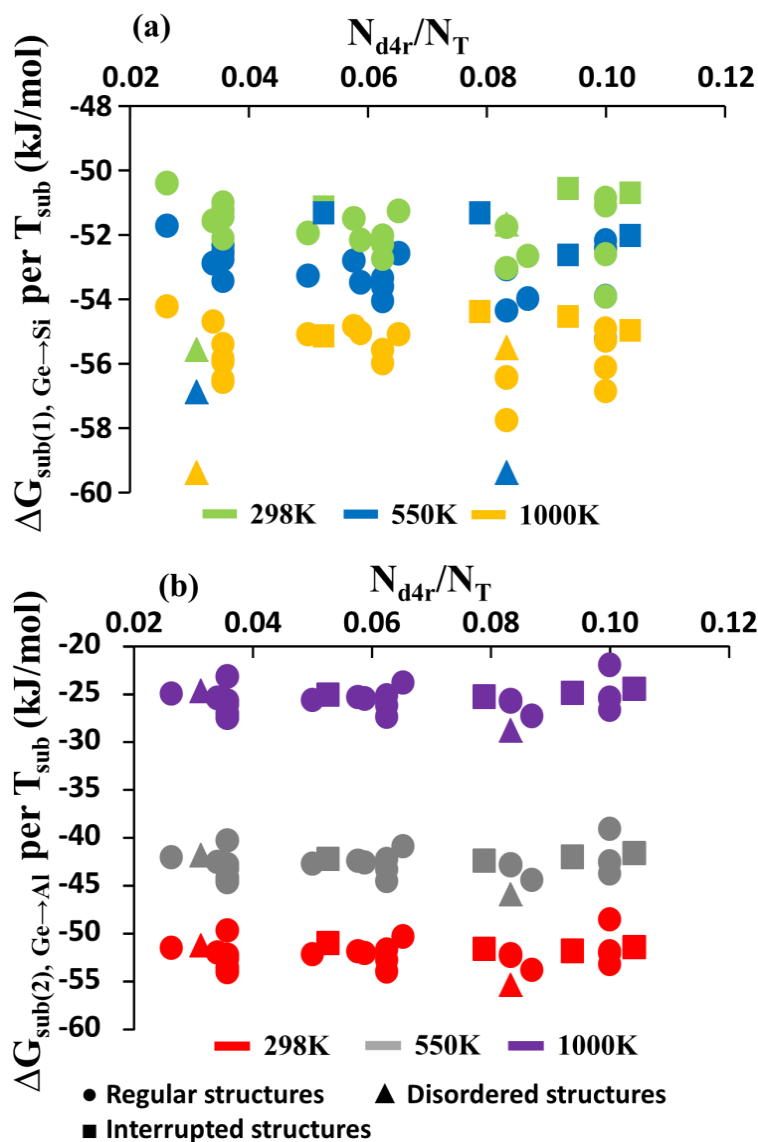


Figure 3- 10: Gibbs free energies of substitution of Ge for Si ($\Delta G_{\text{sub}(1), \text{Ge} \rightarrow \text{Si}}$) departing from Ge occupying the full d4r (a) and Ge for Al ($\Delta G_{\text{sub}(2), \text{Ge} \rightarrow \text{Al}}$) departing from Ge occupying half of the d4r with alternation (b) at different temperatures, normalized to the number of substituted T sites against the number of d4r in the structures over the total T sites ($N_{\text{d4r}}/N_{\text{T}}$). Spheres, triangles and squares correspond to regular, partially disordered and interrupted structures, respectively.

3.4. Conclusion

According to our estimation of framework stability using DFT, silicate and aluminosilicate analogues of germanosilicate zeolites are thermodynamically more stable. This suggests that Ge plays a kinetic role during the crystallization of the zeolite. In addition, the intrinsic stability of germanosilicate zeolites is independent of the framework density. Substituting Ge for other elements such as Si and Al is feasible independently of the distribution of the d4r inside the different structures. This computational study suggests that large pore zeolites that currently can be synthesized with germanosilicate composition only can be converted to silicate and aluminosilicate

variants by isomorphic substitution. These results open the door to future practical applications of a score of large pore zeolites with attractive pore structures. Energy estimations suggest the best procedure to be substitution of part of the Ge with silicon at high temperature in a first step, and substitution of the residual Ge with Al in a second step at lower temperature.

4. Construction of external surface and defect models of IM-12 zeolite

In the previous chapter, the thermodynamic study reflected that all silicogermanates have intrinsically stable (alumino)silicate analogues and can be stabilized by post-treatment substitutions. As a consequence, for our experimental study, we selected one candidate based on the literature work.

The IM-12 zeolite of UTL structural code was discovered at LMM Mulhouse in collaboration with IFPEN^[5]. It is formed by layers connected to each other through d4r. Thus, as seen in chapter 1, the stabilization of this zeolite motivated research works. The different applied post-treatments usually led to the formation of new structures like the COK-14^[9], IPC-2^[10], IPC-4^[10], IPC-6^[158], IPC-7^[158], IPC-9^[235] and IPC-10^[235]. To our knowledge, only Shamzy et al. obtained the aluminosilicate form of UTL, but the treatments led to a loss of the initial microporous volume from 0.21 to 0.14 cm³.g⁻¹ and the structure was just partially maintained^[151]. Hence, we aim to stabilize this silicogermanate having 14 and 12 MR (Figure 4- 1) and to transform it into its aluminosilicate analogue while maintaining the initial microporous volume and the crystallinity. Indeed, the large pore diameters are attractive for the catalytic transformation of bulky molecules.

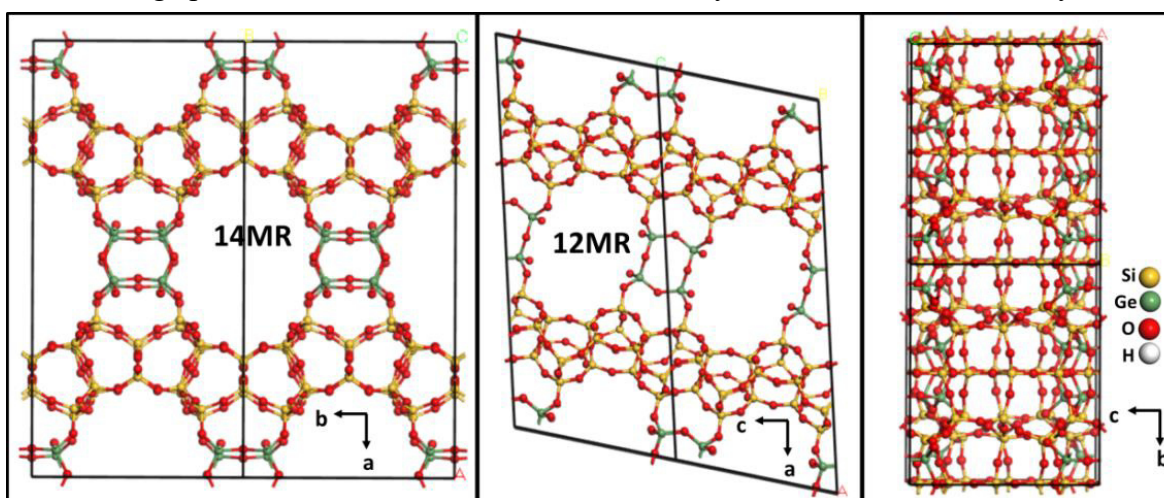


Figure 4- 1 : Representation of the 2D channel system of the UTL structure along the 3 orientations with a Si/Ge of 3.75. The (001) plane is perpendicular to the 14 MR, (010) to the 12 MR. There are no openings along (100).

To reach this goal, Ge should be substituted by Si or Al. The literature and our thermodynamic results confirmed the feasibility of these substitutions. However, an understanding of the preferential substitution positions (surface vs. bulk) of this zeolite is still lacking. In fact, the investigation of possible hydroxyl groups at the external surface of the IM-12 zeolite, and the comparison of their stability with respect to bulk hydroxyl groups could give indications about the

possible active sites in the substituted aluminosilicate form of this zeolite. Thus, studying the surface stability of this structure is the first step toward this understanding.

In this chapter, we will construct theoretical models of realistic external surfaces of the IM-12 zeolite. The stability of these surfaces will be calculated and compared. Their alumination will also be studied. At the end, the energies of substitution of Ge for Si or Al at some surfaces are calculated and compared to those of bulk substitutions.

4.1 Construction of the external surface models of IM-12

The bulk unit cell was obtained from the International Zeolite Association database in its pure siliceous form^[16]. It was then geometrically optimized using the procedure explained in section 2.3.4. IM-12 has two typical morphologies represented in Figure 4- 2 depending on the crystallization conditions: either superposed thin platelet-like crystals giving aggregates of 150x150x200 μm , or gypsum flower-type aggregates formed from more isolated sheets of 5x5 μm and a thickness about 350 nm. The connections between the layers of UTL lying in the (100) plane are assured by d4r units and form the 2D channel system of the UTL. Figure 4- 1 shows the 14 MR along (001), the 12 MR along (010) and no opening along (100). Thus we constructed different slabs by cleavages along (100), (010) and (001) surface orientations following the procedure of Rey et al.^[236] (for zeolite Beta) and Treps et al.^[237] (for H-ZSM-5).

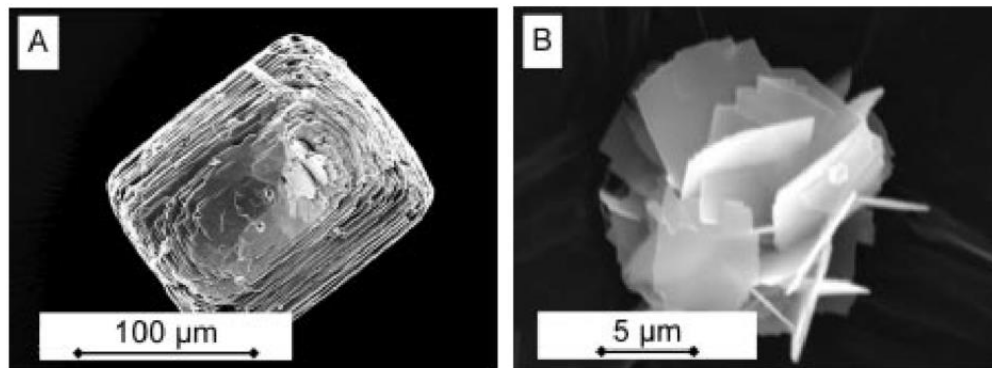


Figure 4- 2 : SEM pictures of IM-12 showing the two possible morphologies depending on the synthesis conditions: (A) static giving superposition of platelet-like crystals and (B) under stirring giving flower-type aggregates ^[5].

The slab is formed by multiplying the unit cell, then cleaving and adding a vacuum slab, so as to delimit a surface. The saturation of Si-O broken bonds was assured by adding dissociated water molecules: H atoms saturated monocoordinated O atoms and OH moieties saturated Si_{III} atoms (Figure 4- 3).

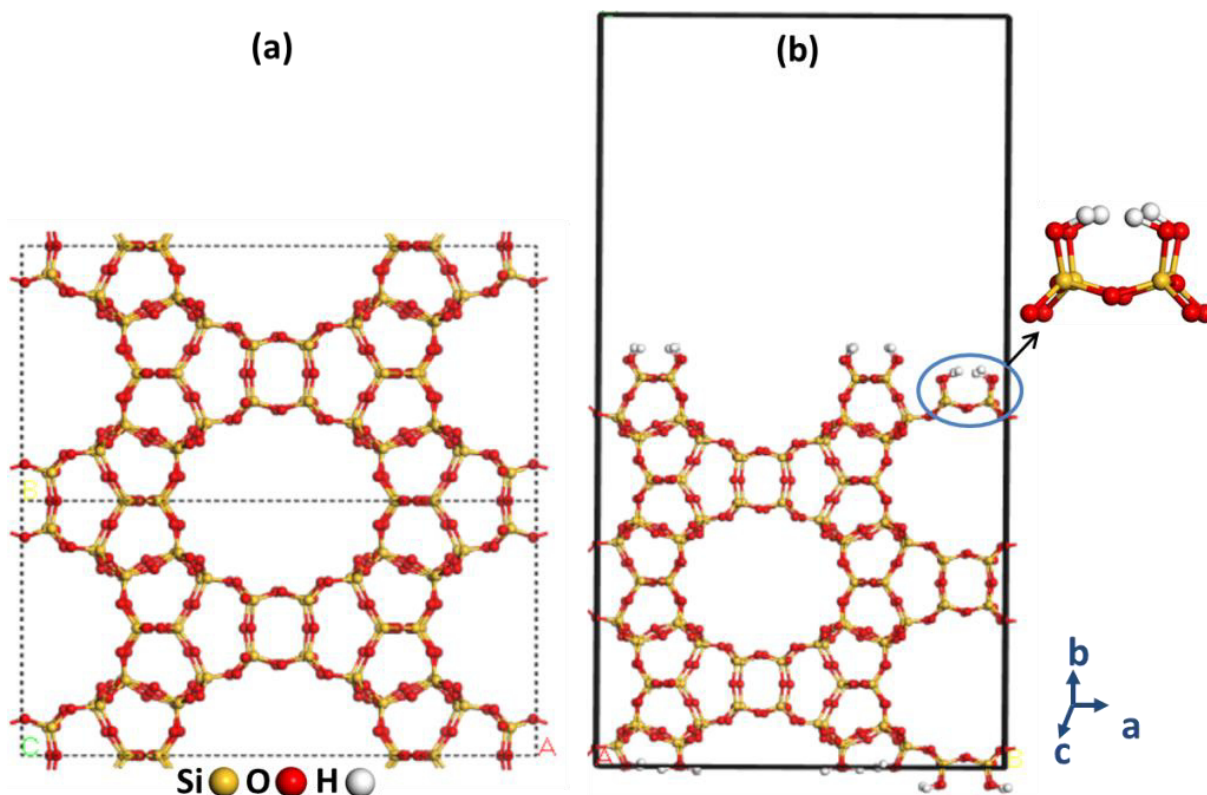


Figure 4- 3 : (a) Construction of the slab by multiplying the unit cell (represented by the dotted line). (b) adding vacuum to the cell. The zoom represent an example of surface hydroxyl. Example of a cleavage done in the (010) orientation.

Since Ge atoms tend to occupy d4r units, the presence of these units at the surface might be critical. Moreover further post treatments should lead to the incorporation of aluminum in these subunits. Thus, for each orientation, we cleaved at different heights. These heights were selected to describe various surface d4r configurations, see Figure 4- 4. For example, we represented surfaces with absence of these units, such as cleavage 2 along (100) and cleavage 1 along (001). Along (001), due to a more complex situation inherent to the tilted orientation with respect to the 12 MR and 14 MR pore systems, only one cleavage was tested with elimination of the d4r of the surface.

We also considered having a s4r at the surface, for example cleavage 3 along (100) and cleavages 1 and 2 along (010). Then we constructed models with d4r units at the surface like cleavage 1 along (100) and cleavage 3 along (010). Finally the upper and lower faces of the slabs were adjusted to be symmetrical. The resulted slabs are represented in Figure 4- 5 and in Figures S4-1 to 7.

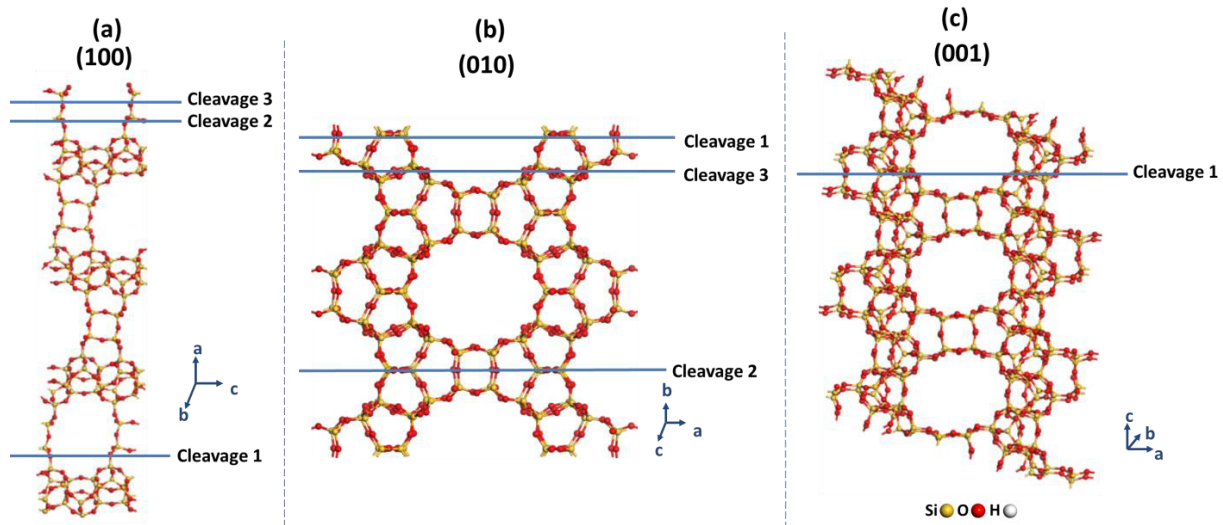


Figure 4- 4 : Different heights of cleavages along (100), (010) and (001) and orientations.

4.2 Stability of studied siliceous external surfaces

The stabilities of the obtained slabs (Figure 4- 5) were evaluated through their surface free energies γ_{surf} (mJ/m²) at the synthesis temperature of the zeolite (450K) and $P_{H_2O}=1$ bar following Eq. 4-1:

$$\gamma_{surf}(T, P_{H_2O}) = \frac{1}{2A} \left(G_{surf}(T, P_{H_2O}) - n_{H_2O} G_{H_2O}(T, P_{H_2O}) - n_{SiO_2} G_{SiO_2,bulk}(T, P_{H_2O}) \right)$$

Eq. 4- 1

With G_{surf} , G_{H_2O} and $G_{SiO_2,bulk}$ respectively the Gibbs free energy of the surface, of water and of one SiO_2 unit cell of the bulk IM-12 zeolite. n_{H_2O} and n_{SiO_2} are respectively the number of water molecules adsorbed on the surface and the number of SiO_2 units in the zeolite surface model. γ_{surf} is normalized to the energy per unit area by dividing by two the surface area A , since the cells used for the study have two similar surfaces, in the upper and lower faces.

The water is considered as an ideal gas and G_{H_2O} is calculated following 2.3.4 while the influence of temperature and pressure are neglected for solid phases meaning that G_{surf} and $G_{SiO_2,bulk}$ are equal to their corresponding electronic energies. γ_{surf} of the different cleavages are reported in Table 4- 1. These energies strongly depend of the amount of water molecules adsorbed on the surface (in the form of Si-OH pairs) and their number over the surface area is also presented in for each γ_{surf} . It is seen from Table 4- 1 that along (100), the difference in terms of stability between the various cleavages is small, and that cleavage 2, free from d4r on the surface is the most stable external surface for this orientation.

Along (010), three cleavages were studied. Cleavage 1 and 2 have s4r at the surface, while for cleavage 3, a d4r is present near the surface. Among the external surfaces with s4r, cleavage 2 is less stable. The reason could be related to the distribution of hydroxyl groups. Cleavage 3 is the less stable due to finite temperature effects, linked to the high OH group coverage, lowering the probability of having a d4r near the surface.

By comparing the surface free energies of the different cleavages, it is seen that (100) is the most stable orientation, followed by (001) and (010).

The equilibrium morphology predicted by the Gibbs-Curie-Wulff law^[238,239] was calculated from the surface free energies at the synthesis conditions, 450K and $P_{H_2O}=1$ bar with the Morphology module of Materials Studio (Dassault Systèmes). It predicts the fibrillar morphology represented in Figure 4- 5. Experimentally, the morphology is flatter than predicted, suggesting that the growth is controlled by kinetics rather than by thermodynamics, making the (100) surface dominate over all other orientations.

Table 4- 1: γ_{surf} (mJ/m²) at 450K and $P_{H_2O}=1$ bar of studied siliceous IM-12 external surfaces along (100), (010) and (001) orientations. θ_{H_2O}/A (nm⁻²) corresponds to the number of H₂O (in the form of Si–OH pairs) divided by the surface area.

Orientation	Cleavage	θ_{H_2O}/A (nm ⁻²)	ΔE_{Surf} (mJ/m ²)	γ_{Surf} (mJ/m ²)
(100)	1	2.33	45	192
	2		-1	146
	3		15	162
(010)	1	20.42	-133	1158
	2	32.08	39	1329
	3		-454	1573
(001)	1	2.98	9	197

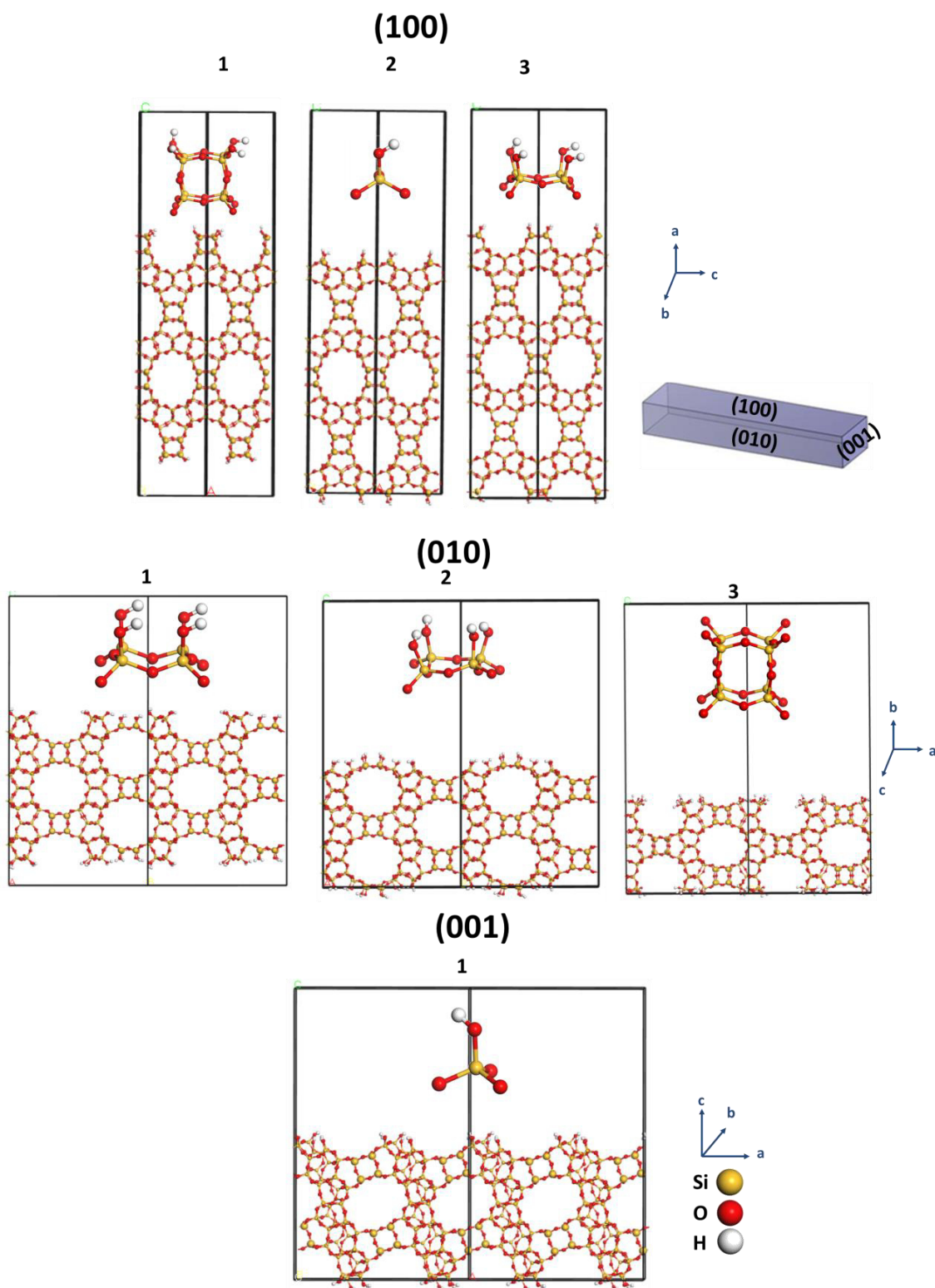


Figure 4- 5 : Different cleavages of IM-12 (UTL) external surfaces along (100), (010) and (001) orientations. The T sites of d4r configurations (d4r, s4r and none) are represented with bigger atoms. Only these d4r configurations at the surface are zoomed. Representation of the equilibrium morphology predicted by the Gibbs-Curie-Wulff law from the surface free energies calculated at 450 K and $P_{H_2O}=1$ bar. The enlarged regions correspond to the d4r, s4r and SiOH representations at the surface.

4.3 Stability of aluminosiliceous external surfaces

When the substitution energies of Si for Al were calculated in the bulk of IM-12, in chapter 3, only bridging Al-(OH)-Si were modeled. For each aluminum, the compensating proton can be added on the different four neighboring oxygen atoms giving four possibilities of bridging aluminols per Al. We studied the different possibilities, for aluminum occupying the full d4r and we found that the positions represented in Figure 4- 6 gave the most stable structure.

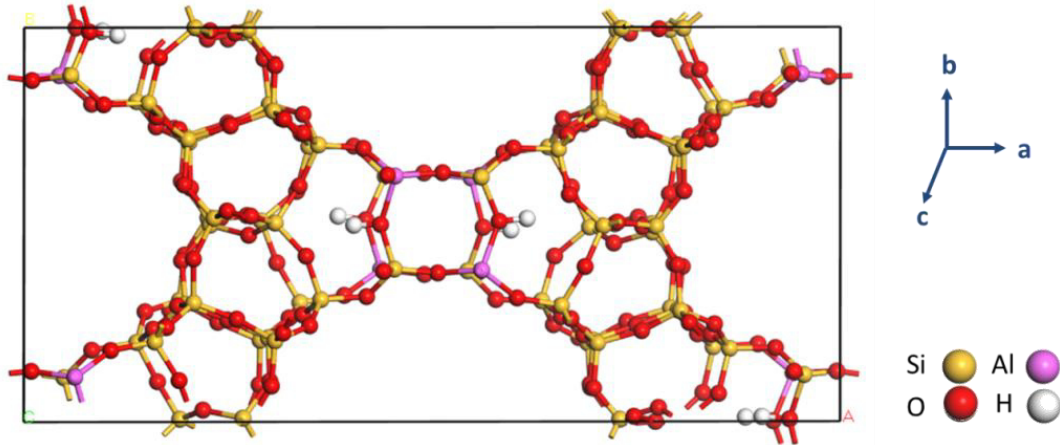


Figure 4- 6: Bulk of IM-12 (UTL) zeolite with Al occupying the full d4r in respect to the Löwenstein rule and with optimal bridging Al-(OH)-Si positions.

However, when Al is incorporated on the external surface through the substitution of surface SiOH (2 substitutions are performed each time, on the top and at the bottom of the slab, to keep it symmetric), this leads to additional types of aluminols, the compensating cation can be directly fixed on the existing OH group giving water molecules adsorbed on Aluminum: Al-(H₂O).

The energies of substitution of Si for Al in the external surface slabs using chloride molecules were calculated following Eq. 4- 2.

❖ Si → Al starting from the siliceous external surface:

$$\Delta E_{sub_{surf,Si \rightarrow Al}} = \frac{(E_{surf,SiAl} + 2E_{SiCl_4} - E_{surf,Si} - 2E_{AlCl_3} - 2E_{HCl})}{2}$$

Eq. 4- 2

With $E_{surf,SiAl}$ and $E_{surf,Si}$ the electronic energies of the aluminosiliceous and siliceous surface slabs respectively.

The aluminations were selectively studied for orientations having either s4r or d4r at the external surface, implying along (100)-cleavages 1/2 and along (010)-cleavages 1/3.

4.3.1 Substitution of Si for Al along (100)

In cleavage 1, since the d4r is exposed to the surface, depending on the Al position, the positions of the compensating cation can lead to Al-(H₂O), such as the Al2 with the compensation hydrogen in the position H4 and to 3 bridging Al-(OH)-Si in Figure 4- 7. On the contrary, if the Al is in

position Al1, the aluminols are limited to four bridging Al-(OH)-Si, Figure 4- 7. The energies of substitution of Si for Al in Table 4- 2 show that when Al occupies position 1, the hydrogen in position H1 is the most stable among the 4 possible bridging aluminols. However, if the Al is in position 2, the Al-(H₂O) is favored over the three remaining possible bridging aluminols. Moreover, by comparing between the different aluminum positions, the bridging aluminols of Al1 is more stable than the Al-(H₂O) of position Al2 (-26 vs. -16 kJ/mol). In classical aluminosilicates like beta and ZSM-5, Al-(H₂O) were always more stable than the bridging aluminols^[236,237]. The specificity of IM-12 might thus be related to the special effect of the d4r at the surface. It was shown for beta and H-ZSM-5 that Al-(H₂O) groups exhibit lower Brønsted acidity with respect to surface bridging OH groups. The presence of more stable bridging sites at the surface d4r of IM-12, may thus assure a high catalytic activity for the zeolite, even at the pore mouth.

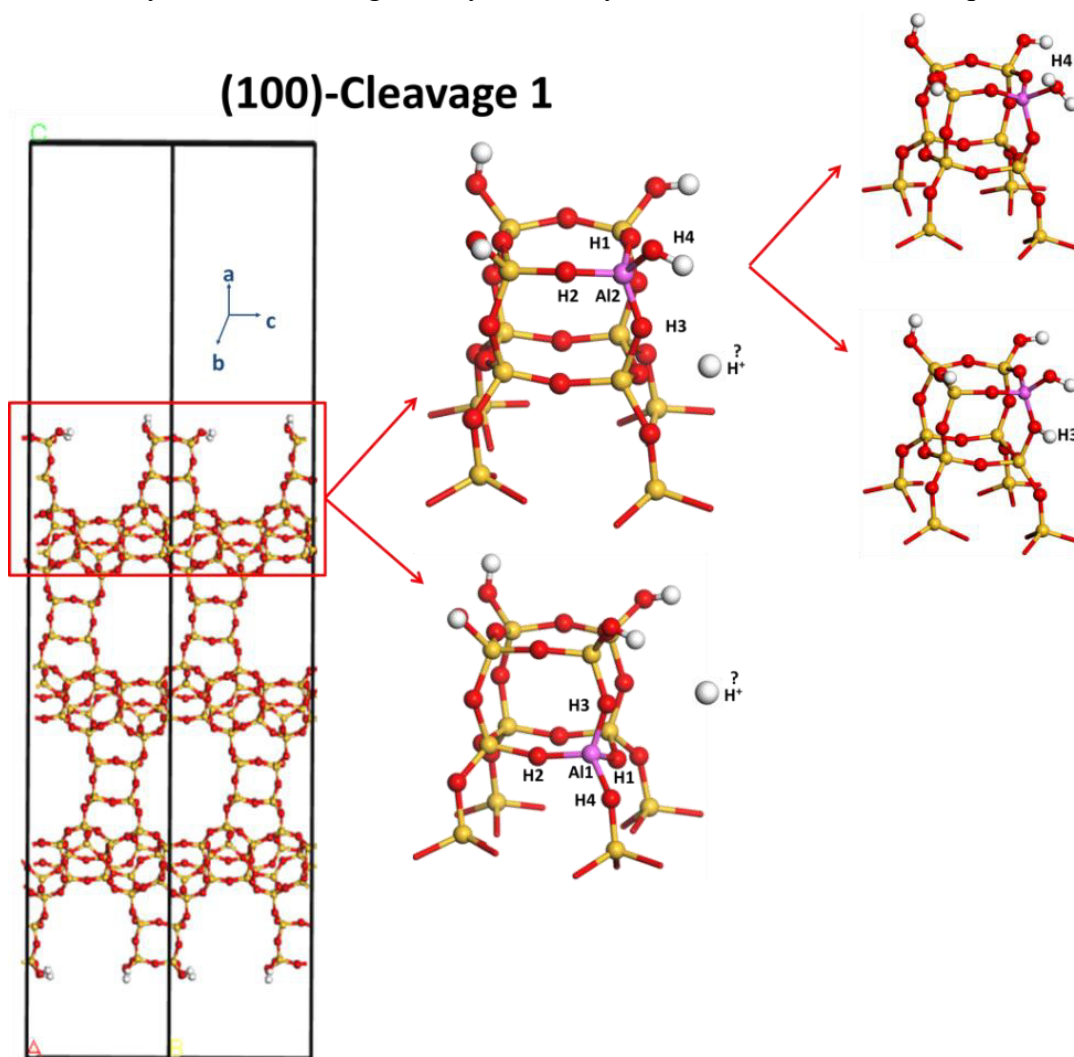


Figure 4- 7: Different aluminum positions along (100)-Cleavage 1, with enlargement of the d4r. H1,2,3,4 represent the possible positions that can be occupied by the compensating cation. H4 and H3 represent an Al-(H₂O) and a bridging Al-(OH)-Si respectively.

The aluminations in the s4r of cleavage 3 (Table 4- 2), where all the aluminum positions lead to the possibility of having 3 bridging Al-(OH)-Si and an Al-(H₂O), shows that for the same aluminum the Al-(H₂O) is favored over the bridging aluminols (-54 vs. -31 kJ/mol).

By comparing cleavage 1 and cleavage 3, the substitution of Si for Al is easier when a s4r is at the surface rather than a d4r (-54 vs. -26 kJ/mol).

Table 4- 2: Energies of substitution of Si for Al ($\Delta E_{\text{sub_Surf, Si}\rightarrow\text{Al}}$) and ($\Delta E_{\text{sub, Si}\rightarrow\text{Al}}$) (kJ/mol) using chloride molecules of IM-12 external surfaces along (100)-cleavages 1/3 and (010)-cleavages 1/3 and of bulk IM-12.

Structure	Al Position	Type of site	H Position	$\Delta E_{\text{sub_Surf, Si}\rightarrow\text{Al}}$ (kJ/mol)/T _{sub}
Bulk	Al (in d4r)	Al-(OH)-Si-	H1	-36
			H2	-34
			H3	-41
			H4	9
(100)-cleavage 1	Al1 (down of d4r)	Al-(OH)-Si-	H1	-26
			H2	-14
			H3	-17
			H4	3
	Al2 (top of d4r)	Al-(H ₂ O)	H1	-4
			H2	-5
			H3	0
			H4	-16
(100)-cleavage 3	Al (in s4r)	Al-(OH)-Si-	H1	-11
			H2	-31
			H3	-5
		Al-(H ₂ O)	H4	-54
(010)-cleavage 1	Al (in s4r)	Al-(OH)-Si-	H	1
		Al-(H ₂ O)	H	-50
(010)-cleavage 3	Al (top of d4r)	Al-(OH)-Si-	H1	-9
			H2	-5
			H3	-19
			H4	-2

4.3.2 Substitution of Si for Al along (010)

Cleavage 1 having a s4r at the external surface, confirms again that when the Al position allows the compensation cation to form the two types of aluminols: bridging Al-(OH)-Si or Al-(H₂O), the latter is always preferential (-50 vs. 1 kJ/mol). For cleavage 3 possessing a d4r near the surface, where only bridging hydroxyls can be formed, position H3 led to the easier aluminations (Figure 4- 8, Table 4- 2).

Among the two different cleavages along (010), cleavage 1 having the s4r at the external surface is more favorable for the aluminations than cleavage 3, where the d4r is near the surface. These results are in agreement with those of substitution along (100).

Moreover, almost all of the studied substitutions gave negative energies reflecting that the obtained aluminosiliceous slabs are more stable than their siliceous analogues.

The difference of the energies of substitution between the bulk and the different cleavages in Table 4- 2, do not exceed 13 kJ/mol reflecting no preferential substitution between the bulk and the surface of this IM-12 zeolite.

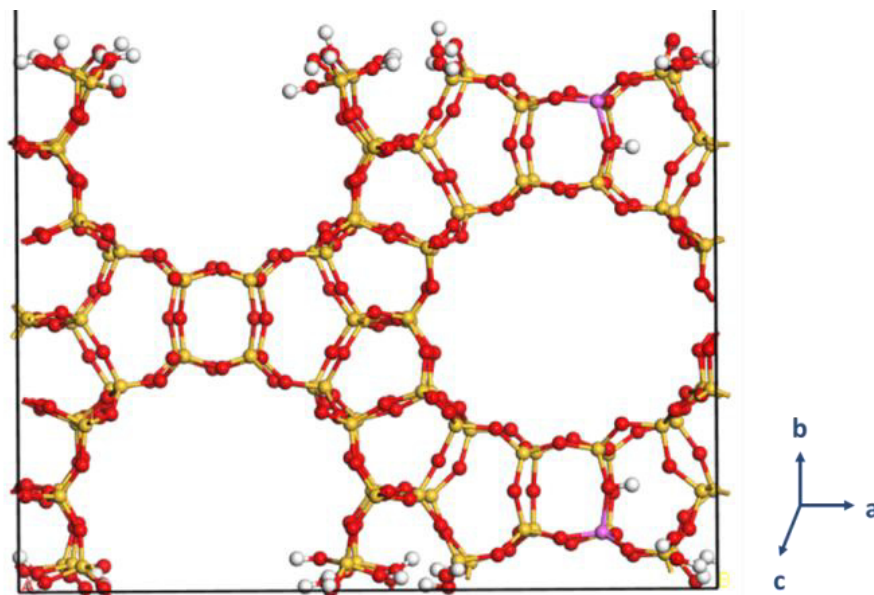


Figure 4- 8: Surface model of the (010)-cleavage 3 showing the most stable position of the compensating cation, H3.

4.4 Dehydration of external surfaces

Almost all the characterization and catalytic testing of zeolites are made at high temperatures, leading to the possible dehydration of Al-(H₂O) sites of the external surface. To represent these dehydrations, the dehydration free energies were calculated at 425K and P_{H₂O}= 10⁻⁴ bar (catalytic test conditions). The translational and rotational degrees of freedom of the gaseous water molecule were considered while that of the zeolitic solid systems were neglected. When the water desorbs, an Al^{III} is formed, however, in some cases, the Al tend to maintain its coordination number constant and makes a bonding with a neighboring oxygen atom giving a 2MR such as in cleavage 3 along (100), see Figure 4- 9. This was also encountered for beta and MFI zeolites^[236,237]. For dehydration along (100)-cleavage 1 and (010)-cleavage 1, the neighboring oxygen was not close enough to form a 2MR and the Al^{III} was formed. The dehydration Gibbs free energies are calculated following Eq. 4- 3.

$$\Delta G_{dehydration}(T, P_{H_2O}) = \frac{(E_{surf,SiAl,dehydrated}(T, P_{H_2O}) + 2G_{H_2O}(T, P_{H_2O}) - E_{surf,SiAl}(T, P_{H_2O}))}{2}$$

Eq. 4- 3

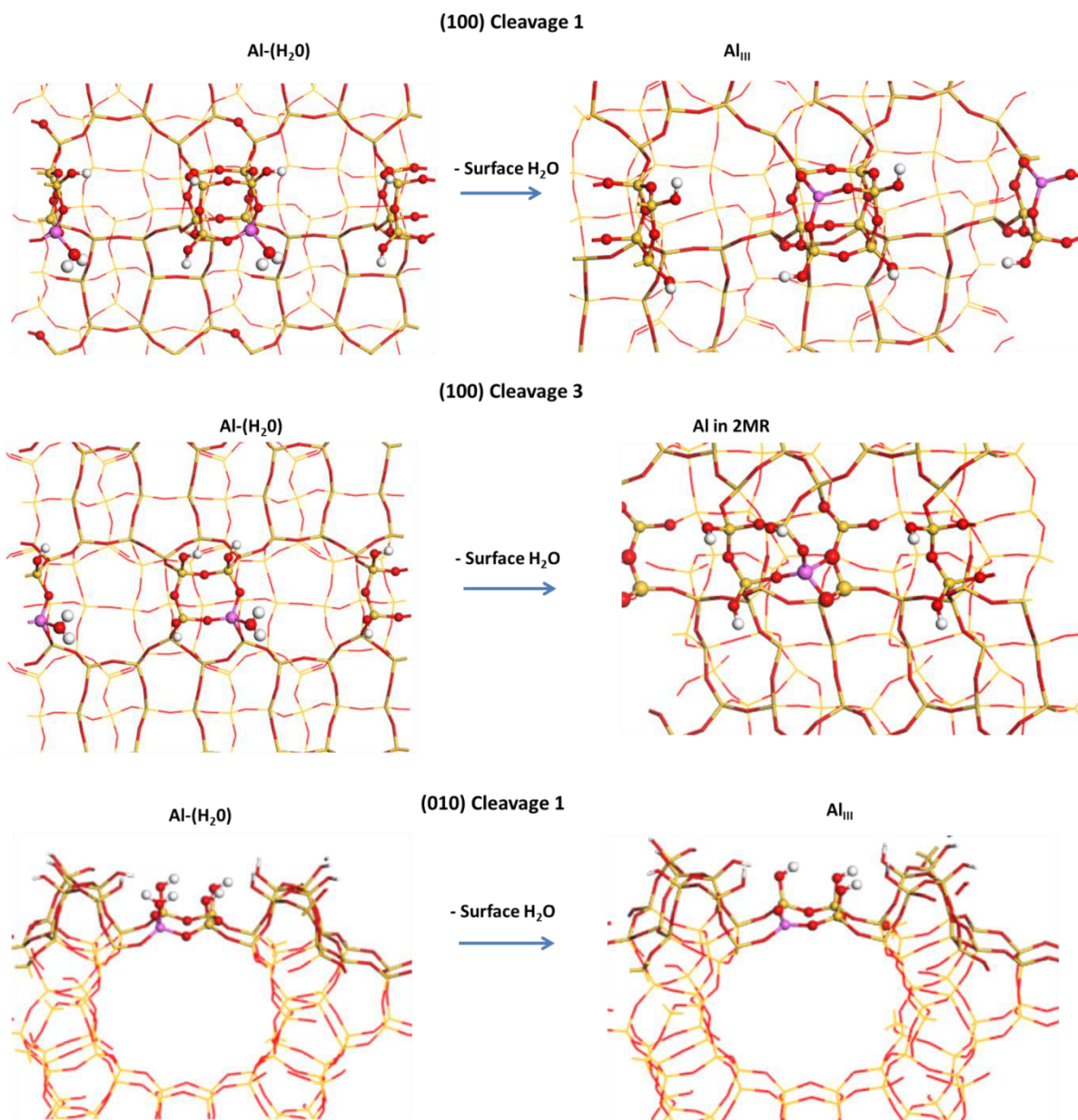


Figure 4- 9: Surface dehydration of Al-(H₂O) along (100) cleavage 1 and 3 and (010) cleavage 1 giving tricoordinated Al, tetracoordinated Al in 2MR and tricoordinated Al respectively.

Figure 4- 10 shows that all the free enthalpy values are positive. This means that under the studied conditions, the sites remain hydrated. Moreover, the s4r is the least capable of dehydrating while the sites with or without d4r are the most capable of generating dehydrated sites, possibly being Lewis sites. It can be attributed to two things: (i) for cleavage 3, an Al^{IV} could have formed instead of an Al^{III}, which is a stabilizing factor, (ii) in the s4r, the OH before dehydration (including the water molecule) are interacting with each other which is a stabilizing factor of the hydrated state, therefore disfavor the desorption of water. For the d4r this is not the case, the OH point towards opposite directions, so no H bond exists, so dehydration is easier, even if we do not generate an Al^{IV}.

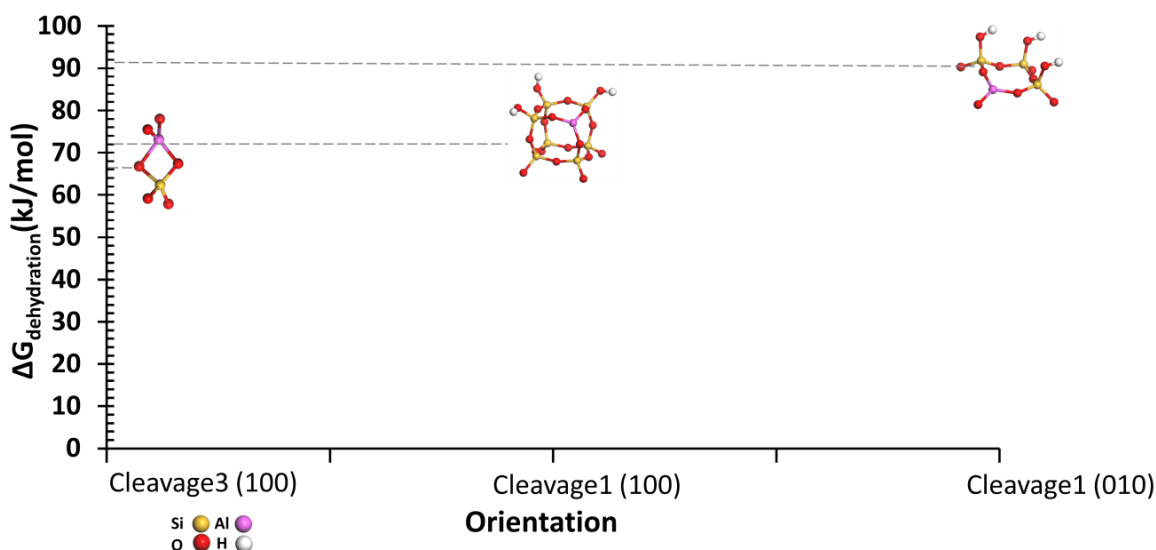


Figure 4- 10: Representation of the dehydration Gibbs free energy and of the Al coordination along (100) cleavage 1/3 and along (010) cleavage 1.

4.5 Thermodynamic substitution of Ge for Si and Al

As mentioned earlier, one of our goals is to study the possibility of substitution of Ge for Si and Al on the external surfaces of the zeolite and to compare them with those of the bulk substitutions, to have an estimation of the preferred localization of the substitution.

Following section 2.3.4 and 3.3, the substitution energies of Ge for Si and Al in the bulk of IM-12 zeolite (UTL) are resumed in Figure 4- 11.

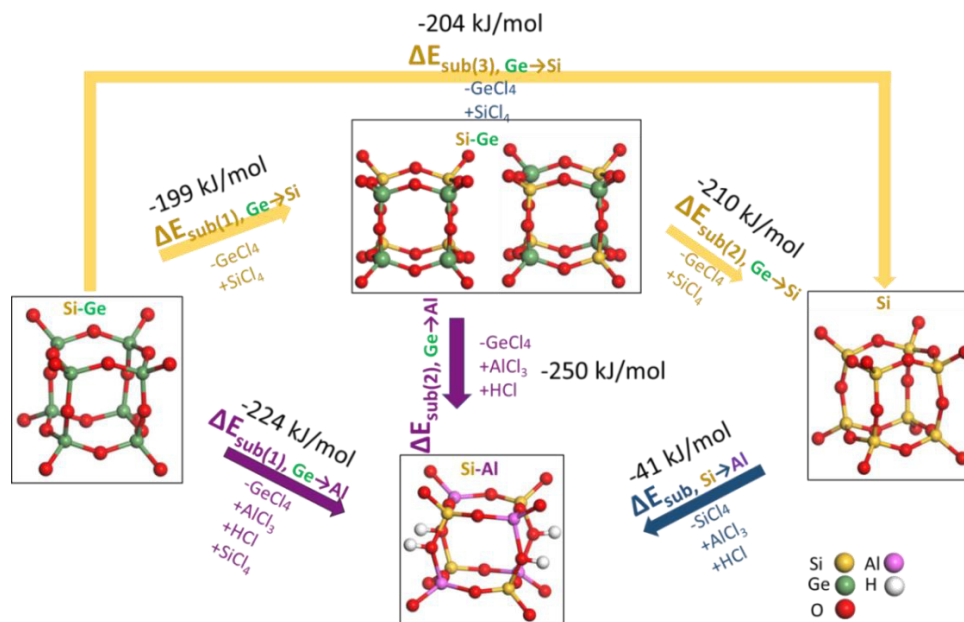


Figure 4- 11: Substitution energies of Ge for Si and Al using chlorides of the bulk of IM-12 (UTL) zeolite. The d4r part of the structures are only shown, the other parts of the structure (with T sites occupied by Si) are omitted for clarity purpose.

Concerning the external surfaces, Cleavage 1 along (010) gives one of the most favorable surfaces for the alumination ($\Delta E_{\text{sub_Surf, Si} \rightarrow \text{Al}}$ (kJ/mol)/ T_{sub} in Table 4- 2) thus was selected for this study. Departing from a silicogermanate (having 1Ge) along (010)-cleavage 1 we calculated the energies of substitutions of Ge for Si and Al giving silicate, aluminosilicate and aluminosilicogermanate. For the aluminosilicate form, one bridging Al-(OH)-Si and one Al-(H₂O) were considered. For the aluminosilicogermanate form, two bridging Al-(OH)-Si, with the proton between the Al-(OH)-Si or the Al-(OH)-Ge and one Al-(H₂O) were studied.

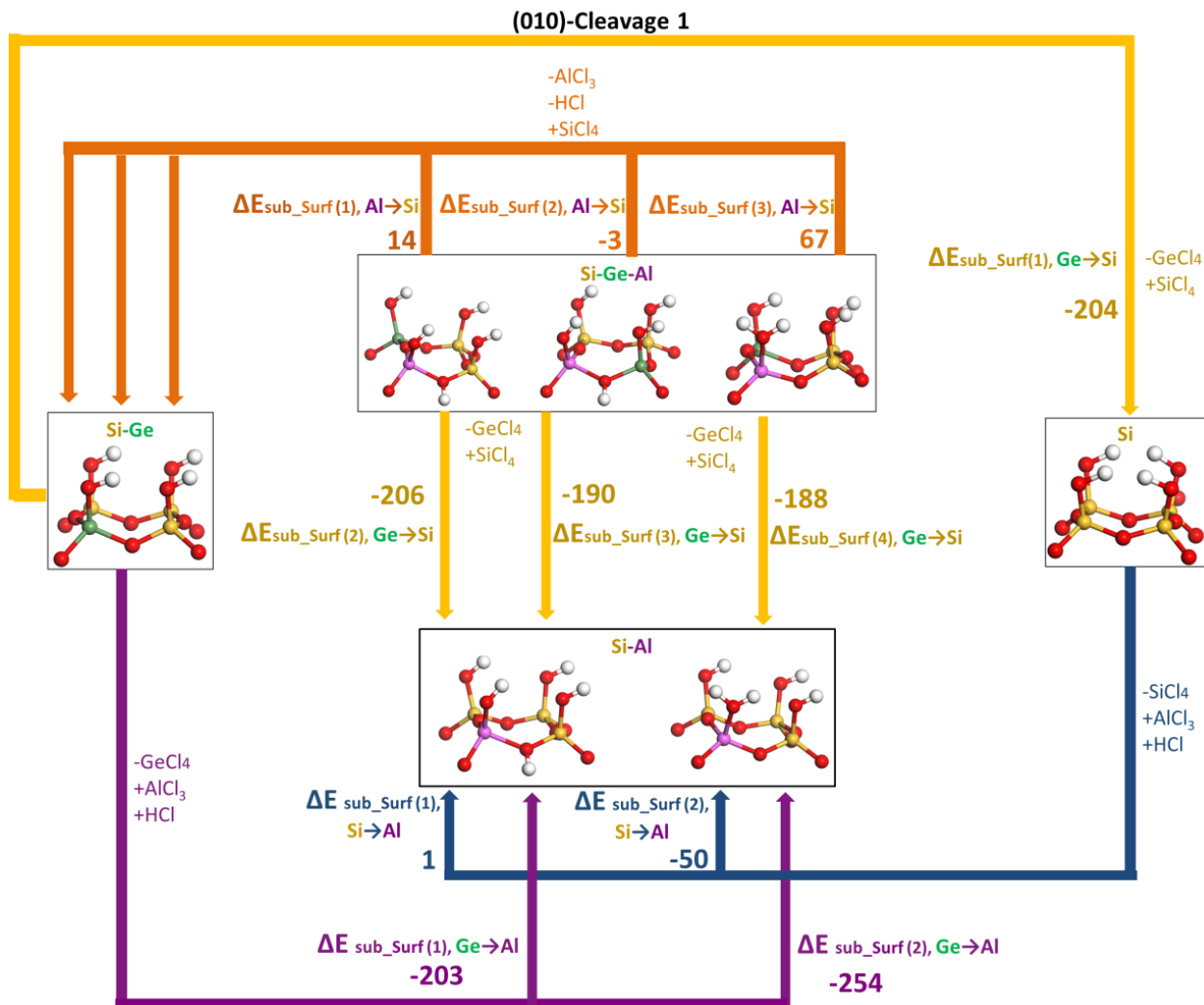


Figure 4- 12: Substitution energies of Ge for Si and Al using chlorides of the bulk on the external surface of IM-12 zeolite along (010)-Cleavage 1. The s4r part of the external surfaces are only shown, the other parts of the structure (with T sites occupied by Si) are omitted for clarity purpose.

The various substitution energies are calculated following these equations:

❖ Ge → Si:

$$\Delta E_{sub_surf(1),Ge \rightarrow Si} = E_{surf,Si} + E_{GeCl_4} - E_{surf,SiGe} - E_{SiCl_4}$$

Eq. 4- 4

$$\Delta E_{sub_surf(2,3,4),Ge \rightarrow Si} = E_{surf,SiAl} + E_{GeCl_4} - E_{surf,SiGeAl} - E_{SiCl_4}$$

Eq. 4- 5

❖ Ge → Al:

$$\Delta E_{sub_surf(1,2),Ge \rightarrow Al} = E_{surf,SiAl} + E_{GeCl_4} - E_{surf,SiGe} - E_{AlCl_3} - E_{HCl}$$

Eq. 4- 6

❖ Si → Al:

$$\Delta E_{sub_surf(1,2),Si \rightarrow Al} = E_{surf,SiAl} + E_{SiCl_4} - E_{surf,Si} - E_{AlCl_3} - E_{HCl}$$

Eq. 4- 7

❖ Al → Si:

$$\Delta E_{sub_surf(1,2,3),Al \rightarrow Si} = E_{surf,SiGe} + E_{AlCl_3} + E_{HCl} - E_{surf,SiGeAl} - E_{SiCl_4}$$

Eq. 4- 8

The energies of substitution are represented in Figure 4- 12. The energies of substitution of Ge for Si are around 200 kJ/mol. For the aluminosilicogermanate, this substitution is easier when the compensating cation is not on the oxygen neighboring the Ge (-206 vs. -190 and -188 kJ/mol). The substitution energies of Ge for Si are almost equal at the external surface and in the bulk.

The energies of substitution of Ge for Al show that the formation of the Al-(H₂O) is preferred over the formation of the bridging Al-(OH)-Si. Again, these energies are so close to those of substitution in the bulk. It is also seen that substitution of Si for Al is easier when an Al-(H₂O) is formed giving a value equal to that of substitution in the bulk (-50 kJ/mol). Finally, it is seen that in the case of aluminosilicogermanate, the substitution of Al for Si is not possible meaning that thermodynamically only the substitution of Ge for Si is possible for this elemental composition.

One can say that thermodynamically, there is no clear preference for the substitution of Ge by Si/Al between the external surface and the bulk of the IM-12.

4.6 Conclusion

The study of different surface cleavages of UTL zeolite along (100), (010) and (001) shows that (100) is the most stable surface. This might justify why the layers of the UTL structure are stacked perpendicular to this direction. The alumination of these surfaces is thermodynamically possible. Alumination forming Al-H₂O are favorable over those giving bridging Si-OH-Al on most

orientations, but not on all possible external surface orientations. Finally, the dehydration at the surface is disfavored for the studied slabs, especially in the case of slabs exposing s4r due to the hydrogen interactions of the hydroxyl groups.

5. Experimental Stabilization of the IM-12 zeolite

In the previous chapters, the thermodynamic study reflected that all silicogermanates have intrinsically stable (alumino)silicate analogues and can be stabilized by post-treatment substitutions. As a consequence, for our experimental study, we selected one candidate based on topological considerations and on the literature work: ‘IM-12 zeolite’. This zeolite usually leads to creation of new structures or partially loses its structure during the post-treatments. Thus, we aim to stabilize this silicogermanate having 14 and 12 MR and to transform it into its aluminosilicate analogue while maintaining the initial microporous volume and the cristallinity.

To reach this goal, the Si/Ge ratio of the structure should be increased in order to reduce the possibility of having structure collapse by the hydrolysis of the Ge-O bonds and to enhance the possibility of respecting the Löwenstein rule. Based on the literature and on our thermodynamic results, Ge can be substituted by Si or Al in the bulk and at the surface of IM-12 zeolite. Substitutions of Ge for Si or Al were always made in aqueous phase using tetraethyl orthosilicate^[7,153], ammonium hexafluorosilicate^[6], polyaluminum chloride solution^[150], aluminum nitrate solution^[154], etc. Since the simple exposure to humidity can cause the hydrolysis of Ge-O bonds on the calcined sample, working in dry gaseous phase may reduce this risk. In our thermodynamic study in chapters 3 and 4, it was proved that substitutions in gaseous phase are feasible, moreover substitutions using chlorides such as silicon tetrachloride and aluminum trichloride were favorable over hydroxides. Experimentally, such an approach has never undertaken the stabilization of silicogermanates in mild conditions however, a silicon tetrachloride treatment in gaseous form was used for the dealumination of aluminosilicates^[190–193].

In our case, the IM-12 zeolite is free from Al, but Ge-O-Ge bonds are likely to exist: thus, we need to incorporate Al and Si. If we consider incorporating aluminum as a first step, the thermodynamic calculations showed that substitution of Ge for Si is favorable to Al for Si (average $\Delta E_{\text{sub, Si} \rightarrow \text{Al}}$ per T substituted atom is -38 kJ/mol while that of $\Delta E_{\text{sub, Ge} \rightarrow \text{Al}}$ is -248 kJ/mol). And if we decide to start with the SiCl₄ treatment, we may favor the second alumination step by increasing the possibility of respecting the Löwenstein rule. Indeed, operating conditions should be optimized to find a good compromise since not all Ge have to be replaced by Si to leave some sites available for Al substitution. As a consequence, it should be possible to combine SiCl₄ and aluminum chloride treatments. We use the mild SiCl₄ treatment for the first time with the aim of substitution of Ge for Si which can allow the stabilization of silicogermanates^[194]. The SiCl₄ treatment unit (2.1.4.1).

The incorporation of Al in silicogermanates plays a double role: increasing the stability of the structure by substituting Ge and inducing the presence of compensation cations such as H⁺. In this work, we have tested two protocols for the incorporation of Al, in gaseous or in aqueous phase

using chlorides: polyaluminum chloride (PAC) solution following the work of Gao et al.^[150] or aluminum chloride (AlCl₃).

In this chapter, we will present the different optimization procedures for the synthesis of IM-12 silicogermanate, the post-treatments with SiCl₄, PAC and AlCl₃ and the physicochemical characterization of the obtained materials.

5.1 Synthesis of the IM-12 zeolite

IM-12 was prepared following the hydrothermal synthesis described in 2.1.2. Different batches were prepared. In the manuscript, the as prepared samples will be indexed with a.p while, for calcined samples only their name will be indicated. The first prepared sample called IM-12_{i,a,p} presented an impurity: the XRD pattern in Figure 5- 1, reveals the UTL structure with some additional peaks of an unidentified phase (peaks with asterisks) and small amounts of another phase, probably the SSZ-31. We suspect that the peaks with asterisks are attributed to crystallized germanium dioxide. The analysis of the source of GeO₂ (bought as amorphous GeO₂) used for this synthesis confirm the presence of crystallized GeO₂. By changing the GeO₂ source with a really amorphous one we have obtained a pure IM-12 sample referred as IM-12_{a,p} (Figure 5- 2) having a Si/Ge molar ratio of 5 and a microporous volume after calcination of 0.21 cm³/g (Figure 5- 3). However we found, that after acid washing of the as prepared IM-12_{i,a,p} sample with HNO₃ (1M) at ambient temperature, peaks attributed to UTL remained unchanged while that of the undesired phase highly decreased (Figure 5- 1). Moreover, the N₂ physisorption indicates a slight increase of the microporous volume from 0.144 to 0.149 cm³/g and an increase of the BET surface area from 431 to 452 m²/g after the acid washing (Figure 5- 2). XRF analysis indicates an increase of the Si/Ge molar ratio from 5 to 7 after the washing. These results suggest that the impurities were outside the pores and the germanium dioxide impurities were eliminated after the washing. Note that in the literature ^[5,134], the microporous volume of IM-12 varies from 0.11 to 0.26 cm³/g.

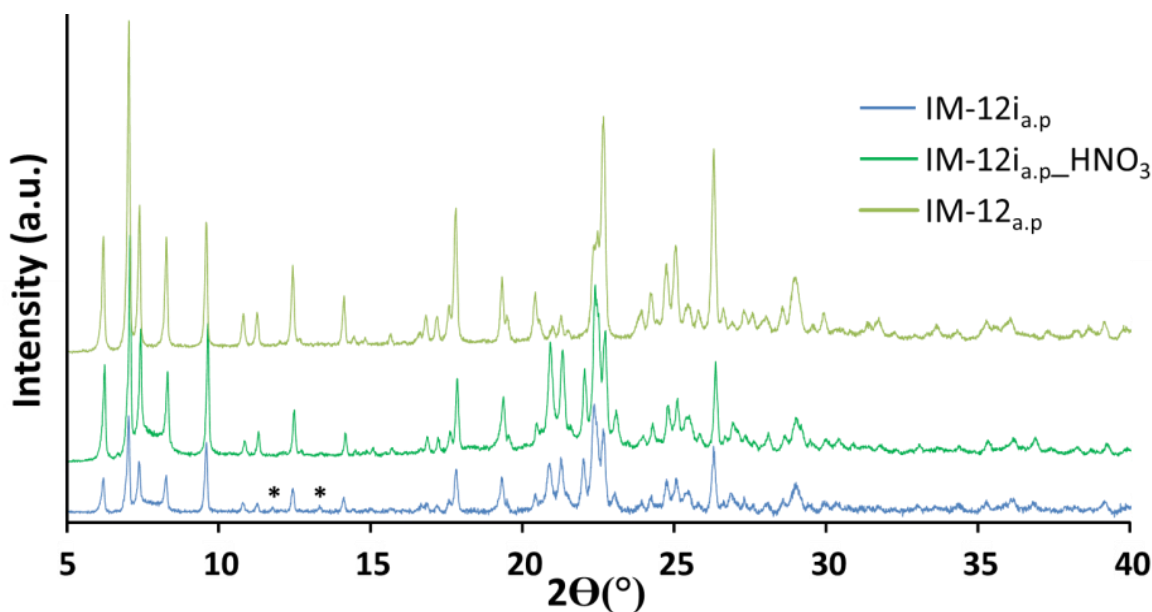


Figure 5- 1: XRD patterns of IM-12_{i,a.p}, IM-12_{i,a.p} washed with HNO₃ and as prepared IM-12_{a.p}. The index a.p refers to ‘as prepared’.

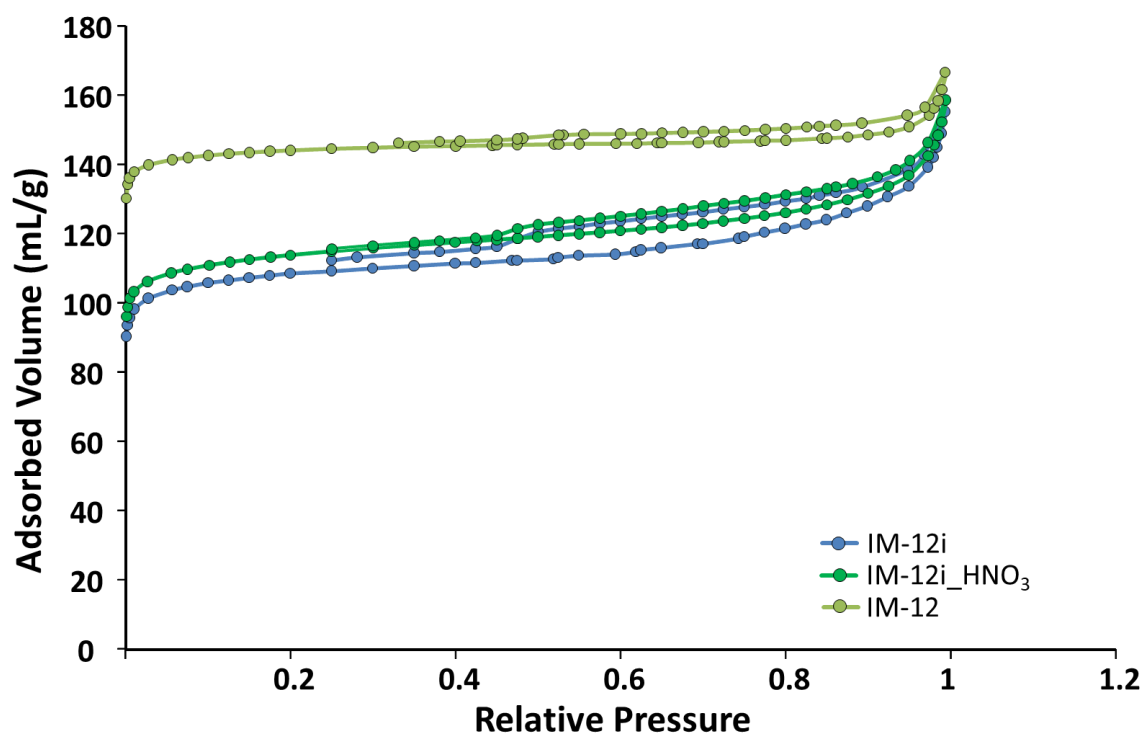


Figure 5- 2: N₂ physisorption isotherm of calcined IM-12_i, calcined IM-12_i washed with HNO₃ and calcined IM-12.

In Figure 5- 3, SEM images of the as prepared IM-12_i, IM-12_i washed with HNO₃ and IM-12 show the typical platelet-like morphology characteristic of IM-12 zeolite^[5]. All samples presented both superposed platelets and aggregated platelets. The average sheet size is 7x6 μm and the average

thickness is 350 nm. Figure 5- 3 also shows that acid washing had no effect on the morphology of IM-12i.

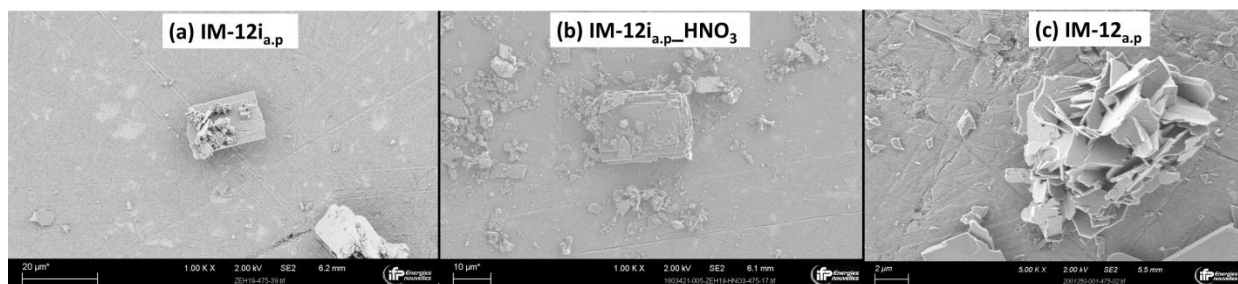


Figure 5- 3: SEM images of IM-12_{i,a,p}, IM-12_{i,a,p} washed with HNO₃ and IM-12_{a,p}. The index a.p refers to as prepared.

Both samples, IM-12_{i,a,p} washed with HNO₃ and IM-12_{a,p} were used for the optimization of the post-treatment procedure, while only IM-12 was used for the preparation of the catalysts.

5.2 Post-treatment optimization

The degree of Si/Ge or Al/Ge substitution depends on different parameters such as the form of the initial sample: as prepared or calcined, the order of substitution (starting with Al or Si treatment), the treatment temperature and amount of Si for the silicon tetrachloride treatment, the duration and the number of treatments using the polyaluminum chloride solution and the trichloride aluminum dissolved in dry ethanol. In the present section, we study the effect of these parameters to select the most appropriate ones.

5.2.1 Optimization of calcination / Si substitution / Al substitution sequence

5.2.1.1 Substitution on the as prepared IM-12

In general, after contact with humidity the structure of calcined silicogermanates collapses completely or partially. The substitution in the presence of the organic structure directing agent (OSDA) could avoid this collapse. This possibility is exemplified by the treatment of an as prepared BEC type zeolite using a polyaluminum chloride solution (PAC)^[150]. This treatment allowed the substitution of Ge for Al and the stabilization of the structure.

To stabilize the IM-12 zeolite following this method, we have treated an as prepared IM-12 with a PAC solution (IM-12_{a,p}_1PAC). The XRD patterns in Figure 5- 4 reveal that after the treatment, the UTL structure was maintained. To check if this treatment stabilized the zeolite, the treated sample was calcined then washed with water (IM-12_{a,p}_1PAC_cal_H₂O wash). As seen in Figure 5- 4, after water washing the structure became highly amorphous. The same amorphization was detected when the as prepared IM-12 was treated with SiCl₄ (S5-Figure 1 in appendix 4) to substitute Ge for Si. This could indicate that the positioning of the structure directing agent inside

the pores of IM-12 blocks the accessibility to the Ge sites and prevent their substitution, justifying their sensitivity to hydrolysis after calcination.

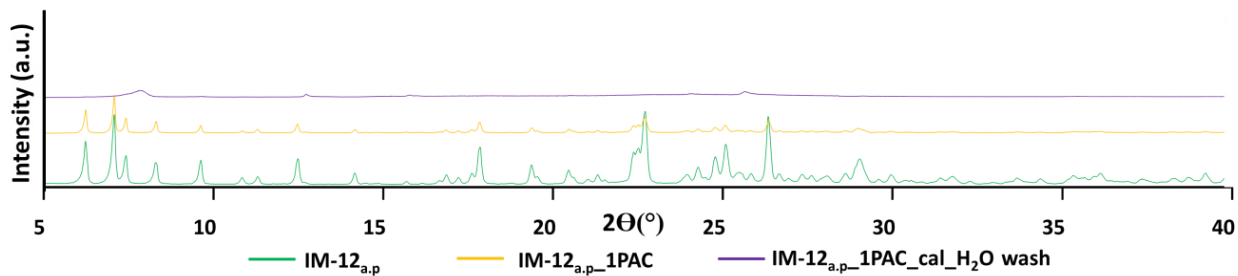


Figure 5- 4 : XRD patterns of as prepared IM-12, as prepared IM-12 treated with PAC and as prepared IM-12 treated with PAC then calcined and washed with water.

A solution for this OSDA localization problem could be the treatment after its removal from the pores through calcination of the zeolite.

5.2.1.2 Substitution on the calcined IM-12

When the calcined IM-12 was treated with PAC solution (IM-12_1PAC), the structure collapsed (Figure 5- 5) due to the hydrolysis of the Ge-O bond.

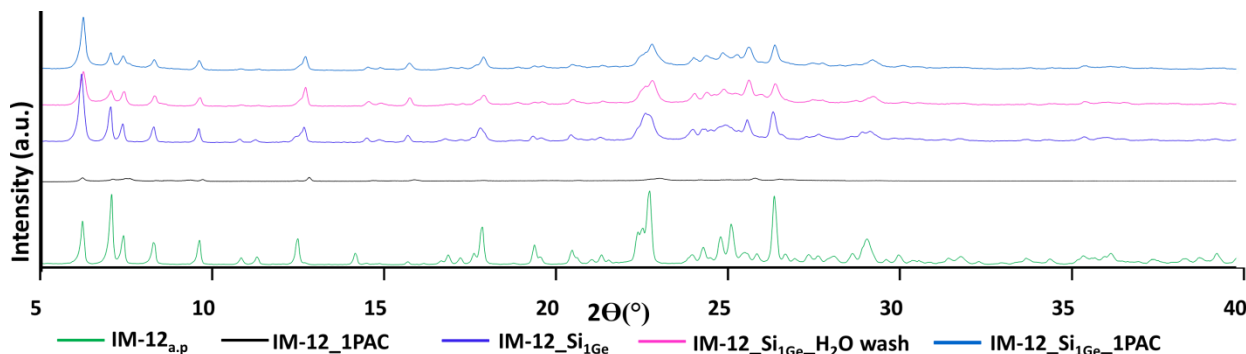


Figure 5- 5 : XRD patterns of as prepared IM-12, calcined IM-12 treated with PAC, calcined IM-12 treated SiCl₄, calcined IM-12 treated SiCl₄ then washed with water and calcined IM-12 treated SiCl₄ then PAC.

Meanwhile, if the calcined zeolite is treated first using SiCl₄ in gaseous phase (IM-12_Si_{1Ge}), the initial structure is maintained, even after water washing (IM-12_Si_{1Ge}_H₂O wash). This is also reflected through the light decrease of the initial microporous volume from 0.21 in the calcined IM-12 to 0.19 cm³/g after the SiCl₄ treatment and to 0.17 cm³/g after water washing (Figure 5- 6). The substitution of Ge for Si is also confirmed by the XRF measurements revealing the increase of the Si/Ge molar ratio from 5 to 10 (Table 5- 1).

The latter zeolite was further treated with the PAC solution to try to incorporate Al in the framework (IM-12_Si_{1Ge}_1PAC). The XRD pattern and N₂ physisorption indicate the conservation

of the UTL structure (Figure 5- 5, Figure 5- 6) with a microporous volume of 0.17 cm³/g. XRF proves the incorporation of Al with a Si/Ge molar ratio of 37 and a Si/Al ratio of 17 (Table 5- 1).

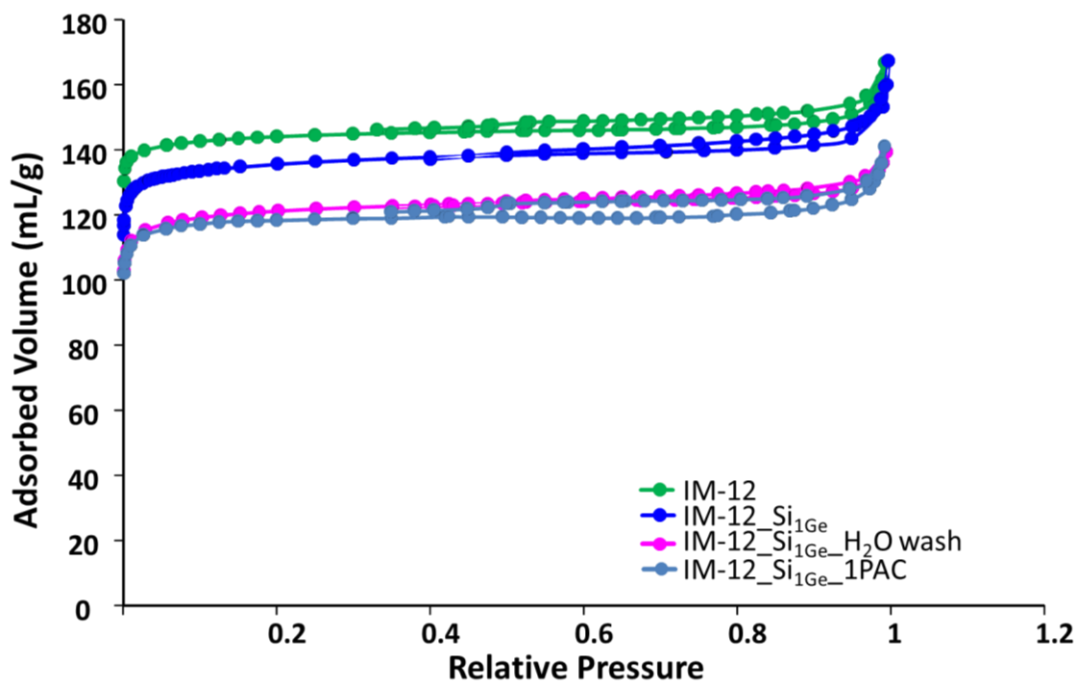


Figure 5- 6 : N₂ Physisorption of the calcined IM-12 and the stable post-treated samples: calcined IM-12 treated with PAC, calcined IM-12 treated SiCl₄, calcined IM-12 treated SiCl₄ then washed with water and calcined IM-12 treated SiCl₄ then PAC.

Table 5- 1 : N₂ physisorption and XRF results of the calcined IM-12 and the stable post-treated samples: calcined IM-12 treated with SiCl₄ and calcined IM-12 treated with SiCl₄ then PAC.

Sample	XRF			N ₂ physisorption		
	Si/Ge (mol)	Si/Al (mol)	(Si+Ge)/Al (mol)	S _{BET} (m ² /g)	Volume at P/P0=0.99 (mL/g)	Microporous Volume (mL/g)
Calcined IM-12	5	-	-	592	0.26	0.21
IM-12 Si ₁ Ge	10	-	-	553	0.26	0.19
IM-12 Si ₁ Ge 1PAC	37	17	17	485	0.22	0.17

Hence the optimum conditions are treating a calcined IM-12 using SiCl₄ followed by a PAC treatment. The next step is then to optimize the conditions of the SiCl₄ treatment.

5.2.2 Optimization of the SiCl₄ treatment

In this section, IM-12i washed with HNO₃ was used for the optimization. The SiCl₄ treatment unit is represented in 2.1.4.1. As deduced from the previous paragraph, the starting material corresponds to the calcined zeolite. The optimization of number of moles of SiCl₄ ($n_{Si} = n_{Ge}$; $2 n_{Ge}$; $3 n_{Ge}$ and $10 n_{Ge}$) and the treatment temperature (room temperature, 250 and 550°C) was then undertaken.

5.2.2.1 Number of moles of Si

To choose the required number of moles of SiCl_4 for the optimal substitution of Ge, we calculated the total amount of Ge present in the zeolite by considering that Ge occupies all the d4r corners. Then we treated the samples with SiCl_4 of equal, double, triple and 10 times this amount. The temperature of treatment was fixed at 550°C and all the samples were calcined *in situ* before the treatments.

XRD patterns (Figure 5- 7) show that in general the initial structure of IM-12i_HNO_3 was maintained for all calcined samples treated with SiCl_4 ($\text{IM-12i_HNO}_3\text{-Si}_{n\text{Ge}}$). For $n_{\text{Si}} < 3n_{\text{Ge}}$, the peak marked with an asterisk in the washed IM-12 was completely divided into two peaks meanwhile at $3n_{\text{Ge}}$ it was split. This split is usually detected after the calcination of IM-12 zeolite^[5]. In addition, no pattern difference between samples treated with $n_{\text{Si}} = 3n_{\text{Ge}}$ and $n_{\text{Si}} = 10 n_{\text{Ge}}$ was detected. Note that the peak marked with an arrow is one of the peaks reflecting the appearance of another phase after the treatment (the SSZ-31 zeolite (*STO) is expected)^[16], however this is not seen for the pure IM-12, and the samples obtained after post-treatment of pure IM-12 (that will be presented in the following). Thus we did not do further investigation for this phase.

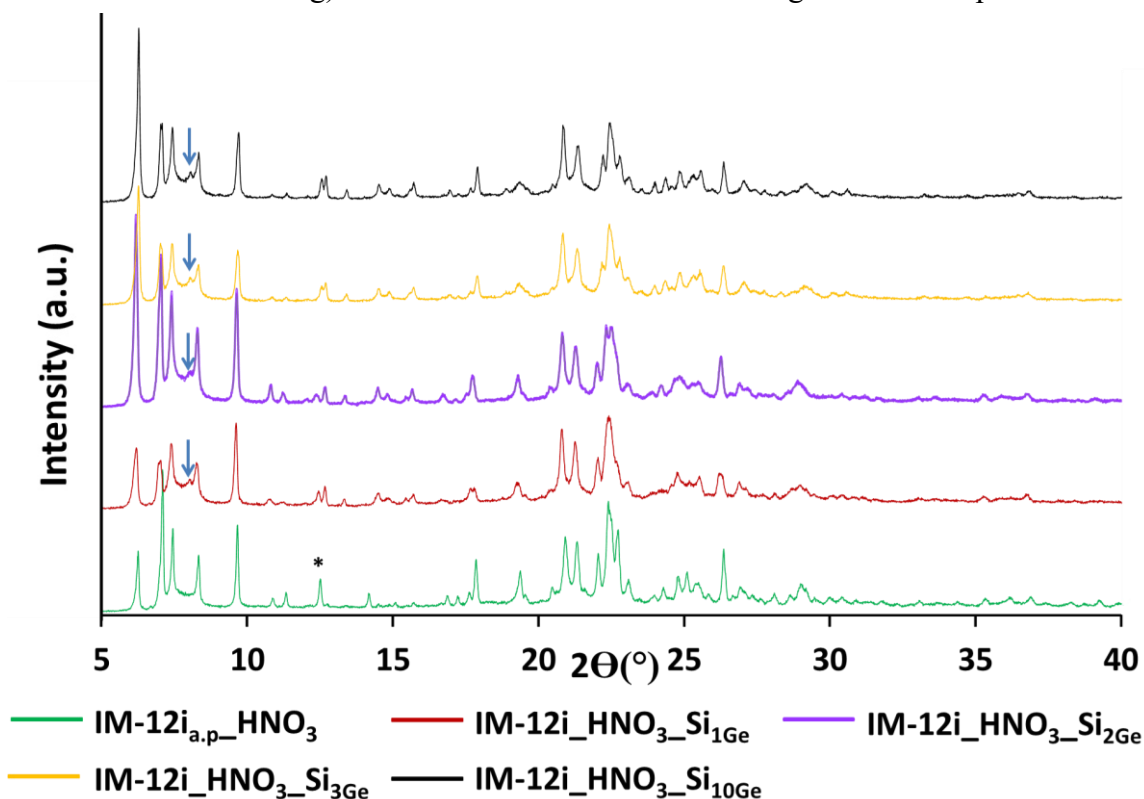


Figure 5- 7 : XRD patterns of as prepared IM-12i_HNO_3 and calcined samples treated with varied amounts of SiCl_4 . * represents the splitting peak and the arrow indicates the presence of SSZ-31 zeolite. a.p means as prepared.

N₂ physisorption indicates that in all cases, the initial BET surface decreased and that treating the sample with $n_{\text{Si}} = 3n_{\text{Ge}}$ is the best compromise (Figure 5- 8 and Table 5- 2) where the loss in microporous and BET surface are the lowest.

Moreover, the XRF results in Table 5- 2, highlights that increasing the amount of SiCl₄, increases the amount of substitution of Ge for Si. The Si/Ge molar ratio increased from 7 (before SiCl₄ treatment) to 8 after the SiCl₄ treatment with $n_{\text{Si}} = 2n_{\text{Ge}}$ then to 16 after SiCl₄ treatment with $n_{\text{Si}} = 3n_{\text{Ge}}$. With further increase of SiCl₄ amounts ($n_{\text{Si}} = 10 n_{\text{Ge}}$), no change in the Si/Ge molar ratio is detected indicating that the maximum yield for substitution is reached with $n_{\text{Si}} = 3n_{\text{Ge}}$.

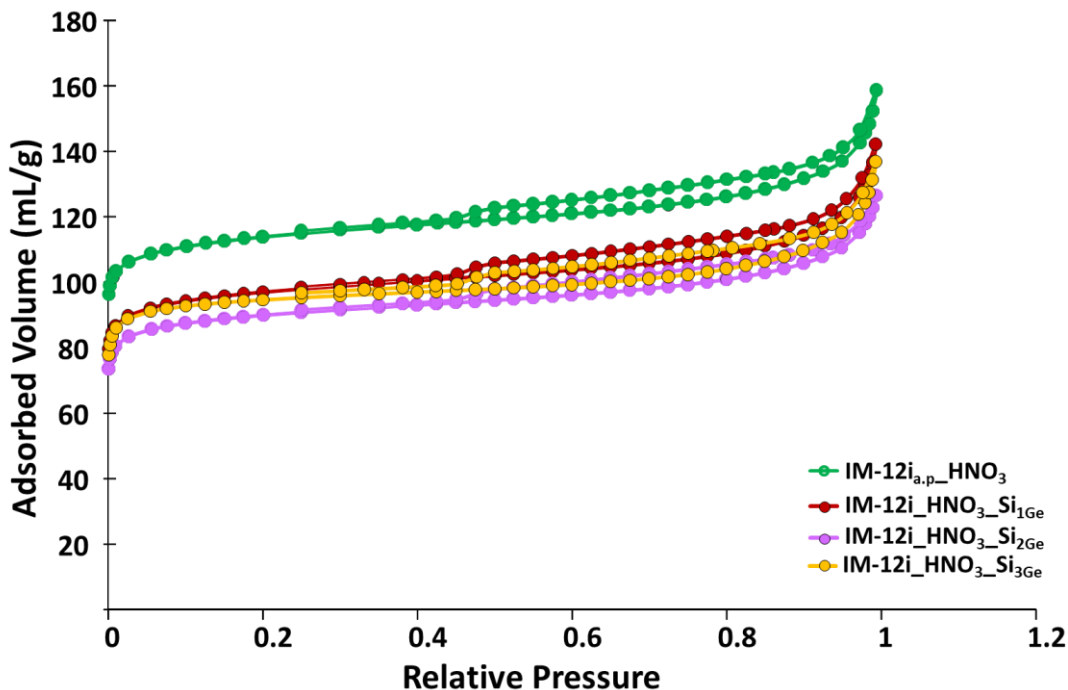


Figure 5- 8 : N₂ physisorption of calcined samples treated with varied amounts of SiCl₄. a.p means as prepared.

Table 5- 2: N₂ physisorption and XRF results of calcined IM-12i_HNO₃ and samples treated with variable amounts of SiCl₄.

Sample	N ₂ physisorption			XRF
	S _{BET} (m ² /g)	Volume at P/P0 =0.99 (mL/g)	Microporous Volume (mL/g)	Si/Ge (mol)
IM-12i_HNO ₃	452	0.245	0.149	7
IM-12i_HNO ₃ _Si ₁ Ge	383	0.220	0.125	7
IM-12i_HNO ₃ _Si ₂ Ge	356	0.195	0.116	8
IM-12i_HNO ₃ _Si ₃ Ge	379	0.211	0.129	16
IM-12i_HNO ₃ _Si ₁₀ Ge	355	0.218	0.126	16

SEM images reflect that treating samples with SiCl_4 do not affect the morphology and the size of the platelets (Figure 5- 9) .

Thus combining the results of the different characterization techniques suggests that the optimum amount of SiCl_4 for IM-12 treatment at 550°C is equal to the triple amount of maximum theoretical Ge present in the zeolite.

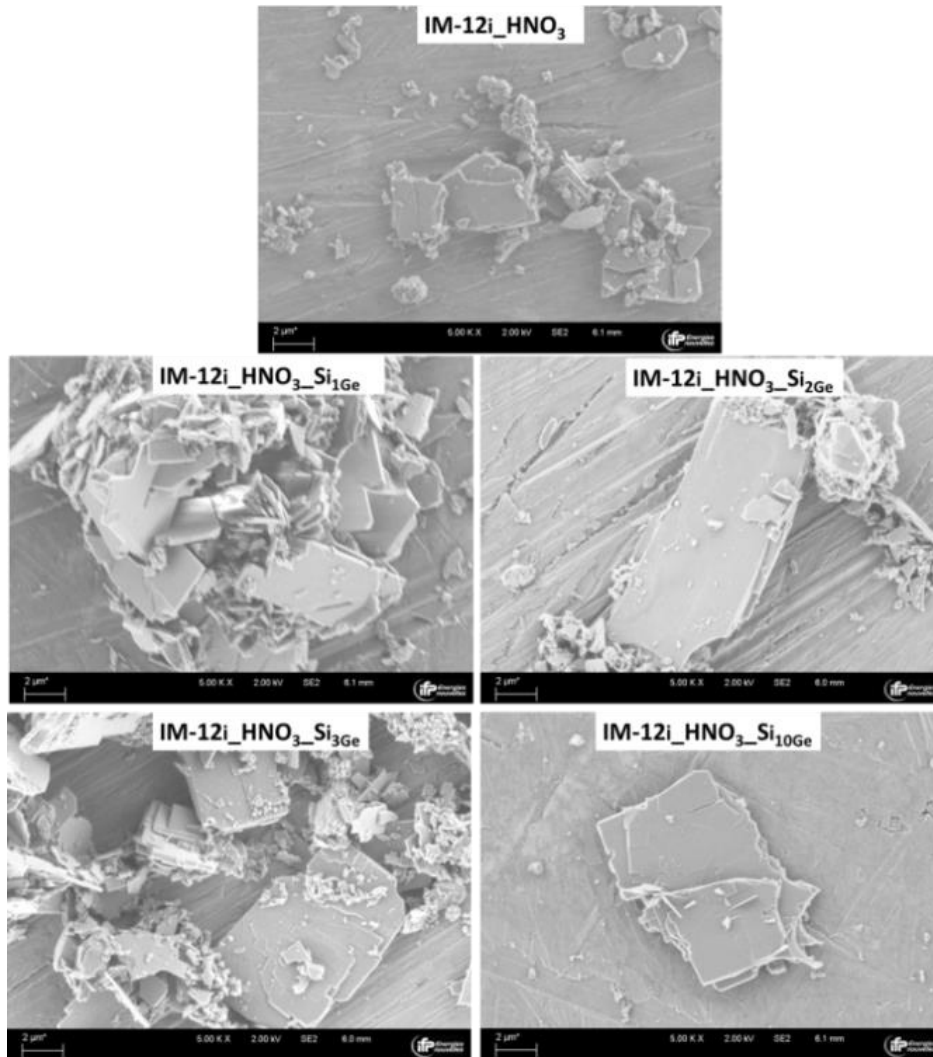


Figure 5- 9: SEM images of as prepared IM-12i_HNO₃ and of calcined samples treated with varied amounts of SiCl₄.

5.2.2.2 SiCl₄ treatment temperature

To check the possibility of the substitution reaction at different temperatures we calculated the substitution Gibbs free energy for temperatures varying from 25°C to 727°C at $P = 0.33$ bar for SiCl_4 and 0.1 bar for GeCl_4 (their vapor pressures respectively at 20°C) by DFT following 2.3.4 and Eq. 3-12/Figure 3- 6. The results are presented in Figure 5- 10. In this temperature range, the

difference of $\Delta G_{\text{sub Ge} \rightarrow \text{Si}}$ per Ge using SiCl_4 is only about 25 kJ/mol, and it remains negative. This points up that treatment at room temperature is thermodynamically feasible. Since the substitution becomes easier by increasing the temperature, we treated the samples at three different temperatures: room temperature, 250°C and at the calcination temperature (550°C). All IM-12i_ HNO_3 samples were calcined *in situ* then treated with SiCl_4 ($n_{\text{Si}} = 3n_{\text{Ge}}$), giving samples IM-12i_ HNO_3 _ $\text{Si}_{n\text{Ge}}$ _ $\text{Temperature}^\circ\text{C}$.

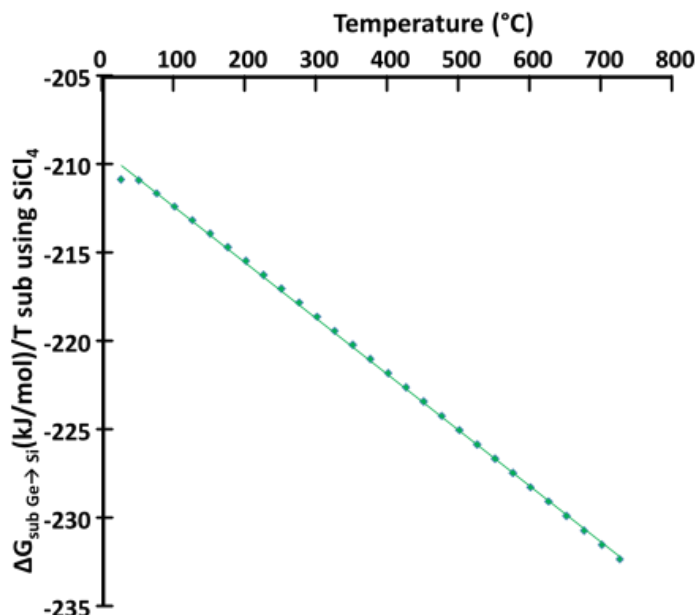


Figure 5- 10: Variation of $\Delta G_{\text{sub Ge} \rightarrow \text{Si}}$ (kJ) per T substituted atom using SiCl_4 at different temperatures, according to DFT.

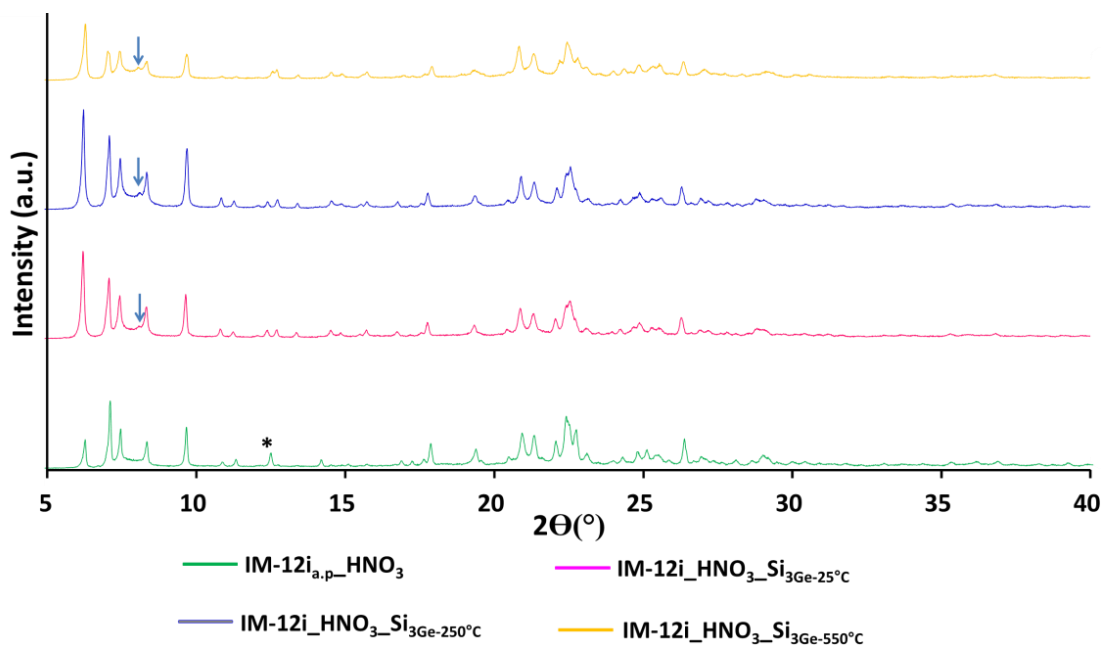


Figure 5- 11: XRD patterns of samples treated at different temperatures.* represents the splitting peak and the arrow indicates the presence of SSZ-31 zeolite. a.p means as prepared.

XRD patterns (Figure 5- 11) show that the initial structure of IM-12 was maintained at different SiCl_4 temperature treatments. At room temperature and 250°C , the peak marked with an asterisk in the washed IM-12i was completely divided into two peaks while it was split at 550°C . This could mean that high temperatures might facilitate the condensation of defects. As mentioned earlier, the peak marked with an arrow is one of the peaks reflecting the appearance of another phase after the treatment that was not detected after treating the initially pure IM-12.

As a consequence, we decided to treat the samples at 550°C having less deformations.

The SiCl_4 treatment has thus been optimized as follows: treatment of the *in situ* calcined sample at 550°C with an amount of SiCl_4 preferentially equal to $3n_{\text{Ge}}$. We do not exclude considering samples for $n(\text{Si}) = 1$ or $2 n(\text{Ge})$ as it is important to know whether a maximal number of Si is wished or not to get a solid that contains significant amount of Al.

5.2.3 Optimization of Polyaluminum chloride (PAC) treatment

Since IM-12 silicogermanates are stable after the SiCl_4 treatment, it is now possible to try the substitution of the remaining Ge with Al^{3+} in order to provide a positive charge responsible of the zeolite reactivity. This was first performed by treating the samples using aqueous PAC solutions. The experimental protocol is described in 2.1.4.2.1.

To optimize this treatment, different parameters have been studied: effect of n_{Si} amount during the substitution of Ge for Si on the following Al incorporation, duration and number of treatments. The temperature of the treatment and the solid: liquid ratio were fixed following the work of Gao et al^[150].

5.2.3.1 Number of moles of Si

To check if the amount of Si used for the substitution of Ge for Si can affect the incorporation of Al, samples previously treated with $n_{\text{Si}} = 1, 2$ and $3n_{\text{Ge}}$ at 550°C were treated using PAC solutions and a solid to liquid ratio of 1:50 at 80°C for 6h. The obtained samples are noted IM-12i_HNO₃_Si_{nGe}_1PAC.

XRD patterns (Figure 5- 12) show that the structure of all the samples treated with SiCl_4 did not collapse after the PAC treatments in aqueous conditions. In addition, for sample treated with $n_{\text{Si}} = 3n_{\text{Ge}}$, the split peak was completely restored after substitution with Al, indicating that Al might fill the possible defects.

N_2 physisorption (Figure 5- 13 and Table 5- 3) not only highlights that PAC treatment of sample with $n_{\text{SiCl}_4} = 3n_{\text{Ge}}$ allowed almost the recovery of the initial microporous volume with a small decrease of BET surface area compared to the parent zeolite (452 vs 434 m^2/g), but it also shows that after PAC treatments, all samples have higher S_{BET} and microporous volumes compared to

samples treated with SiCl_4 . This indicates that this aqueous treatment can extract simultaneously some deposits that are blocking the microporosity of zeolites.

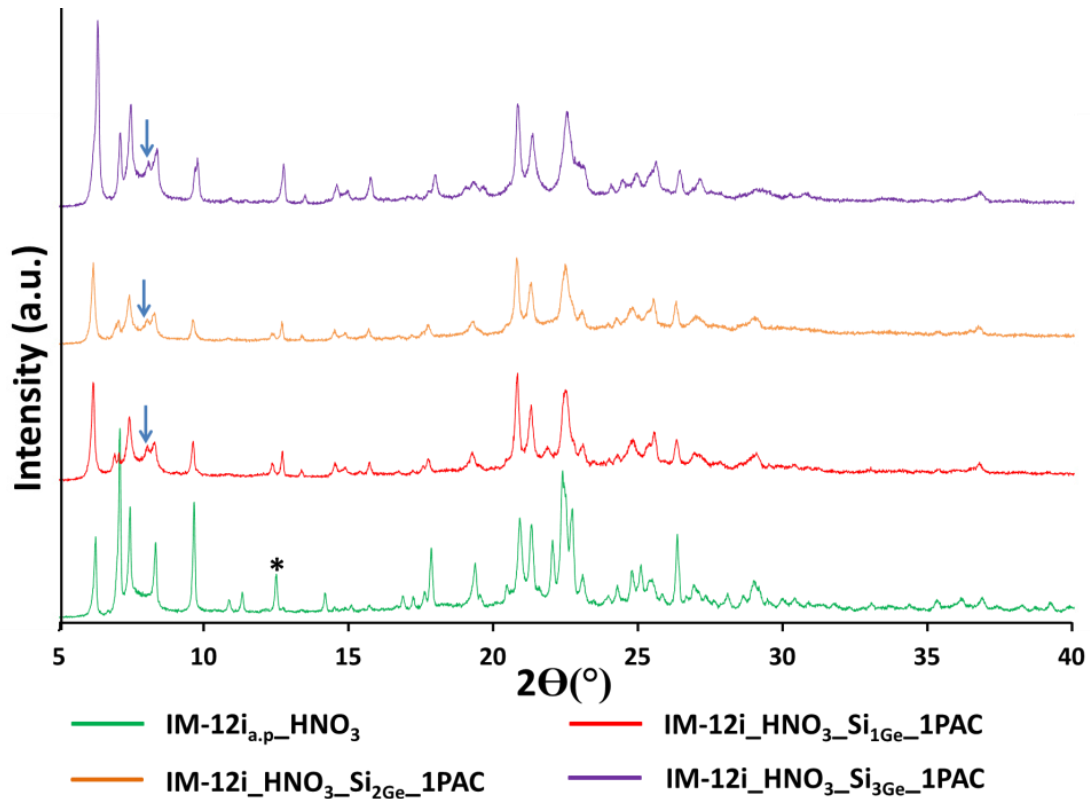


Figure 5- 12 : XRD patterns of samples revealing the n_{SiCl_4} effect on the PAC treatment. * represents the splitting peak and the arrow indicates the possible presence of SSZ-31 zeolite. a.p means as prepared.

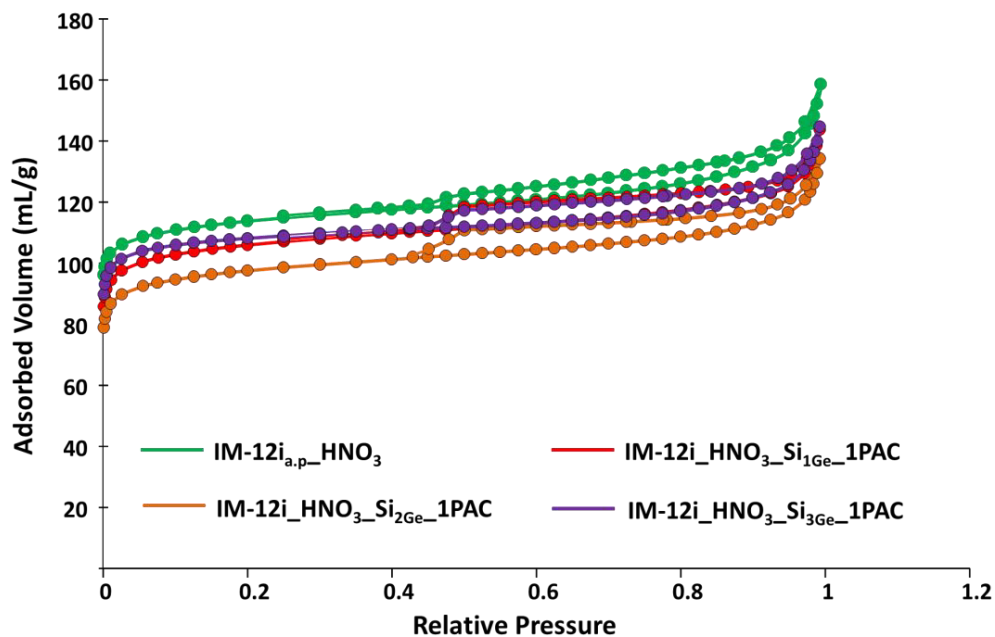


Figure 5- 13 : N_2 isotherms of samples revealing the n_{SiCl_4} effect on the PAC treatment. a.p means as prepared.

XRF results (Table 5- 3) point up that Al is present in the samples. The sample starting with $n_{Si} = 3n_{Ge}$ have the highest Si/Ge and Si/Al molar ratio and also the highest microporous volume, suggesting that extraframework Al probably did not block partially the pores compared to samples treated with $n_{Si} = 1$ and $2 n_{Ge}$.

Table 5- 3: XRF and N₂ physisorption of samples revealing the n_{SiCl_4} effect on the PAC treatment.

Sample	N ₂ physisorption			XRF		
	S _{BET} (m ² /g)	Volume at P/P0 =0.99 (mL/g)	Microporous Volume (mL/g)	Si/Ge (mol)	(Si+Ge)/Al (mol)	Si/Al (mol)
IM-12i_HNO ₃	452	0.245	0.149	7	-	-
IM-12i_HNO ₃ _Si ₁ Ge_1PAC	417	0.222	0.136	26	8	8
IM-12i_HNO ₃ _Si ₂ Ge_1PAC	384	0.208	0.124	23	8	8
IM-12i_HNO ₃ _Si ₃ Ge_1PAC	434	0.224	0.147	37	31	32

SEM images in Figure 5- 14, shows that the platelet-like morphology and size were not affected by the different treatments.

As a consequence, treatment of the sample with $n_{Si} = 3n_{Ge}$ before the PAC treatment was considered as the best compromise.

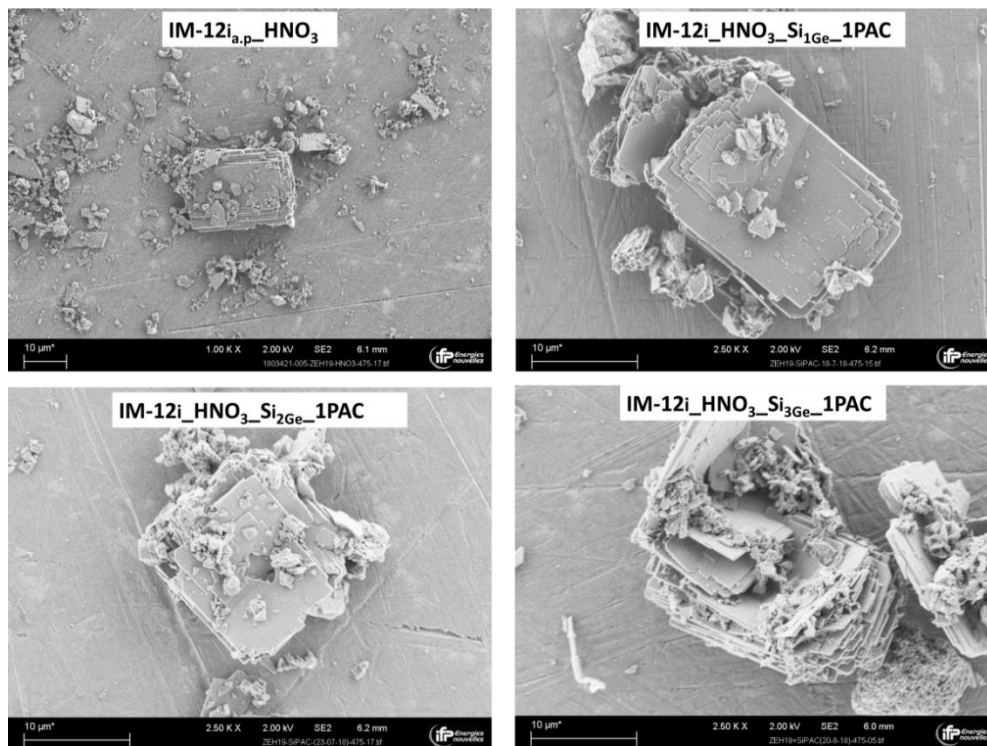


Figure 5- 14: SEM images of samples revealing the n_{SiCl_4} effect on the PAC treatment.

To the best of our knowledge, this is the first time Al is incorporated by PAC treatment in IM-12 without affecting the crystallographic structure^[194,240].

5.2.3.2 Duration of PAC treatment

To study the effect of the duration and the required repetitions of the PAC treatments, IM-12i_HNO₃_Si_nGe was treated as follow: PAC for 6h (IM-12i_HNO₃_Si_nGe_1PAC_{6h}), PAC for 24h (IM-12i_HNO₃_Si_nGe_1PAC_{24h}) and a 2 successive PAC treatments each of 6 hours (IM-12i_HNO₃_Si_nGe_1PAC_{2*6h}). All samples were treated at 80°C with a solid: liquid ratio of 1:50.

The XRD patterns (Figure 5- 15) of the different treatments show that the intensity of sample IM-12i_HNO₃_Si_nGe_1PAC_{24h} is lower than the other samples but all of them have maintained their structure thus no definitive preferable condition was concluded.

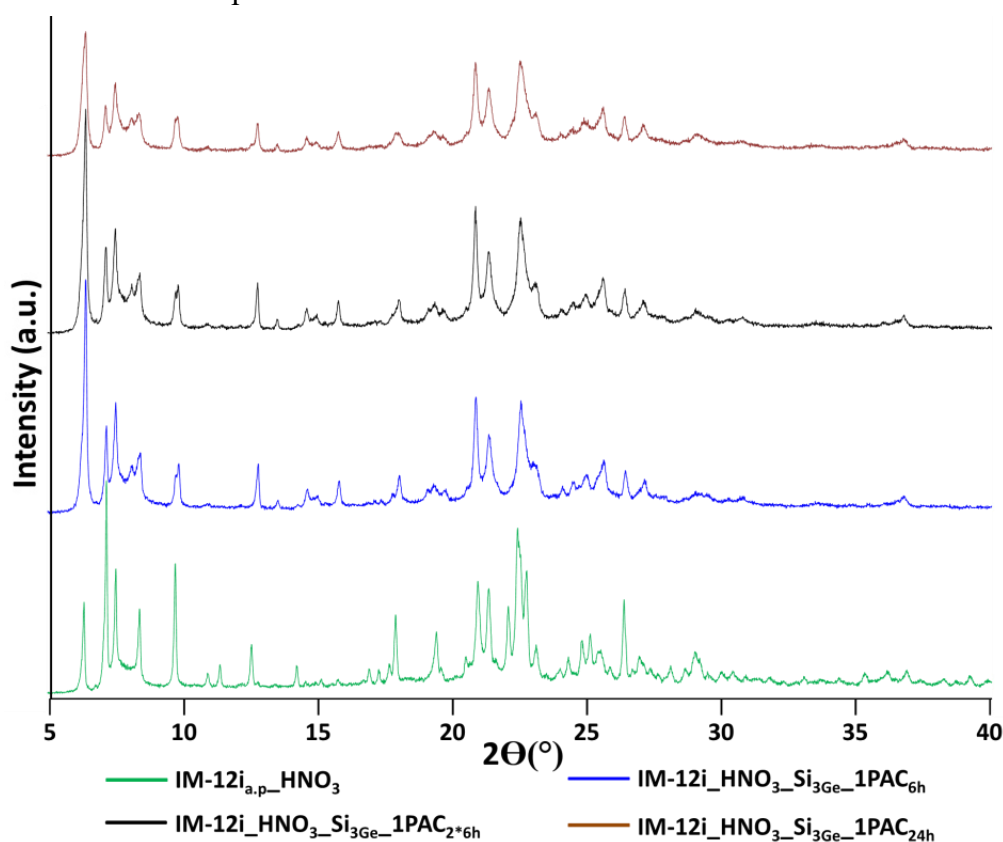


Figure 5- 15: XRD patterns of samples treated with PAC for 6h, 24h and with two successive treatments (2* 6h). a.p means as prepared.

²⁷Al MAS NMR spectra measured following 2.2.7.2 reveals that the three samples have both tetra-coordinated (57 ppm) and hexa-coordinated (9, -2 ppm) aluminum. It also shows, that repeating twice the treatment of 6h increased the Al content by only 6% compared to one treatment of 6h while time extension to 24h led to the incorporation of a double amount of Al (Figure 5- 16).

Quantification of Al based on the relative intensities of the deconvoluted peaks (2.2.7.2) in Table 5- 4, indicates that one PAC treatment, for 6 or for 24h led to the presence of more hexa-coordinated

Al. However, doing twice the treatment of 6h led to a higher proportion of Al^{IV}. Note that the aluminum atoms appearing around 38 are attributed to distorted tetra/penta-coordinated aluminum [166]. The peak at -2 ppm is attributed to hexa-coordinated Al. Sample IM-12i_HNO₃_Si_nGe_PAC_{2*6h} might have higher amounts of Al^{IV} compared to other samples because the PAC treatment include a water washing step. This may allow the elimination of extra framework Al blocking the pores and thus gives access again for Al of following treatments to diffuse and substitute Ge.

Combining these results to XRD results, where the loss of the cristallinity after 24h is more pronounced, reflects that increasing the incorporation of tetra-coordinated Al requires the repetition of PAC treatments. The number of these treatments should be optimized.

Gao et al. [150] showed that an HCl washing step after the PAC treatment helped reducing the amount of extra-framework Al. This was tested on the IM-12 zeolite (without impurity) and the results are in accordance with their work. The proportion of tetracoordinated aluminum slightly decreased while an important loss of extraframework aluminum is seen, Figure 5- 17.

Thus one can say that the optimal conditions after stabilization the IM-12 zeolite are 1PAC treatment for 6 h followed by HCl washing. Indeed, repeating this two steps should increase the amount of incorporated aluminum. This will be discussed in section 5.3.

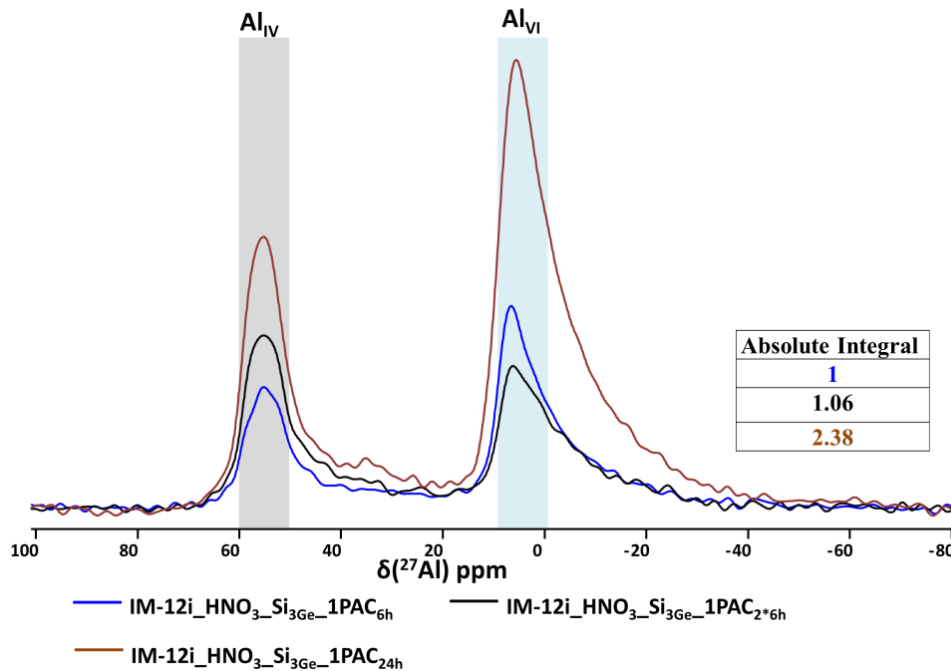


Figure 5- 16: ²⁷Al MAS NMR of samples with PAC treatments for 6h, 24h and of two successive treatments (2* 6h).

Table 5- 4 :Assignment and quantification of aluminum ²⁷Al MAS NMR spectra (Figure 5- 16) of samples with PAC treatments for 6h, 24h and of two successive treatments (2*6h) after deconvolution.

IM-12i_HNO ₃ _	IM-12i_HNO ₃ _	IM-12i_HNO ₃ _
---------------------------	---------------------------	---------------------------

$\delta(^{27}\text{Al})$ ppm	^{27}Al Co- ordination	$\text{Si}_{\text{nGe}}\text{-1PAC}_{6\text{h}}$		$\text{Si}_{\text{nGe}}\text{-1PAC}_{2^*6\text{h}}$		$\text{Si}_{\text{nGe}}\text{-1PAC}_{24\text{h}}$	
		CQ (MHz)	Relative Contribution (%)	CQ (MHz)	Relative Contribution (%)	CQ (MHz)	Relative Contribution (%)
57	Tetra-	2.8	27.5	2.8	38.1	2.8	25.0
38	Penta-/ distorted tetra	2.2	6.8	2.2	9.8	1.6	5.0
9	Hexa	3.8	51.9	3.8	34.9	4.0	49.0
-2	Hexa	5.4	13.9	5.4	17.2	5.6	21.0

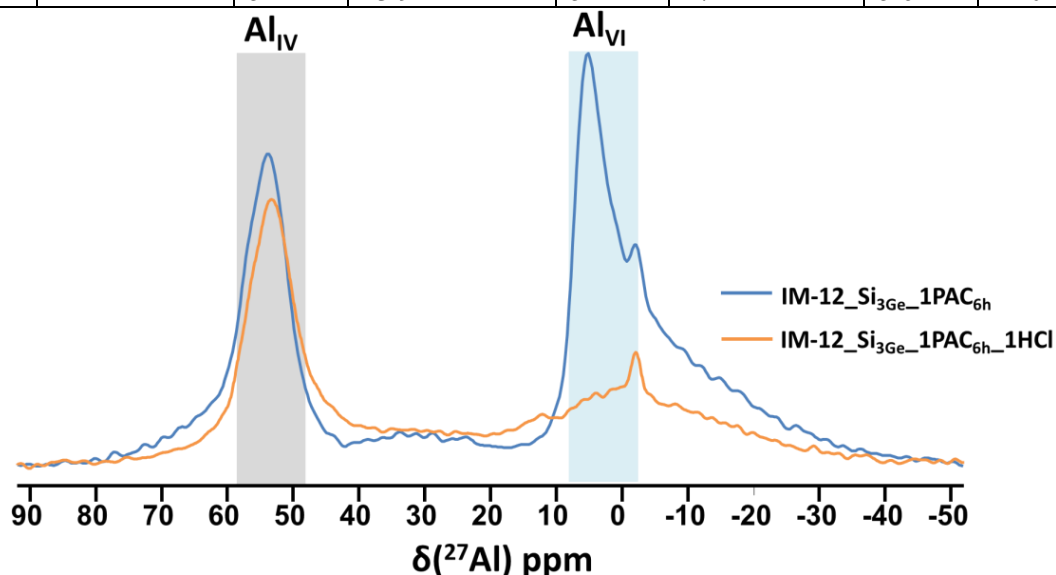


Figure 5- 17: ^{27}Al MAS NMR reflecting the decrease of hexacoordinated aluminum after HCl washing.

5.2.4 Optimization of trichloride aluminum dissolved in dry ethanol treatment

Without contact with an aqueous solution, the IM-12 zeolite conserves its UTL structure even after calcination. To try a treatment in gaseous form we used the SiCl_4 treatment unit described earlier, by replacing SiCl_4 with AlCl_3 . However it was not possible to adapt this unit during this PhD, we needed to assure the sublimation of AlCl_3 under vacuum and a tubing system with controlled temperature to avoid the re-condensation of AlCl_3 before entering the treatment reactor. Instead this gaseous treatment, we tried the treatment of the IM-12 with a solution of AlCl_3 in dry ethanol. To optimize this procedure (2.1.4.3), different parameters such as n_{SiCl_4} , Si substitution/ Al substitution sequence, temperature, addition of compensation cation (adding pure water with $n_{\text{H}_2\text{O}} = n_{\text{Ge}/2}$) were studied. All the treatments were made with $n_{\text{AlCl}_3} = n_{\text{Ge}/2}$ (n_{Ge} being the initial Ge content of the as-prepared zeolite) and for a duration of 6 h.

5.2.4.1 Optimization of n_{SiCl_4} / Si substitution / Al substitution sequence

We first studied if the treatment of the as prepared or calcined IM-12 using aluminum trichloride dissolved in dry ethanol can substitute Ge for Al and assure the stability of the structure. For this purpose, an as prepared and a calcined IM-12 were treated with a solution of AlCl_3 ($n_{\text{Al}} = n_{\text{Ge}/2}$) at

70°C for 6h then calcined. The obtained samples are called IM-12_{a,p}_Al_{70°C}_cal and IM-12_Al_{70°C}_cal respectively. As seen in Figure 5- 18, the structure of both zeolites was maintained after calcination. However, once these samples were washed with water, they both collapsed. Moreover, ICP results indicate that the Si/Ge molar ratio remained constant after the treatments. ICP also demonstrate the incorporation of few amounts of Al, with very high Si/Al molar ratio of 443 and 498 respectively. Indeed these amounts of Al are not enough to stabilize the structure. The non-modification of the Si/Ge molar ratio and of the microporous volume, combined to the Löwenstein rule suggests that these Al are either occupying some defects in the framework or are extraframework species.

Note that such low amounts of Al present high uncertainty measurements for XRF, thus for this series of samples, ICP was used instead. Moreover, Al amounts are lower than the limits of detection of ²⁷Al MAS NMR leading to a lack of identification of the Al coordination that is crucial for choosing the optimum conditions. An alternative to compare between these samples, might be their catalytic testing discussed in chapter 7.

Concerning the N₂ physisorption, the isotherms of all samples exhibit the same shape thus for clarity only one sample is represented in Figure 5- 19 while the rest are presented in S4-Figure 2.

To try to stabilize the obtained samples, a subsequent SiCl₄ treatment step was then undertaken. Since both samples had very similar physicochemical and elemental properties, after calcination, both were treated with SiCl₄ at 550°C with either $n_{\text{SiCl}_4} = n_{\text{Ge}}$ or $n_{\text{SiCl}_4} = 3n_{\text{Ge}}$. The names of the obtained samples are IM-12_{a,p}_Al_{70°C}_cal_Si_{1Ge} and IM-12_Al_{70°C}_cal_Si_{3Ge}. These treatments led to the increase of the Si/Ge molar ratios from 5 to 17 and 37 respectively, reflecting the stabilization of both materials (Table 5- 5). Indeed increasing the amount of n_{SiCl_4} will lead to higher Si/Ge molar ratio between these two resulting samples. However one can note that treating the sample with $n_{\text{SiCl}_4} = 3n_{\text{Ge}}$ increased 7 times the Si/Ge ratio and 1.2 times the (Si+Ge)/Al molar ratio (IM-12_Al_{70°C}_cal vs. IM-12_Al_{70°C}_cal_Si_{3Ge}). While for sample IM-12_{a,p}_Al_{70°C}_cal_Si_{1Ge} the Si/Ge molar ratio increased of a factor of 3.4 and that of (Si+Ge)/Al by 1.14 compared to IM-12_{a,p}_Al_{70°C}_cal. This means that in both cases the amount of SiCl₄ did not affect the amount of Al incorporated in the structure. The latter confirms the DFT results showing that substitution of Ge for Si is favorable over substitution of Al for Si^[241].

On the other hand, before the SiCl₄ treatment sample IM-12_{a,p}_Al_{70°C}_cal had lower (Si+Ge)/Al than IM-12_Al_{70°C}_cal and equal microporous volume (Table 5- 5). After this treatment, the (Si+Ge)/Al effect remained the same while lower microporous volume was detected for sample treated with $n_{\text{Si}} = n_{\text{Ge}}$ (IM-12_{a,p}_Al_{70°C}_cal_Si_{1Ge} vs. IM-12_Al_{70°C}_cal_Si_{3Ge}). Since the Al amount didn't change, this might indicate that the presence of some defects is responsible of the loss in the

microporosity. Probably $n_{\text{Si}}=n_{\text{Ge}}$ are non-sufficient. Thus, one can say that treating the sample with $n_{\text{SiCl}_4}=3n_{\text{Ge}}$ is the optimum condition.

To check if starting with SiCl_4 treatment might increase the incorporation of Al, a calcined IM-12 was treated with SiCl_4 ($n_{\text{SiCl}_4}=3n_{\text{Ge}}$) then with AlCl_3 ($n_{\text{Al}}=n_{\text{Ge}}/2$) at 70°C for 6h giving sample IM-12_Si₃Ge_Al₇₀°C. Compared to sample IM-12_Al₇₀°C_cal_Si₃Ge, both samples have the same microporous volume. IM-12_Al₇₀°C_cal_Si₃Ge has lower (Si+Ge)/Al molar ratio, higher Si/Ge ratio and a better cristallinity showing that starting with AlCl_3 may facilitate the leaching of Ge. However, not knowing the nature of incorporated aluminum, one can suggest that both orders of substitution give materials with high similarity.

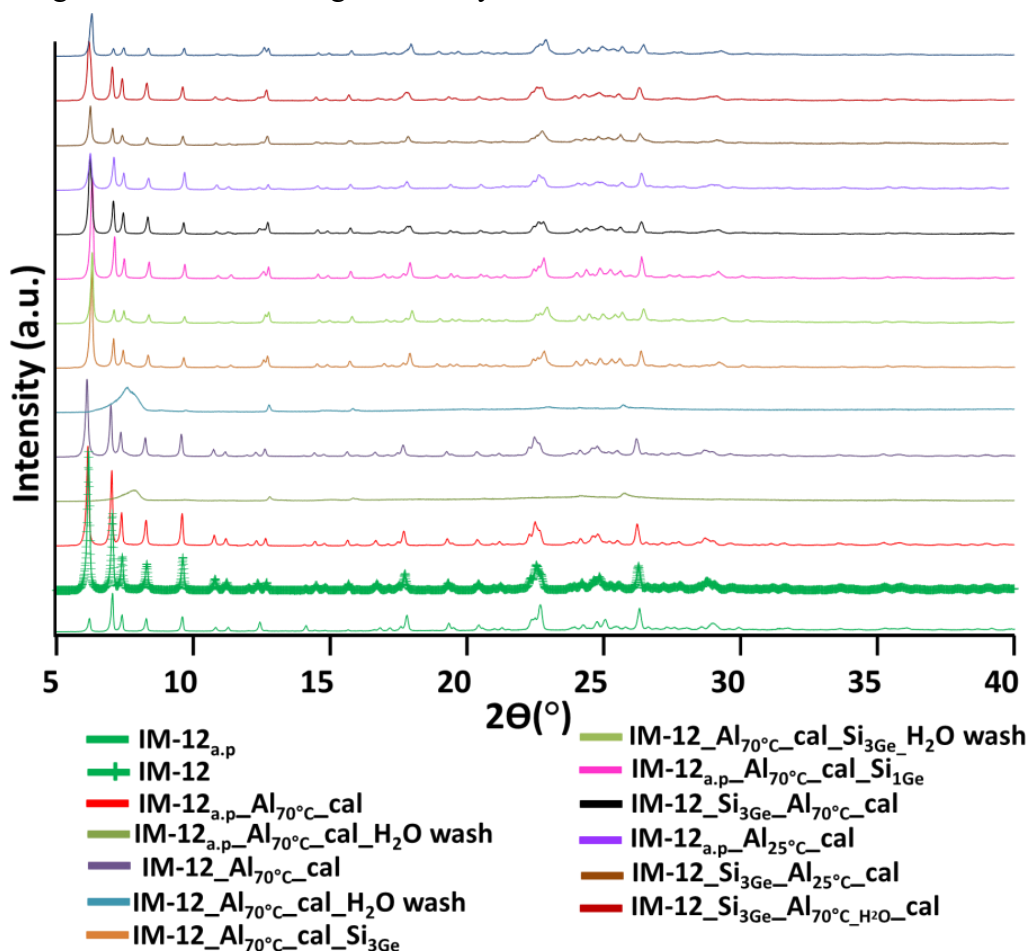


Figure 5- 18 : XRD of IM-12 and of IM-12 samples treated with AlCl_3 dissolved in ethanol at different conditions. a.p means as prepared.

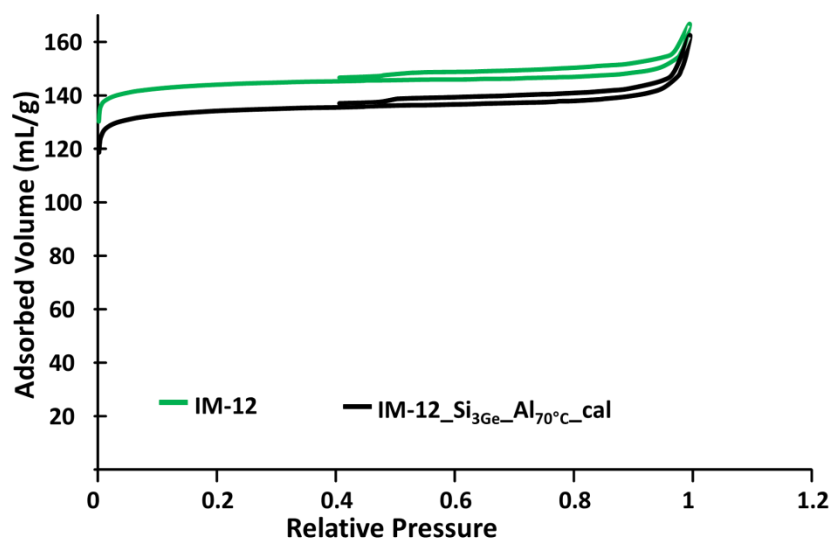


Figure 5- 19 : N₂ physisorption of IM-12 and of IM-12 treated with SiCl₄ ($n_{\text{Si}}=3n_{\text{Ge}}$) then with AlCl₃ at 70°C then calcined.

Table 5- 5: Degree of cristallinity, N₂ physisorption and ICP results of calcined IM-12 and of samples treated with AlCl₃ at different conditions.

Sample	XRD	N ₂ physisorption				ICP		
	Cristallinity Degree (%)	BET Surface (m ² /g)	External Surface (m ² /g)	Volume at P/P0 =0.99 (mL/g)	Microporous Volume (mL/g)	Si/Ge (mol)	(Si+Ge)/Al (mol)	Si/Al (mol)
IM-12 _{a,p}						5	-	-
IM-12	100	592	29	0.258	0.21		-	-
IM-12 _{a,p} _Al70°C_cal		566	32	0.254	0.199	5	375	316
IM-12_Al70°C_cal		566	24	0.254	0.20	5	557	466
IM-12_Al70°C_cal_Si ₃ Ge	112	553	35	0.256	0.194	37	672	655
IM-12 _{a,p} _Al70°C_cal_Si ₁ Ge	115	537	41	0.28	0.186	17	431	407
IM-12_Si ₃ Ge_Al70°C_cal	85	550	31	0.251	0.194	10	701	637
IM-12 _{a,p} _Al25°C_cal		575	26	0.242	0.204	5	423	348
IM-12_Si ₃ Ge_Al25°C_cal	108	590	19	0.251	0.21	11	599	550
IM-12_Si ₃ Ge_Al70°C_H2O_cal	78	560	16	0.249	0.202	10	1224	1113

a.p means as prepared

Degree of cristallinity using calcined IM-12 as a reference.

5.2.4.2 AlCl₃ treatment temperature

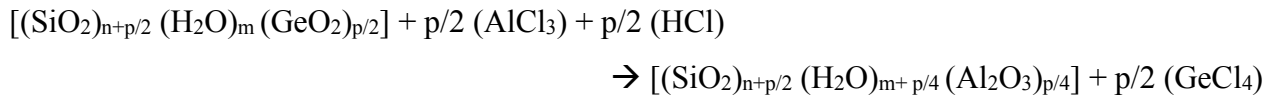
The impact of the temperature of the AlCl₃ dissolved in ethanol treatment was studied on as prepared IM-12, directly treated with AlCl₃ at ambient temperature and 70°C giving samples IM-12_{a,p_Al25°C_cal} and IM-12_{a,p_Al70°C_cal} respectively. It was also studied on previously SiCl₄ (n_{SiCl₄} = 3n_{Ge}) treated samples at ambient temperature giving sample IM-12_{_Si₃Ge_Al25°C_cal} and at 70°C giving sample IM-12_{_Si₃Ge_Al70°C_cal}.

Treating with AlCl₃ the as prepared samples showed quasi-similar microporous volume, equal Si/Ge molar ratios but the sample treated at 70°C had lower (Si+Ge)/Al molar ratio, Table 5- 5.

For samples previously treated with SiCl₄, the AlCl₃ treatment at ambient temperature led to a sample with higher cristallinity, higher microporous volume, equal Si/Ge and lower (Si+Ge)/Al compared to the sample treated at 70°C (Figure 5- 18 and Table 5- 5). This can indicate that the treatment at ambient temperature is better for the cristallinity of the structure.

5.2.4.3 Addition of water

In chapter 3, we used the following equation to calculate the energies of substitution of Ge for Al:



Eq. 5- 1

Experimentally the HCl solutions are highly diluted in water thus cannot be used (same problem as PAC solutions). However, adding just the needed amount of water (n_{H₂O} = n_{Ge/2}) may cause the formation of the compensating proton. Thus we tried adding water experimentally with n_{H₂O} = n_{Ge/2}. The treatment conditions were similar to that of sample IM-12_{_Si₃Ge_Al70°C_cal}, only water was added to the ethanol solution after adding the zeolite to the mixture. The obtained sample is called IM-12_{_Si₃Ge_Al70°C_H₂O_cal}. The latter had slightly higher microporous volume (0.202 vs 0.194 mL/g), equal Si/Ge molar ratio and higher (Si+Ge)/Al molar ratio of 1224 compared to the sample treated without H₂O (the ratio was of 701). This indicates that adding water molecules did not improve the incorporation of Al. One can suggest that there are enough traces of residual water in the zeolite for the incorporation of these little AlCl₃ amounts, even without external addition of water in the medium. Maybe, adding more water degraded the AlCl₃ precursor.

SEM pictures in Figure 5- 20 show that the different treatments did not affect the morphology and the size of the platelets after AlCl₃ treatments with different conditions.

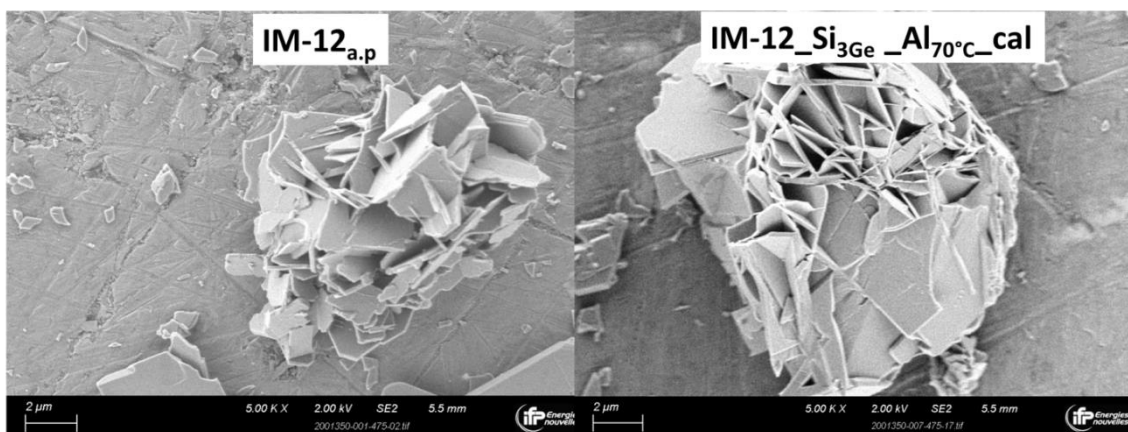


Figure 5- 20: SEM images of the as prepared IM-12 and of IM-12 treated with SiCl_4 ($n_{\text{Si}}=3n_{\text{Ge}}$) then with AlCl_3 at 70°C then calcined. a.p means as prepared.

5.3 Preparation of a series of catalysts by successive PAC treatments

It appears that in the present state of post-treatment optimizations, the PAC treatments appear to be more promising than AlCl_3 treatments to get significant incorporation of Al. Thus, we decided to extend the series of materials prepared by PAC by repeating the treatment sequence. We aim at analyzing the conservation of the UTL microporous structure and the amount/type of incorporated aluminum. As mentioned earlier, a soft treatment of the zeolite with HCl after each PAC treatment helps reducing the amount of undesired hexacoordinated aluminum. For the following parts, the initially pure sample IM-12 (without impurity) is used.

5.3.1 Structural and textural properties

XRD patterns in Figure 5- 21 show that the UTL structure is maintained even after 6 PAC treatments alternated with 6 HCl washing steps. The degrees of cristallinity calculated following 2.2.1 are represented in Table 5- 6. IM-12 treated with SiCl_4 was chosen as reference. It is seen that a loss of cristallinity is induced after each treatment, reaching 30% after 6 PAC and 6 HCl treatments.

N_2 physisorption (Figure 5- 22 and Table 5- 6) shows that after the SiCl_4 treatment (IM-12_ Si_3Ge), 10% of the initial microporous volume is lost. After the first PAC treatment (IM-12_ Si_3Ge _1PAC), this loss increases to 17%. Further treatments (IM-12_ Si_3Ge _1PAC_1HCl, IM-12_ Si_3Ge _2PAC_1HCl and IM-12_ Si_3Ge _2PAC_2HCl) reduced this loss to 12% until reaching 5% with the third PAC treatment (IM-12_ Si_3Ge _3PAC_2HCl). Compared to the XRD, one can say that even with a loss of cristallinity, the microporosity is maintained. This might indicate that some few amounts of Ge are removed from the structure without being replaced and without affecting the microporosity that slightly changed (Figure 5- 23). The BET surface area follows the same trend, a decrease from 592 to 553 and 485 m^2/g respectively for IM-12_ Si_3Ge and IM-12_ Si_3Ge _1PAC is

detected before being quasi-restored ($566 \text{ m}^2/\text{g}$) after the third treatment and reduced again by further treatments until reaching $453 \text{ m}^2/\text{g}$ after six PAC and HCl treatments.

Considering the structural and textural properties of the UTL zeolite, these results indicate that three successive PAC/PAC+HCl treatments are the most promising to provide an efficient catalyst.

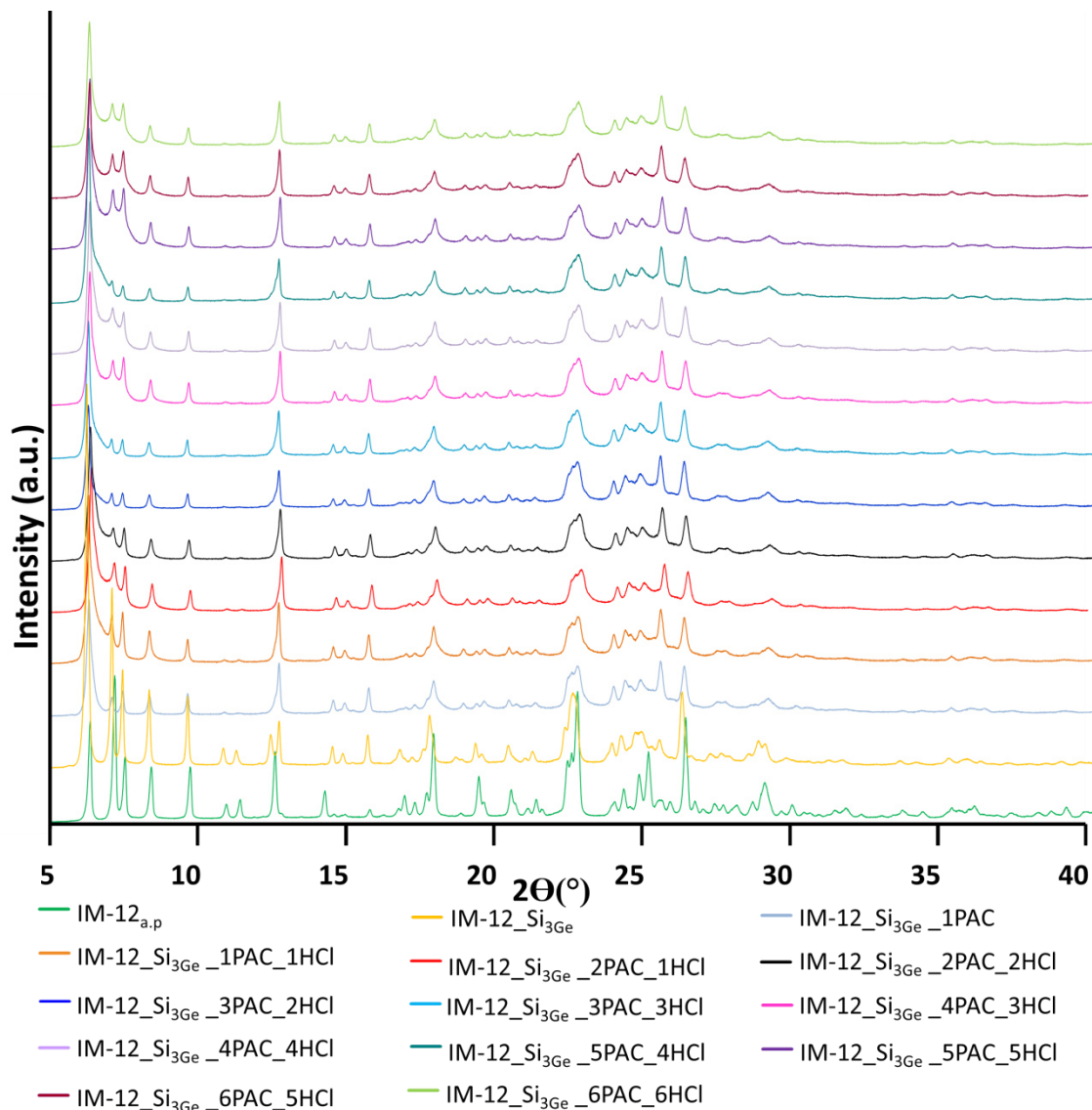


Figure 5- 21: XRD patterns of as prepared IM-12 and of samples treated with SiCl_4 ($n_{\text{SiCl}_4}=3n_{\text{Ge}}$) followed by successive one to six PAC and HCl treatments. a.p means as prepared.

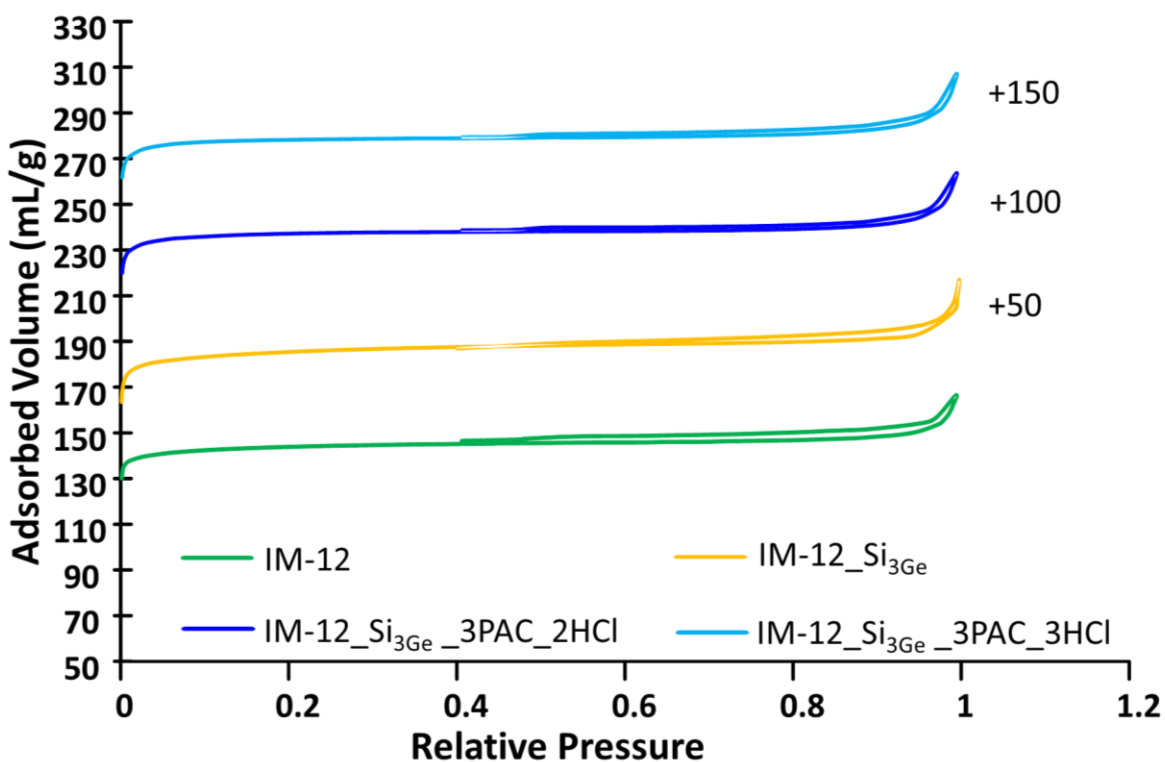


Figure 5- 22 : N₂ physisorption of calcined IM-12 and of samples treated with SiCl₄ ($n_{\text{SiCl}_4}=3n_{\text{Ge}}$) followed by successive PAC and HCl treatments.

SEM photos in Figure 5- 24 show that the different treatments did not affect the morphology and the size of the platelets even after 6 PAC and 6 HCl treatments. The average size is still around 7x6 μm and the average thickness around 350 nm.

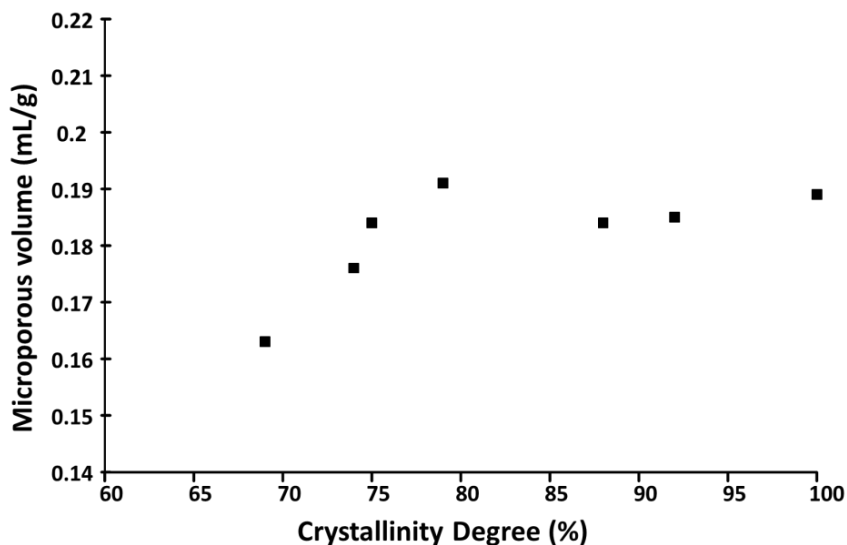


Figure 5- 23 : Evolution of microporosity against the crystallinity of IM-12 treated with PAC and washed with HCl samples.

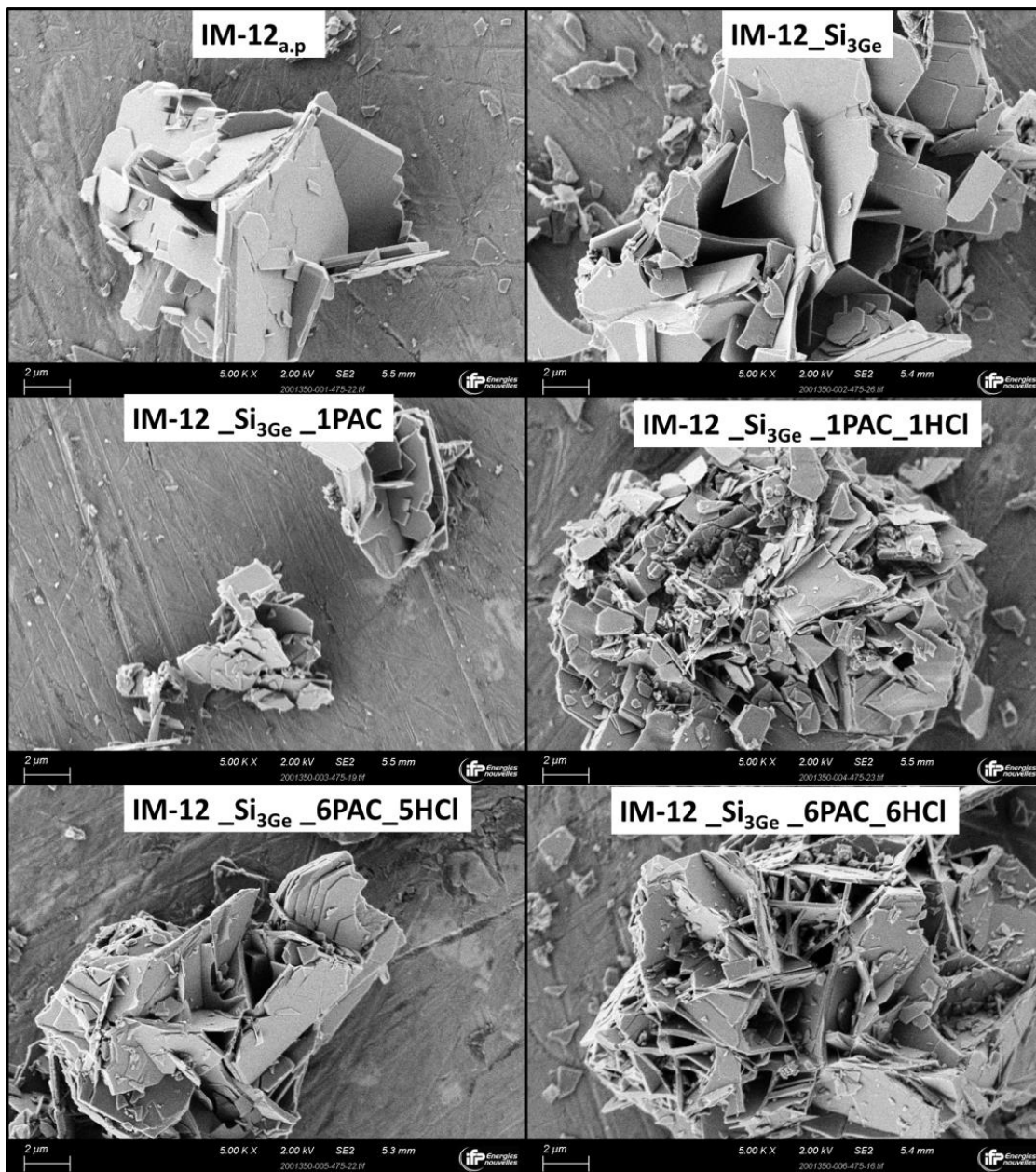


Figure 5- 24: SEM images of the as prepared and post-treated IM-12. a.p means as prepared.

Table 5- 6 : Degree of crystallinity, N₂ physisorption, XRF results and Wavelength shift at maximum absorbance of calcined IM-12 and of samples treated with SiCl₄ (n_{SiCl₄}=3n_{Ge}) followed by successive one to six PAC and HCl treatments.

Sample	XRD	N ₂ physisorption				XRF			ATR-IR	
	Cristallinity Degree (%)	BET Surface (m ² /g)	External Surface (m ² /g)	Volume at P/P0=0.99 (mL/g)	Microporous Volume (mL/g)	Si/Ge (mol)	(Si+Ge)/Al (mol)	Si/Al (mol)	v _{max} (SiOSi) (cm ⁻¹)	v _(d4r) (cm ⁻¹)
IM-12 _{a,p}						5	-	-	1073 / double peak at 1045	570
IM-12		592	29	0.258	0.210		-	-		
IM-12_Si ₃ Ge	100	553	47	0.259	0.189	10	-	-	1054	582
IM-12_Si ₃ Ge_1PAC	91	485	20	0.218	0.174	37	17	17	1047	584
IM-12_Si ₃ Ge_1PAC_1HCl	92	534	41	0.249	0.185	48	40	39	1049	584
IM-12_Si ₃ Ge_2PAC_1HCl	83	523	30	0.240	0.185	103	20	20	1047	584
IM-12_Si ₃ Ge_2PAC_2HCl	88	524	33	0.248	0.184	105	46	45	1045	586
IM-12_Si ₃ Ge_3PAC_2HCl	82	566	24	0.253	0.202	168	22	22	1046	584
IM-12_Si ₃ Ge_3PAC_3HCl	79	529	17	0.243	0.191	173	28	27	1043	584
IM-12_Si ₃ Ge_4PAC_3HCl	75									
IM-12_Si ₃ Ge_4PAC_4HCl	75	529	39	0.247	0.184	138	32	32	1047	584
IM-12_Si ₃ Ge_5PAC_4HCl	69									
IM-12_Si ₃ Ge_5PAC_5HCl	74	486	26	0.243	0.176	148	38	38	1043	584
IM-12_Si ₃ Ge_6PAC_5HCl	65									
IM-12_Si ₃ Ge_6PAC_6HCl	69	453	30	0.243	0.163	164	30	30	1044	586

a.p means as prepared

Degree of cristallinity using IM-12 treated with SiCl₄ as a reference.

5.3.2 Composition of the solids and environment of the Al atoms

5.3.2.1 XRF

The XRF results in Table 5- 6 show an increase of the Si/Ge molar ratio from 5 to 10 after the SiCl₄ treatment justifying the stability of the structure. Further treatments led to an increase of this ratio to 173 after the third PAC/HCl treatments while additional treatments showed an decrease of this ratio that might be explained by some loss of framework Si. The incorporation of Al is detected after the first PAC treatment (IM-12_Si₃Ge_1PAC). After HCl treatment, the Si/Al molar ratio increased from 17 (IM-12_Si₃Ge_1PAC) to 39 (IM-12_Si₃Ge_1PAC_1HCl), the same trend is seen for the second PAC (IM-12_Si₃Ge_2PAC_1HCl) and second HCl washing (IM-12_Si₃Ge_2PAC_2HCl). This increase is due to the partial elimination of undesired hexa-coordinated aluminum. However, the Si/Al molar ratio slightly increased between the third PAC treatment and the third HCl washing, giving the lowest Si/Al ratio of the series of catalysts obtained after HCl washing while further treatments led to an increase of the Si/Al ratio.

5.3.2.2 ²⁷Al MAS NMR

5.3.2.2.1 Attribution of ²⁷Al MAS NMR and Al quantification

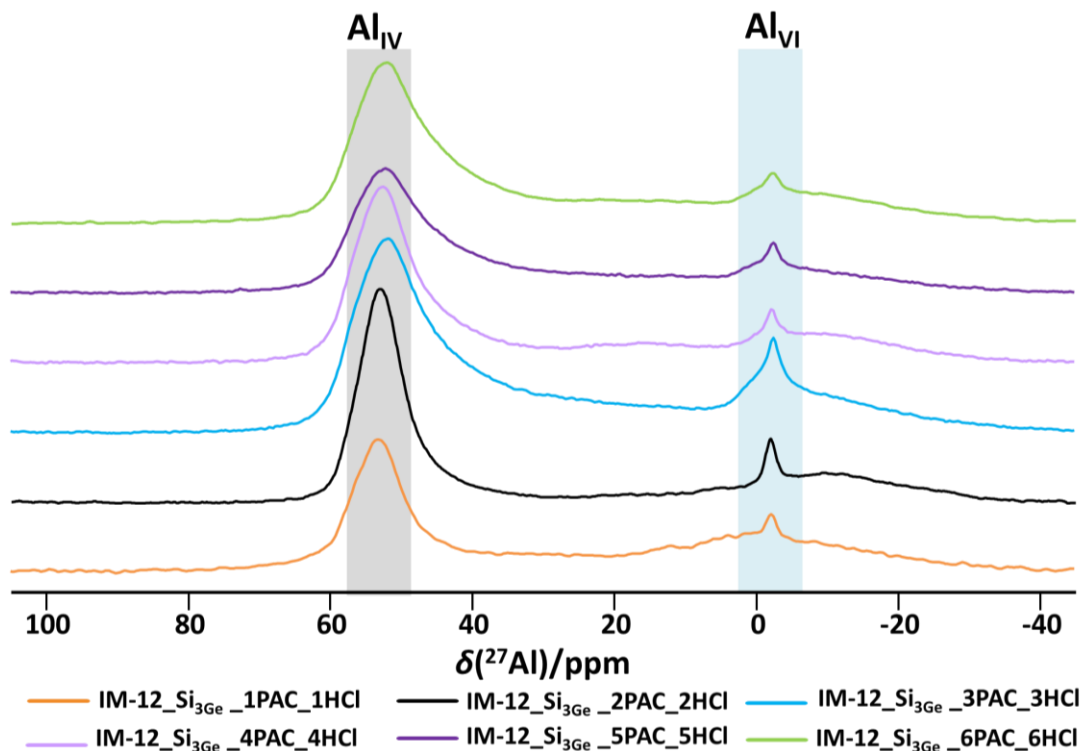


Figure 5- 25 : ²⁷Al NMR of IM-12 samples treated with PAC and washed with HCl.

The ²⁷Al MAS NMR spectra of samples washed with HCl are represented in Figure 5- 25. All samples exhibit both tetra and hexacoordinated aluminum. The deconvolutions of the different

spectra are shown in Figure 5- 26 and in S4-Figure 3 to 11. The different detected chemical shifts are divided between tetraordinated and hexacoordinated Al. Peaks around 63, 53 and 47 ppm are usually attributed to tetraordinated aluminum while the other ones correspond to hexacoordinated aluminum atoms. The chemical shifts of Al obtained from ^{27}Al DFT NMR are represented in Table 5- 8. They were obtained from simulating DFT NMR of the UTL bulk and the different external surface orientations studied in chapter 4. Table 5- 8 shows that incorporated Al in the bulk or at the surface, with different elemental neighboring have shifts between 36 and 47 ppm. This means that the shift at 63.1 is likely not related to framework nor external surface aluminum. Note, however, that the DFT calculations are performed without considering the effect of adsorbed water that may increase the proton mobility around aluminum atoms, thus increase the symmetry of its environment, and affect the chemical shift value. In the literature the peak around 54 ppm is known as Al incorporated in the zeolite framework^[111,150,156]. While the peak at 48 ppm is sometimes considered as distorted tetra or as hexacoordinated aluminum^[242]. Thus to calculate the $\text{Si}/\text{Al}^{\text{IV}}$, two possibilities exist either by considering the different tetraordinated Al or just the framework Al at 54 ppm. We chose the second possibility.

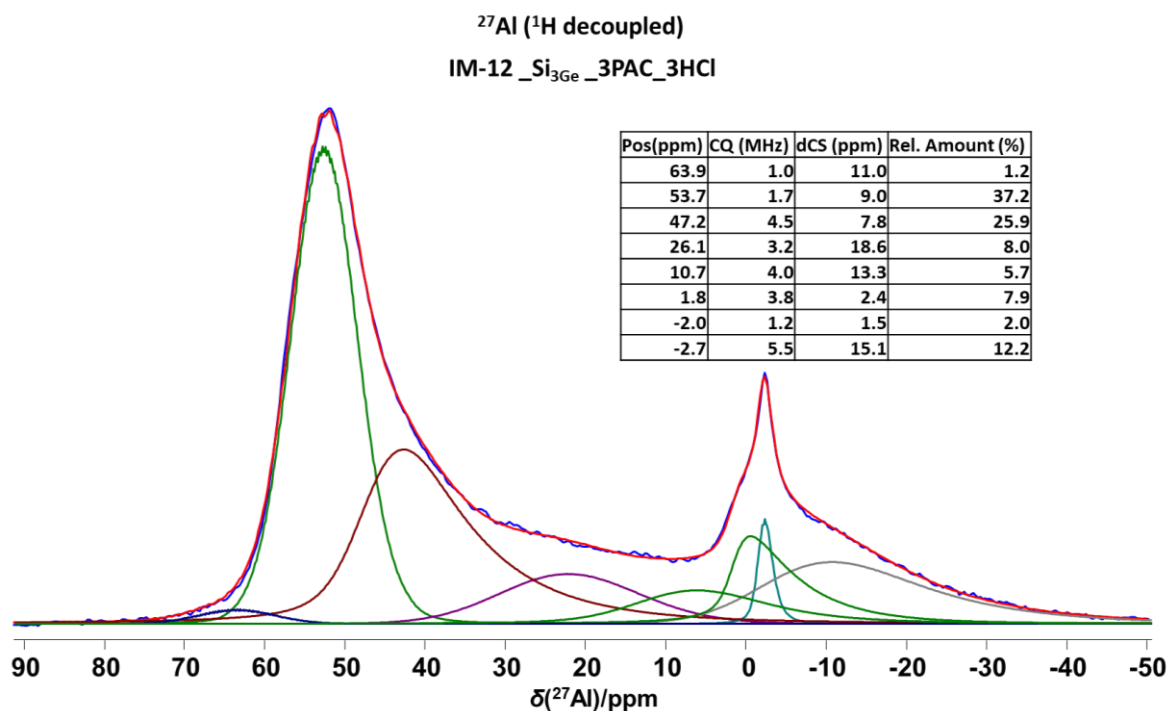


Figure 5- 26 : Deconvoluted ^{27}Al MAS NMR spectra of IM-12 _Si₃Ge _3PAC_3HCl and relative amounts of Al.

After deconvolution, the relative amount of each chemical shift was defined and the Al and the $\text{Si}/\text{Al}^{\text{IV}}$ were quantified by comparing to an external LTA ($\text{Si}/\text{Al}=1$) reference (2.2.7.2.) The results are presented in Table 5- 7. These results show that HCl treatments increases the Si/Al ratios by removing extraframework Al^{VI} but it also eliminates framework Al^{IV} .

Looking at the Si/Al_{total} shows that the lowest Si/Al ratio for samples washed with HCl was reached with IM-12_Si₃Ge_3PAC_3HCl. Further treatments re-increased the ratios. However, among the washed samples, the Si/Al^{IV} is minimal for IM-12_Si₃Ge_6PAC_6HCl, which thus has the lowest Si/Al framework ratio.

Hence, the ²⁷Al MAS NMR proved the successful substitution of Ge for Al in the zeolite framework. Repeating the PAC/ HCl treatments increased these amounts. This might suggest that the repetition allows the accessibility for Al and its incorporation at different accessible sites.

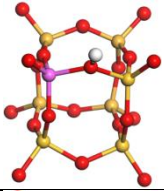
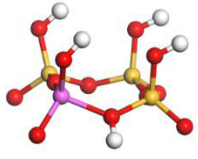
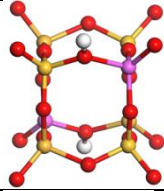
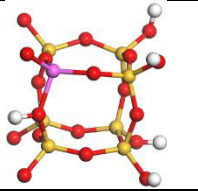
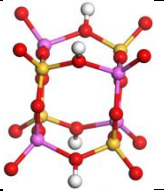
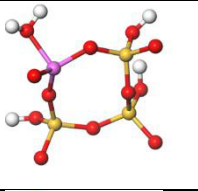
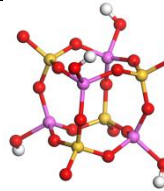
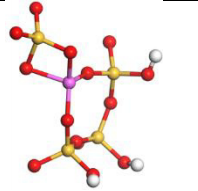
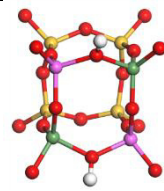
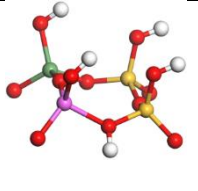
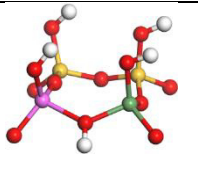
Table 5- 7 : Al and acidity quantifications of treated IM-12 samples and using ²⁷Al MAS NMR and XRF.






Sample	Experimental				Theoretical acidity		Corrected theoretical acidity
	Integral/mass	Si/Al total	Si/Al ^{IV} , zeolite	Si/Al ^{IV} , total	XRF	²⁷ Al MAS NMR (total)	²⁷ Al MAS NMR (zeolite)
					μmol.g ⁻¹		
LTA (Si/Al=1)	1.00	1.0					
IM-12_Si ₃ Ge_1PAC	0.11	17.2	82.9	52.7	912	902	195
IM-12_Si ₃ Ge_1PAC_1HCl	0.05	38.6	104.4	70.0	410	414	156
IM-12_Si ₃ Ge_2PAC_1HCl	0.12	15.2	46.9	36.8	781	1013	342
IM-12_Si ₃ Ge_2PAC_2HCl	0.05	38.5	73.1	58.8	357	415	221
IM-12_Si ₃ Ge_3PAC_2HCl	0.10	18.8	36.2	28.3	713	829	441
IM-12_Si ₃ Ge_3PAC_3HCl	0.07	25.9	69.6	40.3	586	610	232
IM-12_Si ₃ Ge_4PAC_4HCl	0.06	32.0	65.0	47.7	497	497	248
IM-12_Si ₃ Ge_5PAC_5HCl	0.05	35.2	86.8	51.9	421	453	187
IM-12_Si ₃ Ge_6PAC_6HCl	0.07	26.6	59.5	37.0	529	594	271

Si/Al^{IV}, zeolite correspond to the chemical shift at 54 ppm.

Si/Al^{IV}, total correspond to the chemical shifts at 63, 54 and 47 ppm.

Table 5- 8 : Chemical shifts of Al at the bulk and the external surfaces of a UTL zeolite through ^{27}Al DFT NMR.

Form	Bulk		External Surfaces			
	Al distribution	Calculated $\delta^{27}\text{Al}$ (ppm)	Al distribution	Calculated $\delta^{27}\text{Al}$ (ppm)		
SiAl	1 Al per d4r		40	010- Cleavage 1		45
	Half d4r alternated		39	100- Cleavage 1		36
	Full d4r alternated		38	100- Cleavage 3		42
	Full d4r alternated (H outside of d4r)		47	100- Cleavage 3 dehydrated		44
SiGeAl	2Ge and 2Al in the same s4r		41	010- Cleavage 1- Si near H of Al		44
				010- Cleavage 1- Ge near H of Al		43

Si  Al  Ge  H  O 

5.3.2.2.2 Theoretical and corrected theoretical acidities

The chemical formula of the aluminosilicate UTL unit cell is: $[\text{H}_n] [\text{Si}_{76-n}\text{Al}_n\text{O}_{152}]$, which contains 2 d4r. According to the Löwenstein rule, the maximum amount of Al that can occupy the two d4r gives this unit cell: $[\text{H}_8] [\text{Si}_{68}\text{Al}_8\text{O}_{152}]$. Assuming that each Al gives a bridging Si-OH-Al, it is possible to calculate the total Brønsted sites expected concentration, which is equal to $1729 \mu\text{mol.g}^{-1}$

¹. This represents the maximal concentration of bridging Si-OH-Al that can be expected, from a structural point of view.

Such an evaluation can be reconsidered from experimental measurements of the Al content: the amounts of Al used in the UTL unit cell are those of total Al obtained from XRF or from ²⁷Al MAS NMR. These calculated values represent the theoretical acidity.

From these XRF and ²⁷Al MAS NMR theoretical acidities, it is seen that the HCl washing is reducing the total acidity, probably by extracting the extraframework Al.

If only the samples washed by HCl after each PAC treatment are compared, on the basis of XRF, we can expect an acidity that increases after the treatments and reaches a maximum in sample IM-12_Si₃Ge_3PAC_3HCl (610 μmol.g⁻¹), then we expect a decrease after further treatments (497,453, 594 μmol.g⁻¹).

Using the amounts of Al^{IV} deduced from the signal at 54 ppm in the ²⁷Al MAS NMR spectrum, it is possible to reweight the corrected theoretical acidity that is considered to be related to bridging Si-(OH)-Al^{IV}. The results in Table 5- 7, show that these sites represent between 20 and 55% of the total theoretical acidity. This can be due the presence of extraframework aluminum that are reduced after HCl treatments. When only the samples washed by HCl after each PAC are compared, the amount of bridging Si-(OH)-Al increases by repeating the treatments, decreases in IM-12_Si₃Ge_5PAC_5HCl then re-increased again after 6 PAC/HCl treatments. The increase in this latest sample might be related to structural changes discussed previously such as loss of microporosity.

5.3.2.3 ATR-IR

The ATR-IR spectra (Figure 5- 27 and Table 5- 6) of the as prepared IM-12 and the treated samples is in agreement with the XRF results. Only the as prepared sample has a band at 900 cm⁻¹ attributed to Ge-O-Ge.^[243] The absence of this band in the treated samples is in coherence with the increase of the Si/Ge molar ratio from 5 to 10 after the SiCl₄ treatment and above 37 after the PAC treatments. Moreover, the band at 950 cm⁻¹ attributed to asymmetric stretching vibration of Si-O-Ge in the framework^[7,243] decreased after each treatment with the increase of the Si/Ge molar ratios. Moreover, a shift of the band at 1054 cm⁻¹ after the SiCl₄ treatment (IM-12_Si₃Ge) to 1043-1049 cm⁻¹, depending on the PAC treatment and the Si/Al molar ratio, is observed. It suggests the incorporation of the Al in the framework. In addition the band around 580 cm⁻¹ is characteristic of the vibration of d4r units^[7,243] and is present in all samples showing that even after several treatments these building units still exist which is in agreement with the upholding of the UTL structure seen in the XRD patterns. This band present a shift from 570 cm⁻¹ in the as prepared IM-12 to ≈ 582 cm⁻¹ after the treatments suggesting that Ge was replaced by other elements in the d4r. A similar blueshift of 23 cm⁻¹ was seen when Ge was substituted with Si in d4r units^[7].

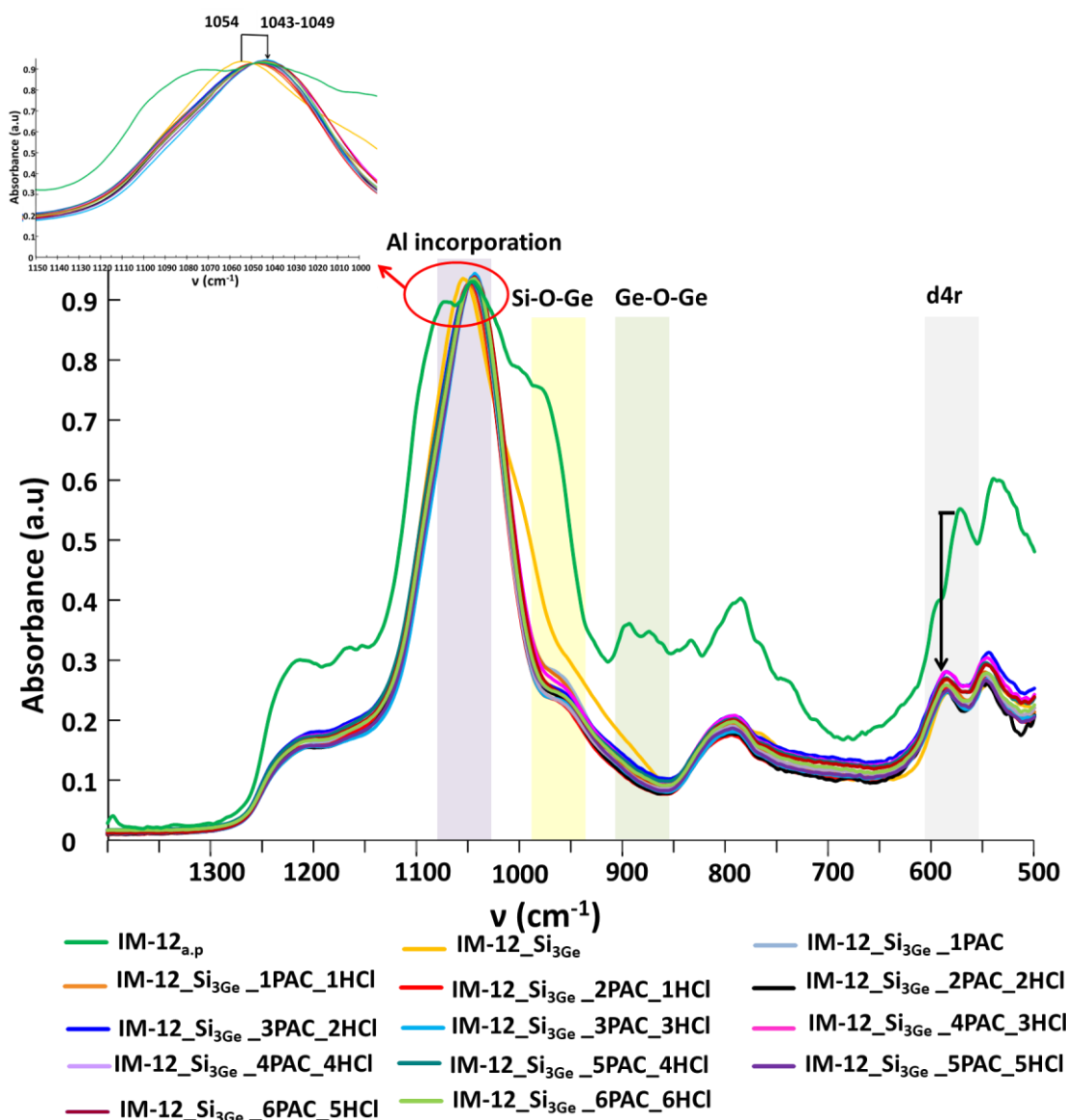


Figure 5- 27: ATR-IR spectra of as prepared IM-12 and treated samples normalized at the maximum absorbance ($\approx 1500\text{cm}^{-1}$). The enlarged region is for SiOSi vibration at maximum absorbance, the absorbance values are indicated in Table 5- 7.

The different characterization showed promising results for the alumination using PAC solutions. The results show that all the treated samples maintain the initial UTL structure. Samples treated 3 times with PAC (IM-12_Si₃Ge_3PAC_2HCl) and then washed with HCl (IM-12_Si₃Ge_3PAC_3HCl) seem to be the best samples in terms of Si/Al ratio, crystallinity and microporosity. A further understanding of the nature of the aluminum is necessary and might explain the effect of each treatment step on the sample.

5.4 Conclusion

The experimental results of this chapter are in accordance with the DFT results (chapters 3 and 4), proving the possibility of stabilization of silicogermanates by experimental post-substitution of Ge

for Si and Al. The structure of the silicogermanate we have selected here, IM-12 (UTL), was maintained with a high microporous volume. It is seen that prior to aluminum substitution, one can start with substitution of Ge for Si, not only to assure the stabilization of the structure for further treatments but also for enhancing the incorporation of Al by obeying to the Löwenstein rule. The treatment unit in gaseous form using SiCl_4 showed promising results for reaching this goal. The substitution of Ge for Al using PAC solutions allowed the incorporation of Al. A multi-step PAC treatment is necessary to incorporate higher tetra- coordinated Al amounts. The alumination using aluminum trichloride also maintained the initial UTL structure in some conditions. The obtained samples had comparable physicochemical characterization compared to the PAC treated samples, however they had much lower aluminum amounts with respect to the samples obtained by PAC treatments.

To the best of our knowledge, this is the first time Al is incorporated by PAC treatment in IM-12 without affecting the crystallographic structure. The only work citing the incorporation of Al in a UTL type zeolite, indicated a loss of the microporous volume from 0.21 to 0.14 mL/g and 5.4% theoretical moles of Al (based on T atoms)^[151]. Herein we report IM-12 zeolites with a microporous loss from 0.210 to 0.202 and 0.191 mL/g and theoretical % moles of Al of 3.4 and 2.4 % respectively.

The nature of acidity, of the interaction of aluminum with its neighborhood using FTIR after the adsorption of pyridine and the experimental and DFT simulated ^{27}Al and ^1H MAS NMR and a comparison of the stability of IM-12 bulk with defects are presented in the following chapter.

6. Understanding of the acidity of stabilized IM-12 zeolite

In the previous three chapters, we demonstrated theoretically (upon thermodynamic considerations) and experimentally that it is feasible to obtain stable aluminosilicogermanate and even aluminosilicate forms of IM-12. We also showed that there is no preference between substitution of Ge for Si or Al in the bulk or at the surface of the IM-12 zeolite. The purpose of this chapter is to identify whether some acid sites are present in the post-treated materials, in which amount, and to propose possible locations for those acid sites. For this purpose, we combine experimental investigations by FTIR and ^1H MAS NMR, and DFT calculations. Then, the Brønsted and Lewis acidities of the treated samples were quantified based on their experimental response to pyridine adsorption using FTIR spectroscopy.

6.1 Identification of the hydroxyl groups by Fourier transform infrared (FTIR)

The nature of OH groups in the calcined IM-12 and the post-treated samples was studied using FTIR spectroscopy. Before the measurements, the samples were pretreated for 10 h at 450°C under secondary vacuum. The calcined IM-12 exhibits a peak around 3742 cm^{-1} attributed to silanols^[151,154,244] and a large band between 3685-3630 cm^{-1} attributed to germanols^[156]. The other post treated samples have three major bands in agreement with Al-UTL of Shamzy et al.^[151]: a silanols band between 3742-3737 cm^{-1} ^[151,154,244], a second band at 3670 cm^{-1} characteristic of extraframework aluminum (EFAL) or of surface aluminols ^[154,245], and a third band at 3636-3629 cm^{-1} attributed to bridging Si-OH-Al I^[154,156].

Table 6- 1 : Hydroxyl quantifications calculated from peak surfaces of hydroxyl groups of zeolites activated at 450°C.

Sample	SiOH 3742-3737 cm^{-1} ($\mu\text{mol.g}^{-1}$)	GeOH 3685-3630 cm^{-1} (au. g^{-1})	EFAL/surface AlOH 3670 cm^{-1} (au. g^{-1})	Si-OH-Al 3636-3629 cm^{-1} ($\mu\text{mol. g}^{-1}$)
Calcined IM-12	94	115	-	-
IM-12 Si_3Ge	330	-	-	-
IM-12 Si_3Ge 1PAC	717	-	-	4
IM-12 Si_3Ge 1PAC 1HCl	632	-	-	3
IM-12 Si_3Ge 2PAC 1HCl	494	-	33	9
IM-12 Si_3Ge 2PAC 2HCl	624	-	6	8
IM-12 Si_3Ge 3PAC 2HCl	505	-	19	16
IM-12 Si_3Ge 3PAC 3HCl	697	-	10	18
IM-12 Si_3Ge 4PAC 3HCl	760	-	-	20
IM-12 Si_3Ge 4PAC 4HCl	625	-	8	29
IM-12 Si_3Ge 5PAC 4HCl	718	-	5	14
IM-12 Si_3Ge 5PAC 5HCl	535	-	-	9
IM-12 Si_3Ge 6PAC 5HCl	648	-	8	17
IM-12 Si_3Ge 6PAC 6HCl	506	-	-	27

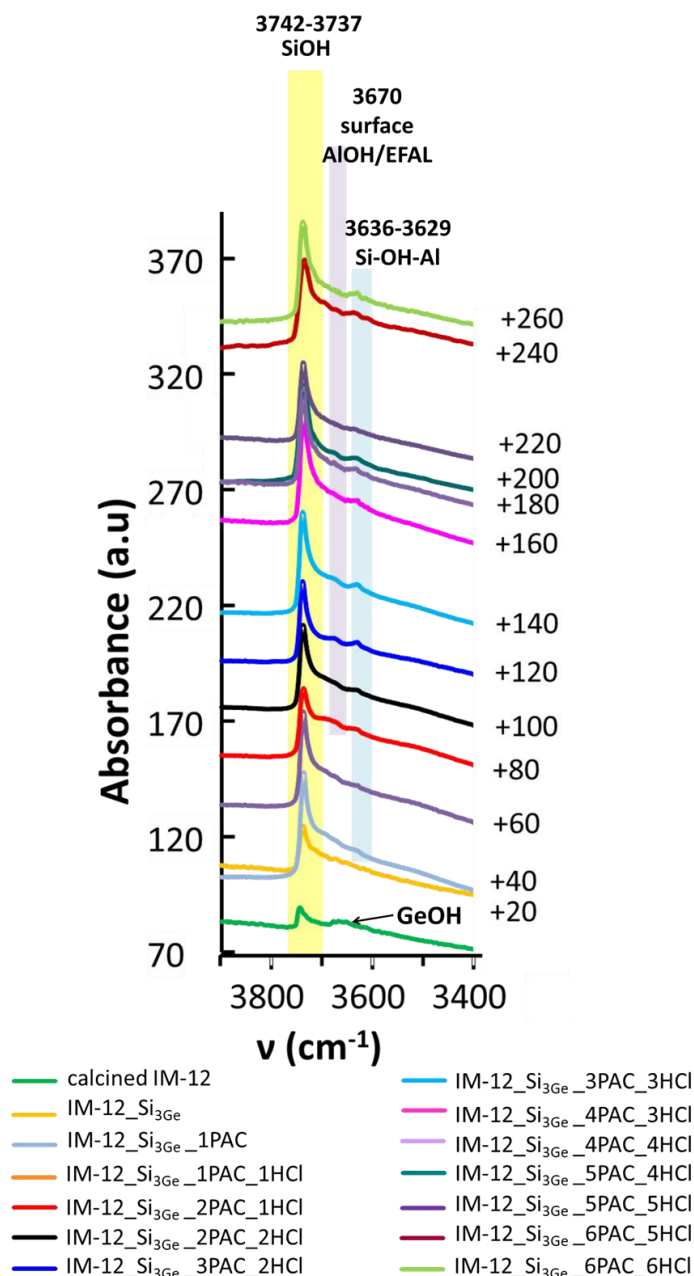


Figure 6- 1 :IR spectra of as prepared and post-treated IM-12, region of hydroxyl vibrations after treatment at 450°C for 10h under secondary vacuum.

The concentrations in $\mu\text{mol.g}^{-1}$ of bridged sites and silanols were calculated using the molar extinction coefficients determined by Emeis (bridging OH groups, around 3630 cm^{-1}) and Gallas et al. (silanols, around 3740 cm^{-1}) equal to $3.7\text{ cm}.\mu\text{mol}^{-1}$ and $3\text{ cm}.\mu\text{mol}^{-1}$ ^[246,247] respectively.

As seen in Figure 6- 1 and Table 6- 1, after the SiCl_4 treatment the band characteristic of germanol decreased (IM-12_Si₃Ge) while the amount of silanols in the latter sample increased (from 94 to $330\text{ }\mu\text{mol.g}^{-1}$). This might indicate that some germanols were replaced by silanols. The amount of silanols strongly increased after the first PAC treatment from 330 to $717\text{ }\mu\text{mol.g}^{-1}$), likely indicating that silanols defects were formed because of the breaking of the Si-O-Ge bonds. However, further treatments reduced the silanols amount which might reflect that some of these defects were filled through the incorporation of Al. For example, this reduction reached

550 $\mu\text{mol.g}^{-1}$, for sample 'IM-12_Si₃Ge_3PAC_2HCl' having the highest microporosity and a good crystallinity. Moreover, after the PAC treatments, two new bands appeared at 3670 and around 3636-3629 cm^{-1} . For the band at 3670 cm^{-1} (EFAL or surface aluminols [154,245]), even if its molar extinction coefficient is not known, we can see that after the second PAC treatment their amount was the highest and that the second HCl washing helped reducing their amounts (33 to 6 au.g^{-1}). Further treatments, led to lower incorporation of these aluminols that were usually eliminated after HCl washing.

The tiny band around 3629 cm^{-1} assigned to bridging Si-(OH)-Al and expected to behave as Brønsted acid sites^[154,156] is detected starting from the first PAC treatment. The amount of bridging Si-(OH)-Al increased after repeating these treatments. After the 5th PAC treatment, their amount decreased. This might be explained by the previously demonstrated loss of microporosity at this stage of treatment. Moreover, the HCl treatments did not lead to a decrease of the bridging groups but sometimes to their increase which might indicate the rearrangement of Al after each HCl step, from 16 to 18, 20 to 29 and 17 to 27 $\mu\text{mol.g}^{-1}$ for the third, fourth and sixth PAC treatments respectively. This is another advantage of the HCl washing step.

The amount of bridging Si(OH)Al in all samples are lower than the maximum possible concentration calculated from the unit cell of the zeolite by respecting the Löwenstein rule (1729 $\mu\text{mol.g}^{-1}$). Moreover, Table 6- 2 shows that these amounts are also low compared to the theoretical corrected concentration of bridging Si-(OH)-Al calculated in chap.5 (corrected theoretical acidity). Notably, part of this difference could be related to the quantification method, for the quantification using ²⁷Al MAS NMR, no molar extinction coefficients is needed. However, this clearly shows that the incorporation of aluminum does not generate one bridging OH group per aluminum, and that other aluminum species are generated.

Thus, from IR experiments, it can be concluded that we succeeded in introducing bridging OH groups in the structure, but in very low amounts. In the other hand, to check if the important amounts of silanols are due to external or internal SiOH. We constructed different IM-12 zeolites with internal defects.

6.2 Construction of bulk models with defects

In chapter 4, we constructed some models for silanols located at the external surface. To compare the structure of these sites with that of internal silanols, we constructed different models by creating defects in the bulk of the silicogermanate IM-12 zeolite.

For this purpose, starting from a UTL silicogermanates with Ge occupying half of the d4r, we, we considered 2 possibilities of Ge distribution: Ge in the same s4r, or Ge alternated between the two s4r of the double ring (Figure 6- 2). Removing Ge from the IM-12 bulk leads to the formation of germanols/silanols. For this purpose, we constructed different bulk models by removing in the both considered possibilities, the following amount/ positions:

- removing 1 Ge

- removing 2 Ge from different s4r
- removing 2 separated Ge from the same s4r
- removing 2 consecutive Ge from the same s4r
- removing 3 Ge from the same s4r
- removing 4 Ge from the same s4r

Finally, we simulated a bulk after full removal of the d4r giving two separated layers similar to surface SiOH.

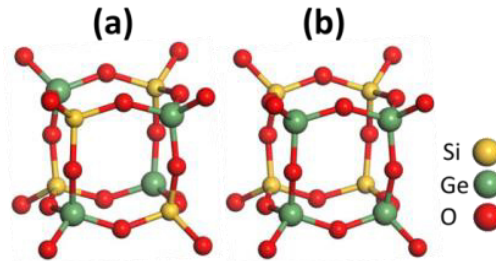


Figure 6- 2 Ge occupying half of the d4r, (a) with alternation and (b) in the same s4r.

The different models are presented in Figure 6- 3 and Figure S6- 1 to 10. The geometry optimization for all models was made following 2.3.4.

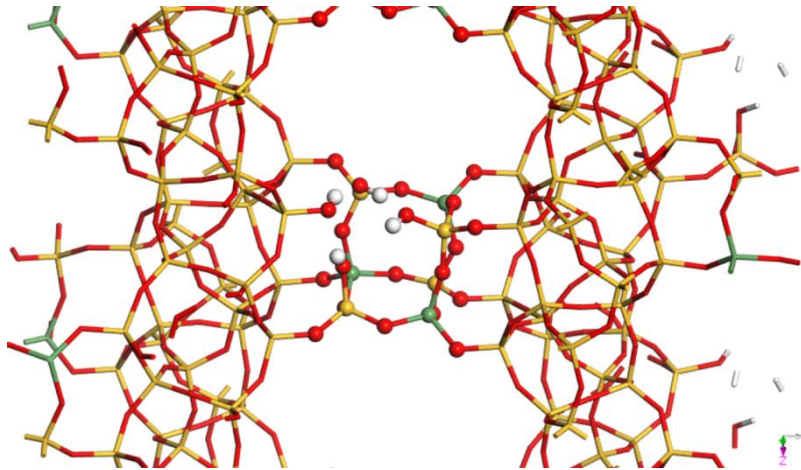


Figure 6- 3: IM-12 bulk model after removal of 1 Ge from bulk initially with Ge alternated between 2 s4r.

To compare the stability of these models, we calculated their cumulated hydration energies per d4r following Eq. 6- 1 and are represented in Figure 6- 4,

$$\Delta E_{cumulated\ hydration} = E_{SiGeOH} + n \cdot E_{[Ge(OH)_4]} - E_{SiGe} - n \cdot E_{H_2O}$$

Eq. 6- 1

With E_{SiGeOH} and E_{SiGe} , the electronic energies of IM-12 with defects and defect-less IM-12 respectively.

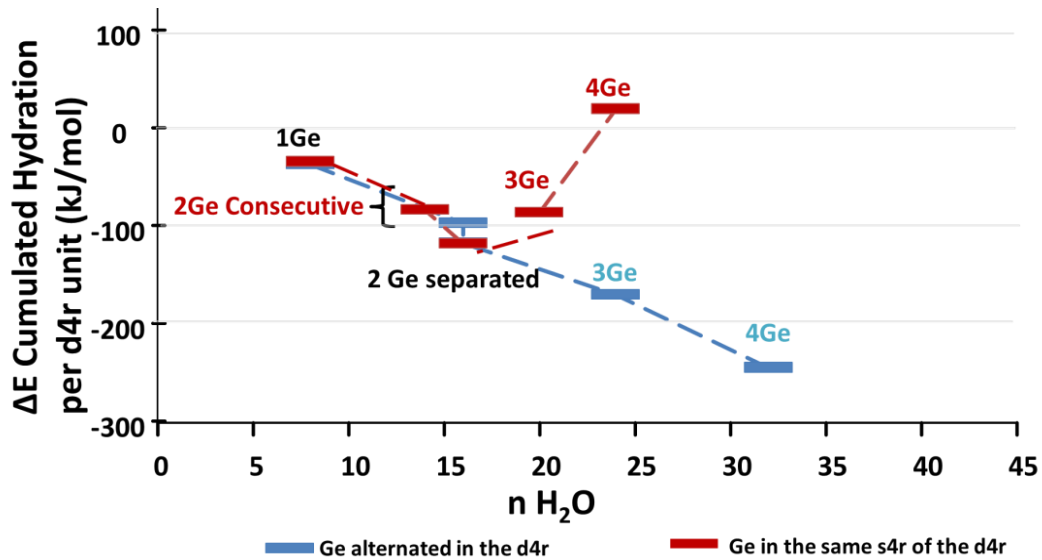


Figure 6- 4: Energies of cumulated hydration per d4r unit of IM-12 bulk zeolite with Ge occupying half of the d4r (with alternation or in the same single s4r of the d4r) and after removal of all d4r units.

As seen in Figure 6- 4, all the energies are negative except for the bulk after for the removal of 4 Ge initially located in the same s4r of the d4r (19 kJ/mol). This means that during the substitution of Ge for Al, forming internal hydroxyl groups is possible. Moreover, the initial distribution of Ge in the d4r has an important effect on the hydrolysis. For example, when Ge are alternated in the d4r, the most stable defected-bulk is after removal of 4Ge. Meanwhile, if the initial bulk had Ge in the same s4r of the d4r, the most stable defected-bulk is after removal of 2 separated Ge, Figure 6- 5. This stabilization is probably due to the hydrogen-bond network that differs from one configuration to another, and that provides stabilizing interactions.

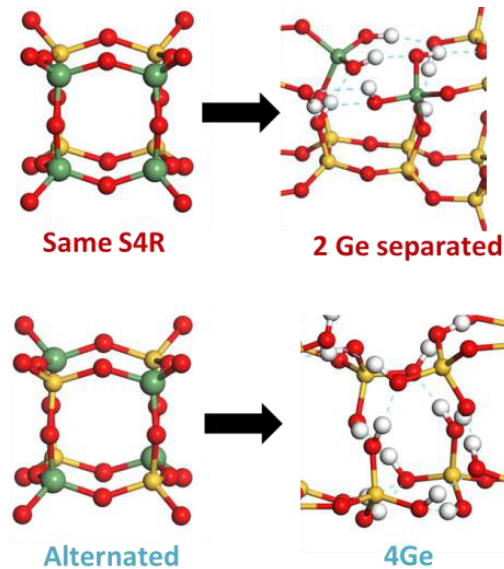


Figure 6- 5: Most stable hydrolyzed IM-12 structures depend on the initial Ge distribution. The dashed lines represent the hydrogen interactions.

6.3 Identification of the hydroxyl groups by ^1H MAS NMR

^1H MAS NMR allows the determination of the OH groups and their quantification. Before the experimental measurements, the samples were dried at 200°C under vacuum for 16 hours. The measurements were made following 2.2.7.2. To attribute the different signals, we simulated using VASP the ^1H DFT NMR following 2.3.4 of the UTL bulk and the different external surfaces by varying the elemental composition. For the bulk, the spectra of several aluminosilicate forms (1 Al in the unit cell, 1 Al per d4r, Al occupying half of the d4r with alternation with Si, Al occupying the full d4r with alternation with Si and occupying the full d4r with alternation with Si after changing the bridging proton position) were simulated. We also simulated the spectra of a bulk having 2Ge and 2Al alternated in the same s4r. To check if the defects in the bulk can be differentiated from surface OH, we simulated the spectra of a silicogermanate bulk after removal of Ge leading to the formation of germanols/silanols, for this purpose we removed 1Ge, 1Ge and changed the orientations of the protons, 2 alternated Ge from the same s4r and 3Ge from the same s4r, as explained in section 6.2. Finally, we simulated a bulk after full removal of the d4r giving two separated layers similar to surface SiOH. For the siliceous external surfaces, the ^1H MAS NMR spectra of the surfaces along (010)-cleavage 1 and (100)-cleavages 1 and 3 were simulated to represent the isolated, donor/acceptor silanols (Figure 6- 6) but also silanols occupying a s4r or a d4r at the surface.

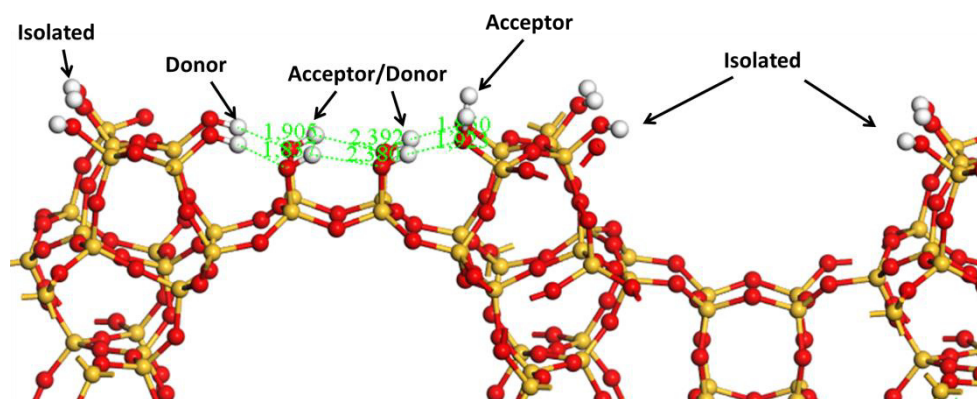


Figure 6- 6: Interactions between hydroxyls of silanols (H - - OH) illustrated with dashed lines at the surface of (010) cleavage 1.

To identify the nature of the hydroxyl groups connected to Al, we simulated aluminosiliceous cleavages 1 along (010) and (100), for each cleavage the spectra with bridging $-\text{Si}(\text{OH})-\text{Al}$ and $\text{Al}-\text{H}_2\text{O}$ were simulated. In addition, the spectra for the cleavages 3 along (100) with $\text{Al}-\text{H}_2\text{O}$ and after dehydration were also calculated. Finally, to check if the impact of a neighboring Ge can be distinguished from that of Si or Al, the spectra of a silicogermanate along (010)-cleavage 1 and those of aluminosilicogermanate (H on the oxygen between the Si and Al, between Ge and Al or forming $\text{Al}-\text{H}_2\text{O}$) were also modeled. The experimental spectra and the DFT calculated chemical shift values are represented in Figure 6- 7.

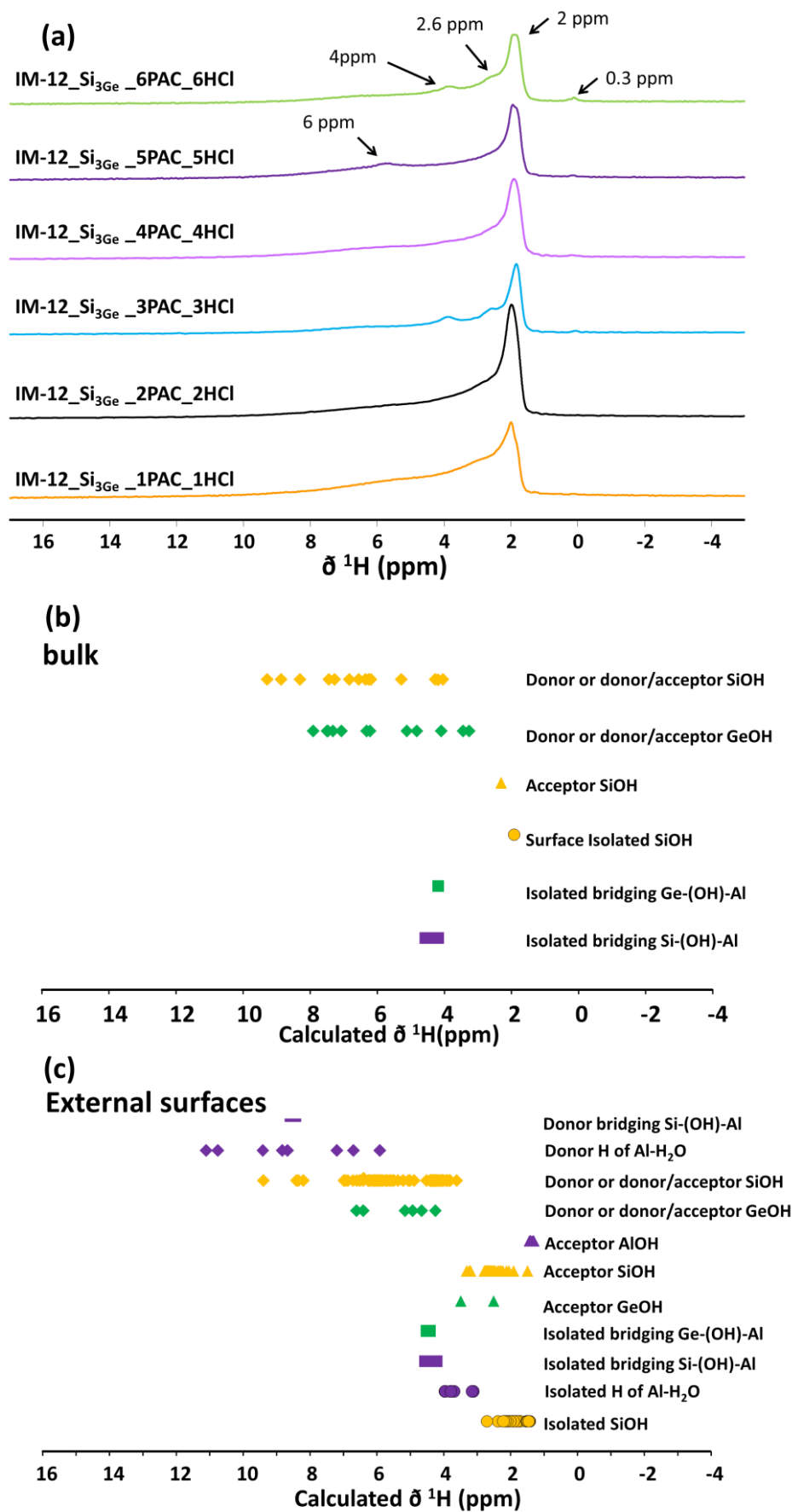


Figure 6- 7: (a) ¹H MAS NMR of post-treated IM-12 zeolite after drying for 16 hours at 200°C under vacuum. (b) and (c) correspond to ¹H NMR DFT calculated chemical shifts of bulk and external surfaces respectively.

6.3.1 Assignment of the ^1H MAS NMR spectra

The experimental ^1H MAS NMR spectra of the post-treated samples, show five signals close to 6, 4, 2.6, 2 and 0.3 ppm.

- 0.3 ppm:

The tiny signal around 0.3 ppm is assigned to the presence of extraframework Al^[248] or to isolated water molecules in the air inside the rf coil but outside the sample^[249].

- Close to 2 ppm:

For other zeolites, the signal close to 2 ppm is usually attributed to isolated/acceptors external surface silanols^[249] or to defects in the framework and in amorphous parts of the sample^[250]. The DFT calculations (Figure 6- 7b,c) assign this zone to isolated and to hydrogen bond acceptor silanols, although some of the hydrogen-bond acceptor Si-OH are also expected at higher chemical shift.

- Close to 2.6 ppm:

Based on the literature, the peak close to 2.6 ppm is assigned to extraframework Al(OH)_n bonded to framework oxygen atoms^[249,251]. In our DFT calculations, we did not consider the interactions with extraframework species thus we can rely on the literature for this assignment. Our DFT calculations however, suggest that some silanols, in particular hydrogen-bond acceptor silanols, may also contribute to part of this peak.

- Close to 4 ppm:

Signals close to 4 ppm account for bridging Si-(OH)-Al^[249-252] behaving as Brønsted acid sites. This attribution is confirmed by our DFT calculations were isolated bulk and surface bridging Si-(OH)-Al are related to this zone. Moreover, according to our calculations, this part of the spectrum can be related to isolated bridging Ge-(OH)-Al. In addition, the calculations show that isolated Al-(H₂O) also resonate at this chemical shift range meaning that it is not exclusively related to bridging aluminols.

- Close to 6 ppm:

The broad signals in this zone are usually attributed to adsorbed residual water molecules^[250,251]. Our DFT calculations show that the chemical shifts above 5 ppm are related to hydrogen-bond donor groups in SiOH, GeOH, bridging Si-(OH)-Al or even in Al-(H₂O). Moreover, these hydrogen bond donor OH groups are correlated to the hydrogen-bond length: the longer the OH bond, the lower is the chemical shift, Figure 6- 8. The same trend was seen for γ -Al₂O₃ surface and edge models^[253].

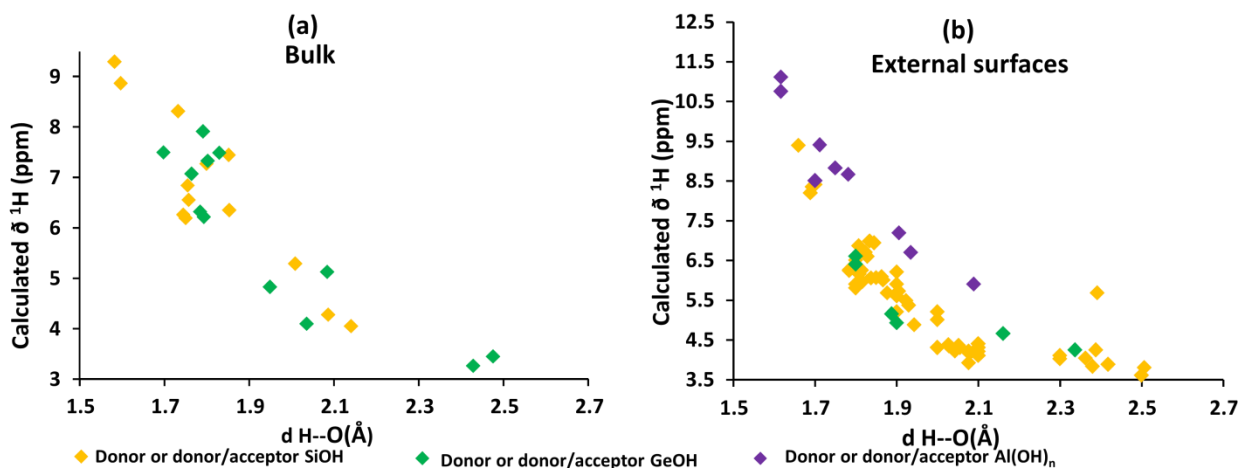


Figure 6- 8: Correlation between H-bond length and ^1H chemical shift for H-bond donor in the bulk (a) and in the different external surfaces (b).

6.3.2 Study of the post-treatment effect using ^1H MAS NMR

Based on these chemical shifts attributions, we can see that sample ‘IM-12_Si₃Ge_1PAC_1HCl’ has a signal at 2 ppm related to isolated or acceptor SiOH but also has a broad band around 2.6 ppm assigned to extraframework aluminols. The broadening might be caused by the dipole-dipole interactions. The intensity of the silanols signal around 2 ppm strongly increased in sample ‘IM-12_Si₃Ge_2PAC_2HCl’ and might reflect the creation of defects. However, for sample ‘IM-12_Si₃Ge_3PAC_3HCl’, the intensity of this signal decreased and a signal around 4 ppm appeared. The latter can be attributed to bridging Si-(OH)-Al or to isolated water molecules adsorbed on a Al indicating the presence of bulk/surface aluminols helping in the reduction of silanols defects. In addition, two well-shaped bands are detected for this sample, at 0.3 and 2.6 ppm reflecting the increase of the amounts of extraframework aluminols and maybe the presence of isolated water outside the sample (0.3 ppm). These results are in agreement with the FTIR results showing that in comparison to the previous samples, this sample has higher amounts of EFAL/surface AlOH (3670 cm⁻¹) and Si-OH-Al (3636-3629 cm⁻¹). After the 4th PAC/4th HCl treatments, the peak of bridging OH groups (4 ppm) was not detected and the signal at 2.6 ppm strongly decreased reflecting the reduction/elimination of previously incorporated Al. Sample ‘IM-12_Si₃Ge_5PAC_5HCl’ has an additional broad band at 6 ppm belonging to the presence of donor groups. Finally, this band decreased for sample ‘IM-12_Si₃Ge_6PAC_6HCl’ and the tiny bands around 4 and 2.6 ppm reappeared indicating the reincorporation of Al. For the last three samples, the tiny signal at 0.3 remained unchanged. To have a clearer determination of which protons are in vicinity of Al, the $^1\text{H}/^{27}\text{Al}$ TRAPDOR spectra were measured for samples ‘IM-12_Si₃Ge_3PAC_3HCl’ and ‘IM-12_Si₃Ge_5PAC_5HCl’.

6.3.3 Assignment and comparison of $^1\text{H}/^{27}\text{Al}$ TRAPDOR spectra

$^1\text{H}/^{27}\text{Al}$ TRAPDOR (transfer of populations in double resonance) NMR allows to study individually the different aluminum species through their dipolar coupling to nearby proton

nuclei. Thus it can be used to distinguish between the Brønsted, Lewis acid sites and non-framework Al. The general principle of this technique and the conditions of the experimental measurements are presented in 2.2.7.2. Along the experiment, a continuous ^{27}Al irradiation is applied during the evolution of a spin echo pulse sequence executed on the ^1H channel, as a result, the signals of proton groups that are strongly coupled with Al will be eliminated while those of proton groups not interacting with Al are not affected^[250].

As seen in Figure 6- 9, the $^1\text{H}/^{27}\text{Al}$ TRAPDOR of sample ‘IM-12_Si₃Ge_3PAC_3HCl’ exhibits 5 peaks at 6, 4, 2.6, 2 and 0.3ppm.

The decrease in the intensity of the signals around 6, 4 and 2.6 ppm highlights the presence of donor OH groups, bridging Si-(OH)-Al and extraframework aluminols respectively. In the other hand, after ^{27}Al irradiation, the peaks at 2 ppm and 0.3 remained unchanged. This reflects that these two signals are not corresponding to groups interacting with Al. This confirms that the band at 2 ppm correspond to SiOH and suggests that the peak at 0.3 ppm is not attributed to extraframework Al but rather to other hydroxyl groups such as isolated water molecules outside the sample^[249].

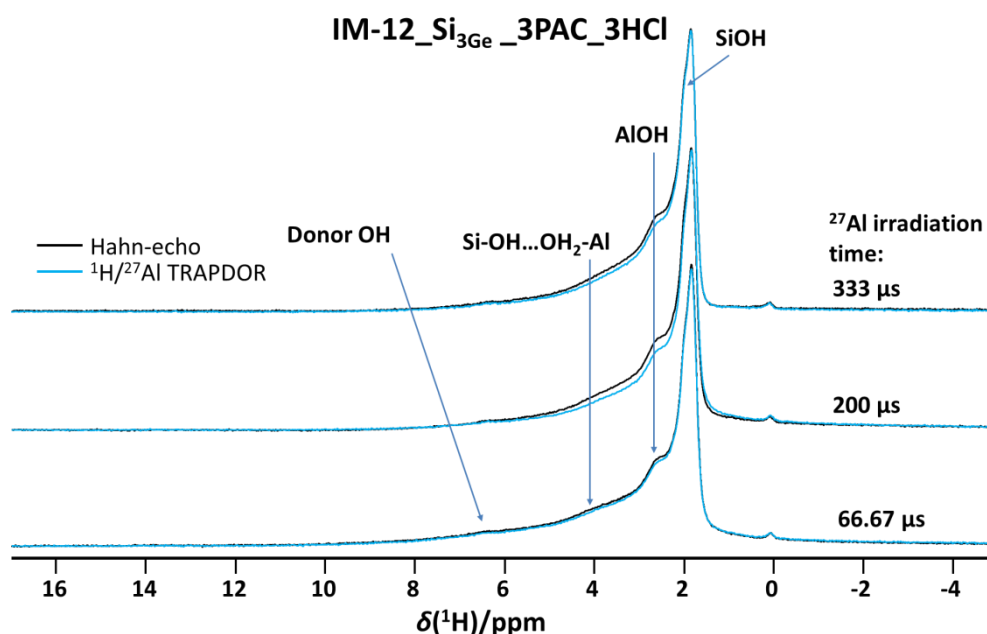


Figure 6- 9: $^1\text{H}/^{27}\text{Al}$ TRAPDOR spectra of sample ‘IM-12_Si₃Ge_3PAC_3HCl’ at different ^{27}Al irradiation time.

6.4 Brønsted and Lewis acidities measured by pyridine adsorption

In the previous section, the nature of OH groups was defined using FTIR and $^1\text{H}/^{27}\text{Al}$ MAS NMR spectroscopies and quantified using FTIR spectroscopy. Only the bridging OH groups were considered a priori as Brønsted acid sites which may exclude the acidity related to other sites. To discriminate between Brønsted acid sites (BAS) and Lewis acid sites (LAS), the adsorption and thermodesorption at 150°C of pyridine followed by FTIR were measured.

After pretreatment under secondary vacuum at 450°C for 10 hours and contact with pyridine at room temperature, the zeolites undergo desorption stages (150°C for 2 hours, 250°C, 350°C and 450°C for 1 hour). Figure 6- 10 shows that bridging Si-OH-Al (3629 cm⁻¹) are accessible to the pyridine since after contact with pyridine their corresponding band disappeared, as well as that of most silanols.

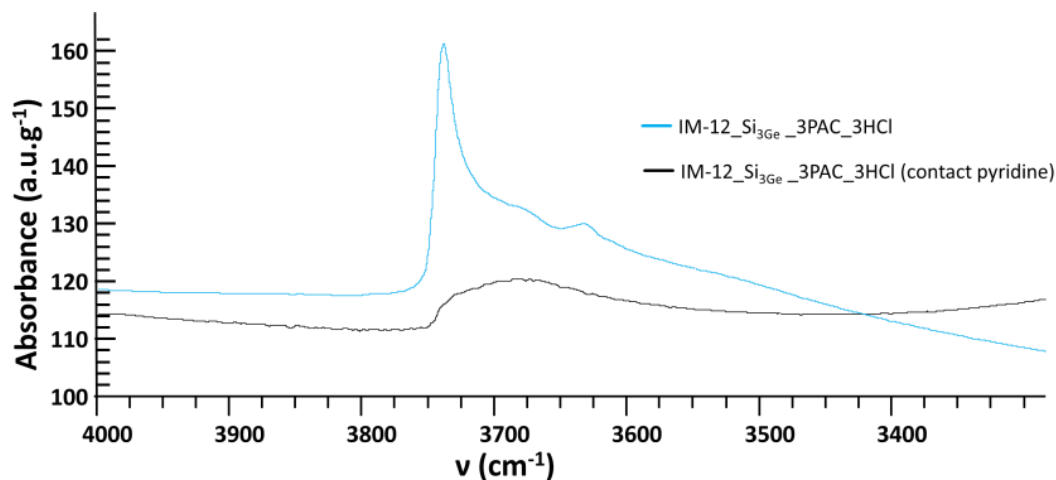


Figure 6- 10: OH region of the spectrum of IM-12_Si₃Ge_3PAC_3HCl activated at 450°C and after contact with pyridine at ambient temperature for 10 min.

The FTIR spectra after desorption at 150°C in Figure 6- 11, show a band at 1545 cm⁻¹ (ring vibration of the C-C bonds of the pyridinium ion) indicating that these are strong acid BAS sites^[111,154,156,246]. The band at 1455 cm⁻¹ (vibration of C-C bond due to coordinated pyridine) reflect the presence of LAS sites^[154,246] and the one at 1445 cm⁻¹ is related to physisorbed pyridine^[154]. The molar extinction coefficient of pyridine adsorbed on IM-12 is not defined, thus we used the coefficients of Emeis (measured on 5 zeolites and 2 amorphous silica-aluminas)^[246] assuming that they are independent of the catalyst or the strength of the acid site. Their values are 1.67 and 2.22 cm.μmol⁻¹ for the Brønsted and Lewis acid sites respectively. Using these values, the amounts of BAS and LAS are calculated following 2.2.8 and presented in **Table 6- 2**. The BAS and LAS amounts reflect the importance of the HCl washing step, usually leading to a decrease of the Lewis acid sites (71 to 34 μmol.g⁻¹) and to an increase of the Brønsted acidity (19 to 24 μmol.g⁻¹). This suggests that a rearrangement of the acid sites has taken place.

It is also seen that the Brønsted site amounts are much lower than the corrected theoretical acidity obtained by ²⁷Al MAS NMR where no molar extinction coefficient is considered but also because not all the Al^{IV} are strong enough to give a pyridinium ion. From the BAS and LAS amounts, we can see that repeating the treatments increased the amount of acid sites until reaching a maximum with 3 PAC(/HCl) treatments. With additional post-treatment steps, the acidity decreases suggesting that the optimal number of PAC+ HCl washing is 3. Figure 6- 12 highlights the good correlation between the amounts of BAS and bridging Si-(OH)Al.

Compared to other zeolites, the amounts of Brønsted and Lewis acid sites are very low, for example, the ZSM-5 having a total Si/Al ratio of 40, has 243 and 38 $\mu\text{mol.g}^{-1}$ of BAS and LAS respectively^[254].

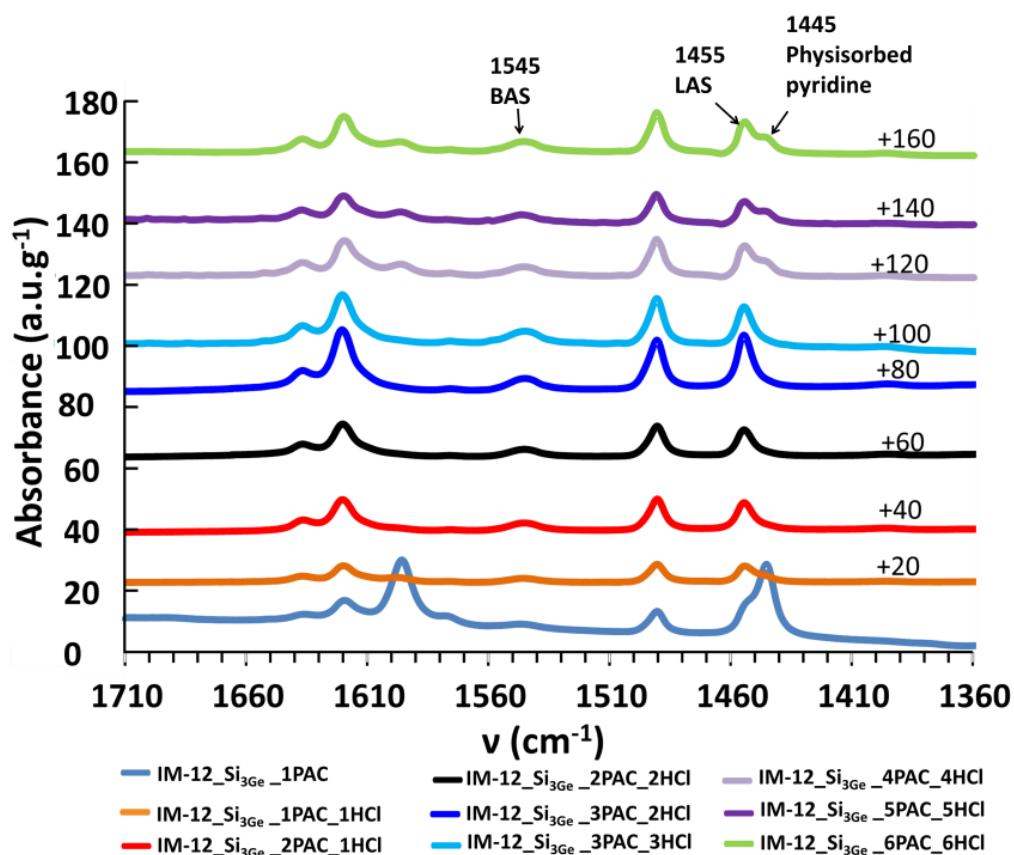


Figure 6- 11: Pyridine zone of IR spectra after subtraction of the activation spectra and the thermodesorption of pyridine at 150°C on the PAC treated IM-12 samples.

Table 6- 2: Amounts of acid sites following theoretical, corrected and IR approximation of IM-12 samples treated with PAC/HCl.

Sample	$\mu\text{mol.g}^{-1}$						
	Theoretical acidity		Corrected Theoretical acidity $^{27}\text{Al MAS NMR}$ (Al ^{IV})	IR			
	XRF	$^{27}\text{Al MAS NMR}$		OH zone Si-(OH)-Al	Pyridine adsorption BAS LAS Total		
IM-12 Si ₃ Ge 1PAC	912	902	195	4	19	71	90
IM-12 Si ₃ Ge 1PAC 1HCl	410	414	156	3	24	34	58
IM-12 Si ₃ Ge 2PAC 1HCl	781	1013	342	9	46	75	121
IM-12 Si ₃ Ge 2PAC 2HCl	357	415	221	8	43	69	112
IM-12 Si ₃ Ge 3PAC 2HCl	713	829	441	16	70	137	207
IM-12 Si ₃ Ge 3PAC 3HCl	586	610	232	18	81	96	177
IM-12 Si ₃ Ge 4PAC 4HCl	497	497	248	29	55	51	106
IM-12 Si ₃ Ge 5PAC 5HCl	421	453	187	9	42	46	88
IM-12 Si ₃ Ge 6PAC 6HCl	529	594	271	27	63	57	120

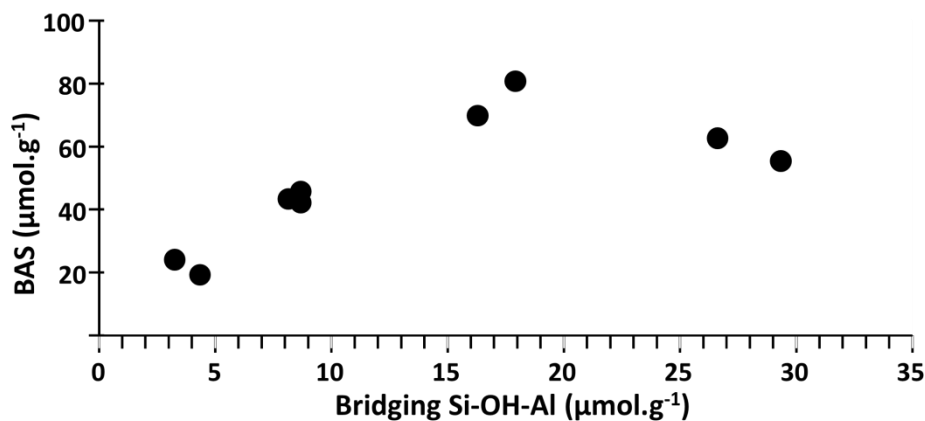


Figure 6- 12: Variation of amounts of Brønsted acid sites against the amount of bridging Si-OH-Al.

6.5 Conclusion

The spectroscopic analyses confirmed the successful incorporation of Al in the IM-12 using PAC post-treatments, although the amount of bridging acids sites is low with respect to other zeolites and with respect to expectations from the aluminum content in the post-treated zeolites. In addition, the acidity results are in agreement with the structural characterization presented in the previous chapter. Samples IM-12_Si₃Ge_3PAC and IM-12_Si₃Ge_3PAC_3HCl had the highest microporous volume and acidity. By doing further treatments, a loss of the crystallinity, microporosity and acidity is detected suggesting the creation of defects. One can say that the optimal conditions for the optimization of IM-12 is to do a SiCl₄ treatment followed by 3PAC and HCl washings. The next step is to check if these IM-12 catalysts, having only few BAS and LAS sites compared to other zeolites such as ZSM-5 and CBV-712 and to the expected theoretical acidity, are active catalytically.

7. Catalytic testing of IM-12 in the hydroisomerization of hydrocarbons

In the previous chapters, we showed that obtaining IM-12 zeolites exchanged with small amounts of aluminum is possible, leading to small amounts of Brønsted acid sites. It is now important to know whether these features lead to efficient catalysts. In the present chapter, a series of bi-functional catalysts with IM-12 as acid phase, prepared by PAC treatments and some of those prepared by AlCl_3 treatments, are tested for the hydroisomerization of n-alkanes. Platinum is used as the hydro-dehydrogenation phase. In the first section, the results for the hydroisomerization of n-decane (10 carbon atoms) are presented. This model reaction gives information about the pore topology and the possible localization of the active sites^[180,181,184,186,187]. The catalytic conversion of alkanes with different carbon chain lengths might give insights on the accessibility of the active sites. Hence, the second part of this chapter discusses the hydroisomerization of n-hexadecane (16 carbon atoms).

7.1. Hydroisomerization of n-decane

Nine bi-functional catalysts were prepared using IM-12 post-treated with the PAC treatments, plus three samples containing AlCl_3 -post-treated samples. They were then tested in the hydroisomerization of n-decane (2.1.6.1). In addition, the zeolite treated only with SiCl_4 was also tested as an acid phase. For this test, the Pt was introduced in the samples by incipient wetness impregnation of the zeolites (2.1.5.1). These samples were compared based on their conversion, isomerization and cracking selectivity, to understand the effect of the alumination method (PAC vs. AlCl_3), number of PAC treatments and effect of HCl washing.

7.1.1. Hydroisomerization of n-decane over Pt/IM-12_ Si_3Ge

To verify whether the IM-12 zeolite treated with SiCl_4 (which still has few amounts of Ge) is active or not in the absence of Al, the IM-12_ Si_3Ge was impregnated with Pt (0.3 wt. %) and tested in the hydroisomerization of decane.

The conversion of n-decane was plotted against the reaction temperature (Figure 7- 1.a). The temperature at 50% of conversion is an indicator of the mass activity of the zeolite. It shows that IM-12_ Si_3Ge has a very low activity since the decane was only converted at very high temperatures, 310°C at 50% of decane conversion. The temperature at 50% of conversion is around 190°C for other zeolites like the USY type zeolite^[255]. According to the hydroconversion of decane mechanism presented in chapter 1, skeletal isomerization is prior to cracking. It is thus usual to report the isomerization and “cracking” selectivity as a function of the conversion (Figure 7- 1.b). The latter shows that most products are not C_{10} isomers products but cracked products. The distribution of the cracked products according to the carbon number of the fragments at 35% hydrocracking in (Figure 7- 1.c, shows a high amount of C_1 and a very high total amount of cracked products (if only primary cracking occurs, 100 moles of n-decane

should give 200 moles of cracked products). This feature can be assigned to the absence of acidity in the zeolite, that makes the catalyst behave as a monofunctional metallic catalyst, rather than a bi-functional one. Thus indicates that the dominant reaction that takes place is hydrogenolysis. This confirms the need of aluminations steps in the preparation of the zeolite in order to generate some Brønsted acidity.

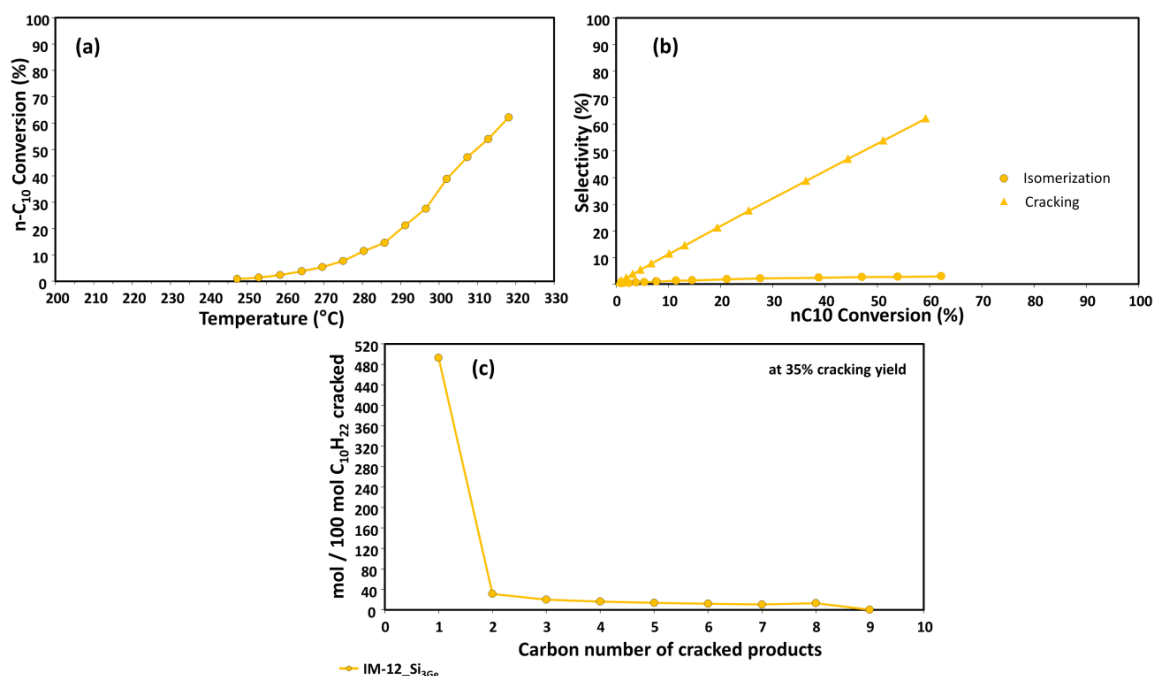


Figure 7- 1: (a) Conversion of n-decane against reaction temperature, (b) yield of n-decane skeletal isomers and cracked products against n-decane conversion, (c) carbon number distribution of cracked products at 35% n-decane cracking yield of the 0.3 wt.% Pt/IM-12_Si_{3Ge} catalyst.

7.1.2. Hydroisomerization of n-decane over IM-12 bi-functional catalysts prepared by PAC treatments

7.1.2.1. Activity and isomerization selectivity

The bi-functional catalysts prepared by PAC treatments and incipient wetness impregnation with Pt have as an acid phase the IM-12 zeolite with different Si/Al ratios. Since the amounts of Al are low in the different samples, the amount of impregnated Pt was fixed to 0.3 wt.%. The representation of the conversion of n-decane against the reaction temperature (Figure 7- 2.a) shows that compared to the non-aluminated sample (Figure 7- 1.a), all the catalysts are more active. The temperature at 50% of decane conversion representing the mass activity varies between 156 and 190° for the PAC treated IM-12 samples, while for USY zeolites, these temperatures are of 192, 210 and 252°C with Si/Al of 5.8, 13 and 30 respectively^[255]. Moreover, it is seen that samples treated 3 times with PAC, with or without acid washing, have the highest activities (Figure 7- 2.a and b). These two figures also show that the activity is not linear with the total amount of Al^{IV} measured by ²⁷Al MAS NMR (5.3.2.2.2) but rather depends to the number of treatment that may affect the type of acidity, such as the Brønsted acidity. This is confirmed by Figure 7- 3, showing that the activity increases with the amount of BAS measured

by pyridine adsorption. To check this effect, we calculated the turnover frequency (TOF), in s^{-1} of Brønsted acid sites according to Eq. 7- 1:

$$TOF = \frac{F_{0(Alkane)}}{w_{cat.} * n_A} \ln\left(\frac{1}{1-x}\right)$$

Eq. 7- 1

with $F_{0(Alkane)}$ as the molar flow of n-decane at the entrance of the reactor ($\mu\text{mol}\cdot\text{s}^{-1}$), $w_{cat.}$ is the mass of the catalyst (g), n_A is the amount of Brønsted acid sites per gram of catalyst ($\mu\text{mol}\cdot\text{g}^{-1}$) calculated from pyridine adsorption (Table 6- 2) and x is the n-decane conversion at 161°C. The TOF values represented in Table 7- 1 show that samples IM-12_Si₃Ge_3PAC_2HCl and IM-12_Si₃Ge_3PAC_3HCl having the highest amounts of Brønsted acidity have also the highest TOF of the Brønsted acid sites. This means that the active sites differ from one catalyst to another, in terms of nature and/or location.

Following the post-treatment sequence, it also shows that the TOF of the Brønsted acid sites of the catalyst increases until reaching the third PAC treatment. Afterwards, a loss in the activity is detected.

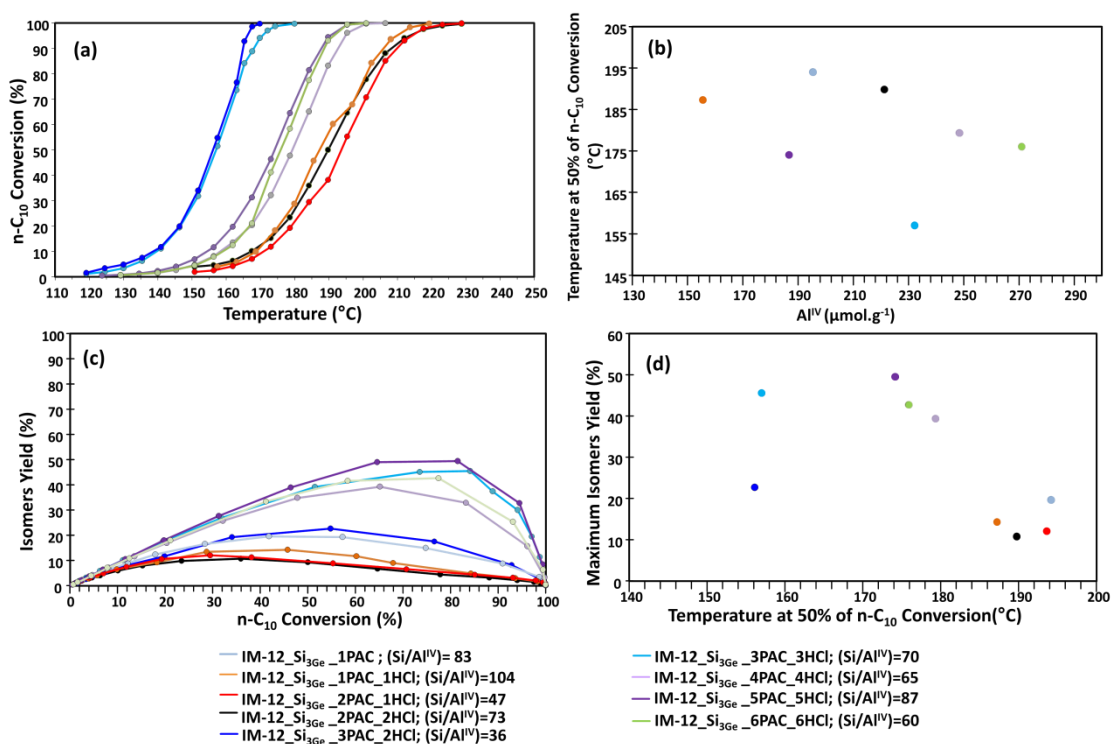


Figure 7- 2: (a) Conversion of n-decane against reaction temperature. (b) Temperature at 50% of n-decane conversion against the amount of Al^{IV} calculated following the corrected theoretical acidity of ²⁷Al MAS NMR at 54ppm. (c) Yield of n-decane skeletal isomers against n-decane conversion. (d) Maximum isomers yield against the temperature at 50% of n-decane conversion of 0.3 wt. % Pt/IM-12 bi-functional catalysts with IM-12 treated with PAC.

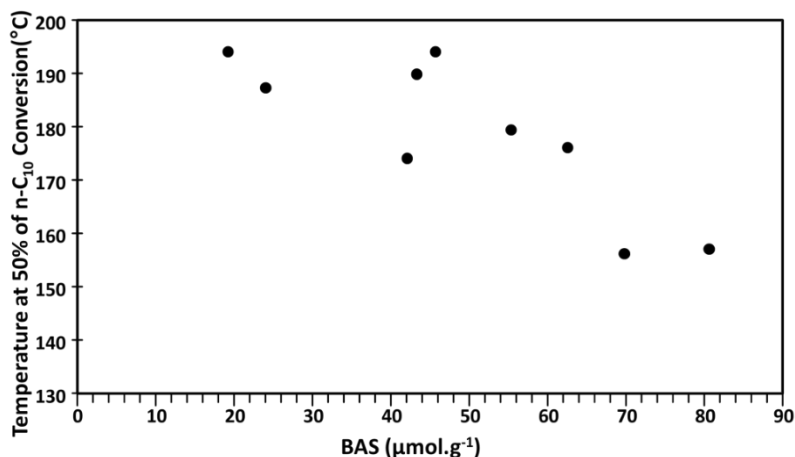


Figure 7- 3: Variation of the temperature at 50% of n-decane conversion against the amount of Brønsted acid sites of IM-12 PAC post-treated samples.

The yield of the skeletal isomers against the n-decane conversion is presented in Figure 7- 2.c. As expected, two types of reaction products are observed: skeletal isomers and cracked products. For a given solid acid, the maximum isomerization yield is attained when the balance of acidity and (de)hydrogenation is reached. Just like the mass activity and the turnover frequency, the maximum isomerization yield is not related to the Si/Al^{IV} ratio but to the effect of the treatment (Figure 7- 2.d.). An important increase of the maximum isomerization yield is detected after the third HCl washing (from 23 to 46%). Sample IM-12_Si₃Ge_5PAC_5HCl has the highest isomerization yield, Figure 7- 2.c and d. However, sample IM-12_Si₃Ge_3PAC_3HCl corresponds to the best compromise between the activity and the selectivity for decane skeletal isomers. Comparing to USY zeolites, having isomers yield around 50% with higher amounts of Al (Si/Al varying between 5.8 and 30, Figure 7- 4^[255]) reflects that the most selective IM-12 catalysts have interesting selectivity (slightly lower than USY). These differences support the fact that active sites may exhibit different features from one zeolite to another, in terms of nature and / or location.

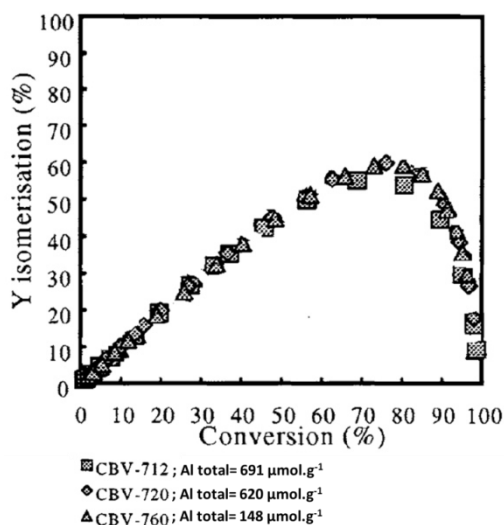


Figure 7- 4: Yield of n-decane skeletal isomers against n-decane conversion of USY type zeolites. The total amount of Al was measured using ammonia TPD. Adapted from^[255].

7.1.2.2. Detailed analysis of the isomers distribution: insights toward localization of the active sites

The PCP mechanism (1.4.2.1) leads to the formation of four positional isomers of methylnonane (2-, 3-, 4- and 5-methylnonane). All of them were detected for all samples. Isomers with methyl on 2- and 5- positions are formed via one PCP intermediate (or transition state) while 3- and 4- can be formed via two possible routes (Figure 7- 5).

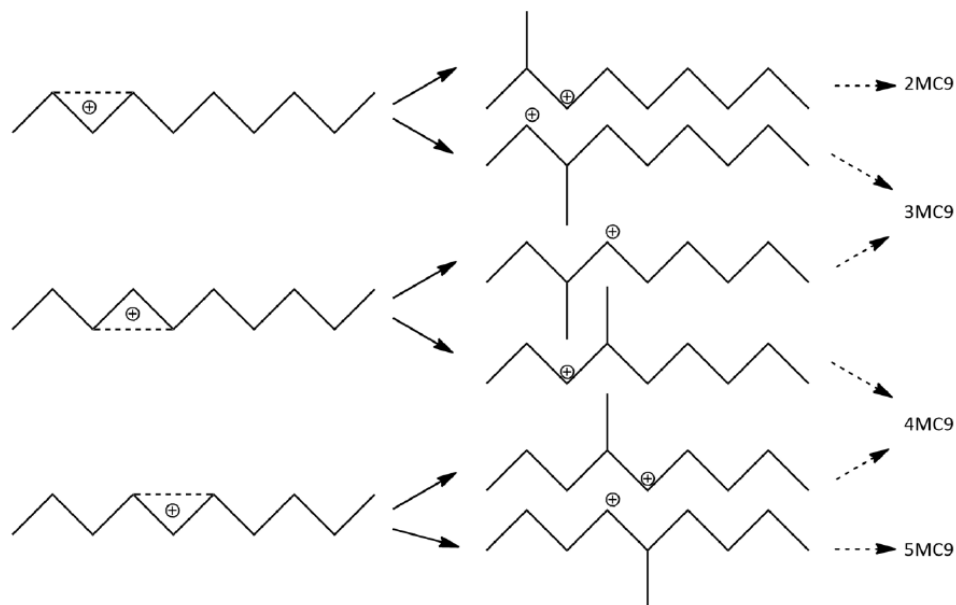


Figure 7- 5 : Formation of methylbranched n-decane skeletal isomers via protonated cyclopropane (PCP) structures. Adapted from ^[184].

Since 2-methylnonane is the less bulky isomer, for the quantification of shape selectivity, the differences in size and geometry of the transition state or differences in the diffusion of olefins from acid sites to metals, a refined constraint index (CI°) can be defined. It is the ratio of the yield of 2-methylnonane to 5-methylnonane at 5% isomerization yield (1.4.3). The constraint index CI° in Table 7- 1, show that before the third treatment, this index is higher than 2.7 thus characteristic of pore mouth catalysis^[256]. After the third treatment, the shape selectivity decreased. This suggests that starting from this treatment, more acid sites are incorporated inside the porosity of the zeolite. Samples IM-12_Si₃Ge_3PAC_3HCl and IM-12_Si₃Ge_5PAC_5HCl exhibit the lowest shape selectivity.

The composition of methyl-branched isomers against the decane conversion is plotted in Figure 7- 6 and in Figure S7-1. For all samples, 2-, 3- and 4-Methylnonane predominated over 5-methylnonane. In fact, the distribution of methylnonanes slightly changed with the conversion yield suggesting that the distribution at the thermal equilibrium was quickly reached^[257]. This reflects the presence of wide pores (12 MR and above)^[188].

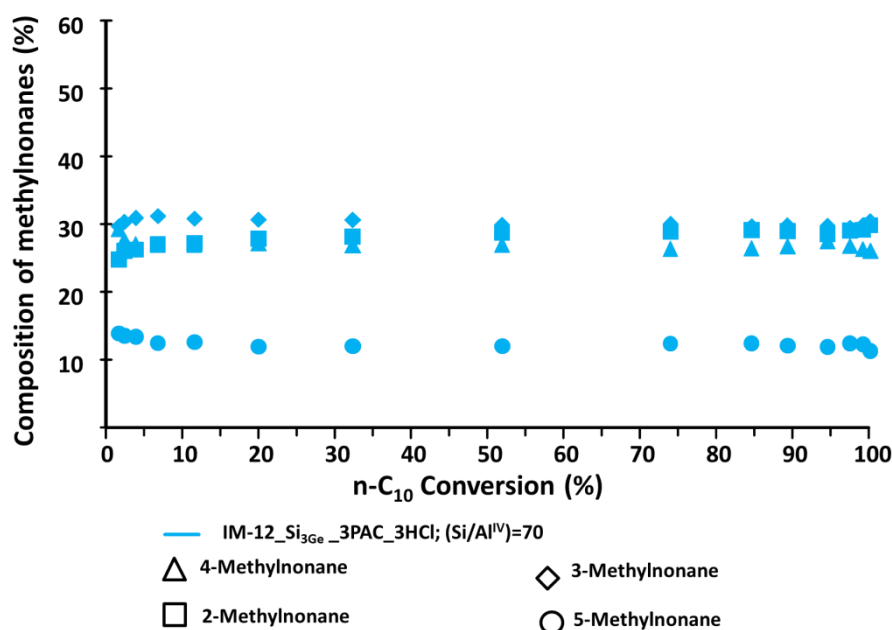


Figure 7- 6: Distribution of the four methylnonane isomers obtained from n-decane hydroconversion on bi-functional 0.3 wt.% Pt/IM-12 bi-functional catalysts with IM-12 treated with PAC.

The amount of ethyl-branched C₁₀ skeletal isomers varies between 7.4 and 12% while the propyl-branched isomers were almost absent. The presence of such considerable amount of ethyl-branched isomers (>5 %) is an indicator of large pores zeolites with at least 12-MR, such as USY type zeolite of Si/Al ratio of 5.8 having a yield of 11.7%^[255]. The ratio of 3-ethyloctane over 4-ethyloctane at 5% isomerization yield is also an indicator of steric constraints. In fact, the equilibrium of the EC₈ is reached via ethyl shifts. Thus a deviation from the thermodynamic equilibrium (0.6) reflect the presence of steric constraints limiting these shifts. Table 7- 1 show that this ratio increases from 0.31 and reaches 0.63 in sample IM-12_Si₃Ge_3PAC_3HCl then decreases afterwards. This might reflect again that these zeolites have maintained their large pores but their decane criteria and their acidic activity are dependent of the amounts of Brønsted acid sites and their localization. Sample IM-12_Si₃Ge_3PAC_3HCl is the nearest to the thermodynamic equilibrium, have the highest amount of Brønsted sites and a CI° index > 2 suggesting that this sample might have more sites near/ at the pore mouth. The amount of di-branched isomers at maximum isomerization yield were around 50% for all samples and sample IM-12_Si₃Ge_3PAC_3HCl had the highest amounts, Table 7- 1.

7.1.2.3. Analysis of the cracking products

After the isomerization, comes the cracking by β-scission. The distribution of the cracked products according to the carbon number of the fragments at 35% cracking yield is represented in Figure 7- 7. All samples, independently from the treatment number have a ‘bell shape’ characteristic of large pore zeolites with a maximum for symmetric C₅ cracked products^[176]. It also shows a symmetric cracking between the different fragments indicating the absence of secondary cracking. The small dimensionality index for all samples in Table 7- 1 (≤5) confirms

the symmetrical distribution of cracked products^[258]. The low DI values suggest the pore system to be 2- or even 3-dimensional. Such multidimensional pore system allows the fragments from the primary cracking step to be efficiently evacuated and the limited residence time prevents the fragments from undergoing an additional cracking step.

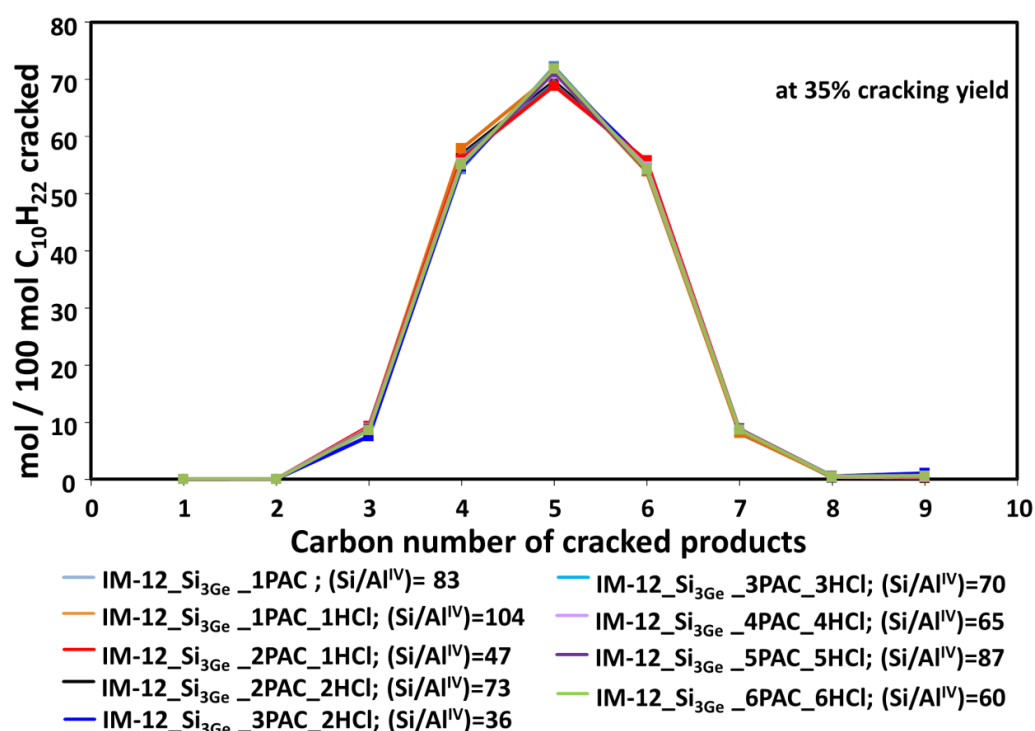


Figure 7- 7: Carbon number distribution of cracked products at 35% n-decane cracking yield of 0.3 wt.% Pt/IM-12 bi-functional catalysts with IM-12 treated with PAC.

Moreover, the yield of isopentane (Table 7- 1) exhibits high values for all samples (> 35%). For example, this yields is around 50% for USY type zeolites^[255]. In addition, its yields in the fractions of C₅ cracked products in Figure 7- 8 show that it was high in all samples. This criterion reflects the presence of large pores necessary for the formation of high branching of C₁₀. In fact, with higher C₁₀ branching, the probability for central β-scission increases giving high yields of iC₅^[184].

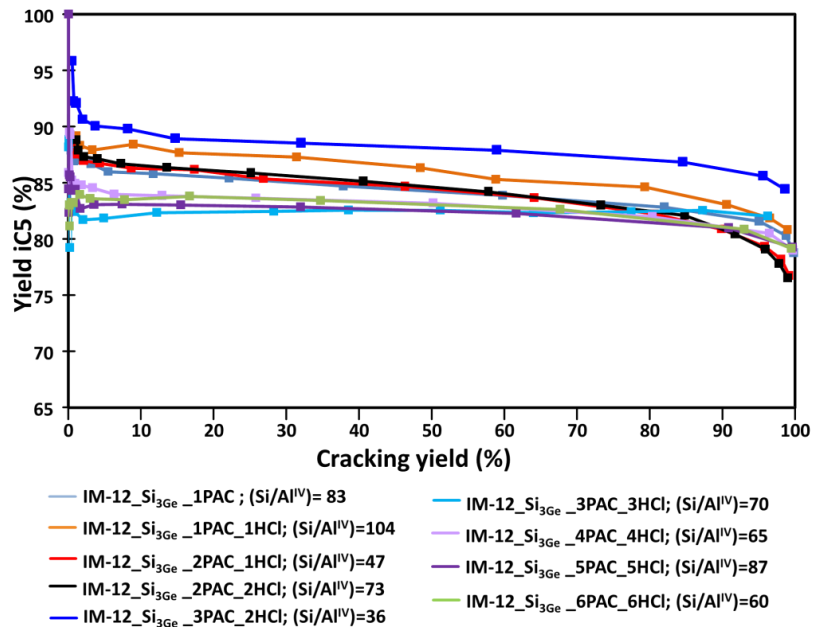


Figure 7- 8: Yield of isopentane (iC₅) as a fraction of C₅ cracked products against cracking yield of 0.3 wt.% Pt/IM-12 bi-functional catalysts with IM-12 treated with PAC.

Table 7- 1: n-decane test criteria for 0.3 wt.% Pt/IM-12 bi-functional catalysts with IM-12 treated with PAC or AlCl₃.

Sample	Decane test criteria										
	Si/Al ^{IV}	CI°	at 5% isomerization yield			at maximum isomerization yield	at 35% cracking yield				TOF ^{a,b} (10 ³ s ⁻¹)
			%EtC8 in monobranched isomers	3-EtC8/4-EtC8	%4-prC7 in monobranched isomers	%dibranched isomers	C3-C7	C4-C6	iC5	DI	
							(mol/100 mol C ₁₀ cracked)				
IM-12_Si₃Ge_1PAC	83	2.6	12.1	0.34	0	39.1	0.38	1.35	58.75	1.73	1.5 ^a
IM-12_Si₃Ge_1PAC_1HCl	104	3.02	9.4	0.47	0.1	45.8	1.02	4.10	62	5.12	1.5 ^a
IM-12_Si₃Ge_2PAC_1HCl	47	3.22	9.6	0.41	0.2	42.3	0.47	0.18	58.6	0.65	0.7 ^a
IM-12_Si₃Ge_2PAC_2HCl	73	3.11	8.7	0.57	0.0	43.8	0.74	1.33	59.54	2.07	1.0 ^a
IM-12_Si₃Ge_3PAC_2HCl	36	2.82	6.9	0.61	0	46.3	0.61	0.65	63.10	0.65	12.1 ^a
IM-12_Si₃Ge_3PAC_3HCl	70	2.05	9.6	0.63	0	51.4	0.87	0.17	63.08	1.03	9.4 ^a
IM-12_Si₃Ge_4PAC_4HCl	65	2.46	9.4	0.49	0	44.1	0.17	0.63	59.22	0.8	1.8 ^a
IM-12_Si₃Ge_5PAC_5HCl	87	2.03	9.6	0.44	0	44.9	0.02	0.94	59	0.97	3.4 ^a
IM-12_Si₃Ge_6PAC_6HCl	60	2.52	7.4	0.39	0	45.7	0.05	0.89	59.95	0.94	1.5 ^a
IM-12_Si₃Ge_Al₂₅°C_cal	550*	1.35	11.6	0.42	0	15.8	9.61	3.79	2.09	13.4	1.3 ^b
IM-12_Si₃Ge_Al₇₀°C_cal	637*	1.47	11.2	0.5	0	28.3	5.06	2.71	19.82	7.77	5.3 ^b
IM-12_Si₃Ge_Al₇₀°C_H₂O_cal	1113*	1.44	11.7	0.46	0	31.2	3.5	1.72	21.28	5.22	12.2 ^b

Si/Al^{IV} is measured by ²⁷Al MAS NMR for samples treated with PAC and with ICP for samples treated with AlCl₃ marked with an asterisk.

CI° is the refined constraint index: 2MeC9/5MeC9 at 5% isomerization

DI is the dimensionality index: |C3-C7|+|C4-C6| at 35% cracking yield.

TOF is the turnover frequency calculated following Eq. 7- 1 (a) at 161°C for PAC treated samples (b) at 247 °C for AlCl₃ treated samples. Different temperatures were chosen since samples treated with PAC are 100% converted at the temperature of 5 % of conversion of n-decane on samples treated with AlCl₃.

7.1.3. Hydroisomerization of n-decane over IM-12 bi-functional catalysts prepared by AlCl₃ treatments

Sample IM-12_Si₃Ge_Al₂₅°C_cal, sample IM-12_Si₃Ge_Al₇₀°C_cal and sample IM-12_Si₃Ge_Al₇₀°C_H₂O_cal (5.2.4) were tested in the hydroisomerization of n-decane.

7.1.3.1. Activity and isomerization selectivity

As seen in Figure 7- 9.a, the three samples are more active than the non aluminated IM-12_Si₃Ge (Figure 7-). This means that the few amounts of Al not detectable by ²⁷Al MAS NMR and FTIR spectroscopies, provided an acidic activity to the zeolite. In the other hand, all of them are less active than the samples treated with PAC (Figure 7- 2.a). This might be related to the lower Al amounts (Si/Al between 550 and 1113 by ICP).

Figure 7- 9.a and b show that the activity of the catalyst increases with the increase of the Si/Al ratio. As a consequence, samples treated at 70°C are more active than samples treated at ambient temperature even with lower amounts of acid sites per gram. Sample IM-12_Si₃Ge_Al₇₀°C_H₂O_cal has the best activity. The turnover frequency (TOF), in s⁻¹ per total acid site (from ICP) was also quantified according to Eq. 7- 1. However, due to the much lower activity of these samples with respect to PAC treated samples, it was evaluated at a higher temperature of 247°C.

The TOF values represented in Table 7- 1 confirm that sample IM-12_Si₃Ge_Al₇₀°C_H₂O_cal has the highest activity even if it has the lower amount of acid sites per gram. It also exhibits the best selectivity for isomers, Figure 7- 9.c. The maximum isomers yields plotted against the temperature at 50% of decane conversion confirm these results. However, the acidic activity of this series of catalysts is so low and probably the activity is mostly due to the cracking of decane on the metal sites (Figure 7- 10). This indicates that the selectivity is dependent of the balance between the metal sites and the acid sites rather than the intrinsic distribution of the sites. Thus sample IM-12_Si₃Ge_Al₇₀°C_H₂O_cal having the lowest total amount of Al (measured by ICP) compared to the other two samples but having a better selectivity might indicate that this sample had more Al in the framework that assured better balance with the metal sites than the other samples. However, in the absence of ²⁷Al MAS NMR measurements, due to lack of sensibility this hypothesis could not be verified.

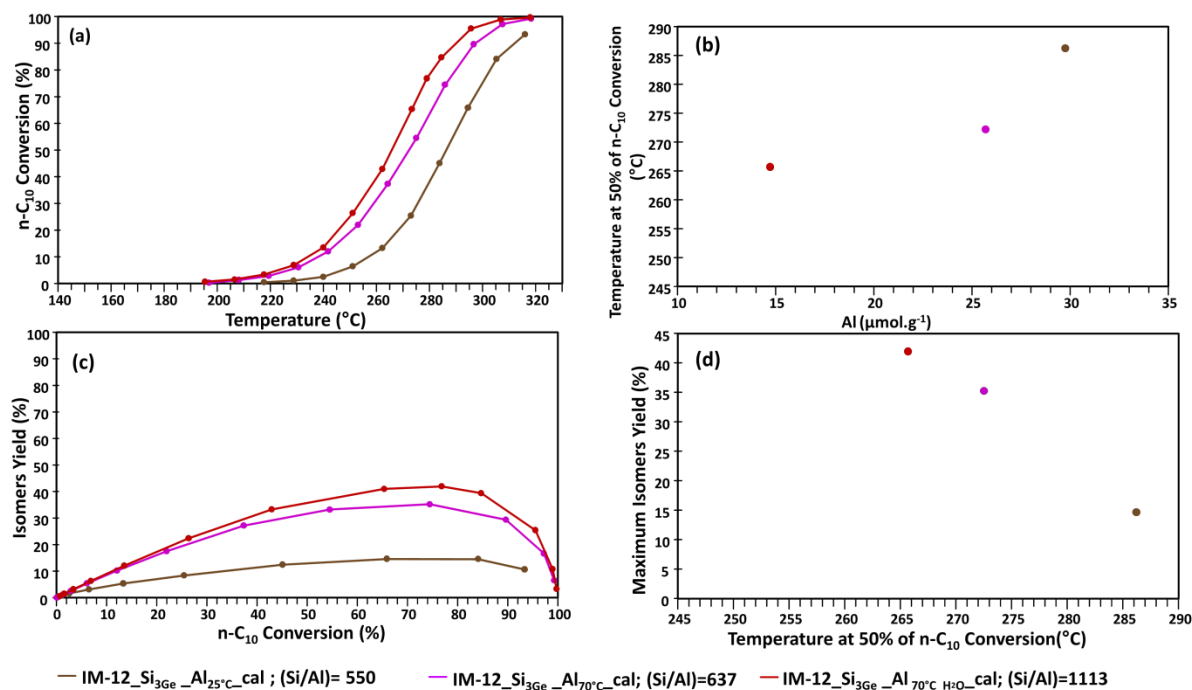


Figure 7- 9: (a) Conversion of n-decane against reaction temperature. (b) Temperature at 50% of n-decane conversion against the amount of Al calculated following the theoretical acidity measured by ICP. (c) Yield of n-decane skeletal isomers against n-decane conversion. (d) Maximum isomers yield against the temperature at 50% of n-decane conversion of 0.3 wt. % Pt/IM-12 bi-functional catalysts with IM-12 treated with AlCl₃.

7.1.3.2. Detailed analysis of the isomer distribution: insights toward localization of the active sites

All samples have a constraint index (Table 7- 1) equal to unity reflecting that no shape selectivity exists. They also present the four positional methylnonane isomers (Figure 7- 10 and Figure S7-2). At low conversion, 3 and 4 positions dominated. After reaching the thermodynamic equilibrium via alkyl shifts, 2-3-4 positions dominated over 5 methylnonane. Moreover, the three samples presented a significant amount of Ethylbranched C₁₀ skeletal isomers that require large pores. This might indicate that the sites are near the pore mouth. The amounts of di-branched isomers at maximum isomerization yield, Table 7- are high, also reflecting the presence of large pores. However, they are lower than those of PAC treated samples (31 vs. 51% by considering the highest amounts for each treatment). This could be related to lower amount of acid sites catalyzing the skeletal rearrangements.

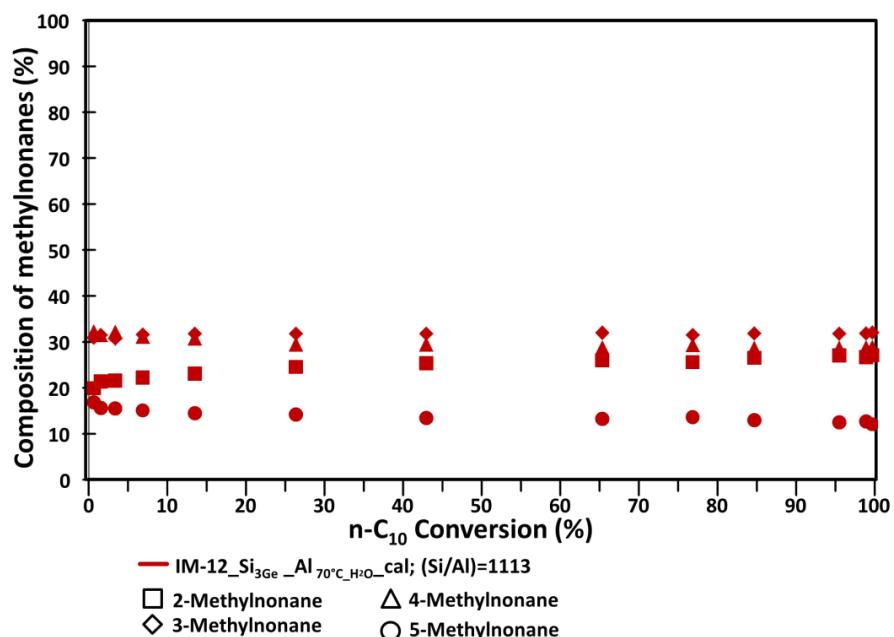


Figure 7- 10: Distribution of the four methylnonane isomers obtained from n-decane hydroconversion on bi-functional 0.3 wt. % Pt/IM-12 bi-functional catalysts with IM-12 treated with AlCl₃.

7.1.3.3. Analysis of the cracking products

These samples present cracking even at low decane conversion. Figure 7- 11 shows the distribution of the cracked products according to the carbon number of the fragments at a cracking yield of 35%. A high amount of C₁ is detected and the amount of cracked products is higher than 200 moles for 100 moles decane. This indicates that hydrogenolysis is taking place. The acidity of this bifunctional catalyst is so low and the activity of metal sites is dominating. Note that samples treated with AlCl₃ at 70°C had higher acidity compared to that treated at 25°C.

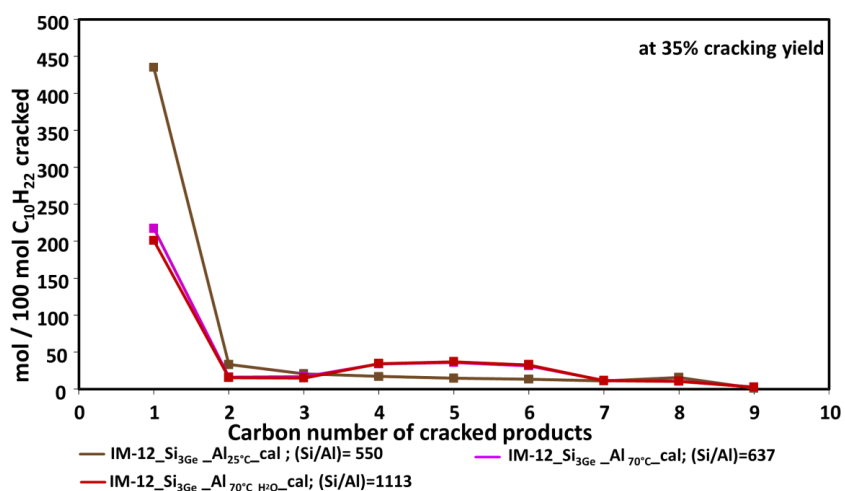


Figure 7- 11: Carbon number distribution of cracked products at 35% n-decane cracking yield of 0.3 wt. % Pt/IM-12 bi-functional catalysts with IM-12 treated with AlCl₃.

Based on the results given in this section, one can say that treating the samples with AlCl_3 at 70°C in dry ethanol with adding water ($n_{\text{H}_2\text{O}} = n_{\text{Ge}}$) is the optimal condition for the concerned parameters. The decrease of the shape selectivity depending on the treatment AlCl_3 versus PAC may suggest different localization of acid sites. However, the very low acidity of the samples treated with AlCl_3 makes the catalysts express their metallic function too strongly, in particular hydrogenolysis. The main challenge thus remains the increase of the aluminum content in these samples and to generate Brønsted acidity necessary for the acid activity.

7.2. Hydroisomerization of n-hexadecane over IM-12 bi-functional catalysts prepared by PAC or AlCl_3 treatments

For these catalytic tests, the bi-functional catalysts were prepared by mechanical mixture of the IM-12 zeolite (treated with PAC or AlCl_3) with alumina impregnated with 1% or 2% Pt following 2.1.5.2. Sample IM-12_Si₃Ge_2PAC_2HCl, sample IM-12_Si₃Ge_4PAC_4HCl and sample IM-12_Si₃Ge_Al_{25°C}_cal were tested. A CBV-712 sample (USY zeolite) was also tested in the same conditions. This zeolite has 12 member rings and a Si/Al ratio of 6.5, the amount of Brønsted acid sites is $225 \mu\text{mol.g}^{-1}$ (measured from pyridine adsorption) and the microporous volume is 0.275 mL.g^{-1} .

7.2.1. Activity and isomerization selectivity

To check if the acid phase is the limiting phase, we tested the catalysts with different amounts of Pt. Figure 7- 12.d shows that the activity and the selectivity of all samples remain almost constant irrespectively of the Pt content (1 or 2%). This highlights the presence of a limiting acid phase. This means that the latter defines the catalytic properties of the bifunctional catalyst. The conversion of n-hexadecane plotted against the reaction temperature in Figure 7- 12.a. Sample IM-12_Si₃Ge_2PAC_2HCl have almost the same activity than sample IM-12_Si₃Ge_4PAC_4HCl (Si/Al^{IV} ratios of 73 and 65 respectively). However, in the decane test (Figure 7- 2.a), sample IM-12_Si₃Ge_4PAC_4HCl was significantly more active. The pyridine adsorption showed that these two samples have close Brønsted (43 and $55 \mu\text{mol.g}^{-1}$) and Lewis (69 vs $51 \mu\text{mol.g}^{-1}$) acidities for IM-12_Si₃Ge_2PAC_2HCl and IM-12_Si₃Ge_4PAC_4HCl respectively. This is confirmed by the n-hexadecane test. Should these two samples have different types of acid sites, the activity differences should be more pronounced in the n-hexadecane test with respect to the n-decane test, as the reactant is more bulky in the first case. Since it is not the case, one may conclude that some of the active sites of IM-12_Si₃Ge_4PAC_4HCl are accessible to n-decane but not to n-hexadecane, whereas on IM-12_Si₃Ge_2PAC_2HCl, both molecules access similar amount of sites. A tentative explanation for this would be that the active sites of IM-12_Si₃Ge_2PAC_2HCl are closer to the pore mouth than for the IM-12_Si₃Ge_4PAC_4HCl sample.

Consistently with its very low amount of acid sites, IM-12_Si₃Ge_AlCl₂₅°C is less active than the PAC treated samples in the conversion of n-hexadecane and does not reach 100% of n-hexadecane conversion in the operating conditions range in play, thus will not be considered in the discussion. Sample CBV-712 (Y zeolite) having a lower Si/Al ratio is the most active sample, Figure 7- 12.b. Using Eq. 7- , the turnover frequencies (TOF) calculated at 235°C of hexadecane conversion on Brønsted acid sites (calculated by pyridine adsorption) are presented in Table 7- 2. IM-12 bifunctional catalysts are 2 to 3 times more active than CBV-712 zeolites indicating that IM-12 catalysts can be promising catalysts if the number and accessibility for their active sites is improved by optimizing further the post-treatment conditions, and by introducing mesoporosity or by decreasing the crystal size of IM-12 zeolites (around 7x6 μm and the average thickness around 350 nm) vs. crystal size between 0.6 and 1.6 μm for CBV-712.

Table 7- 2: Turnover frequencies (TOF) calculated at 235°C of hexadecane conversion on Brønsted acid sites (calculated by pyridine adsorption) over IM-12 catalysts treated with PAC and USY type catalysts.

Sample	TOF (10 ³ s ⁻¹) at 235°C
IM-12_Si ₃ Ge_2PAC_2HCl (1%Pt)	58.1
IM-12_Si ₃ Ge_2PAC_2HCl (2%Pt)	58.1
IM-12_Si ₃ Ge_4PAC_4HCl (1%Pt)	54.9
IM-12_Si ₃ Ge_4PAC_4HCl (2%Pt)	45.5
CBV-712 (1%Pt)	19.1
CBV-712 (2%Pt)	21.1

The yield of n-hexadecane isomers against the conversion in Figure 7- 12.b shows that, after reaching the maximum isomerization for CBV-712, cracking dominates (at high conversion), as expected. However, sample IM-12_Si₃Ge_2PAC_2HCl and sample IM-12_Si₃Ge_4PAC_4HCl have a less usual behavior: they reach a maximum of isomerization, cracking dominates, and then the isomerization yield unexpectedly increases again. This might reflect the coking of the catalysts. As a hypothesis, the coking blocks the microporosity of the samples, hence only active sites located at the pore mouth and at the surface of the crystals are accessible. As a consequence, the consecutive reactions due to the diffusion of the molecules within the crystal leading to secondary products are limited and the selectivity for isomerization improves again. In addition, Figure S7-3 shows the evolution of conversion over time. There are 2 GC analyzes, therefore 2 measured conversions for a given temperature. This figure reflects that at high temperatures, for the PAC treated samples, systematically the second value of conversion is lower than that of the first measurement. This is in agreement with the deactivation of the catalyst. Further work should be done to confirm this hypothesis, like characterization of spent catalysts (coke content, microporous volume).

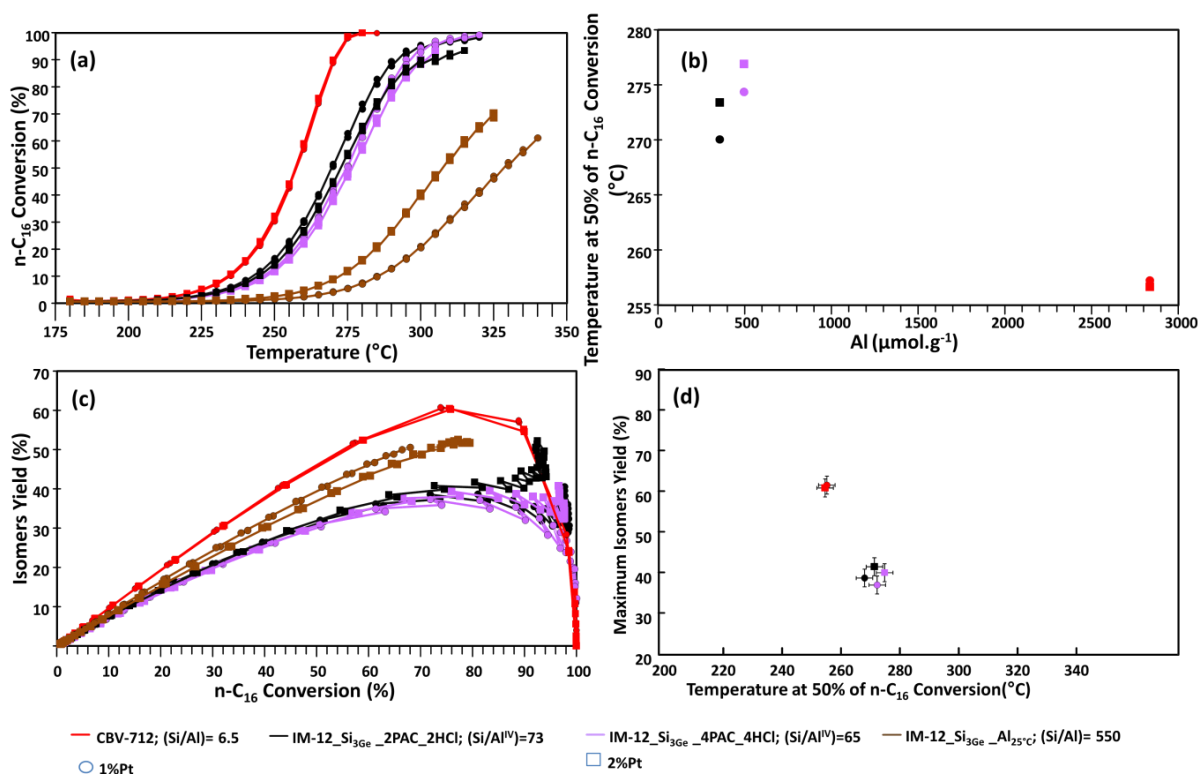


Figure 7- 12: (a) Conversion of n-hexadecane against reaction temperature. (b) Temperature at 50% of n-hexadecane conversion against the amount of Al calculated following the theoretical acidity by XRF. (c) Yield of n-hexadecane skeletal isomers against n-hexadecane conversion. (d) Maximum isomers yield against the temperature at 50% of n-hexadecane conversion of IM-12 bi-functional catalysts treated with PAC or AlCl₃ and of CBV-712 (USY zeolite). All zeolites are mixed with alumina impregnated with 1 and 2% Pt. The bi-functional catalyst is composed of 5 wt.% zeolite and wt.95% of Pt-alumina.

The maximum isomers yield against the temperature at 50% of n-hexadecane conversion in Figure 7- 12.d shows that sample IM-12_Si₃Ge_2PAC_2HCl and sample IM-12_Si₃Ge_4PAC_4HCl are similar in terms of activity and selectivity. Indeed, sample CBV-712 (Y zeolite) exhibits better selectivity toward hydroisomerization, likely due to the presence of mesoporosity and the 3D channel system.

All these features show that despite the existence of 14MR in IM-12, the accessibility of active sites, probably also linked to coking, remains a hurdle to optimal performance of the bifunctional catalysts. This is probably due to the very large platelet size of the present IM-12 samples (5.3).

7.2.2. Detailed analysis of the isomer distribution: insights toward localization of the active sites

Figure 7- 13 shows that all samples presented both mono and multi-branched isomers at low conversion. This means that both of them are primary products. The Pt loading did not affect the distribution of the products.

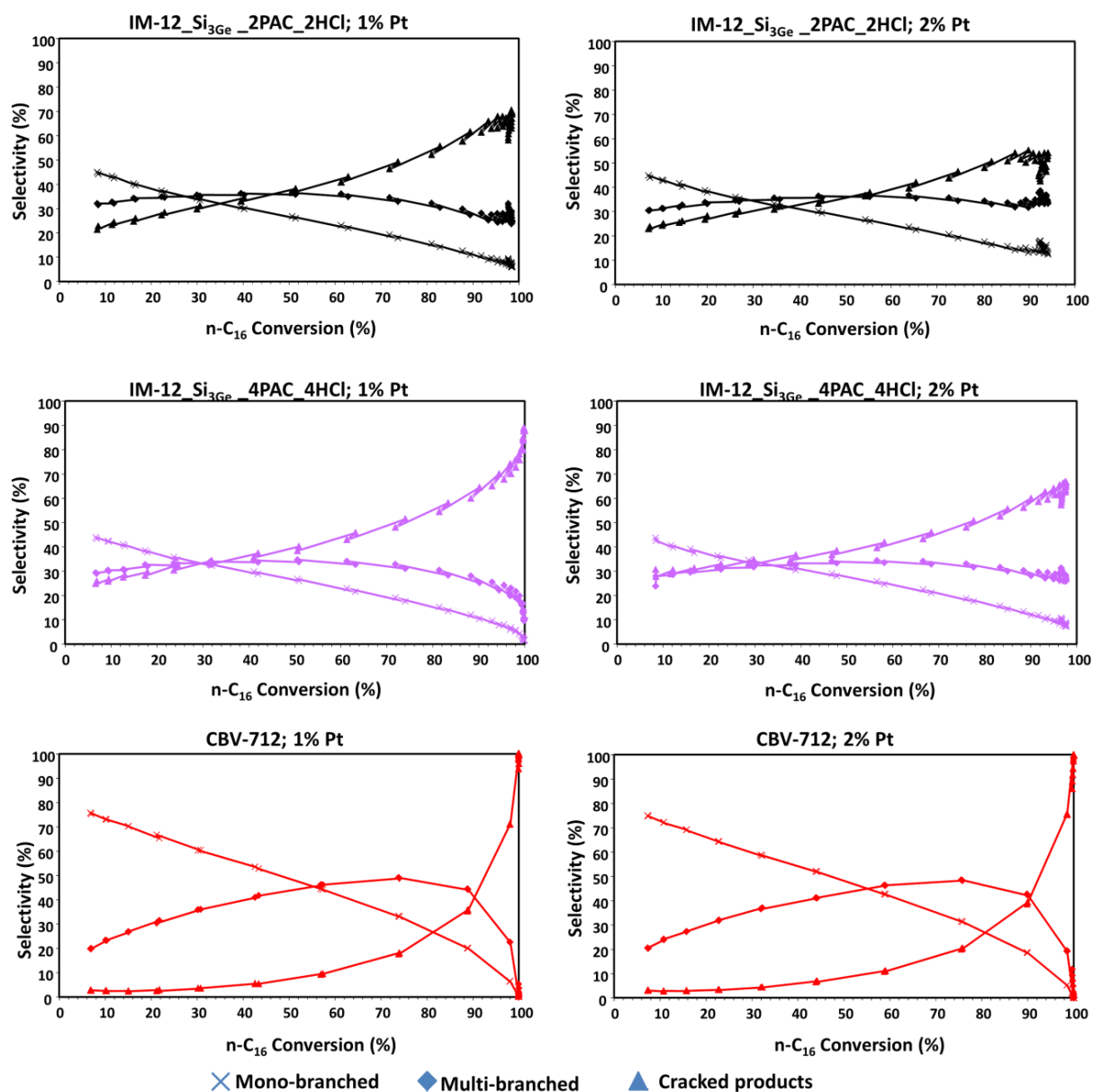


Figure 7- 13: Products distribution against the conversion of n-hexadecane of IM-12 bi-functional catalysts treated with PAC and of CBV-712 (Y zeolite). All zeolites are mixed with alumina impregnated with 1 and 2% Pt. The bi-functional catalyst is composed of 5% wt. zeolite and 95% wt. of Pt-alumina.

For all samples, the mono-branched (MB) isomers are predominant until reaching 30 and 50% of n-hexadecane conversion for IM-12 and CBV-712 respectively. Afterwards, multi-branched isomers (MTB) dominate then reach a maximum around 50 and 75% of n-C₁₆ conversion for IM-12 and CBV-712 respectively. At higher conversion, the decrease of mono-branched isomers in parallel to the increase of multi-branched isomers amounts reflect the consecutive skeletal rearrangement of the MB isomers into MTB over acid sites before hydrogenation on Pt sites.

Moreover, compared to the CBV-712, even at low conversion, the IM-12 catalysts have very high multibranched isomers/ monobranched isomers ratios and important amounts of cracked products. Figure 7- 14 shows the non-symmetric distribution of hexadecane cracked products over IM-12 catalysts reflecting the presence of overcracking, the minima and maxima distributions between the cracked products are due to « cage and window » effects. The bell shape in the case of CBV-712 indicates that only primary cracking took place. Considering the pore openings, 12 MR for CBV-712 and 12x14 MR for the IM-12, this behavior is unexpected. Larger pores should lead to less overcracking, different reasons could lead to this unexpected results. The first one might be related to the important mesoporosity of CBV-712 absent in IM-12. Another reason could be the large size of IM-12 sheets (around 7x6 μm and the average thickness around 350 nm) vs. crystal size between 0.6 and 1.6 μm for CBV-712 and the 3D channel system pores in CBV-712 vs. the 2D system in IM-12. These topological differences are leading to intra-particle diffusional limitations inside the IM-12 compared to the CBV-712. Inside the porosity of IM-12, the characteristic times of diffusion of hydrocarbons are too long compared to the characteristic times of a chemical reaction. Ultimately, consecutive reactions are favored. Since the characteristic diffusion time is dependent on the characteristic size of the crystal r and the diffusion coefficient D ($t = r^2 / D$)^[259] thus decreasing the size of the crystals should avoid this problem.

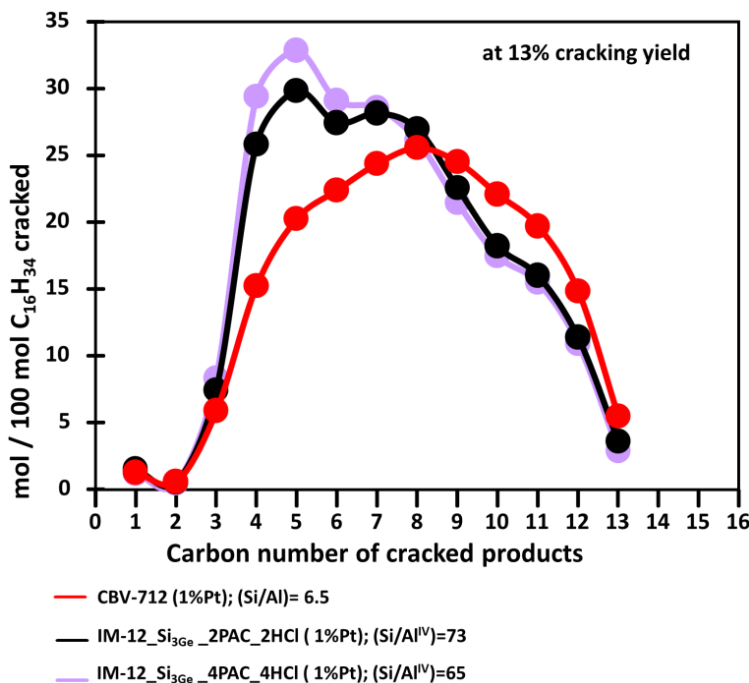


Figure 7- 14: Carbon number distribution of cracked products at 13% n-hexadecane cracking yield of IM-12 bi-functional catalysts treated with PAC and of CBV-712 (Y zeolite). All zeolites are mixed with alumina impregnated with 1 % Pt. The bi-functional catalyst is composed of 5% wt. zeolite and 95% wt. of Pt-alumina.

The evolution of mono-branched hexadecane isomers distribution along n-hexadecane conversion is plotted in Figure 7- 15. All samples presented the methyl-branched hexadecane isomers and 3-ethyl-tetradecane. However 6/7/8-methylpentadecanes are not shown since they could not be separated by gas chromatography. All samples led to the same mono-branched distribution independently of the Pt loading.

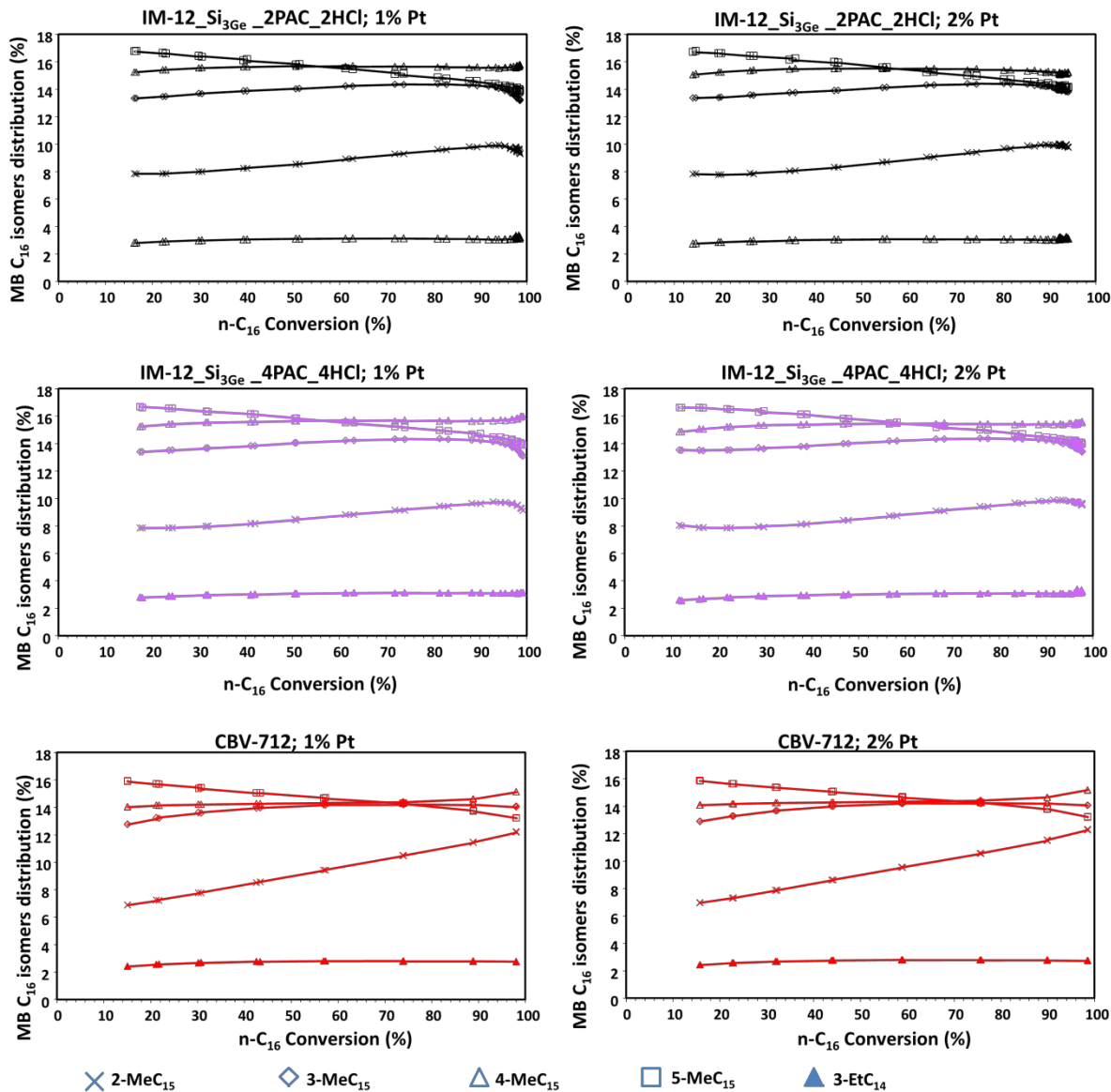


Figure 7- 15: Distribution of mono-branched isomers against the hexadecane conversion for of IM-12 bi-functional catalysts treated with PAC and of CBV-712 (Y zeolite). All zeolites are mixed with alumina impregnated with 1 and 2% Pt. The bi-functional catalyst is composed of 5% wt. zeolite and 95% wt. of Pt-alumina. 6/7/8-methylpentadecanes contribution are not shown for clarity.

Based on the isomerization mechanism presented in 1.4.2.1, the methyl-branched isomers are formed via PCP intermediates. As expected, for all samples the amount of 2-MeC₁₅ at low conversion is the lowest (1PCP intermediate lead to 2-Methylbranched isomers versus 2 PCPs for

other positions). And indeed, 5-MeC₁₅ amounts are the highest since the migration of methyl towards central positions is faster than towards side chains. Afterwards, for CBV-712 (Y zeolite), the thermodynamic equilibrium (MB branched composition of around 15%) is reached via successive methyl shifts explaining the decrease of 5-MeC₁₅ and the increase of 2-MeC₁₅^[260]. Moreover, for PAC treated samples, the amount of 2-MeC₁₅ rises faster depending on the conversion than in CBV-712. Here again, this might reflect that the consecutive reactions had enough time to occur inside the IM-12. Samples treated with PAC presented a deviation from the equilibrium distribution. This might reflect, that IM-12 had some steric constraints for methyl-shifts. This is again surprising if one considers the pore aperture of IM-12 with respect to zeolite Y, and indicates that the contribution of the mesoporosity, crystallite size and network dimensionality (2D versus 3D) presently dominate over the pore aperture.

Indeed in all samples, the amount of 3-ethyltetradecane is low since the latter is formed by a second type B isomerization of methyl-C₁₅ (compete with the preferential formation of di-branched isomers) or by protonated cyclobutane (PCB) intermediates less stable than PCP intermediates.

Since for IM-12, the coking at high conversion disturbed the cracking reactions, we limited our study of this test to the analysis of isomerization products.

7.3. Conclusion

IM-12 based bifunctional catalysts were evaluated in the n-decane and n-hexadecane hydroconversion tests and compared with USY (CBV712) base bifunctional catalysts. The IM-12 (14x12 MR) catalysts obtained from post-treatments presented a promising catalytic activity. In both tests, the selectivity reflected the presence of large pores but with slightly narrower pores when compared to USY type zeolites (12 MR). Attractive features for the decane test, are the high isomerization yields, the formation of dibranched skeletal isomers and the preference for central cracking of long chains. The activity of these zeolites with higher Si/Al ratios is promising when comparing to other zeolites. The TOF indicates that each site of the PAC treated samples is 3 times more active than in CBV-712 samples. Thus one can say, that by improving the accessibility to the active sites of IM-12 zeolites either by introducing mesoporosity or by reducing the crystal size to decrease the diffusional path, may lead to promising catalysts.

Conclusions and Perspectives

In a context where the catalytic transformation of bulky molecules is aimed, silicogermanates are attractive as they benefit from having structures with extra-large pores compared to traditional aluminosilicates zeolites. However, after calcination, these materials are unstable in the presence of water and their lack of acidity makes the incorporation of Al in the framework necessary. These two limitations can be solved by substituting Ge for Si and Al. In this work, an IM-12 zeolite (14x12 MR) was stabilized and presented catalytic activity in the hydroconversion of n-alkanes.

Ab initio calculations (in DFT, density functional theory) show that all silicogermanates attributed by the IZA and their (alumino) silicates analogs are intrinsically stable. It also shows that the substitution of Ge by Si and Al is thermodynamically possible and that chloride sources are favored over hydroxides. Based on this conclusion, no thermodynamic preference for the choice of candidate was retained. Thus the choice of the latter was based on the analysis of the literature. IM-12 (UTL) is a silicogermanate with pore openings of 14 and 12 T atoms (T = Si or Ge). The post-treatment of this silicogermanate has often led to new structures with smaller pores or to the partial maintaining of the initial structure with a significant loss of microporosity. Thus, stabilizing this silicogermanate without reducing its microporosity constituted the challenge of this thesis.

The stabilization of this zeolite through the substitution of Ge by Si was for the first time performed by a treatment using SiCl_4 in gas phase. To introduce Al into the zeolite, two modes of alumination were tested: either with an aqueous solution of polyaluminum chloride (PAC) or with a solution of aluminum trichloride in ethanol. After an optimization study of the different treatments, and for the first time to our knowledge, aluminum was incorporated into the zeolite using the PAC solution without significant changes in its initial structure or its microporous volume. ^{27}Al MAS NMR revealed the presence of tetra and hexa-coordinated aluminum. In the other hand, the treatment with AlCl_3 , allowed the conservation of the UTL structure and the incorporation of very low amounts of aluminum. These Al are below the limit of detection of ^{27}Al MAS NMR and infrared (FTIR) thus this treatment requires more optimization.

To define the nature of acid sites in IM-12 samples treated with PAC, the hydroxyl groups were observed by FTIR. The spectra showed the presence of a significant amount of silanols, and very small amounts of Si-OH-Al bridged acid sites, as well as Al-OH on the surface or as extraframework atoms. These distributions reflect that Al did not substitute all the Ge atoms extracted from the lattice, causing this increase in the amount of silanols. In order to determine whether the substitutions took place at the external or internal surface of the zeolite, models representing possible orientations of the external surface as well as defects were constructed. It has

been shown that thermodynamically, the substitution at the outer surface or the interior of the zeolite corresponds to a similar energy gain. These same models were then used for the simulation by DFT of chemical shifts in MAS NMR. The experimental proton MAS NMR spectra of the different IM-12 samples were assigned by combining data from the literature and the simulated chemical shifts. The different assignments reflected the presence of silanols, Al-(H₂O) bonded with a framework oxygen and Si-OH-Al bridged sites. To quantify the different types of hydroxyl groups linked to Al, more specifically, BAS and LAS acidities, the adsorption of pyridine as a basic probe molecule, was monitored by FTIR. This analysis proves the presence of very small amounts of Brønsted and Lewis acid sites compared to conventional zeolites.

Finally, these materials were engaged in the preparation of bi-functional catalysts which have been evaluated for the hydro-isomerization of n-alkanes. Two n-alkanes were tested: n-decane and n-hexadecane. The hydro-isomerization of n-decane is a model reaction providing information on the topology of zeolites and the location of active sites. Based on the different criteria of this model reaction, it has been shown that these catalysts have maintained their large pore openings. On the other hand, some of them seem to have diffusion limitations linked to the distribution of the acidity inside the porosity of these big crystals (around of 7x6 μm with thicknesses of the order of 350 nm). This distribution may be different depending on the stages of alumination treatment. The second reaction studied is that of the hydro-isomerization of n-hexadecane. The increase in the size of the carbon chain is indeed likely to provide information on the accessibility of acid sites. The hydroisomerization of n-hexadecane confirmed some of the results obtained for n-decane, but the ranking between samples in terms of activity is not the same between n-decane and n-hexadecane conversion. An interpretation of these features was made in terms of different locations of acid sites in the crystals (inner part of the particles *versus* pore mouth). Finally, these tests show that the IM-12 zeolites treated with PAC exhibit significant activity (in terms of TOF) compared to other zeolites having a higher Al content. The samples treated with AlCl₃ exhibit a too low acidity to observe its significant expression: the corresponding bifunctional catalysts exhibit the feature of a nearly pure metallic phase (hydrogenolysis).

This work showed theoretically and experimentally, that substitution of Ge by Si and Al assured the stabilization and the functionalization of the IM-12 zeolite.

The obtained material treated with PAC presented a promising activity with low amounts of Al. To increase these amounts, more specifically framework Al, the alumination process should be improved. Repeating the PAC treatment helped increasing the Brønsted acidity but after a lot of aqueous treatments, some loss of microporosity started (notably after 5 PAC and 5 HCl washing). As a consequence, one can imagine to make a treatment in dry environment. For example by developing a gas phase treatment similar to that of SiCl₄. Another way is optimizing the treatment

of AlCl_3 dissolved in ethanol by changing the treatment conditions. For example, treating the sample with AlCl_3 dissolved in ethanol, in the presence of HCl represent exactly the simulated reaction and should give promising results.

In addition, increasing the accessibility to the active sites by post-treatments can improve the catalytic performance of these zeolites. For example, the diffusion limitations can be avoided through working on smaller IM-12 crystals, and / or by introducing mesoporosity into the samples. Defining the diffusion time through the temporal analysis of products (TAP) inside these samples and comparing them to other zeolites such as USY might help to choose the adapted treatment for this diffusion problem and its efficiency. Introducing mesoporosity into these crystals was not possible due to the instability of silicogermanates, but thanks to the stabilization with the SiCl_4 treatment, we can imagine further treatments aiming at introducing this mesoporosity. This would undoubtedly allow the generation of a greater number of sites close to the pore mouth and significantly improve both activity and selectivity.

Moreover, the successful substitution of Ge for Si is proved experimentally thus understanding the mechanism of this substitution through DFT is of great importance and may gave insights for choosing the adapted experimental treatment.

Finally, substitution of Ge for Si using SiCl_4 in gas form gave very satisfactory results for the IM-12 zeolite. This treatment was not used before for this purpose. Thus testing it on other zeolites might indicate that this unit is universal and can assure the stabilization of the silicogermanate family opening perspectives toward their industrial use.

To select some representative silicogermanates that could be made a priority in future investigations, a topological study was made. The main obstacle to the success of the substitution of Ge by post-treatments is the sensitivity of the silicogermanates with respect to hydrolysis. The critical nature of these reactions is expected to depend on the respective positions of Ge in the framework, itself a consequence of the spatial distribution of d4r in the framework. To compare different silicogermanates topologies, we have considered a full hydrolysis approach which consists of eliminating all d4r units from the frameworks followed by a comparison of the residual structures. This led to the classification of hydrolyzed structures in three major families. Hydrolysis of the first family gave separated layers (such as IM-12, Figure 1.a). That of a second family provided nano-rods (such as IM-20, Figure 1.b) while for the third family thin nanowires connected by oxygen bonding remained (such as ITQ-33, Figure 1.c). A systematic study of the ability of the silicogermanates belonging to these various families, to be substituted and provide efficient acidic catalysts, will be useful in the future.

IM-12 already represent the first family, hence the two next candidates to be chosen can be the ITQ-33 (ITT) and the IM-20 (UWY).

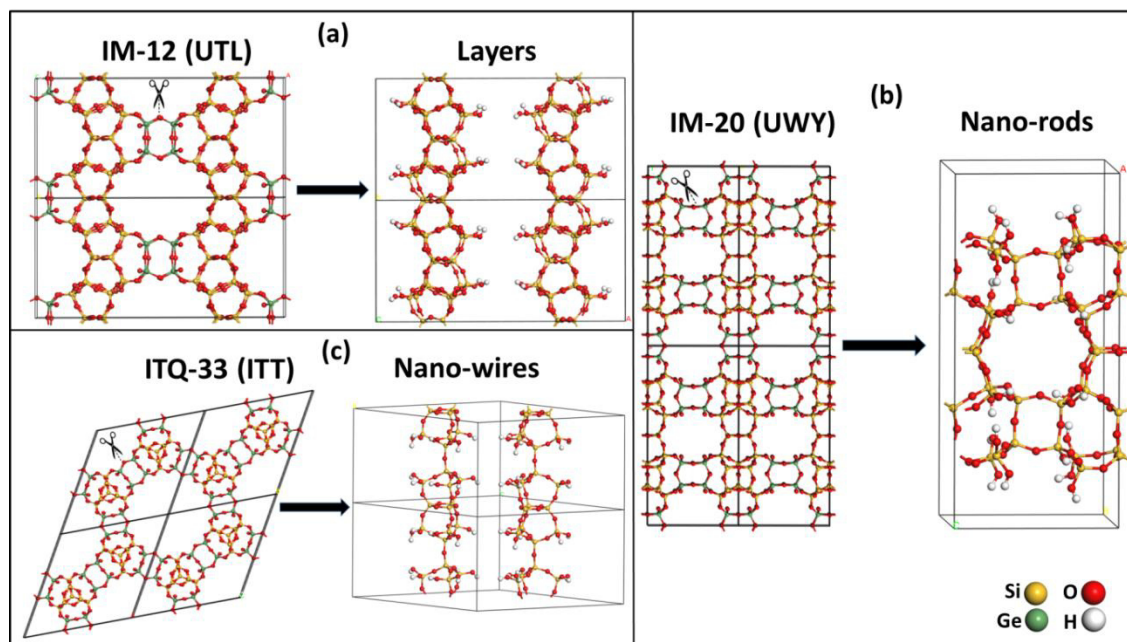


Figure 1 : Classification of silicogermanates into 3 families based on a full hydrolysis topological study.

References

- [1] P.A. Jacobs; E.M. Flanigen; J.C. Jansen; H. van Bekkum, Introduction to Zeolite Science and Practice, 2001, **137**, 11-35.
- [2] B. M. Lok; C. A. Messina; R. L. Patton; R. T. Gajek; T. R. Cannan; E. M. Flanigen, Silicoaluminophosphate Molecular Sieves: Another New Class of Microporous Crystalline Inorganic Solids, *J. Am. Chem. Soc.*, 1984, **106**, 6093-6095.
- [3] J. Sun; C. Bonneau; A. Cantín; A. Corma; M. J. Díaz-Cabañas; M. Moliner; D. Zhang; M. Li; X. Zou, The ITQ-37 Mesoporous Chiral Zeolite, *Nature*, 2009, **458**, 1154-1157.
- [4] A. Corma; M. J. Díaz-Cabañas; J. L. Jordá; C. Martínez; M. Moliner, High-Throughput Synthesis and Catalytic Properties of a Molecular Sieve with 18- and 10-Member Rings, *Nature*, 2006, **443**, 842-845.
- [5] J.-L. Paillaud; B. Harbuzaru; J. Patarin; N. Bats, Extra-Large-Pore Zeolites with Two-Dimensional Channels Formed by 14 and 12 Rings, *Science*, 2004, **304**, 990-992.
- [6] P. A. Kots; A.V. Kurkin; V.L. Sushkevich; A.N. Fitch.; V.V. Chernyshev; I. I. Ivanova, Synchrotron XRD and NMR Evidence of Germanium Redistribution During Silylation of BEC-Type Germanosilicate, *CrystEngComm*, 2017, **19**, 5982-5988.
- [7] H. Xu; J.-G. Jiang; B. Yang; L. Zhang; M. He; P.Wu, PostSynthesis Treatment Gives Highly Stable Siliceous Zeolites Through the Isomorphous Substitution of Silicon for Germanium in Germanosilicates, *Angew. Chem.*, 2014, **126**, 1379-1383.
- [8] F. Gao; M. Jaber; K. Bozhilov; A. Vicente; C. Fernandez; V. Valtchev, Framework Stabilization of Ge-Rich Zeolites via Postsynthesis Alumination, *J. Am. Chem. Soc.*, 2009, **131**, 16580-16586.
- [9] E. Verheyen, J. Lennart, K. Van Havenbergh, E. Breynaert, N. Kasian, E. Gobechiya, K. Houthoofd, C. Martineau, M. Hinterstein, F. Taulelle, V. Van Speybroeck, M. Waroquier, S. Bals, G Van Tendeloo, C.E.A. Kirschhock., J.A. Martens, Design of Zeolite by Inverse Sigma Transformation, *Nat. Mater.*, 2012, **11**, 1059-1064.
- [10] W. J. Roth; P. Nachtigall; R. E. Morris; P. S. Wheatley; V. R. Seymour; S. E. Ashbrook; P. Chlubná; L. Grajciar; M. Položij; A. Zukal; O. Shvets; J. Cejka, A Family of Zeolites with Controlled Pore Size Prepared Using a Top-down Method, *Nat. Chem.*, 2013, **5**, 628-633.
- [11] P.St. Petkov, H. A. Aleksandrov, V. Valtchev, and G. N. Vayssilov, Framework Stability of Heteroatom-Substituted Forms of Extra-Large-Pore Ge-Silicate Molecular Sieves: The Case of ITQ-44, *Chem. Mater.*, 2012, **24**, 2509-2518.
- [12] D. Plee, Zéolites, *techniques de l'ingénieur*, 2003, **J6675**, 1-4.
- [13] Y. D. G. Edanol; K. A. S. Usman; S. C. Buenviaje; M. E. Mantua; L. P. Payawan, Utilizing Silica from Rice Hull for the Hydrothermal Synthesis of Zeolite Y, *Kimika*, 2018, **29**, 17-21.

- [14] C. Baerlocher; D. Olson; L. B. McCusker; W. M. Meier, Atlas of Zeolite Framework Types, *Structure Commission of the International Zeolite Association, Elsevier*, 2007, **Ed 6**, 3-11.
- [15] M. E. Davis; R. F. Lobo, Zeolite and Molecular Sieve Synthesis, *Chem. Mater.*, 1992, **4**, 756-768.
- [16] <http://www.iza-online.org>.
- [17] A. F. Cronstedt, Ron Och Beskriting Om En Obekant Bärg Art, Som Kallas Zeolites, *Akad. Handl. Stockholm*, 1756, **18**, 120-130.
- [18] A. Damour, Über Das Bleigummi Und Thonerdhaltiges Phosphorsaures Bleioxyd Von Huelgoat, *Ann. Mines*, 1840, **17**, 191.
- [19] M.G. Washington; I. F. Earl, The Pneumatolytic and Hydrothermal Alteration and Synthesis of Silicates, *Economic Geology*, 1937, **32**, 607-761.
- [20] H. Eichhorn, Ueber Die Einwirkung Verdünnter Salzlösungen Auf Silicate, *Poggendorf Ann. Phys. Chem.*, 1858, **105**, 126-133.
- [21] H. de St. Claire-Deville, Reproduction De La Levyne, *Compt. Rend.*, 1862, **54**, 324.
- [22] G. Friedel, Sur Quelques Proprietes Nouvelles Des Zeolithes, *Bull. Soc. Franc. Mineral. Cristallogr.*, 1896, **19**, 94-118.
- [23] F. Grandjean, Étude Optique De L'absorption Des Vapeurs Lourdes Par Certaines Zéolithes, *Compt. Rend.*, 1909, **149**, 866-868.
- [24] O. Weigel; E. Steinhoff, Adsorption of Organic Liquid Vapors by Chabazite, *Z. Kristallogr.*, 1925, **61**, 125-154.
- [25] W. H. Taylor, The Structure of Analcite ($\text{NaAlSi}_2\text{O}_6 \cdot \text{H}_2\text{O}$), *Z. Kristallogr.*, 1930, **74**.
- [26] R. M. Barrer, Syntheses and Reactions of Mordenite., *J. Chem. Soc.*, 1948, **0**, 2158-2163.
- [27] E. M. Flanigen, B. M. Lok, R. L. Patton; S.T. Wilson, in Y. Murakami, A. Ijima and J.W. Ward, New Developments in Zeolite Science and Technology, *Studies in Surface Science and Catalysis Elsevier*, 1986, **28**, 103-112.
- [28] R. Szostak, Molecular Sieves, Principles of Synthesis and Identification, *Blackie Academic and Professional*, 1998, **5**, 208-244.
- [29] www.marketwatch.com/press-release/synthetic-zeolites-market-worth-59-billion-by-2023.
- [30] C. S. Cundy; P. A. Cox, The Hydrothermal Synthesis of Zeolites: Precursors, Intermediates and Reaction Mechanism, *Microporous Mesoporous Mater.*, 2005, **82**, 1-78.
- [31] R. M. Barrer; J. W. Baynham; F. W. Bultitude; W. M. Meier, Hydrothermal Chemistry of the Silicates., *J. Am. Chem. Soc.*, 1959, **0**, 195-208.
- [32] E. M. Flanigen; D. W. Breck, A Mechanism of Crystal Growth Is Proposed; Extensive Heterogeneous Nucleation Occurs During Formation of the Highly Supersaturated Gels. Crystal Growth in the Solid Phase Then Proceeds by a Series of Depolymerization-Polymerization Reactions, Catalyzed by Excess Hydroxyl Ion. There Is No Significant

Solution of the Solid Phase During Crystallization., *137th Meet, ACS, Div. Inorg. Chem.*, 1960, **33-M**.

- [33] C. S. Cundy; P. A. Cox, The Hydrothermal Synthesis of Zeolites: History and Development from the Earliest Days to the Present Time, *Chem. Rev.*, 2003, **103**, 663-702.
- [34] D. W. Breck, Crystalline Molecular Sieves, *J. Chem. Educ.*, 1964, **41**, 678-689.
- [35] G. T. Kerr, Chemistry of Crystalline Aluminosilicates. I. Factors Affecting the Formation of Zeolite a, *J. Phys. Chem.*, 1966, **70**, 1047-1050.
- [36] S. P. Zhdanov, Some Problems of Zeolite Crystallization, *Adv. Chem. Ser.*, 1974, **101**, 20-43.
- [37] R. L. Wadlinger, G.T. Kerr, E. J. Rosinski, Catalytic Composition of a Crystalline Zeolite, *U.S. Patent 3308069*, 1967.
- [38] E. G. Derouane; S. Determerie; Z. Gabelica; N. Blom, Synthesis and Characterization of ZSM-5 Type Zeolites I. Physico-Chemical Properties of Precursors and Intermediates, *Appl. Catal.*, 1981, **1**, 201-224.
- [39] C. D. Chang; A. T. Bell, Studies on the Mechanism of ZSM-5 Formation, *Catal. Lett.*, 1991, **8**, 305-316.
- [40] S. L. Burkett; M. E. Davis, Mechanism of Structure Direction in the Synthesis of Si-ZSM-5: An Investigation by Intermolecular ^1H - ^{29}Si CP MAS NMR, *J. Phys. Chem.*, 1994, **98**, 4647-4653.
- [41] R. Ravishankar; C.E.A Kirschhock.; P.P. Knops-Gerrits; E. J. P. Feijen, P. J. Grobet; P. Vanoppen, F. C. De Schryver, G. Mieke, H. Fuess, B. J. Schoeman, P.A. Jacobs, J.A Martens, Characterization of Nanosized Material Extracted from Clear Suspensions for MFI Zeolite Synthesis, *J. Phys. Chem. B*, 1999, **103**, 4960-4964.
- [42] : Kirschhock, C. E. A.; V. Buschmann; S. Kremer; R. Ravishankar; C. J. Y. Houssin; B. L. Mojet; R. A. van Santen; P. J. Grobet; P. A. Jacobs; J. A. Martens, Zeosil Nanoslabs: Building Blocks in NPr_4N^+ - Mediated Synthesis of MFI Zeolite, *Angew. Chem. Int. Ed.*, 2001, **40**, 2637-2640.
- [43] C. E. A. Kirschhock; R. Ravishankar; F. Verspeurt; P. J. Grobet; P. A. Jacobs; J. A. Martens, Identification of Precursor Species in the Formation of MFI Zeolite in the TPAOH-TEOS-H₂O System, *J. Phys. Chem. B*, 1999, **103**, 4965-4971.
- [44] C. E. A. Kirschhock; R. Ravishankar; L. van Looveren; P. A. Jacobs; J. A. Martens, Mechanism of Transformation of Precursors into Nanoslabs in the Early Stages of MFI and MEL Zeolite Formation from TPAOH-TEOS-H₂O and TBAOH-TEOS-H₂O Mixtures, *J. Phys. Chem. B*, 1999, **103**, 4972-4978.
- [45] C. E. A. Kirschhock; R. Ravishankar; P. A. Jacobs; J. A. Martens, Aggregation Mechanism of Nanoslabs with Zeolite MFI-Type Structure, *J. Phys. Chem. B*, 1999, **103**, 11021-11027.

- [46] C. T. G. Knight; S. D. Kinrade, Comment on “Identification of Precursor Species in the Formation of MFI Zeolite in the TPAOH–TEOS–H₂O System”, *J. Phys. Chem. B*, 2002, **106**, 3329-3332.
- [47] C. E. A. Kirschhock; S. P. B. Kremer; P. J. Grobet; P. A. Jacobs; J. A. Martens, New Evidence for Precursor Species in the Formation of MFI Zeolite in the Tetrapropylammonium Hydroxide–Tetraethyl Orthosilicate–Water System, *J. Phys. Chem. B*, 2002, **106**, 4897-4900.
- [48] D. D. Kragten; J. M. Fedeyko; K. R. Sawant; J. D. Rimer; D. G. Vlachos; R. F. Lobo; M. Tsapatsis, Structure of the Silica Phase Extracted from Silica/(TPA)OH Solutions Containing Nanoparticles, *J. Phys. Chem. B*, 2003, **107**, 10006-10016.
- [49] A. Aerts; C. E. A. Kirschhock; J. A. Martens, Methods for in Situ Spectroscopic Probing of the Synthesis of a Zeolite, *Chem. Soc. Rev.*, 2010, **39**, 4626-4642.
- [50] O. V. Shvets; N. Kasian; A. Zukal; J. Pinkas; J. Čejka, The Role of Template Structure and Synergism Between Inorganic and Organic Structure Directing Agents in the Synthesis of UTL Zeolite, *Chem. Mater.*, 2010, **22**, 3482-3495.
- [51] A. W. C. Van Den Berg; G. Baak; H. Van Koningsveld; J. C. Jansen; T. Maschmeyer, Synthesis, Structural Characterization, and Thermal Stability of a New Layered Germanate Structure, Na₄Ge₁₆O₂₈(OH)₁₂, *Inorg. Chem.*, 2004, **43**, 2888-2894.
- [52] G. Sastre; A. Corma, Predicting Structural Feasibility of Silica and Germania Zeolites, *J. Phys. Chem. C*, 2010, **114**, 1667-1673.
- [53] G.V. Gibbs; M.B. Boisen; F.C. Hill; O. Tamada; R.T. Downs, SiO and GeO Bonded Interactions as Inferred from the Bond Critical Point Properties of Electron Density Distributions, *Phys. Chem. Miner.*, 1998, **25**, 574-584.
- [54] J. Plévert; T. M. Gentz; A. Laine; H. Li; V. G. Young; O. M. Yaghi; M. O’Keeffe, A Flexible Germanate Structure Containing 24-Ring Channels and with Very Low Framework Density, *J. Am. Chem. Soc.*, 2001, **123**, 12706-12707.
- [55] Y. Zhou; H. Zhu; Z. Chen; M. Chen; Y. Xu; H. Zhang; D. Zhao, A Large 24-Membered-Ring Germanate Zeolite-Type Open-Framework Structure with Three-Dimensional Intersecting Channels, *Angew. Chem.*, 2001, **113**, 2224-2226.
- [56] A. Corma, M. T. Navarro, F. Rey, J. Rius, S. Valencia, Pure Polymorph C of Zeolite Beta Synthesized by Using Framework Isomorphous Substitution as a Structure-Directing Mechanism, *Angew. Chem. Int. Ed.*, 2001, **40**, 2277-2280.
- [57] J. M. Newsam, M. M. J. Treacy, W. T. Koetsier, C. B. De Gruyter, Structural Characterization of Zeolite Beta, *Proc. R. Soc. Lond. A*, 1988, **420**.
- [58] A. Corma; M. T. Navarro; F. Rey; S. Valencia, ITQ-16, a New Zeolite Family of the Beta Group with Different Proportions of Polymorphs A, B and C, *Chem. Commun.*, 2001, **0**, 1720-1721.

- [59] N. Bats; L. Rouleau; J.-L. Paillaud; P. Caullet; Y. Mathieu; S. Lacombe, Recent Developments in the Use of Hexamethonium Salts as Structure Directing Agents in Zeolite Synthesis, *Studies in Surface Science and Catalysis Elsevier Science B.V.*, **154**, 283-288.
- [60] L. Q. Tang, M. S. Dadachov, X. D. Zou, Synthesis and Structures of New Silicogermanates, *Studies in Surface Science and Catalysis Elsevier*, 2004, **154**, 739-745.
- [61] L. Tang; L. Shi; C. Bonneau; J. Sun; H. Yue; A. Ojuva; B.-L. Lee; M. Kritikos; R. G. Bell; Z. Bacsik; J. Mink; X. Zou, A Zeolite Family with Chiral and Achiral Structures Built from the Same Building Layer, *Nat. Mater.*, 2008, **7**, 381-385.
- [62] W. Hua; H. Chen; Z.-B. Yu; X. Zou; J. Lin; J. Sun, A Germanosilicate Structure with 11×11×12-Ring Channels Solved by Electron Crystallography, *Angew. Chem. Int. Ed.*, 2014, **53**, 5868-5871.
- [63] Y. Chen; J. Su; S. Huang; J. Liang; X. Lin; F. Liao; J. Sun; Y. Wang; J. Lin; H. Gies, PKU-20, *Microporous Mesoporous Mater.*, 2016, **224**, 384-391.
- [64] F.-J. Chen; Y. Xu; H.-B. Du, An Extra-Large-Pore Zeolite with Intersecting 18-, 12-, and 10-Membered Ring Channels, *Angew. Chem. Int. Ed.*, 2014, **53**, 9592-9596.
- [65] Z.-H. Gao; F.-J. Chen; L. Xu; L. Sun; Y. Xu; H.-B. Du, A Stable Extra-Large-Pore Zeolite with Intersecting 14- and 10-Membered-Ring Channels, *Chem. Eur. J.*, 2016, **22**, 14367-14372.
- [66] Y. Luo; S. Smeets; F. Peng; A. S. Etman; Z. Wang; J. Sun; W. Yang, Synthesis and Structure Determination of Large-Pore Zeolite SCM-14, *Chem. Eur. J.*, 2017, **23**, 16829-16834.
- [67] D. J. Earl; A. W. Burton; T. Rea; K. Ong; M. W. Deem; S.-J. Hwang; S. I. Zones, Synthesis and Monte Carlo Structure Determination of SSZ-77: A New Zeolite Topology, *J. Phys. Chem. C*, 2008, **112**, 9099-9105.
- [68] J. H. Kang; D. Xie; S. I. Zones; S. Smeets; L. B. McCusker; M. E. Davis, Synthesis and Characterization of CIT-13, a Germanosilicate Molecular Sieve with Extra-Large Pore Openings, *Chem. Mater.*, 2016, **28**, 6250-6259.
- [69] Y. Wang; W. Yunchen; S. Jie; S. Xiaowei; W. Wan; J. Yu, Interrupted Silicogermanate with 10-Ring Channels: Synthesis and Structure Determination by Combining Rotation Electron Diffraction and Powder X-Ray Diffraction, *Inorg. Chem.*, 2017, **4**, 1654-1659.
- [70] J. Jiuxing; J. L. Jorda; Y. Jihong; L. A. Baumes; E. Mugnaioli; M. J. Diaz-Cabanas; U. Kolb; C. Avelino, Synthesis and Structure Determination of the Hierarchical Meso-Microporous Zeolite ITQ-43, *Science*, 2011, **333**, 1131-1134.
- [71] Y. Yun; M. Hernandez; W. Wan; X. Zou; J. L. Jorda; A. Cantin; F. Rey; A. Corma, The First Zeolite with a Tri-Directional Extra-Large 14-Ring Pore System Derived Using a Phosphonium-Based Organic Molecule, *Chem. Commun.*, 2015, **51**, 7602-7605.

- [72] J. Jiang; Y. Yun; X. Zou; J. L. Jorda; A. Corma, ITQ-54: A Multi-Dimensional Extra-Large Pore Zeolite with $20 \times 14 \times 12$ -Ring Channels, *Chem. Sci.*, 2015, **6**, 480-485.
- [73] M. O. Cichocka; Y. Lorgouilloux; S. Smeets; J. Su; W. Wan; P. Caullet; N. Bats; L. B. McCusker; J.-L. Paillaud; X. Zou, Multidimensional Disorder in Zeolite IM-18 Revealed by Combining Transmission Electron Microscopy and X-Ray Powder Diffraction Analyses, *Cryst. Growth Des.*, 2018, **18**, 2441-2451.
- [74] Y. Wang; J. Song; H. Gies, The Substitution of Germanium for Silicon in AST-Type Zeolite, *Solid State Sci.*, 2003, **5**, 1421-1433.
- [75] A. Corma; M. T. Navarro; F. Rey; S. Valencia, Synthesis of Pure Polymorph C of Beta Zeolite in a Fluoride-Free System, *Chem. Commun.*, 2001, **0**, 1486-1487.
- [76] L. Shi; Y. Yuan; N. Zhang; S. Lin; T. Yu; J. Wang, Synthesis and Characterization of BEC-Zeotype Germanosilicates and B-Substituted Zeolitic Materials, *J. Porous. Mater.*, 2016, **23**, 647-654.
- [77] K. Jiao; Z. Zhang; X. Xu; Z. Lv; J. Song; C. Lin; J. Sun; M. He; H. Gies, Synthesis and Characterization of Germanosilicate Molecular Sieves: GeO₂/SiO₂ Ratio, H₂O/TO₂ Ratio and Temperature, *Dalton Trans.*, 2017, **46**, 2270-2280.
- [78] Z.-B. Yu; Y. Han; L. Zhao; S. Huang; Q.-Y. Zheng; S. Lin; A. Córdova; X. Zou; J. Sun, Intergrown New Zeolite Beta Polymorphs with Interconnected 12-Ring Channels Solved by Combining Electron Crystallography and Single-Crystal X-Ray Diffraction, *Chem. Mater.*, 2012, **24**, 3701-3706.
- [79] J. Su; Y. Wang; J. Lin; J. Liang; J. Sun; X. Zou, A Silicogermanate with 20-Ring Channels Directed by a Simple Quaternary Ammonium Cation, *Dalton Trans.*, 2013, **42**, 1360-1363.
- [80] T.z. Ren; K. E. Christensen; J. Grins; K. Jansson; L. Shi; M. Edén; X. Zou, SU-57 – an Aluminosilicogermanate with a DFT Topology and Variable Composition, *Microporous Mesoporous Mater.*, 2009, **117**, 285-291.
- [81] X. Liu; W. Mao; J. Jiang; X. Lu; M. Peng; H. Xu; L. Han; S.-A. Che; P. Wu, Topotactic Conversion of Alkali-Treated Intergrown Germanosilicate CIT-13 into Single-Crystalline ECNU-21 Zeolite as Shape-Selective Catalyst for Ethylene Oxide Hydration, *Chem. Eur. J.*, 2019, **25**, 4520-4529.
- [82] M. Hernández-Rodríguez; J. L. Jordá; F. Rey; A. Corma, Synthesis and Structure Determination of a New Microporous Zeolite with Large Cavities Connected by Small Pores, *J. Am. Chem. Soc.*, 2012, **134**, 13232-13235.
- [83] J. Jiang; J. L. Jorda; M. J. Diaz-Cabanas; J. Yu; A. Corma, The Synthesis of an Extra-Large-Pore Zeolite with Double Three-Ring Building Units and a Low Framework Density, *Angew. Chem. Int. Ed.*, 2010, **49**, 4986-4988.
- [84] J. Jiang; Y. Xu; P. Cheng; Q. Sun; J. Yu; A. Corma; R. Xu, Investigation of Extra-Large Pore Zeolite Synthesis by a High-Throughput Approach, *Chem. Mater.*, 2011, **23**, 4709-4715.

- [85] K. Qian; Y. Wang; Z. Liang; J. Li, Germanosilicate Zeolite ITQ-44 with Extra-Large 18-Rings Synthesized Using a Commercial Quaternary Ammonium as a Structure-Directing Agent, *RSC Adv.*, 2015, **5**, 63209-63214.
- [86] R. Bai; Q. Sun; N. Wang; Y. Zou; G. Guo; S. Iborra; A. Corma; J. Yu, Simple Quaternary Ammonium Cations-Templated Syntheses of Extra-Large Pore Germanosilicate Zeolites, *Chem. Mater.*, 2016, **28**, 6455-6458.
- [87] A. Corma; M. J. Diaz-Cabanas; J. Jiand; D. L. Dorset; S. L. Soled; K. G. Strohmaier, Extra-Large Pore Zeolite (ITQ-40) with the Lowest Framework Density Containing Double Four- and Double Three-Rings, *PNAS*, 2010, **107**, 13997-14002.
- [88] T. Blasco; A. Corma; M.J. Díaz-Cabañas; F. Rey; J. A. Vidal-Moya; C. M. Zicovich-Wilson, Preferential Location of Ge in the Double Four-Membered Ring Units of ITQ-7 Zeolite, *J. Phys. Chem. B*, 2002, **106**, 2634-2642.
- [89] S. Leiva; M. J. Sabater; S. Valencia; G. Sastre; V. Fornés; F. Rey; A. Corma, A New Synthesis Method for the Preparation of ITQ-7 Zeolites and the Characterisation of the Resulting Materials, *Compt. Rend. Chimie*, 2005, **8**, 369-378.
- [90] M. Moliner, T. Willhammar, W. Wan, J. González, F. Rey, J. L. Jorda, X. Zou, A. Corma, Synthesis Design and Structure of a Multipore Zeolite with Interconnected 12- and 10-MR Channels, *J. Am. Chem. Soc.*, 2012, **134**, 6473-6478.
- [91] T. Boix; M. Puche; M. A. Cambor; A. Corma, Synthetic Porous Crystalline Material ITQ-13, Its Synthesis and Use, *U.S. Patent 6471941B1*, 2002.
- [92] A. Corma; M. Puche; F. Rey; G. Sankar; S. J. Teat, A Zeolite Structure (ITQ-13) with Three Sets of Medium-Pore Crossing Channels Formed by 9- and 10-Rings, *Angew. Chem. Int. Ed.*, 2003, **42**, 1156-1159.
- [93] A. Corma; M. J. Diaz-Cabanas; J.L. Jorda; F. Rey; K. Boulahya; J. M. Gonzalez-Calbet, High-Resolution Transmission Electron Microscopy (HRTEM) and X-Ray Diffraction (XRD) Study of the Intergrowth in Zeolites ITQ-13/ITQ-34, *J. Phys. Chem. C*, 2009, **113**, 9305-9308.
- [94] J. A. Vidal-Moya; T. Blasco; F. Rey; A. Corma; M. Puche, Distribution of Fluorine and Germanium in a New Zeolite Structure ITQ-13 Studied by ¹⁹F Nuclear Magnetic Resonance, *Chem. Mater.*, 2003, **15**, 3961-3963.
- [95] R. Castañeda; A. Corma; V. Fornés; J. Martínez-Triguero; S. Valencia, Direct Synthesis of a 9 × 10 Member Ring Zeolite (Al-ITQ-13): A Highly Shape-Selective Catalyst for Catalytic Cracking, *J. Catal.*, 2006, **238**, 79-87.
- [96] X. Chen; G. Jing-Qi; W. Shu-Jie; K. Qiu-Bin, Effect of Silica Source on the Hydrothermal Synthesis of ITQ-13 Zeolite, *Acta Phys.-Chim. Sin.*, 2009, **25(11)**, 2275-2278.
- [97] C. Xu; J. Guan; S. Wu; M. Jia; T. Wu; Q. Kan, Catalytic Performance of Zeolite ITQ-13 with 9- and 10-Member Rings for Methane Dehydroaromation, *Reac. Kinet. Mech. Cat.*, 2010, **63**, 165.

- [98] L. Li; X. Cui; S. Xu; J. Li; Z. Qin; J. Wang, Effect of Ge Content on the Synthesis and Structure of Ge-ITQ-13 Zeolite, *Mat. Express*, 2015, **5**, 73-78.
- [99] L. Li; Y. Chen; S. Xu; J. Li; M. Dong; Z. Liu; H. Jiao; J. Wang; W. Fan, SI-Oriented Control of Al Locations in the Framework of Al-Ge-ITQ-13 for Catalyzing Methanol Conversion to Propene, *J. Catal.*, 2016, **344**, 242-251.
- [100] X. Liu; Y. Chu; Q. Wang; W. Wang; C. Wang; J. Xu; F. Deng, Identification of Double Four-Ring Units in Germanosilicate ITQ-13 Zeolite by Solid-State NMR Spectroscopy, *Magn. Reson.*, 2017, **87**, 1-9.
- [101] Q. Wu; X. Liu; L. Zhu; X. Meng; F. Deng; F. Fan; Z. Feng; C. Li; S. Maurer; M. Feyen; U. Müller; F.-S. Xiao, Solvent-Free Synthesis of ITQ-12, ITQ-13, and ITQ-17 Zeolites, *Chin. J. Chem.*, 2017, **35**, 572-576.
- [102] P. Zeng; X. Guo; X. Zhu; Q. Guo; Y. Wang; S. Ren; B. Shen, On the Synthesis and Catalytic Cracking Properties of Al-ITQ-13 Zeolites, *Microporous Mesoporous Mater.*, 2017, **246**, 186-192.
- [103] A. Corma; M. J. Diaz-Cabanas; J. L. Jorda; F. Rey; G. Sastre; K. G. Strohmaier, A Zeolitic Structure (ITQ-34) with Connected 9- and 10-Ring Channels Obtained with Phosphonium Cations as Structure Directing Agents, *J. Am. Chem. Soc.*, 2008, **130**, 16482-16483.
- [104] A. Corma; M. J. Diaz-Cabanas; J. L. Jorda; F. Rey; K. Boulahya; J. M. Gonzalez-Calbet, High-Resolution Transmission Electron Microscopy (HRTEM) and X-Ray Diffraction (XRD) Study of the Intergrowth in Zeolites ITQ-13/ITQ-34, *J. Phys. Chem. C*, 2009, **113**, 9305-9308.
- [105] A. Corma; M. Moliner; M. J. Diaz-Cabanas; J. M. Serra Alfaro; R. Castañeda, Microporous Crystalline Material, Zeolite ITQ-33, Preparation Method Thereof and Use of Same, *European Patent 1847510A1*, 2006.
- [106] M. Moliner, M. J. Díaz-Cabañas, V. Fornés, C. Martínez, A. Corma, Synthesis Methodology, Acidity and Catalytic Behavior of the 18 X 1-Member Ring Pores ITQ-33 Zeolite, *Book of abstracts 4th FEZA Conference*, 2008, **028**.
- [107] M. Bjørgen; A. H. Grave; Saepurahman; A. Volynkin; K. Mathisen; K. P. Lillerud; U. Olsbye; S. Svelle, Spectroscopic and Catalytic Characterization of Extra Large Pore Zeotype H-ITQ-33, *Microporous Mesoporous Mater.*, 2012, **151**, 424-433.
- [108] Q. Kun; S. Xiao-Wei; X. Da; L. Ji-Yang, Synthesis and Characterization of Extra-large 18-Ring Zeolite ITQ-33 Using Phosphonium as Structure-directing Agent, *Chem. J. Chinese U.*, 2012, **33**, 2141-2145.
- [109] L. Liu; Z.-B. Yu; H. Chen; Y. Deng; B.-L. Lee; J. Sun, Disorder in Extra-Large Pore Zeolite ITQ-33 Revealed by Single Crystal XRD, *Cryst. Growth Des.*, 2013, **13**, 4168-4171.
- [110] L. Wu; J. Hughes; M. Moliner; A. Navrotsky; A. Corma, Experimental Energetics of Large and Extra-Large Pore Zeolites: Pure Silica Beta Polymorph C (BEC) and Ge-Containing ITQ-33, *Microporous Mesoporous Mater.*, 2014, **187**, 77-81.

- [111] Z. Zhang; Y. Guo; X. Liu, Solid State NMR Techniques Study the Structural Characteristics of as-Synthesized ITQ-33, *J. Phys. Chem. C*, 2017, **121**, 11568-11575.
- [112] K. Qian; J. Li; J. Jiang; Z. Liang; J. Yu; R. Xu, Synthesis and Characterization of Chiral Zeolite ITQ-37 by Using Achiral Organic Structure-Directing Agent, *Microporous Mesoporous Mater.*, 2012, **164**, 88-92.
- [113] F.-J. Chen; Z.-H. Gao; L.-L. Liang; J. Zhang; H.-B. Du, Facile Preparation of Extra-Large Pore Zeolite ITQ-37 Based on Supramolecular Assemblies as Structure-Directing Agents, *CrystEngComm*, 2016, **18**, 2735-2741.
- [114] R. Castañeda; A. Corma; V. Fornés; F. Rey; J. Rius, Synthesis of a New Zeolite Structure ITQ-24, with Intersecting 10- and 12-Membered Ring Pores, *J. Am. Chem. Soc.*, 2003, **125**, 7820-7821.
- [115] A. Cantín, A. Corma, M. J. Diaz-Cabanas, J. L. Jordá, M. Moliner, Rational Design and HT Techniques Allow the Synthesis of New IWR Zeolite Polymorphs, *J. Am. Chem. Soc.*, 2006, **128**, 4216-4217.
- [116] W. H. Fu, Z. Yuan, Z. Wang, Y. Wang, W. Yang, M. Y. He, Direct Synthesis of Hydrothermally Stable Ge-IWR Zeolites, *Dalton Trans.*, 2017, **46**, 6692-6699.
- [117] D. L. Dorset; K. G. Strohmaier; C. E. Kliewer; A. Corma; M. J. Díaz-Cabañas; F. Rey; C. J. Gilmore, Crystal Structure of ITQ-26, a 3D Framework with Extra-Large Pores, *Chem. Mater.*, 2008, **20**, 5325-5331.
- [118] A. Corma; F. Rey; S. Valencia; J. L. Jordá; J. Rius, A Zeolite with Interconnected 8-, 10- and 12-Ring Pores and Its Unique Catalytic Selectivity, *Nat. Mater.*, 2003, **2**, 493-497.
- [119] G. Sastre; A. Pulido; R. Castañeda; A. Corma, Effect of the Germanium Incorporation in the Synthesis of EU-1, ITQ-13, ITQ-22, and ITQ-24 Zeolites, *J. Phys. Chem. B*, 2004, **108**, 8830-8835.
- [120] X. Liu; U. Ravon; F. Bosselet; G. Bergeret; A. Tuel, Probing Ge Distribution in Zeolite Frameworks by Post-Synthesis Introduction of Fluoride in as-Made Materials, *Chem. Mater.*, 2012, **24**, 3016-3022.
- [121] R. Yuan; N. Claes; E. Verheyen; A. Tuel; S. Bals; E. Breynaert; J. A. Martens; C. E. A. Kirschhock, Synthesis of an IWW-Type Germanosilicate Zeolite Using 5-Azonia-Spiro[4,4]Nonane as a Structure Directing Agent, *New J. Chem.*, 2016, **40**, 4319-4324.
- [122] A. CORMA; F. Rey; J. Rius; M. J. Sabater; S. Valencia, Supramolecular Self-Assembled Molecules as Organic Directing Agent for Synthesis of Zeolites, *Nature*, 2004, **431**, 287-290.
- [123] J. E. Schmidt; S. I. Zones; D. Xie; M. E. Davis, The Synthesis of Aluminophosphate and Germanosilicate LTA Using a Triquaternary Structure Directing Agent, *Microporous Mesoporous Mater.*, 2014, **200**, 132-139.

- [124] B. Harbuzaru; J.-L. Paillaud; J. Patarin; N. Bats; L. Simon; C. Laroche, IM-11 Crystalline Solid with Structure Type LTA, and a Process for Its Preparation, *U.S. Patent 7,056,490 B2*, 2006.
- [125] L. Bieseki; R. Simancas; J. L. Jordá; P. J. Bereciartua; Á. Cantín; J. Simancas; S. B. Pergher; S. Valencia; F. Rey; A. Corma, Synthesis and Structure Determination via Ultra-Fast Electron Diffraction of the New Microporous Zeolitic Germanosilicate ITQ-62, *Chem. Commun.*, 2018, **54**, 2122-2125.
- [126] Y. Luo; S. Smeets; Z. Wang; J. Sun; W. Yang, Synthesis and Structure Determination of SCM-15, *Chemistry (Weinheim an der Bergstrasse, Germany)*, 2019, **25**, 2184-2188.
- [127] Y. Chen; S. Huang; X. Wang; L. Zhang; N. Wu; F. Liao; Y. Wang, Synthesis and Characterization of a Layered Silicogermanate PKU-22 and Its Topotactic Condensation to a Three-Dimensional STI-Type Zeolite, *Cryst. Growth Des.*, 2017, **17**, 5465-5473.
- [128] N. Zhang; L. Shi; T. Yu; T. Li; W. Hua; C. Lin, Synthesis and Characterization of Pure STW-Zeotype Germanosilicate, Cu- and Co-Substituted STW-Zeotype Materials, *J. Solid State Chem.*, 2015, **225**, 271-277.
- [129] L. B. McCusker; C. Baerlocher; A. W. Burton; S. I. Zones, A Re-Examination of the Structure of the Germanosilicate Zeolite SSZ-77, *Solid State Sci.*, 2011, **13**, 800-805.
- [130] C. Zhang; E. Kapaca; J. Li; Y. Liu; X. Yi; A. Zheng; X. Zou; J. Jiang; J. Yu, An Extra-Large-Pore Zeolite with 24×8×8-Ring Channels Using a Structure-Directing Agent Derived from Traditional Chinese Medicine, *Angew. Chem. Int. Ed.*, 2018, **57**, 6486-6490.
- [131] Y. Lorgouilloux; M. Dodin; J.-L. Paillaud; P. Caullet; L. Michelin; L. Josien; O. Ersen; N. Bats, IM-16: A New Microporous Germanosilicate with a Novel Framework Topology Containing D4r and Mtw Composite Building Units, *J. Solid State Chem.*, 2009, **182**, 622-629.
- [132] Y. Lorgouilloux; M. Dodin; E. Mugnaioli; C. Marichal; P. Caullet; N. Bats; U. Kolb; J.-L. Paillaud, IM-17: A New Zeolitic Material, Synthesis and Structure Elucidation from Electron Diffraction ADT Data and Rietveld Analysis, *RSC Adv.*, 2014, **4**, 19440-19449.
- [133] Y. Mathieu; J.-L. Paillaud; P. Caullet; N. Bats, Synthesis and Characterization of IM-10, *Microporous Mesoporous Mater.*, 2004, **75**, 13-22.
- [134] O. V. Shvets; A. Zukal; N. Kasian; N. Zilková; J. Cejka, The Role of Crystallization Parameters for the Synthesis of Germanosilicate with UTL Topology, *Chem. Eur. J.*, 2008, **14**, 10134-10140.
- [135] A. Corma; M. J. Diaz-Cabanas; F. Rey; S. Nicolopoulos; K. Boulahya, ITQ-15: The First Ultralarge Pore Zeolite with a Bi-Directional Pore System Formed by Intersecting 14- and 12-Ring Channels, and Its Catalytic Implications, *Chem. Commun.*, 2004, 1356-1357.
- [136] M. Dodin; J.-L. Paillaud; Y. Lorgouilloux; P. Caullet; E. Elkaïm; N. Bats, A Zeolitic Material with a Three-Dimensional Pore System Formed by Straight 12- and 10-Ring

- Channels Synthesized with an Imidazolium Derivative as Structure-Directing Agent, *J. Am. Chem. Soc.*, 2010, **132**, 10221-10223.
- [137] B. W. Boal; M. W. Deem; D. Xie; J. H. Kang; M. E. Davis; S. I. Zones, Synthesis of Germanosilicate Molecular Sieves from Mono- and Di-Quaternary Ammonium OSDAs Constructed from Benzyl Imidazolium Derivatives: Stabilization of Large Micropore Volumes Including New Molecular Sieve CIT-13, *Chem. Mater.*, 2016, **28**, 2158-2164.
- [138] D. S. Firth; S. A. Morris; P. S. Wheatley; S. E. Russell; A. M. Z. Slawin; D. M. Dawson; A. Mayoral; M. Opanasenko; M. Položij; J. Čejka; P. Nachtigall; R. E. Morris, Assembly–Disassembly–Organization–Reassembly Synthesis of Zeolites Based on Cfi -Type Layers, *Chem. Mater.*, 2017, **29**, 5605-5611.
- [139] A. Corma, M. J. Diaz-Cabanas, J. Martinez-Triguero, F. Rey, J. Rius, A Large-Cavity Zeolite with Wide Pore Windows and Potential as an Oil Refining Catalyst, *Nature*, 2002, **418**, 514-517.
- [140] A. CORMA; M. J. Díaz-Cabañas; F. Rey, Synthesis of ITQ-21 in OH– Media, *Chem. Commun.*, 2003, 1050-1051.
- [141] B. B. Schaack; W. Schrader; A. Corma; F. Schüth, Nucleation of ITQ-21 Studied by ESI-MS, *Chem. Mater.*, 2009, **21**, 4448-4453.
- [142] Jiuxing Jiang; Yan Xu; Peng Cheng; Qiming Sun; Jihong Yu; Avelino Corma; and Ruren Xu, Investigation of Extra-Large Pore Zeolite Synthesis by a High-Throughput Approach, *Chem. Mater.*, 23, **2011**, 4709-4715.
- [143] L. Tang; M. S. Dadachov; X. Zou, SU-12:A Silicon-Substituted ASU-16 with Circular 24-Rings and Templated by a Monoamine, *Chem. Mater.*, 2005, **17**, 2530-2536.
- [144] L. Q. Tang, Novel Framework Materials: Organically Templated Silicogermanates and Hybrid Fluorotitanates, *Doctoral Dissertation-Department of Structural Chemistry Stockholm University*, 2005.
- [145] L. Tang; X. Zou, SU-21, a Layered Silicogermanate with Organic Amines Covalently-Bonded to Germanium, *Microporous Mesoporous Mater.*, 2007, **101**, 24-29.
- [146] L. Tang; X. Ren; A. K. Inge; T. Willhammar; D. Grüner; J. Yu; X. Zou, A Stacking Faults-Containing Silicogermanate with 24-Ring Channels and Unbranched Zweier Silica Double Chains, *Cryst. Growth Des.*, 2012, **12**, 3714-3719.
- [147] G. Sastre, J. A. Vidal-Moya, T. Blasco, J. Rius, J. L. Jordà, M. T. Navarro, F. Rey, A. Corma, Preferential Location of Ge Atoms in Polymorph C of Beta Zeolite (ITQ-17) and Their Structure-Directing Effect: A Computational, XRD, and NMR Spectroscopic Study, *Angew. Chem. Int. Ed.*, 2002, **41**, 4722-4726.
- [148] B. Harbuzaru; J.-L. Paillaud; J. Patarin; N. Bats, IM-12 Crystallized Solid and Its Process Preparation, *U.S. Patent 20050067604A1*, 2005.

- [149] J.-L. Paillaud; Y. Lorgouilloux; B. Harbuzaru; P. Caullet; J. Patarin; N. Bats, Structure Orienting Role of Germanium in Zeolite Synthesis, *Studies in Surface Science and Catalysis Elsevier*, 2007, **170**, 389-396.
- [150] F. Gao, M. Jaber, K. Bozhilov, A. Vicente, C. Fernandez, V. Valtchev, Framework Stabilization of Ge-Rich Zeolites via Postsynthesis Aluminations, *J. Am. Chem. Soc.*, 2009, **131**, 16580-16586.
- [151] M. V. Shamzhy; P. Eliašová; D. Vitvarová; M. V. Opanasenko; D. S. Firth; R. E. Morris, Post-Synthesis Stabilization of Germanosilicate Zeolites ITH, IWW, and UTL by Substitution of Ge for Al, *Chem. Eur. J.*, 2016, **22**, 17377-17386.
- [152] V. I. Kasneryk, M. V. Shamzhy, M. V. Opanasenko, J. Čejka, Tuning of Textural Properties of Germanosilicate Zeolites ITH and IWW by Acidic Leaching, *J. Energy Chem.*, 2016, **25**, 318-326.
- [153] A. Rodríguez-Fernández; F. J. Llopis; C. Martínez; M. Moliner; A. Corma, Increasing the Stability of the Ge-Containing Extra-Large Pore ITQ-33 Zeolite by Post-Synthetic Acid Treatments, *Microporous Mesoporous Mater.*, 2018, **267**, 35-42.
- [154] M. Shamzhy; F. S. de O. Ramos, Tuning of Acidic and Catalytic Properties of IWR Zeolite by Post-Synthesis Incorporation of Three-Valent Elements, *Catal. Today*, 2015, **243**, 76-84.
- [155] L. Burel; N. Kasian; A. Tuel, Quasi All-Silica Zeolite Obtained by Isomorphous Degermanation of an as-Made Germanium-Containing Precursor, *Angew. Chem. Int. Ed.*, 2014, **53**, 1360-1363.
- [156] V. Kasneryk; M. Opanasenko; M. Shamzhy; Z. Musilová; Y.S Avadhut; M. Hartmann; J. Čejka, Consecutive Interlayer Disassembly–reassembly During Aluminations of UOV Zeolites: Insight into the Mechanism, *J. Mater. Chem. A*, 2017, **5**, 22576-22587.
- [157] V. Kasneryk; M. Shamzhy; M. Opanasenko; P. S. Wheatley; S. A. Morris; S. E. Russell; A. Mayoral; M. Trachta; J. Čejka; R. E. Morris, Expansion of the ADOR Strategy for the Synthesis of Zeolites: The Synthesis of IPC-12 from Zeolite UOV, *Angew. Chem. Int. Ed.*, 2017, **56**, 4324-4327.
- [158] P.S. Wheatley; P. Chlubná-Eliášová; H. Greer; W. Zhou; V. R. Seymour; D. M. Dawson; S. E. Ashbrook; A. B. Pinar; L. B. McCusker; M. Opanasenko; J. Čejka; R. E. Morris, Zeolites with Continuously Tuneable Porosity, *Angew. Chem. Int. Ed.*, 2014, **53**, 13210-13214.
- [159] Peng Mingming; Jiang Jingang; Liu Xue; Ma Yue; Jiao Meichen; Xu Hao; Wu Hailong; He Mingyuan; Wu Peng, Breaking Structural Energy Constraints: Hydrothermal Crystallization of High-Silica Germanosilicates by a Building-Unit Self-Growth Approach, *Chem. Eur. J.*, 2018, **24**, 13297-13305.
- [160] J. H. Kang; D. Xie; S. I. Zones; M. E. Davis, Transformation of Extra-Large Pore Germanosilicate CIT-13 Molecular Sieve into Extra-Large Pore CIT-5 Molecular Sieve, *Chem. Mater.*, 2019, **31**, 9777-9787.

- [161] J. E. Schmidt; M.E. Davis; B. W. Boal; J. H. Kang; D. Xie, Germanosilicate Compositions and Methods of Preparing the Same, *U.S. Patent 20170252729A1*, 2017.
- [162] J. H. Kang; D. Xie; S. I. Zones; M. E. Davis, Fluoride-Free Synthesis of Germanosilicate CIT-13 and Its Inverse Sigma Transformation to Form CIT-14, *Chem. Mater.*, 2020, **32**, 2014-2024.
- [163] X. Liu; N. Kasian; A. Tuel, New Insights into the Degermanation Process of ITQ-17 Zeolites, *Microporous Mesoporous Mater.*, 2014, **190**, 171-180.
- [164] P. Chlubná-Eliášová; Y. Tian; A. B. Pinar; M. Kubů; J. Čejka; R. E. Morris, The Assembly-Disassembly-Organization-Reassembly Mechanism for 3D-2D-3D Transformation of Germanosilicate IWW Zeolite, *Angew. Chem. Int. Ed.*, 2014, **53**, 7048-7052.
- [165] J.V. Smith, Topochemistry of Zeolites and Related Materials. 1. Topology and Geometry, *Chem. Rev.*, 1988, **88**, 149-182.
- [166] E. Verheyen; S. Pulinthanathu; K. Thomas; J. Dendooven; M. De Prins; G. Vanbutsele G.; E. Breynaert; J.-P. Gilson; C. E. A. Kirschhock; C. Detavernier; J. A. Martens, Catalytic Activation of OKO Zeolite with Intersecting Pores of 10- and 12-Membered Rings Using Atomic Layer Deposition of Aluminium, *Chem. Commun.*, 2014, **50**, 4610-4612.
- [167] W. J. Roth; O. V. Shvets; M. Shamzhy; P. Chlubná; M. Kubů; P. Nachtigall; J. Čejka, Postsynthesis Transformation of Three-Dimensional Framework into a Lamellar Zeolite with Modifiable Architecture, *J. Am. Chem. Soc.*, 2011, **133**, 6130-6133.
- [168] M. Mazur; P. Chlubná-Eliášová; J. W. Roth; J. Čejka, Intercalation Chemistry of Layered Zeolite Precursor IPC-1P, *Catal. Today*, 2014, **227**, 37-44.
- [169] Y. Asakura; N. Kawaura; Y. Kuroda; M. Koike; H. Wada; A. Shimojima; K. Kuroda, Synthesis of a Single-Crystalline Macroporous Layered Silicate from a Macroporous UTL-Type Zeolite and Its Accelerated Intercalation, *Chem. Eur.J.*, 2017, **23**, 11022-11029.
- [170] M. Shamzhy, M. Opanasenko, Y. Tian, K. Konyshcheva, O. Shvets, R. E. Morris, J. Čejka, Germanosilicate Precursors of ADORable Zeolites Obtained by Disassembly of ITH, ITR, and IWR Zeolites, *Chem. Mater.*, 2014, **26**, 5789-5798.
- [171] M. Navarro; S. A. Morris; Á. Mayoral; J. Čejka; R. E. Morris, Microwave Heating and the Fast ADOR Process for Preparing Zeolites, *J. Mater. Chem. A*, 2017, **5**, 8037-8043.
- [172] M. Trachta; O. Bludský; J. Čejka; R. E. Morris; P. Nachtigall, From Double-Four-Ring Germanosilicates to New Zeolites: In Silico Investigation, *Chemphyschem*, 2014, **15**, 2972-2976.
- [173] M. Trachta; P. Nachtigall; O. Bludský, The ADOR Synthesis of New Zeolites: In Silico Investigation, *Catal. Today*, 2015, **243**, 32-38.
- [174] D.D. Eley, P.W. Selwood, Paul B. Weisz, A.A. Balandin, J.H. De Boer, P.J. Debye, P.H. Emmett, J. Horiuti, W. Jost, G. Natta, E.K. Rideal, H.S. Taylor, Polyfunctional Heterogeneous Catalysis, *Advances in Catalysis Elsevier*, 1962, **13**, 137-190.

- [175] C. Bouchy; G. Hastoy; E. Guillon; J. A. Martens, Fischer-Tropsch Waxes Upgrading via Hydrocracking and Selective Hydroisomerization, *Oil Gas Sci. Technol. - Rev. IFP*, 2009, **64**, 91-112.
- [176] J. Weitkamp, Catalytic Hydrocracking-Mechanisms and Versatility of the Process, *ChemCatChem*, 2012, **4**, 292-306.
- [177] J. A. Martens; D. Verboekend; K. Thomas; G. VANBUTSELE; J. P. Gilson; J. Perez-Ramirez, Hydroisomerization of Emerging Renewable Hydrocarbons Using Hierarchical Pt/H-ZSM-22 Catalyst, *ChemSusChem*, 2013, **6**, 421-425.
- [178] H. L. Coonradt; W. E. Garwood, Mechanism of Hydrocracking. Reactions of Paraffins and Olefins, *Ind. Eng. Chem. Process. Des. Dev.*, 1964, **3**, 38-45.
- [179] J. A. Schwarz; C. Contescu; A. Contescu, Methods for Preparation of Catalytic Materials, *Chem. Rev.*, 1995, **95**, 477-510.
- [180] J. A. Martens; P. A. Jacobs; J. B. Moffat, Conceptual Background for the Conversion of Hydrocarbons on Heterogeneous Acid Catalysts, *Theoretical aspects of heterogeneous catalysis- Van Nostrand Reinhold*, 1990, 52-109.
- [181] J.A. Martens; R. Parton; L. Uytterhoeven; P.A. Jacobs, Selective Conversion of Decane into Branched Isomers - a Comparison of Platinum/ZSM-22, Platinum/ZSM-5 and Platinum/USY Zeolite Catalysts, *Appl. Catal.*, 1991, **76**, 95-116.
- [182] R. Hoffmann, Extended Hückel Theory. IV. Carbonium Ions, *J. Chem. Phys.*, 1964, **40**, 2480-2488.
- [183] J. Rey; A. Gomez; P. Raybaud; C. Chizallet; T. Bučko, On the Origin of the Difference Between Type a and Type B Skeletal Isomerization of Alkenes Catalyzed by Zeolites, *Journal of Catalysis*, 2019, **373**, 361-373.
- [184] J. A. Martens; M. Tielen; P. A. Jacobs, Estimation of the Void Structure and Pore Dimensions of Molecular Sieve Zeolites Using the Hydroconversion of N-Decane, *zeolites*, 1984, **4**, 98-107.
- [185] J. Mason, Conventions for the Reporting of Nuclear Magnetic Shielding (or Shift) Tensors Suggested by Participants in the NATO ARW on NMR Shielding Constants at the University of Maryland, College Park, July 1992, *Solid State Nucl. Magn. Reson.*, 1993, **2**, 285-288.
- [186] J.A. Martens; P.A. Jacobs, The Potential and Limitations of the N-Decane Hydroconversion as a Test Reaction for Characterization of the Void Space of Molecular Sieve Zeolites, *zeolites*, 1986, **6**, 334-348.
- [187] W. Souverijns; L. Rombouts; J. A. Martens; P. A. Jacobs, Molecular Shape Selectivity of EUO Zeolites, *Microporous Mater.*, 1995, **4**, 123-130.
- [188] F. Marques Mota; C. Bouchy; E. Guillon; A. Fécant; N. Bats; J. A. Martens, IZM-2, *J. Catal.*, 2013, **301**, 20-29.

- [189] B. D. Vandegheuchte; J. W. Thybaut; A. Martínez; M. A. Arribas; G. B. Marin, N-Hexadecane Hydrocracking Single-Event MicroKinetics on Pt/H-Beta, *Appl. Catal. A.*, 2012, **441-442**, 10-20.
- [190] Beyer H. K.; Belenykaja I. M.; Hange F.; Tielen M.; Grobet P. J.; Jacobs P. A., Preparation of High-Silica Faujasites by Treatment with Silicon Tetrachloride, *J. Chem. Soc., Faraday Trans. 1*, 1985, **81**, 2889-2901.
- [191] J. A. Martens, H. Geerts, P. J. Grobet, P.A. Jacobs, Dealumination of Zeolite Y with SiCl₄: A Two-Step Reaction, *J. CHEM. SOC., CHEM. COMMUN.*, 1990, **0**, 1418-1419.
- [192] D. Yuan; C. Kang; W. Wang; H. Li; X. Zhu; Y. Wang; X. Gao; B. Wang; H. Zhao; C. Liu; B. Shen, Creation of Mesostructured Hollow Y Zeolite by Selective Demetallation of an Artificial Heterogeneous Al Distributed Zeolite Crystal, *Catal. Sci. Technol.*, 2016, **6**, 8364-8374.
- [193] C. Pagis; A. R. Morgado Prates; N. Bats; A. Tuel; D. Farrusseng, High-Silica Hollow Y Zeolite by Selective Desilication of Dealuminated NaY Crystals in the Presence of Protective Al Species, *CrystEngComm*, 2018, **20**, 1564-1572.
- [194] E. El Hayek, B. Harbuzaru, C. Chizallet, J.A. Martens, Méthode De Stabilisation De Matériaux Silicogermanates Microporeux En Présence De SiCl₄, *INPI Number: 19/11.342.*, application date: 11/10/2019.
- [195] A. G. Stepanov, *Basics of Solid-State NMR for Application in Zeolite Science*, in *Zeolites and Zeolite-Like Materials*. Elsevier, 2016, 137-188.
- [196] B.M. Fung; A.K. Khitrin; K. Ermolaev, An Improved Broadband Decoupling Sequence for Liquid Crystals and Solids, *J. Magn. Reson.*, 2000, **142**, 97-101.
- [197] D. Massiot; F. Fayon; M. Capron; I. King; S. Le Calvé; B. Alonso; J.-O. Durand; B. Bujoli; Z. Gan; G. Hoatson, Modelling One- and Two-Dimensional Solid-State NMR Spectra, *Magn. Reson. Chem.*, 2002, **40**, 70-76.
- [198] M. Houlleberghs; A. Hoffmann; D. Dom; C. E. A. Kirschhock; F. Taulelle; J. A. Martens; E. Breynaert, Absolute Quantification of Water in Microporous Solids with ¹H Magic Angle Spinning NMR and Standard Addition, *Anal. Chem*, 2017, **89**, 6940-6943.
- [199] P. Hohenberg and W. Kohn, Inhomogeneous Electron Gas, *Phys. Rev.*, 1964, **136**, B864-B871.
- [200] W. Kohn and L. J. Sham, Self-Consistent Equations Including Exchange and Correlation Effects, *Phys. Rev.*, 1965, **140**, A1133-A1138.
- [201] J. P. Perdew; K. Burke; M. Ernzerhof, Generalized Gradient Approximation Made Simple, *Phys. Rev. Lett.*, 1996, **77**, 3865-3868.
- [202] S. N. Steinmann; C. Corminboeuf, Comprehensive Benchmarking of a Density-Dependent Dispersion Correction, *J. Chem. Theory Comput.*, 2011, **7**, 3567-3577.

- [203] G. Kresse; D. Joubert, From Ultrasoft Pseudopotentials to the Projector Augmented-Wave Method, *Phys. Rev. B*, 1999, **59**, 1758-1775.
- [204] G. Kresse; J. Hafner, Ab Initio Molecular-Dynamics Simulation of the Liquid-Metal-Amorphous-Semiconductor Transition in Germanium, *Phys. Rev. B*, 1994, **49**, 14251-14269.
- [205] G. Kresse; J. Furthmüller, Efficiency of Ab-Initio Total Energy Calculations for Metals and Semiconductors Using a Plane-Wave Basis Set, *Comput. Mater. Sci.*, 1996, **6**, 15-50.
- [206] <http://www.iza-online.org/>.
- [207] K. Larmier; C. Chizallet; N. Cadran; S. Maury; J. Abboud; A.-F. Lamic-Humblot; E. Marceau; H. Lauron-Pernot, Mechanistic Investigation of Isopropanol Conversion on Alumina Catalysts, *ACS Catal.*, 2015, **5**, 4423-4437.
- [208] C. J. Pickard; F. Mauri, All-Electron Magnetic Response with Pseudopotentials NMR Chemical Shifts, *Phys. Rev. B*, 2001, **63**, 245101-1- 245101-13.
- [209] J. R. Yates; C. J. Pickard; F. Mauri, Calculation of NMR Chemical Shifts for Extended Systems Using Ultrasoft Pseudopotentials, *Phys. Rev. B*, 2007, **76**, 024401-024411.
- [210] A. Corma, M. J. Diaz-Cabanas, J. L. Jorda, C. Martinez; M. Moliner, High-Throughput Synthesis and Catalytic Properties of a Molecular Sieve with 18- and 10-Member Rings, *Nature*, 2006, **443**, 842-845.
- [211] Q. Li; A. Navrotsky; F. Rey; A. Corma, Thermochemistry of $(\text{Ge}_x\text{Si}_{1-x})\text{O}_2$ Zeolites, *Microporous Mesoporous Mater.*, 2003, **59**, 177-183.
- [212] W. J. Roth; P. Nachtigall; R. E. Morris; J. Čejka, Two-Dimensional Zeolites: Current Status and Perspectives, *Chem. Rev.*, 2014, **114**, 4807-4837.
- [213] P. Cautlet; J. L. Guth; J. Hazm; J. M. Lamblin; H. Gies, Synthesis, Characterization and Crystal Structure of the New Clathrasil Phase Octadecasil, *Eur. J. Solid State Inorg. Chem.*, 1991, **28**, 345-361.
- [214] L. A. Villaescusa; P. A. Barrett; M. A. Cambor, Calcination of Octadecasil: Fluoride Removal and Symmetry of the Pure SiO_2 Host, *Chem. Mater.*, 1998, **10**, 3966-3973.
- [215] Z. Liu; T. Ohsuna; O. Terasaki; M. A. Cambor; M. J. Diaz-Cabañas; K. Hiraga, The First Zeolite with Three-Dimensional Intersecting Straight-Channel System of 12-Membered Rings, *J. Am. Chem. Soc.*, 2001, **123**, 5370-5371.
- [216] A. Cantín; A. Corma; M. J. Díaz-Cabañas; J. L. Jordá; M. Moliner; F. Rey, Synthesis and Characterization of the All-Silica Pure Polymorph C and an Enriched Polymorph B Intergrowth of Zeolite Beta, *Angew. Chem. Int. Ed.*, 2006, **45**, 8013-8015.
- [217] ITQ- 7: A New Pure Silica Polymorph with a Three- Dimensional System of Large Pore Channels, *Angew. Chem. Int. Ed.*, 1999, **38**, 1997-2000.
- [218] J.-Q. Song; B. Marler; H. Gies, Synthesis of ITQ-7 with a New Template Molecule and Its Crystal Structure Analysis in the as Synthesized Form, *Compt. Rend. Chimie*, 2005, **8**, 341-352.

- [219] L. Tang; X. Ren; A. K. Inge; T. Willhammar; D. Grüner; J. Yu; X. Zou, A Stacking Faults-Containing Silicogermanate with 24-Ring Channels and Unbranched Zweier Silica Double Chains, *Cryst. Growth Des.*, 2012, **12**, 3714–3719.
- [220] Y. Bouzidi; J.-L. Paillaud; L. Simon; V. Valtchev, Seeded Synthesis of Very High Silica Zeolite a, *Chem. Mater.*, 2007, **19**, 652-654.
- [221] E. M. Flanigen; J. M. Bennett; R. W. Grose; J. P. Cohen; R. L. Patton; R. M. Kirchner; J. V. Smith, Silicalite, a New Hydrophobic Crystalline Silica Molecular Sieve, *Nature*, 1978, **271**, 512-516.
- [222] G. T. Kokotailo; S. L. Lawton; D. H. Olson; W. M. Meier, Structure of Synthetic Zeolite ZSM-5, *Nature*, 1978, **272**, 437-438.
- [223] E. Galli; G. Gottardi, The Crystal Structure of Stilbite, *Miner. Petrogr. Acta*, 1966, **12**, 1-10.
- [224] T. Conradsson; M.S. Dadachov; X.D. Zou, Synthesis and Structure of (Me₃N)₆[Ge₃₂O₆₄](H₂O)_{4:5}, a Thermally Stable Novel Zeotype with 3D Interconnected 12-Ring Channels, *Microporous Mesoporous Mater.*, 2000, **41**, 183-191.
- [225] C. J. Dawson; R. Sanchez-Smith; P. Rez; M. O’Keeffe; M. M. J. Treacy, Ab Initio Calculations of the Energy Dependence of Si–O–Si Angles in Silica and Ge–O–Ge Angles in Germania Crystalline Systems, *Chem. Mater.*, 2014, **26**, 1523-1527.
- [226] W. Loewenstein, Distribution of Aluminum in the Tetrahedra of Silicates and Aluminates, *Am. Min.*, 1954, **39**, 92-96.
- [227] J. Haines; O. Cambon; E. Philippot; L. Chapon; S. Hull, A Neutron Diffraction Study of the Thermal Stability of the A-Quartz-Type Structure in Germanium Dioxide, *J. Solid State Chem.*, 2002, **166**, 434-441.
- [228] Q. Li; A. Navrotsky; F. Rey; A. Corma, Enthalpies of Formation of Ge-Zeolites, *Microporous Mesoporous Mater.*, 2004, **74**, 87-92.
- [229] Y. G. Bushuev; G. Sastre, Feasibility of Pure Silica Zeolites, *J. Phys. Chem. C*, 2010, **114**, 19157-19168.
- [230] R. A. van Santen; G. J. Kramer, Reactivity Theory of Zeolitic Bronsted Acidic Sites, *Chem. Rev.*, 1995, **95**, 637-660.
- [231] G. J. Kramer; A. J. M. de Man; R. A. van Santen, Zeolites Versus Aluminosilicate Clusters: The Validity of a Local Description, *J. Am. Chem. Soc.*, 1991, **113**, 6435-6441.
- [232] I. Petrovic; A. Navrotsky; M. E. Davis; S. I. Zones, Thermochemical Study of the Stability of Frameworks in High Silica Zeolites, *Chem. Mater.*, 1993, **5**, 1805-1813.
- [233] G. Sastre; A. Pulido; A. Corma, An Attempt to Predict and Rationalize Relative Stabilities and Preferential Germanium Location in Si/Ge Zeolites, *Microporous Mesoporous Mater.*, 2005, **82**, 159-163.

- [234] M. O. Keeffe; O.M. Yaghi, Germanate Zeolites: Contrasting the Behavior of Germanate and Silicate Structures Built from Cubic T_8O_{20} Units (T=Ge or Si), *Chem. Eur. J.*, 1999, **5**, 2796-2801.
- [235] M. Mazur; P. S. Wheatley; M. Navarro; W. J. Roth; M. Položij; A. Mayoral; P. Eliášová; P. Nachtigall; J. Čejka; R. E. Morris, Synthesis of 'Unfeasible' Zeolites, *Nature chemistry*, 2016, **8**, 58-62.
- [236] J. Rey; P. Raybaud; C. Chizallet, Ab Initio Simulation of the Acid Sites at the External Surface of Zeolite Beta, *ChemCatChem*, 2017, **9**, 2176-2185.
- [237] L. Treps; A. Gomez; T. d. Bruin; C. Chizallet, Environment, Stability and Acidity of External Surface Sites of Silicalite-1 and ZSM-5 Micro and Nano Slabs, Sheets, and Crystals, *ACS Catalysis*, 2020, **10**, 3297-3312.
- [238] P. Curie, Sur La Formation Des Cristaux Et Sur Les Constantes Capillaires De Leurs Différentes Faces, *bulmi*, 1885, **8**, 145-150.
- [239] G. Wulff, Zur Frage Der Geschwindigkeit Des Wachstums Und Der Auflösung Der Krystallflächen, *Z. Kristallogr. - Cryst. Mater.*, 1901, **34**, 449-530.
- [240] E. El Hayek, B. Harbuzaru, C. Chizallet, J.A. Martens, Matériau De Type Structural UTL Ayant Une Bonne Résistance Structural En Présence D'eau, Un Volume Microporeux Élevé Et Des Sites Actifs Dans Sa Structure, *INPI Number: 20/00.344.*, application date: 15/01/2020.
- [241] E. El Hayek; B. Harbuzaru; J. A. Martens; C. Chizallet, Ab Initio Investigation of the Relative Stability of Silicogermanates and Their (Alumino)Silicates Counterparts, *Microporous Mesoporous Mater.*, 2020, **306**, 110425-110434.
- [242] B. Vallaey; S. Radhakrishnan; S. Heylen; C. V. Chandran; F. Taulelle; E. Breynaert; J. A. Martens, Reversible Room Temperature Ammonia Gas Absorption in Pore Water of Microporous Silica-Alumina for Sensing Applications, *Phys. Chem. Chem. Phys.*, 2018, **20**, 13528-13536.
- [243] Le Xu; M. K. Choudhary; K. Muraoka; W. Chaikittisilp; T. Wakihara; J. D. Rimer; T. Okubo, Bridging the Gap Between Structurally Distinct 2D Lamellar Zeolitic Precursors Through a 3D Germanosilicate Intermediate, *Angew. Chem.*, 2019, **131**, 14671-14675.
- [244] M. Moliner; M. J. Díaz-Cabañas; V. Fornés; C. Martínez; A. Corma, Synthesis Methodology, Stability, Acidity, and Catalytic Behavior of the 18×10 Member Ring Pores ITQ-33 Zeolite, *J. Catal.*, 2008, **254**, 101-109.
- [245] N.-Y. Topsøe; K. Pedersen; E. G. Derouane, Infrared and Temperature-Programmed Desorption Study of the Acidic Properties of ZSM-5-Type Zeolites, *J. Catal.*, 1981, **70**, 41-52.
- [246] Emeis C.A., Determination of Integrated Molar Extinction Coefficients for Infrared Adsorption, *J. Catal.*, 1993, **141**, 347-354.

- [247] J. P. Gallas; J. C. Lavalley; A. Burneau; O. Barres, Comparative Study of the Surface Hydroxyl Groups of Fumed and Precipitated Silicas. 4. Infrared Study of Dehydroxylation by Thermal Treatments, *Langmuir*, 1991, **7**, 1235-1240.
- [248] M. Seiler; W. Wang; M. Hunger, Local Structure of Framework Aluminum in Zeolite H-ZSM-5 During Conversion of Methanol Investigated by in Situ NMR Spectroscopy, *J. Phys. Chem. B*, 2001, **105**, 8143-8148.
- [249] Freude D., Enhanced Resolution in the ^1H NMR Spectra of Zeolite H-ZSM-5 by Heteronuclear Dipolar-Dephasing Spin-Echo MAS, *Chemical Physics Letters*, 1995, **235**, 69-75.
- [250] Deng F., Yue Y., Ye C., $^1\text{H}/^{27}\text{Al}$ TRAPDOR NMR Studies on Aluminum Species in Dealuminated Zeolites, *Solid State Nucl. Magn. Reson.*, 1998, **10**, 151-160.
- [251] D. Freude, H. Ernst, I. Wolf, Solid-State Nuclear Magnetic Resonance Studies of Acid Sites in Zeolites, *Solid State Nucl. Magn. Reson.*, 1994, **3**, 271-286.
- [252] D. FREUDE, H. ERNST, M. HUNGER, H. PFEIFER, Magic-Angle-Spinning NMR Studies of Zeolite SAPO-5, *Chemical Physics Letters*, 1988, **143**, 477-481.
- [253] A. T.F. Batista; D. Wisser; T. Pigeon; D. Gajan; F. Diehl; M. Rivallan; L. Catita; A.-S. Gay; A. Lesage; C. Chizallet; P. Raybaud, Beyond $\Gamma\text{-Al}_2\text{O}_3$ Crystallite Surfaces: The Hidden Features of Edges Revealed by Solid-State ^1H NMR and DFT Calculations, *J. Catal.*, 2019, **378**, 140-143.
- [254] E. Verheyen; C. Jo; M. Kurttepelii; G. Vanbutsele; E. Gobechiya; T. I. Korányi; S. Bals; G. van Tendeloo; R. Ryoo; C. E.A. Kirschhock; J. A. Martens, Molecular Shape-Selectivity of MFI Zeolite Nanosheets in N-Decane Isomerization and Hydrocracking, *J. Catal.*, 2013, **300**, 70-80.
- [255] J.A. Martens; E. Benazzi; J. Brendlé; S. Lacombe; R. Le Dred, Catalytic Performances of Pillared Beidellites Compared to Ultrastable Y Zeolites in Hydrocracking and Hydroisomerisation Reactions, *Studies in Surface Science and Catalysis Elsevier Science B.V.*, 2000, **130**, 293-298.
- [256] J.A. Muñoz Arroyo; G.G. Martens; G.F. Froment; G.B. Marin; P.A. Jacobs; J.A. Martens, Hydrocracking and Isomerization of N-Paraffin Mixtures and a Hydrotreated Gasoil on Pt/ZSM-22: Confirmation of Pore Mouth and Key-lock Catalysis in Liquid Phase, *Appl. Catal. A-Gen.* 2000, **192**, 9-22.
- [257] R. A. Alberty; C. A. Gehrig, Standard Chemical Thermodynamic Properties of Alkane Isomer Groups, *J. Phys. Chem. Ref. Data*, 1984, **13**, 1173-1197.
- [258] Souverijns, W., Verrelst, W., Vanbutsele, G., Martens, J. A. & Jacobs, P. A, Micropore Structure of Zeolite MCM-22 as Determined by the Decane Catalytic Test Reaction, *J. Chem. Soc. Chem. Commun.*, 1994, 1671-1672.

- [259] H. van Bekkum, J.C. Jansen, P.A. Jacobs and E.M. Flanigen, Diffusion in Zeolite Molecular Sieves, *Studies in Surface Science and Catalysis Elsevier Science B.V.*, 2001, **137**, 525-577.
- [260] Michael J. Girgis and Y. Peter Tsao, Impact of Catalyst Metal–Acid Balance in N-Hexadecane Hydroisomerization and Hydrocracking, *Ind. Eng. Chem. Res.*, 1996, **35**, 386-396.

Appendix chapter 3

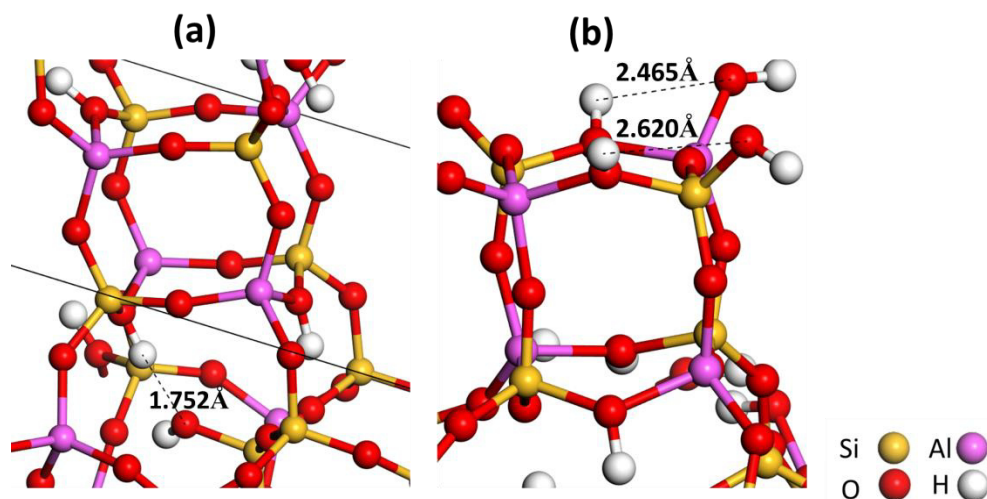


Figure S3- 1: Interactions between hydroxyls of interrupted frameworks and compensation hydrogen atoms illustrated with dashed lines inside an $-IRY$ (a) and location of the interrupted sites on the $d4r$ units of the $-ITV$ (b) aluminosilicate structures.

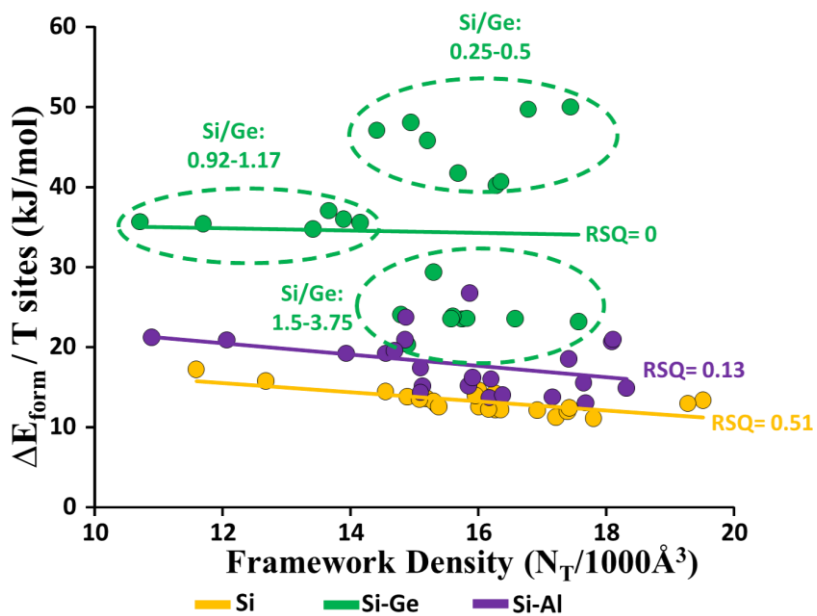


Figure S3- 2: Framework density effect on the energies of formation per T sites ($\Delta E_{\text{form}}/T$ sites), of normal and disordered silicates (yellow), silicogermanates (green) and aluminosilicates (purple). Si, Si-Ge and Si-Al represent silicates, silicogermanates with Ge occupying the full $d4r$ and aluminosilicates respectively. Si/Ge is the ratio of T sites occupied by Si over the T sites occupied by Ge.

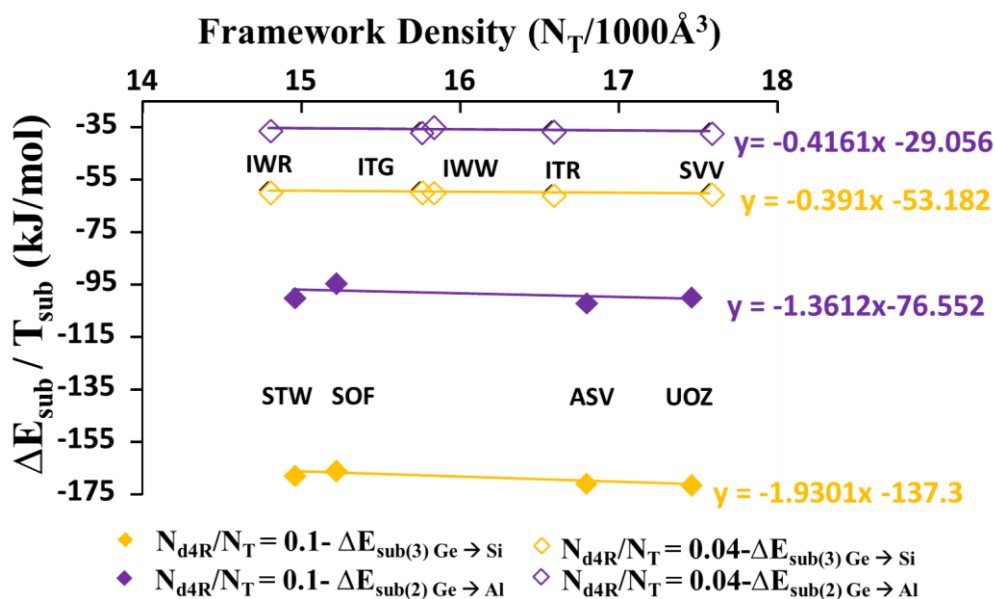


Figure S3- 3: Energies of full substitution of Ge for Si $\Delta E_{\text{sub}(3), \text{Ge} \rightarrow \text{Si}}$ (yellow) and of Ge for Al $\Delta E_{\text{sub}(2), \text{Ge} \rightarrow \text{Al}}$ (purple) normalized to the number of substituted T sites against the framework density of regular and disordered structures having a number of d4r over the number of T sites (N_{d4r}/N_T) equal to 0.04 and 0.1.

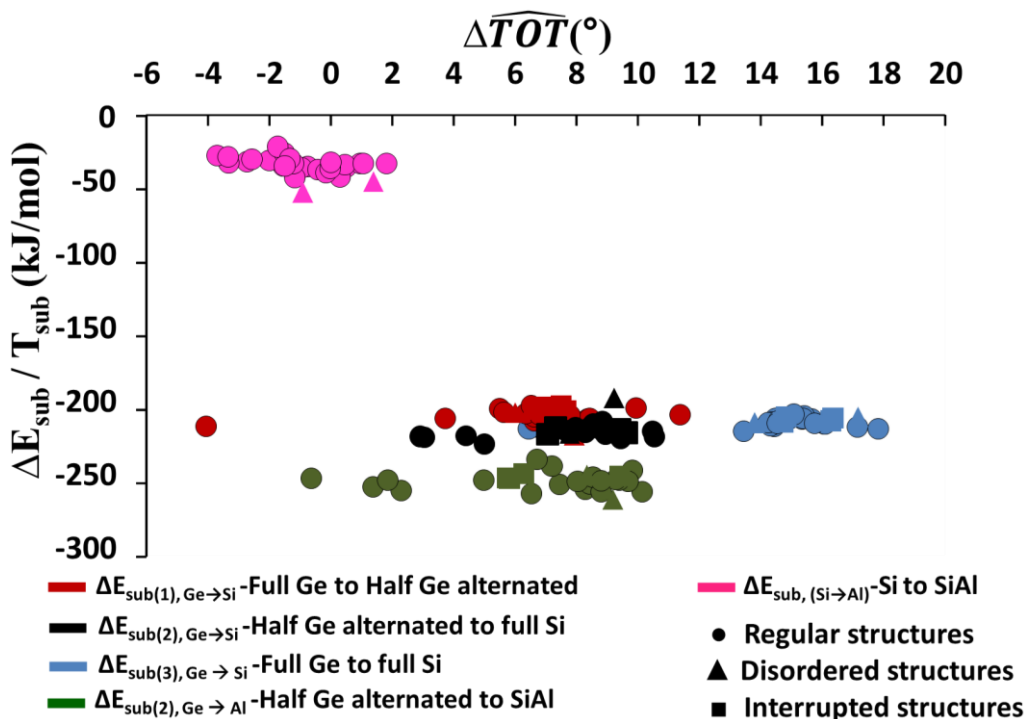


Figure S3- 4: Energies of substitution per T substituted atoms ($\Delta E_{\text{sub}} / T_{\text{sub}}$) of : Ge for Si departing from Ge occupying the full d4r to half Ge alternated, departing from half Ge alternated to full silicate and from full Ge in the d4r to full silicate respectively. Substitution of Ge for Al $\Delta E_{\text{sub}(2), \text{Ge} \rightarrow \text{Al}}$ departing from Ge occupying half of the d4r with alternation. $\Delta E_{\text{sub}, \text{Si} \rightarrow \text{Al}}$ departing from full silicate to aluminosilicate with Al alternated in the d4r . $\Delta \overline{TOT}$ corresponds to the difference of angles in the d4r between the initial and the substituted zeolite.

Table S3- 1: Cell parameters (Å) of the silicates, silicogermanates and aluminosilicates after geometry optimization compared to those of silicates from IZA. Full d4r is for Ge occupying all the d4r. Half d4r alternated and same s4r stand for Ge occupying half of the d4r.

IZA Structural code	IZA Silicates			Our Work												Aluminosilicates		
	a	b	c	Silicates			Silicogermanates											
				a	b	c	Full d4r			half d4r alternated			half d4r same s4r					
Regular	a	b	c	a	b	c	a	b	c	a	b	c	a	b	c	a	b	c
	(A)																	
ASV ^[60]	8.6740	8.6740	13.9190	8.5391	8.5391	14.0510	8.9752	8.9752	14.7923	8.7840	8.7840	14.3924	8.7652	8.7652	14.4190	8.7496	8.7575	14.4425
BEC ^[56,75-77]	12.7690	12.7690	12.9770	12.7266	12.7266	13.2642	13.1611	13.1611	13.5239	12.9157	12.9157	13.4315	12.8997	12.8997	13.4288	12.9507	12.9194	13.1423
IRN ^[82]	19.6410	18.4574	16.5655	19.6901	18.5225	16.5971	19.8466	19.0400	16.8880	19.7294	18.8323	16.8557	19.8522	18.4307	16.6603	20.0586	18.4247	16.7568
IRR ^[83-86]	19.0315	19.0315	14.1008	19.1114	19.1114	14.1854	19.6899	19.6899	14.4623	19.3771	19.3771	14.3434	19.2890	19.2890	14.3832	19.6551	19.6723	14.2587
ITG ^[90]	12.7411	12.6989	20.9990	12.9355	12.6285	21.2287	13.0406	12.8463	21.3936	13.0568	12.7432	21.3630	13.0685	12.7059	21.3060	12.9175	12.6904	21.2452
ITR ^[103,104]	11.6731	21.9694	25.1700	11.6967	22.0197	25.2513	11.7094	22.2538	25.9255	11.6960	22.2778	25.6261	11.6490	22.2854	25.5777	11.6741	22.0816	25.3156
ITT ^[4,105,107-111]	18.8677	18.8677	11.6332	19.0036	19.0036	11.5999	19.6196	19.6196	11.7960	19.2797	19.2797	11.6989	19.1851	19.1851	11.7224	19.4339	19.5478	11.5352
IWR ^[114-116]	21.2325	13.3024	12.6759	21.3018	13.5395	12.6384	21.5229	13.6520	12.8832	21.4207	13.6187	12.7514	21.3753	13.6232	12.7520	21.3755	13.6705	12.6650
IWS ^[117]	26.6887	26.6887	12.9078	26.7203	26.7203	13.0905	27.5967	27.5967	13.3114	27.1877	27.1877	13.1929	27.1398	27.1398	13.2054	27.5693	27.1794	13.0225
IWW ^[118-121]	41.6908	12.7128	12.7114	41.9895	12.9274	12.6176	42.3461	12.9871	12.8716	42.2909	13.0128	12.7576	42.2601	12.9995	12.7531	41.9854	13.0009	12.6640
POS ^[62]	18.7661	18.7661	11.6939	18.8915	18.8915	11.7177	19.4848	19.4848	11.9075	19.2808	19.2808	11.7886	19.1773	19.1773	11.8230	19.4205	19.3366	11.5988
SOF ^[61]	20.3320	12.0850	10.2750	20.3769	12.1399	10.3166	21.0154	12.4216	10.4959	20.7459	12.4079	10.4055	20.5677	12.4386	10.3310	20.5641	12.7309	10.1052
SOR ^[66,125]	20.9277	17.7028	7.5877	21.0668	17.6975	7.6058	21.5708	17.9270	7.9124	21.1697	17.5305	7.6290	21.1695	17.8490	7.7304	21.3027	16.4875	7.7436
SOV ^[126]	24.6308	26.6513	12.7267	24.9330	26.7684	12.7135	25.4342	27.6301	13.1088	24.9937	27.1820	12.8815	24.8066	26.9108	12.8471	24.6183	26.9371	12.7876
STW ^[61,128]	11.8870	11.8870	29.9150	11.9763	11.9763	30.1764	12.4297	12.4297	29.9990	12.3254	12.2758	30.0190	12.2454	12.2454	30.2563	12.3195	12.4651	30.4254
SVV ^[67,129]	13.1231	13.3734	21.2620	13.1705	13.4646	21.2644	13.1966	13.5708	21.3174	13.1884	13.5233	21.3138	13.1746	13.5061	21.2746	13.2418	13.4432	21.3533
UOS ^[131]	19.9055	7.5460	9.0683	19.9300	7.5968	9.1090	20.2589	7.8924	9.2181	20.0633	7.7684	9.1687	20.0053	7.7975	9.1947	19.3528	7.8895	9.0259
UOV ^[132]	12.7177	21.9894	38.7639	12.6650	22.2428	39.0242	12.7792	22.4314	39.3458	12.7303	22.3919	39.2935	12.7444	22.3780	39.2229	12.7466	22.2840	39.0861
UOZ ^[133]	8.6209	8.6209	27.5436	8.5935	8.5935	28.0896	8.7429	8.7429	29.9963	8.7273	8.7273	28.5131	8.7135	8.7135	28.5133	8.8007	8.7976	28.5289
UTL ^[5,50,134,135]	28.9964	13.9679	12.4493	29.2404	14.0346	12.4635	29.9209	14.0598	12.5173	29.5463	14.0410	12.4941	29.6826	14.0503	12.4792	29.7284	14.0340	12.4699
UWY ^[136]	25.1100	12.7330	11.5100	25.1748	12.7273	11.5827	25.5940	12.9532	11.8285	25.4689	12.8422	11.7282	25.3311	12.7911	11.6336	25.3295	12.9291	11.5167
Interrupted																		
-IFT ^[71]	18.8890	22.8023	29.0815	19.0045	22.9209	29.2772	19.5648	23.0719	29.2611	19.4203	22.9662	29.2354	19.3083	22.9395	29.2218	19.4249	22.9129	29.2951
-IFU ^[72]	26.0358	25.5895	15.8248	26.1672	25.5710	15.9071	27.2750	26.0285	16.5553	26.8986	25.6463	16.2519	26.9349	25.5510	16.2793	27.2073	25.7455	16.5565
-IRY ^[87]	15.9499	15.9499	31.0796	16.0892	16.0512	31.1723	16.7768	16.6956	31.6519	16.4751	16.4020	31.4939	16.4121	16.3428	31.4940	16.6219	16.5544	31.4156
-ITV ^[3,84,112,113]	26.3099	26.3099	26.3099	26.3047	26.3073	26.3073	26.2979	26.3342	26.3342	26.3002	26.3352	26.3547	26.2999	26.3294	26.3200	26.4294	26.1581	26.4098
Partially Disordered																		
*CTH ^[65,68,137,138]	10.4578	27.7607	27.2023	10.4433	27.9143	27.5152	10.4065	27.9272	28.2821	10.1470	27.7089	27.7765	10.1088	27.6222	27.7870	10.1022	27.6753	27.9439
*UOE ^[73]	9.0869	7.5548	10.4761	9.0996	7.5859	10.5026	9.2092	7.8734	10.5289	9.1499	7.7130	10.5323	9.0589	7.7526	10.3265	8.7640	8.7640	10.4145

(-) for interrupted; (*) for disordered structures

Table S3- 2: Framework density of all structures after geometry optimization

IZA Structural code	N _{d4r} /N _T	IZA	Our work		
		Silicates	Silicates	Silicogermanates (Ge in the full d4r)	Aluminosilicates
Framework density (T/1000Å ³)					
Regular					
ASV ^[60]	0.10	19.1	19.5	16.8	18.1
BEC ^[56,75-77]	0.06	15.1	14.9	13.7	14.6
IRN ^[82]	0.09	15.3	15.2	14.4	14.9
IRR ^[83-86]	0.06	11.8	11.6	10.7	10.9
ITG ^[90]	0.04	16.6	16.3	15.7	16.2
ITR ^[103,104]	0.04	17.4	17.2	16.6	17.2
ITT ^[4,105,107-111]	0.07	12.8	12.7	11.7	12.1
IWR ^[114-116]	0.04	15.6	15.4	14.8	15.1
IWS ^[117]	0.06	14.8	14.6	13.4	13.9
IWW ^[118-121]	0.04	16.6	16.4	15.8	16.2
POS ^[62]	0.06	15.5	15.3	14.2	14.7
SOF ^[61]	0.10	16.4	16.3	15.2	15.9
SOR ^[66,125]	0.08	17.1	16.9	15.7	17.6
SOV ^[126]	0.06	13.3	15.1	13.9	15.1
STW ^[61,128]	0.10	16.4	16	14.9	14.9
SVV ^[67,129]	0.04	18	17.8	17.6	17.7
UOS ^[131]	0.08	17.6	17.4	16.3	17.4
UOV ^[132]	0.03	16.2	16	15.6	15.9
UOZ ^[133]	0.10	19.5	19.3	17.4	18.1
UTL ^[5,50,134,135]	0.03	15.6	15.4	14.9	15.1
UWY ^[136]	0.05	16.3	16.2	15.3	15.9
Interrupted					
-IFT ^[71]	0.05	12.1	11.9	11.5	11.7
-IFU ^[72]	0.09	12.1	12	10.9	11
-IRY ^[87]	0.08	11.1	10.9	9.9	10.2
-ITV ^[3,84,112,113]	0.10	10.5	10.5	10.5	10.5
Partially Disordered					
*CTH ^[65,68,137,138]	0.03	16.2	16	15.6	16.4
*UOE ^[73]	0.08	17.6	17.4	16.4	18.3

(-) for interrupted. (*) for disordered structures

Table S3- 3: Energies of formation of silicogermanates and their silicate and aluminosilicates counterparts and energies of substitution of Ge for Si and Al following Figure 3- 6.

	$\Delta E_{form} / T$ (kJ/mol)			$\Delta E_{sub} / T$ (kJ/mol)								
	Si	Si-Ge	Si-Al	Ge→Si					Ge→Al			Si→Al
IZA Structural code	(full d4r)	(full d4r)	(full d4r)	Full Ge →Half Ge alternated	Full Ge →Half Ge in the s4r	Full Ge →Silicate	Half Ge alternated →Silicate	Half Ge in the s4r →Silicate	Full Ge →Aluminosilicate	Half Ge alternated → Aluminosilicate	Half Ge in the s4r → Aluminosilicate	Silicate → Aluminosilicate
Regular												
ASV ^[60]	13	50	21	-82.60	-84.22	-170.12	-87.51	-85.90	-183.93	-101.32	-99.71	-13.81
BEC ^[56,75-77]	14	37	19	-51.77	-54.43	-106.87	-55.10	-52.44	-114.66	-62.89	-60.23	-7.79
IRN ^[82]	14	47	21	-71.91	-75.59	-149.83	-77.92	-74.24	-160.89	-88.98	-85.30	-11.05
IRR ^[83-86]	17	36	21	-46.63	-45.68	-95.61	-48.99	-49.94	-103.85	-57.22	-58.17	-8.24
ITG ^[90]	12	23	14	-28.73	-29.23	-59.13	-30.40	-29.90	-65.14	-36.41	-35.91	-6.01
ITR ^[103,104]	11	24	14	-29.22	-30.17	-60.10	-30.88	-29.93	-65.11	-35.89	-34.94	-5.01
ITT ^[4,105,107-111]	16	35	21	-52.47	-51.52	-106.89	-54.42	-55.37	-115.57	-63.10	-64.05	-8.68
IWR ^[114-116]	13	24	15	-28.59	-29.55	-59.07	-30.48	-29.52	-64.21	-35.62	-34.66	-5.14
IWS ^[117]	14	35	19	-48.17	-49.16	-98.98	-50.81	-49.82	-106.67	-58.50	-57.51	-7.68
IWW ^[118-121]	12	24	16	-28.71	-29.63	-59.18	-30.48	-29.56	-62.90	-34.19	-33.27	-3.71
POS ^[62]	13	36	20	-51.05	-53.52	-105.94	-54.89	-52.42	-112.86	-61.81	-59.34	-6.92
SOF ^[61]	14	46	27	-80.19	-81.46	-165.35	-85.16	-83.89	-174.02	-93.83	-92.55	-8.66
SOR ^[66,125]	12	42	16	-69.41	-70.07	-141.07	-71.66	-71.00	-155.30	-85.89	-85.23	-14.23
SOV ^[126]	13	36	17	-51.31	-52.86	-106.07	-54.76	-53.22	-115.41	-64.10	-62.55	-9.34
STW ^[61,128]	15	48	24	-79.81	-81.90	-167.21	-87.40	-85.31	-179.27	-99.46	-97.37	-12.06
SVV ^[67,129]	11	23	13	-28.84	-29.40	-59.91	-31.07	-30.51	-65.51	-36.67	-36.11	-5.60
UOS ^[131]	12	40	18	-67.70	-68.35	-139.76	-72.06	-71.41	-150.80	-83.11	-82.46	-11.05
UOV ^[132]	13	24	15	-27.59	-28.24	-56.86	-29.27	-28.62	-61.47	-33.88	-33.23	-4.61
UOZ ^[133]	13	50	21	-84.72	-85.68	-170.80	-86.08	-85.12	-183.97	-99.24	-98.29	-13.16
UTL ^[5,50,134,135]	13	20	14	-20.81	-21.05	-42.95	-22.14	-21.90	-46.75	-25.94	-25.71	-3.81
UWY ^[136]	12	29	16	-40.78	-41.59	-84.02	-43.24	-42.43	-90.61	-49.83	-49.02	-6.59
Interrupted												
-IFT ^[71]	17	35	-14	-42.40	-42.71	-88.14	-45.74	-45.44	-94.43	-52.03	-51.72	-6.29
-IFU ^[72]	14	44	-21	-74.61	-75.84	-154.90	-80.29	-79.06	-166.96	-92.35	-91.12	-12.06
-IRY ^[87]	18	42	-13	-62.64	-62.62	-129.89	-67.25	-67.27	-140.92	-78.27	-78.29	-11.03
-JTV ^[3,84,112,113]	15	49	-89	-83.61	-85.62	-173.71	-90.10	-88.09	-185.54	-101.93	-99.92	-11.83
Partially Disordered												
*CTH ^[65,68,137,138]	14	24	14	-27.29	-27.82	-51.39	-24.09	-23.57	-57.98	-30.69	-30.16	-6.59
*UOE ^[73]	12	41	15	-67.59	-68.26	-139.76	-72.17	-71.50	-154.90	-87.31	-86.64	-15.13

(-) for interrupted. (*) for disordered structures

Table S3- 4: Gibbs free energies of substitution of Ge for Si ($\Delta G_{\text{sub}(1), \text{Ge} \rightarrow \text{Si}}$) and Ge for Al ($\Delta G_{\text{sub}(2), \text{Ge} \rightarrow \text{Al}}$) at different temperatures.

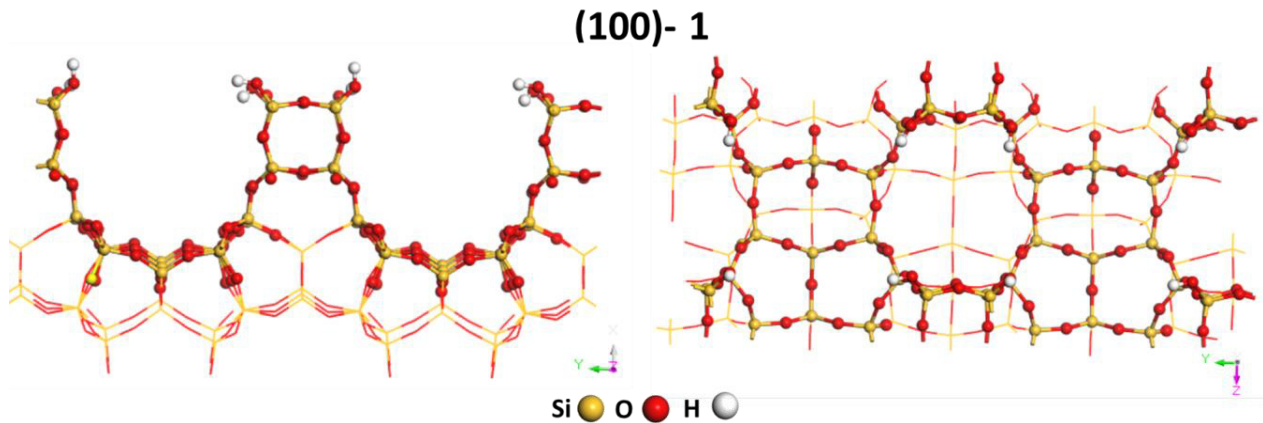
	$\Delta G_{\text{sub}(1), \text{Ge} \rightarrow \text{Si}}$			$\Delta G_{\text{sub}(2), \text{Ge} \rightarrow \text{Al}}$		
	Temperature (K)					
	298	550	1000	298	550	1000
IZA						
Structural code						
Regular						
ASV ^[60]	-53	-54	-56	-53	-44	-27
BEC ^[56,75-77]	-53	-54	-57	-53	-43	-26
IRN ^[82]	-53	-54	-56	-54	-44	-27
IRR ^[83-86]	-51	-53	-55	-52	-42	-25
ITG ^[90]	-51	-53	-55	-54	-44	-27
ITR ^[103,104]	-52	-53	-56	-53	-43	-26
ITT ^[4,105,107-111]	-51	-53	-55	-50	-41	-24
IWR ^[114-116]	-51	-52	-55	-52	-43	-26
IWS ^[117]	-52	-53	-56	-52	-43	-25
IWW ^[118-121]	-51	-53	-55	-50	-40	-23
POS ^[62]	-52	-53	-56	-52	-42	-25
SOF ^[61]	-51	-52	-55	-48	-39	-22
SOR ^[66,125]	-53	-54	-57	-52	-43	-26
SOV ^[126]	-52	-54	-56	-54	-45	-27
STW ^[61,128]	-51	-52	-55	-52	-43	-25
SVV ^[67,129]	-51	-53	-55	-54	-45	-27
UOS ^[131]	-52	-53	-56	-52	-43	-26
UOV ^[132]	-52	-53	-55	-52	-43	-25
UOZ ^[133]	-54	-55	-58	-52	-42	-25
UTL ^[5,50,134,135]	-50	-52	-54	-51	-42	-25
UWY ^[136]	-52	-53	-56	-52	-43	-26
Interrupted						
-IFT ^[71]	-51	-53	-55	-52	-42	-25
-IFU ^[72]	-51	-52	-55	-51	-42	-25
-IRY ^[87]	-51	-52	-54	-52	-42	-25
-ITV ^[3,84,112,113]	-51	-52	-55	-51	-42	-24
Partially Disordered						
*CTH ^[65,68,137,138]	-56	-57	-59	-51	42	-25
*UOE ^[73]	-52	-53	-56	-55	-46	-29

(-) for interrupted. (*) for disordered structures

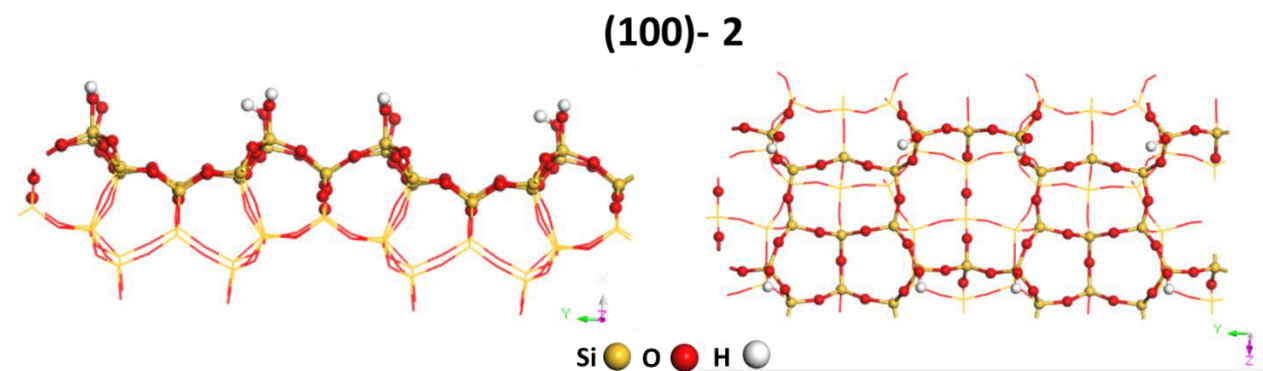
Table S3-5: Si-O and Ge-O bond lengths (\AA) computed for the BEC structure are various Si/Ge ratio.

Composition		Average Si-O, Si out of d4r	Average Si-O, Si in d4r	Average Ge-O
Silicate		1.618	1.624	-
Silicogermanate	Half occupation of d4r Ge in same s4r	1.620	1.624	1.778
	Half occupation of d4r Alternated	1.622	1.628	1.767
	Full occupation of d4r	1.625	-	1.774

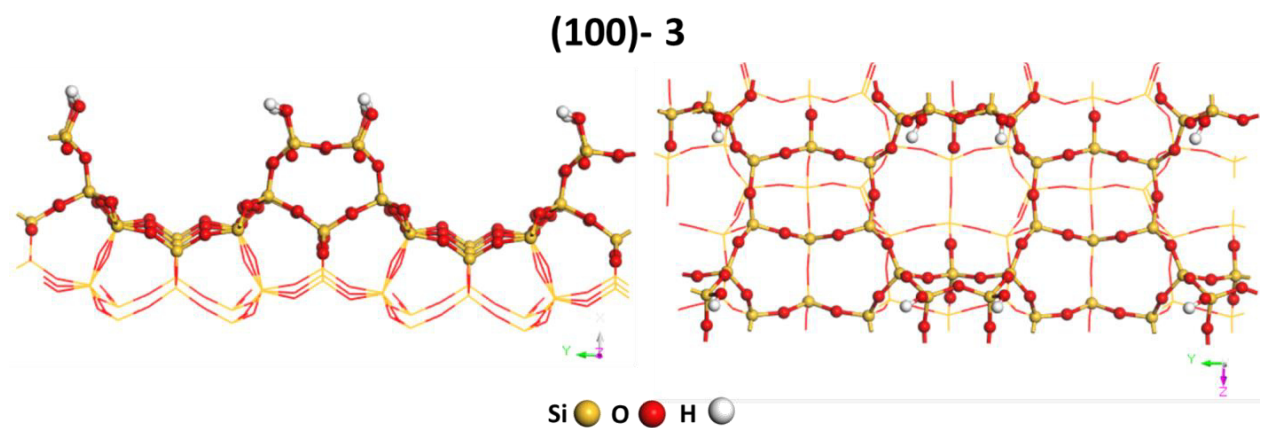
Appendix Chapter 4



S4- Figure 1: Side view and top view of the upper face of the siliceous surface following orientation (100) – Cleavage 1.

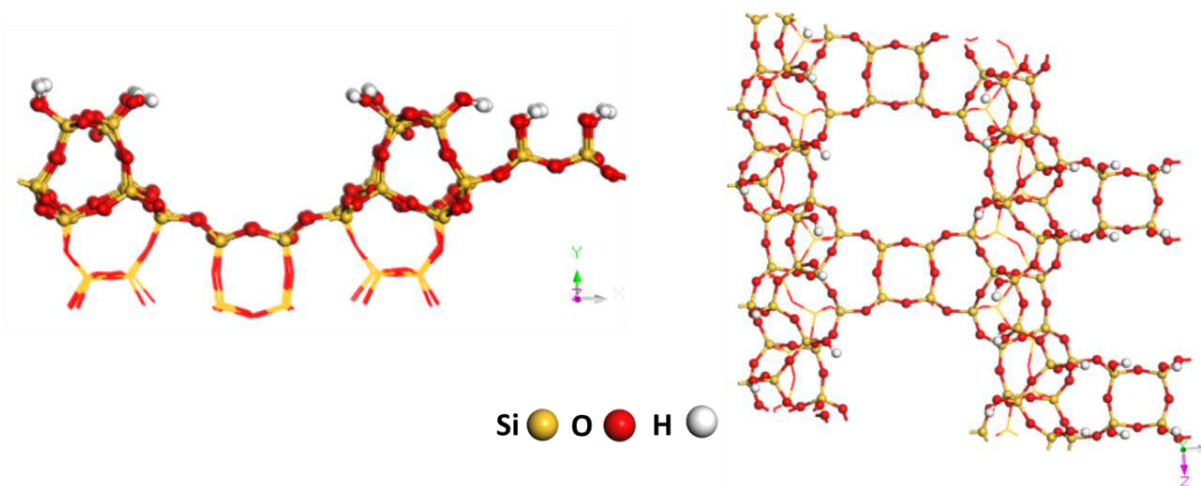


S4- Figure 2: Side view and top view of the upper face of the siliceous surface following orientation (100) – Cleavage 2.



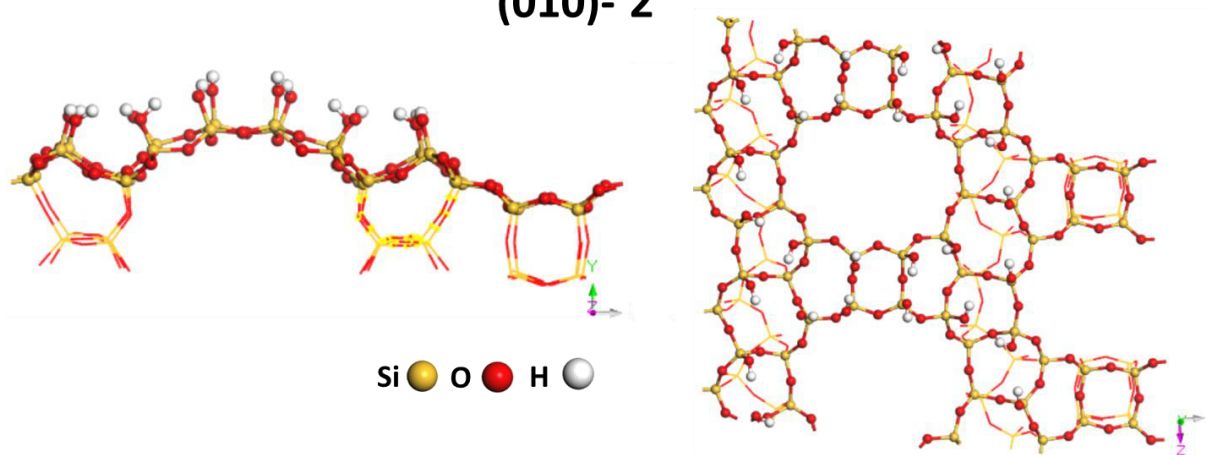
S4- Figure 3: Side view and top view of the upper face of the siliceous surface following orientation (100) – Cleavage 3.

(010)- 1



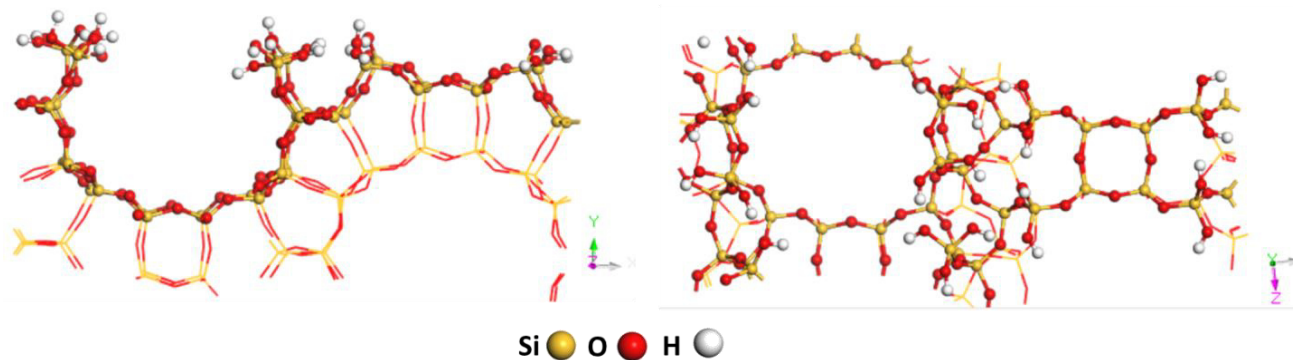
S4- Figure 4: Side view and top view of the upper face of the siliceous surface following orientation (010) – Cleavage 1.

(010)- 2



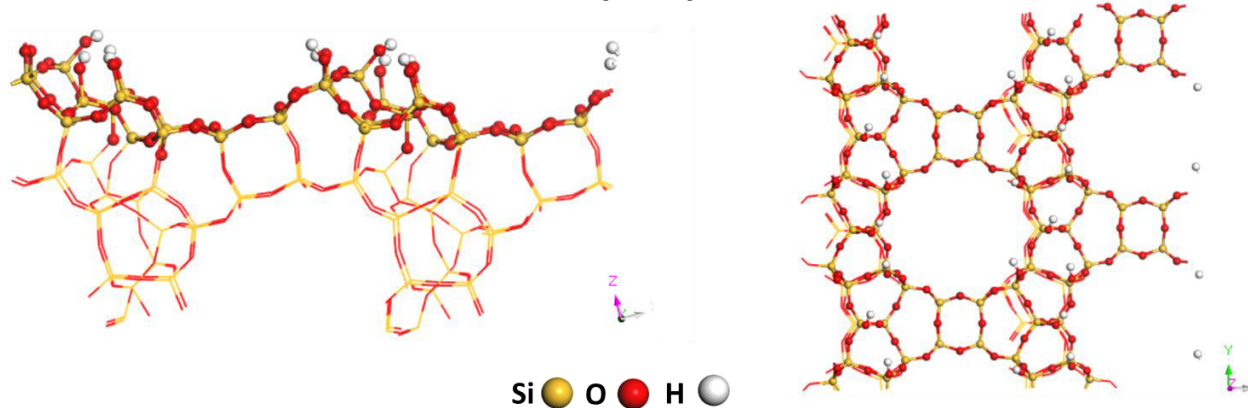
S4- Figure 5: Side view and top view of the upper face of the siliceous surface following orientation (010) – Cleavage 2.

(010)- 3



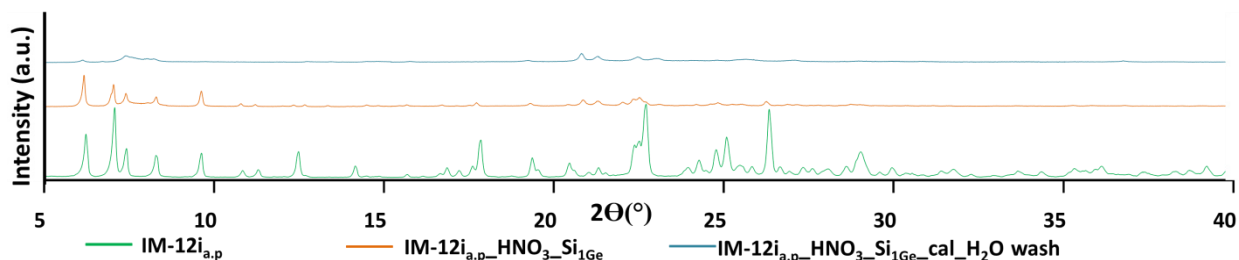
S4- Figure 6: Side view and top view of the upper face of the siliceous surface following orientation (010) – Cleavage 3.

(001)- 1

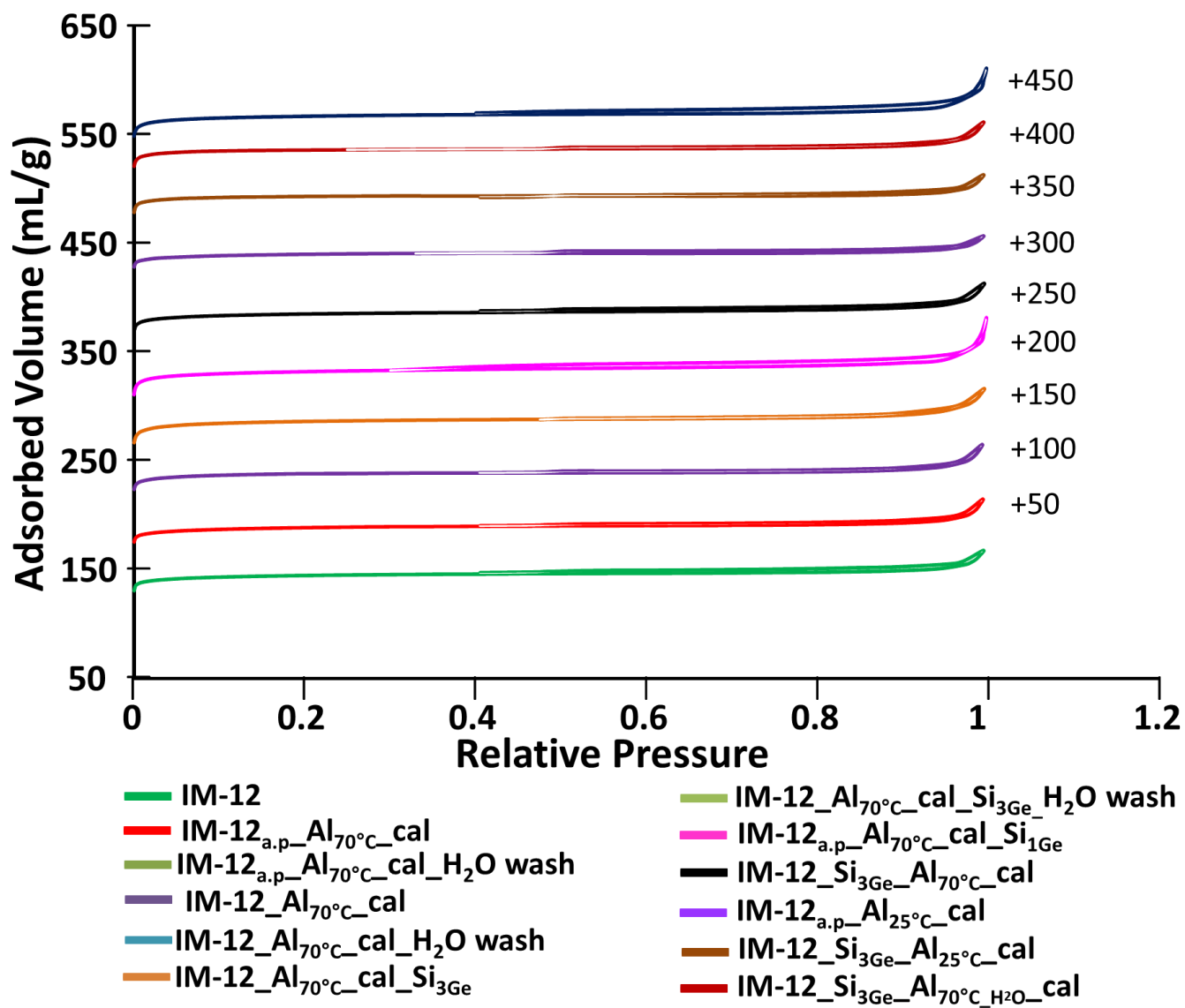


S4- Figure 7: Side view and top view of the upper face of the siliceous surface following orientation (001) – Cleavage 1.

Appendix chapter 5

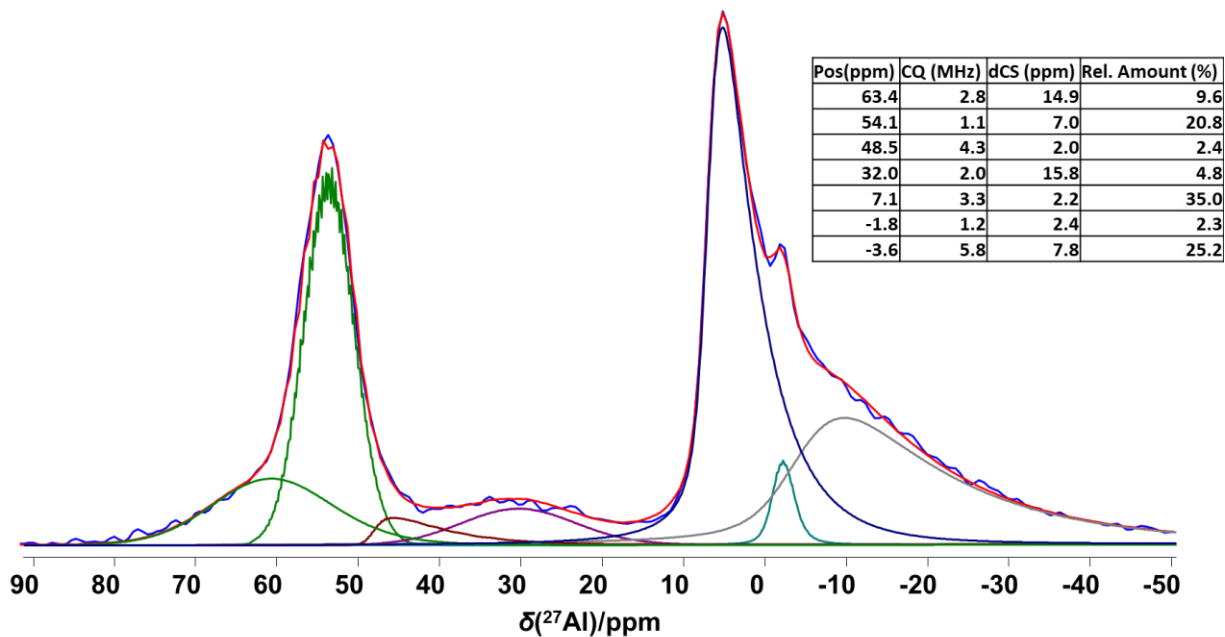


S5-Figure 1 : XRD patterns of as prepared IM-12, as prepared IM-12 treated with SiCl₄ and as prepared IM-12 treated with SiCl₄ then calcined and washed with water.



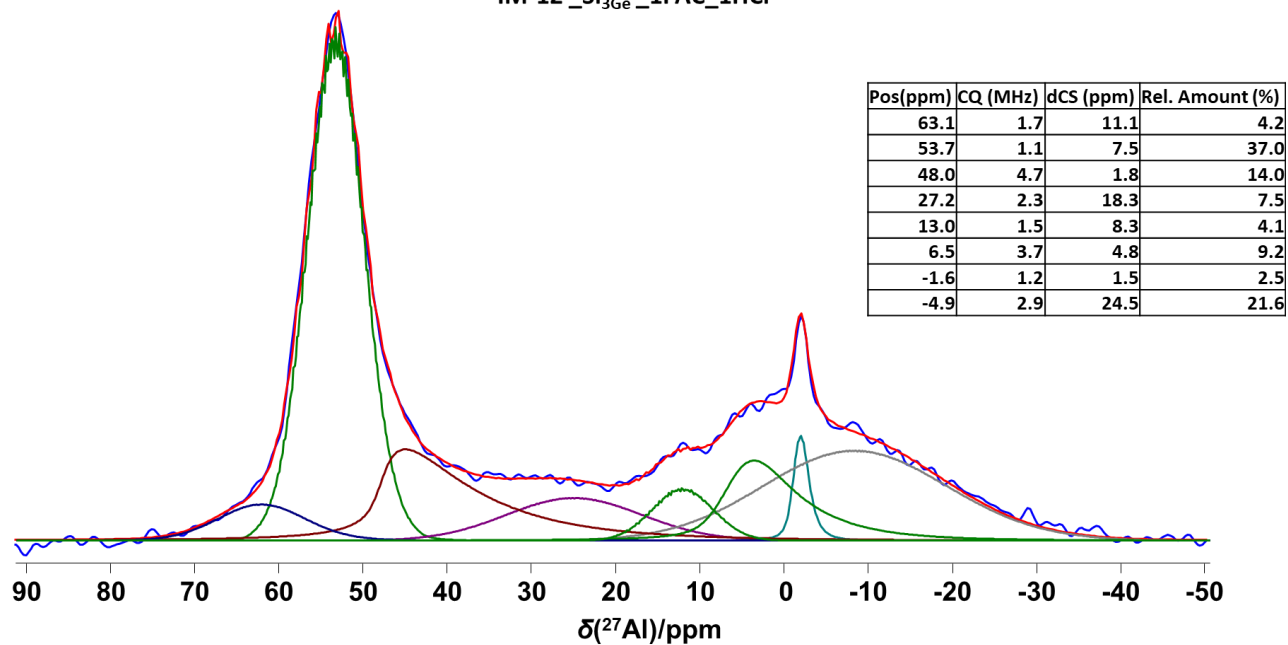
S5-Figure 2: N₂ physisorption of IM-12 treated with AlCl₃ dissolved in ethanol at different conditions.

²⁷Al (¹H decoupled)
IM-12 _Si₃Ge _1PAC

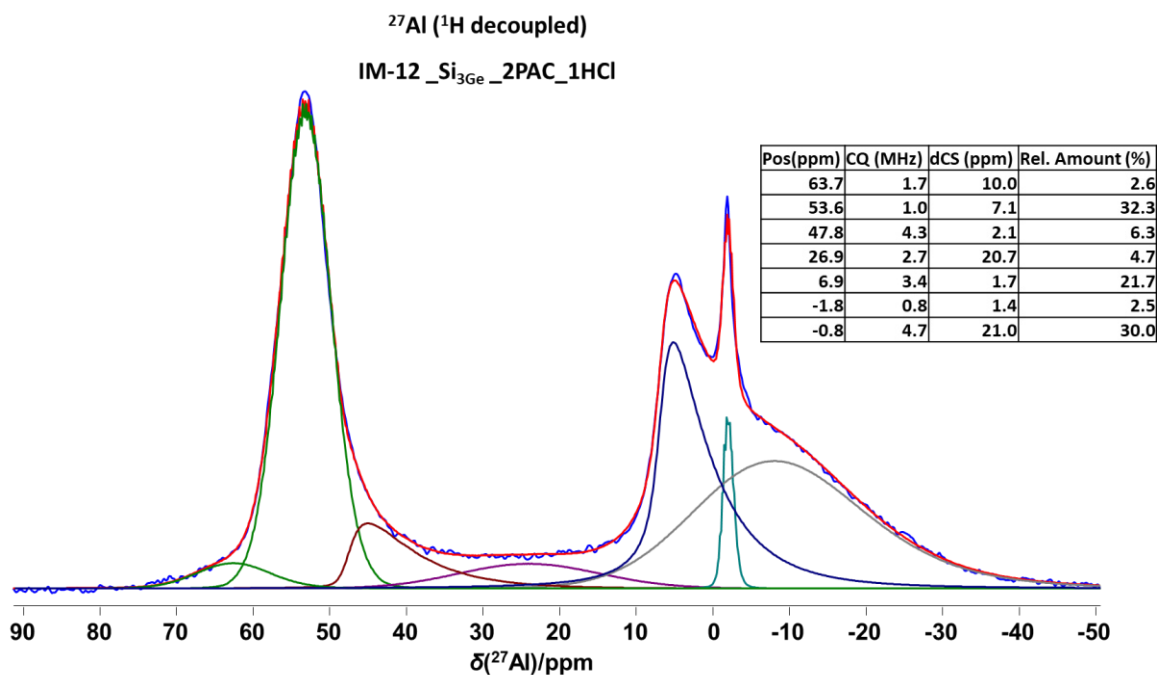


S5-Figure 3: deconvoluted ²⁷Al MAS NMR spectra of IM-12 _Si₃Ge _1PAC and Al quantification.

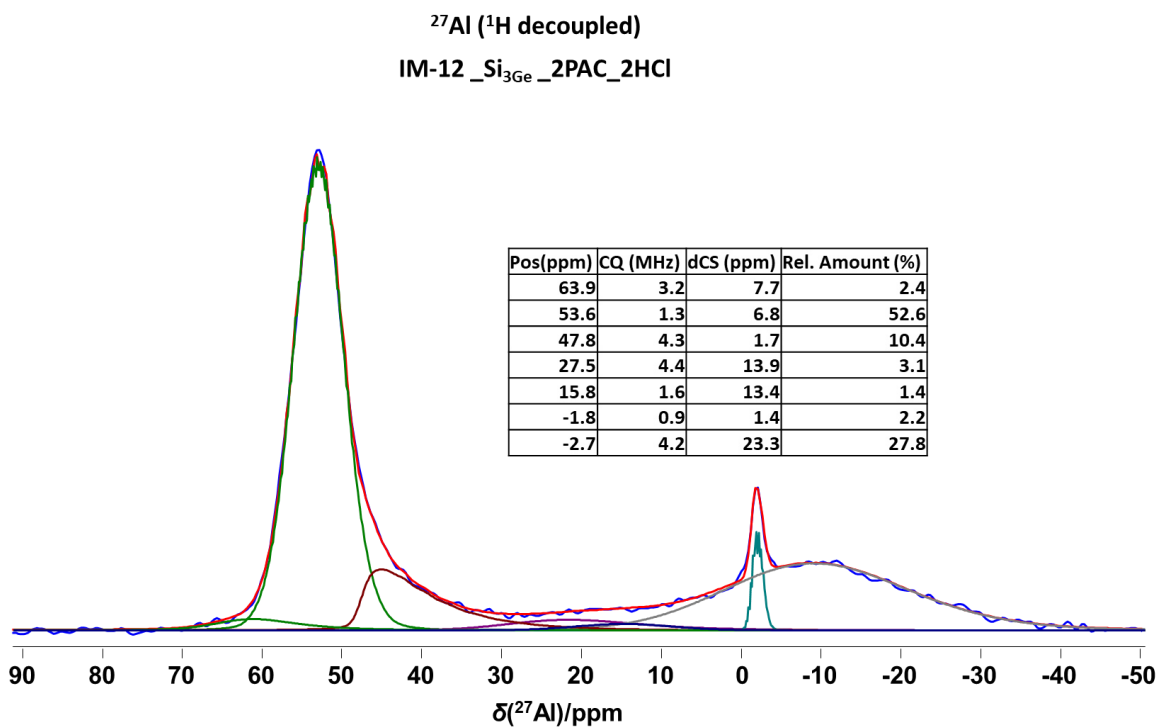
²⁷Al (¹H decoupled)
IM-12 _Si₃Ge _1PAC_1HCl



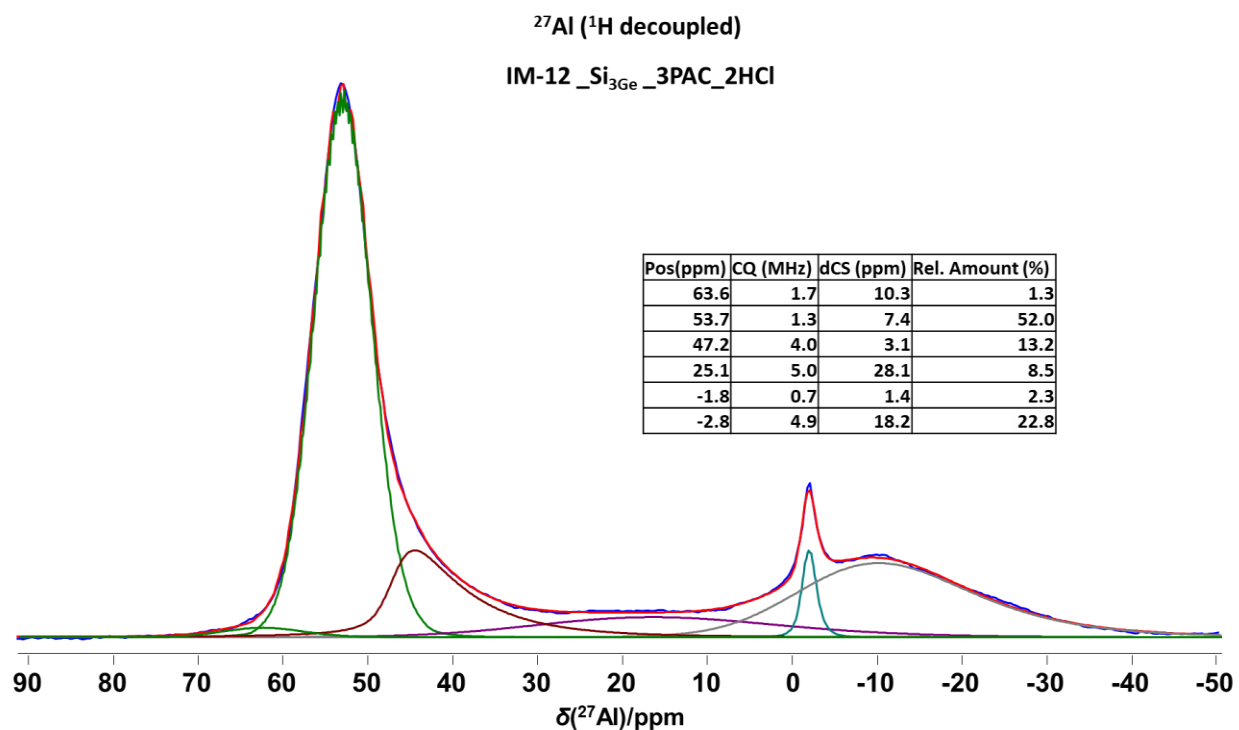
S5-Figure 4: deconvoluted ²⁷Al MAS NMR spectra of IM-12 _Si₃Ge _1PAC_1HCl and Al quantification.



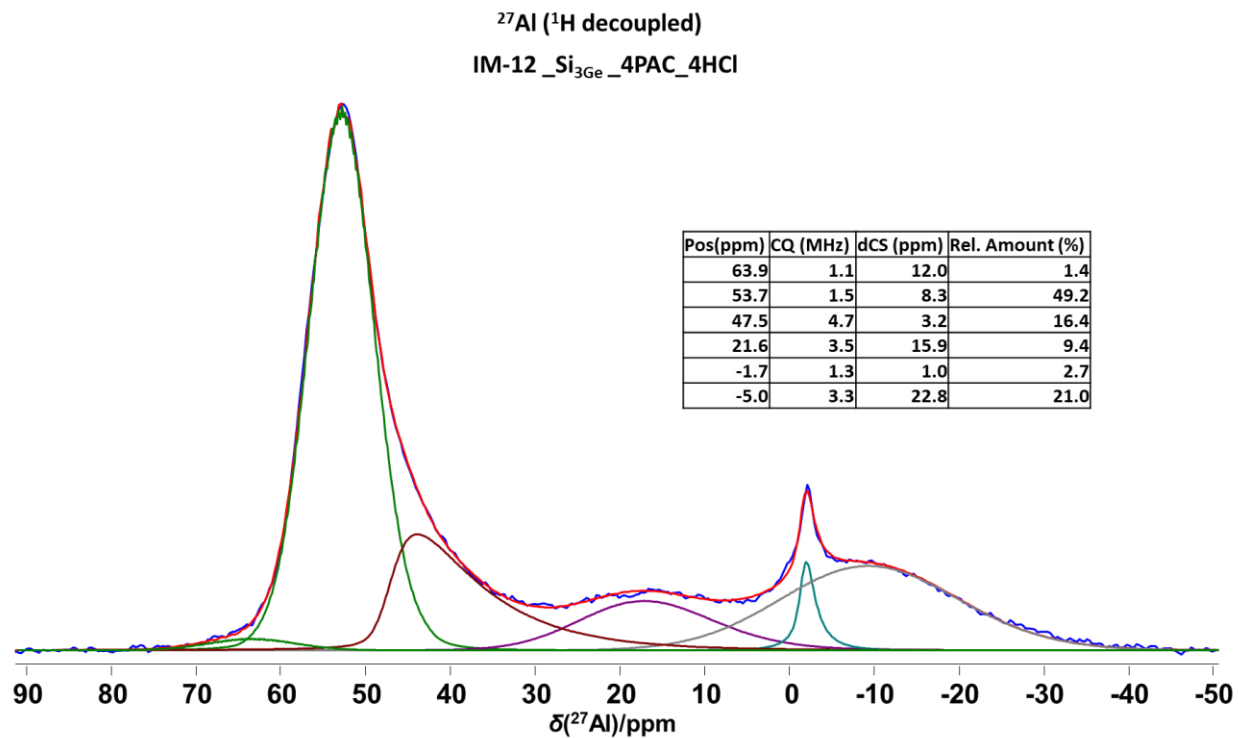
S5-Figure 5: deconvoluted ²⁷Al MAS NMR spectra of IM-12_Si₃Ge_2PAC_1HCl and Al quantification.



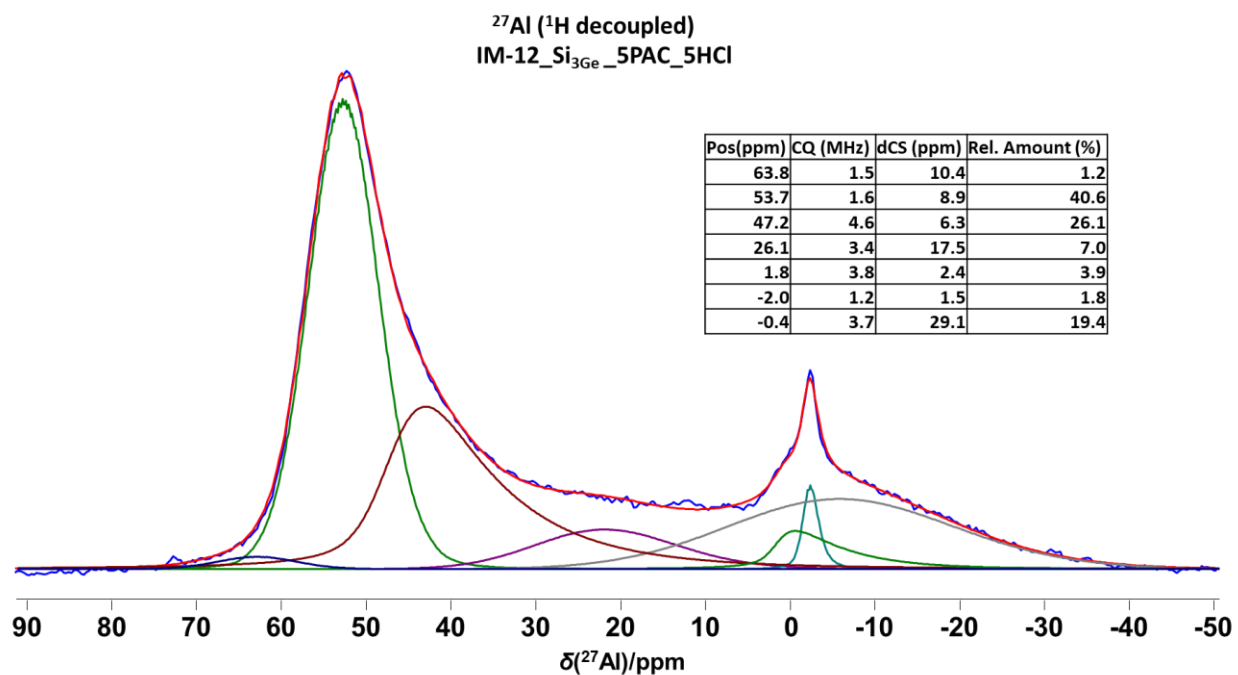
S5-Figure 6: deconvoluted ²⁷Al MAS NMR spectra of IM-12_Si₃Ge_2PAC_2HCl and Al quantification.



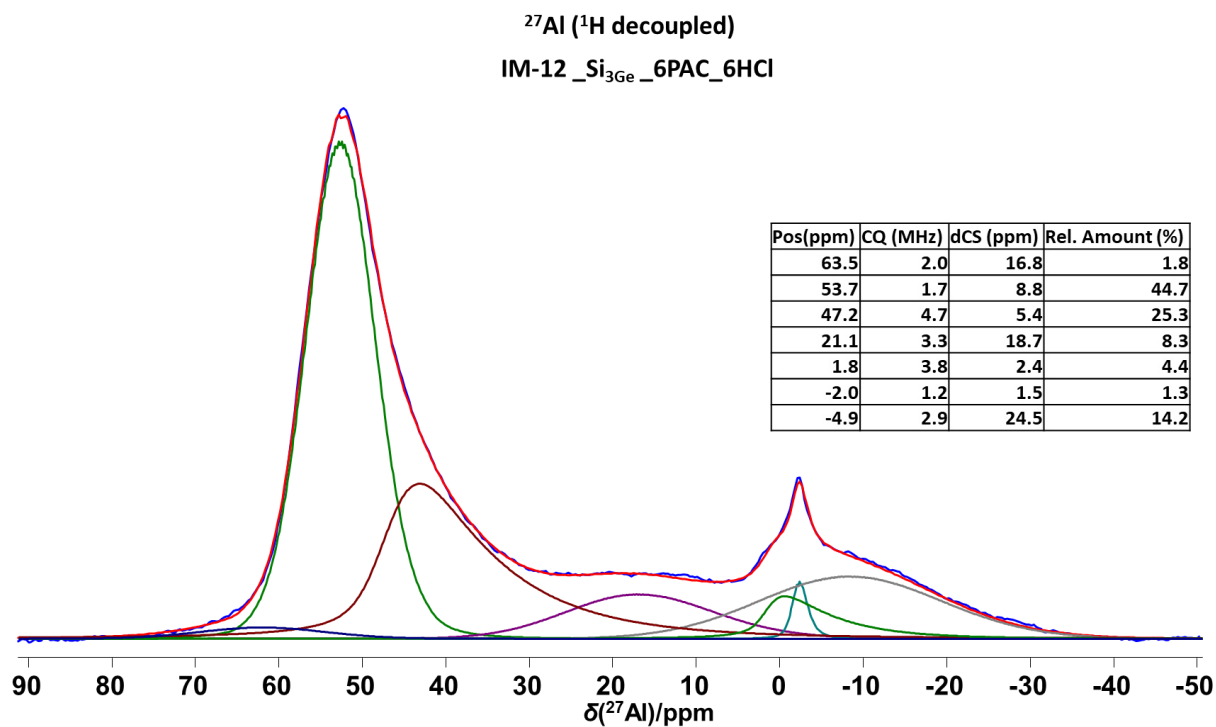
S5-Figure 7: deconvoluted ²⁷Al MAS NMR spectra of IM-12 _Si₃Ge _3PAC_2HCl and Al quantification.



S5-Figure 8: deconvoluted ²⁷Al MAS NMR spectra of IM-12 _Si₃Ge _4PAC_4HCl and Al quantification.

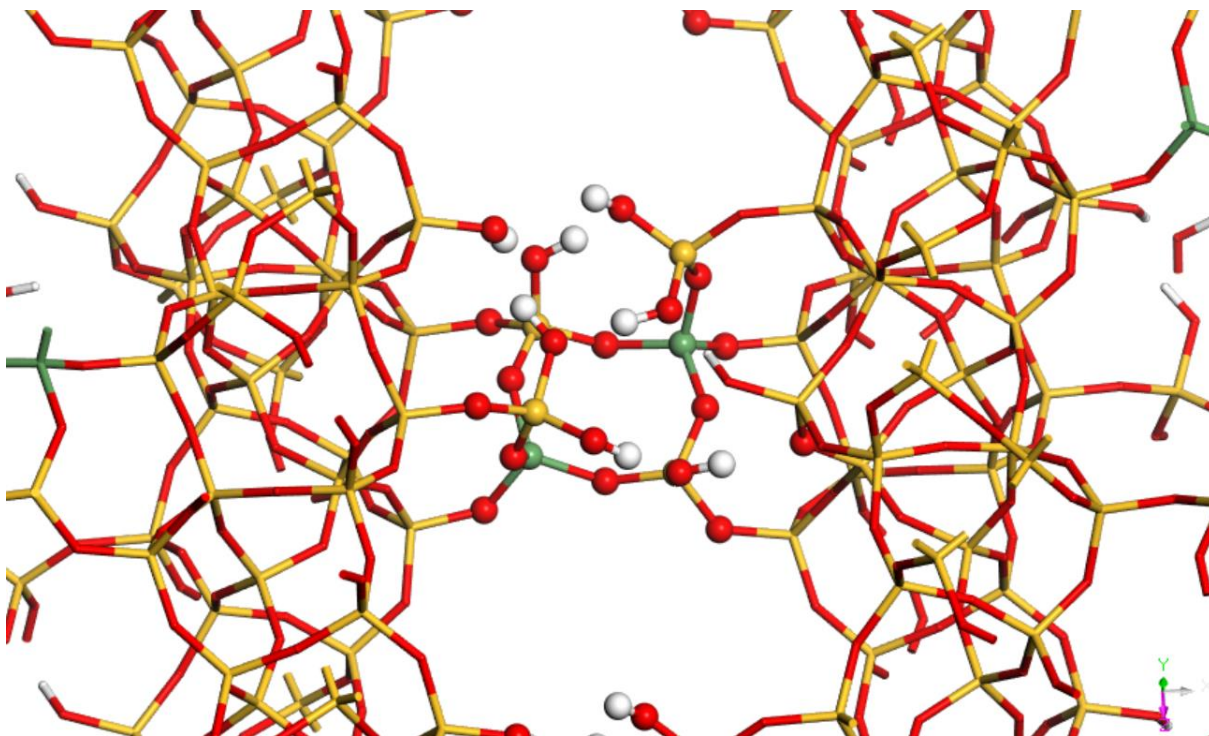


S5-Figure 9: deconvoluted ²⁷Al MAS NMR spectra of IM-12_Si₃Ge_5PAC_5HCl and Al quantification.

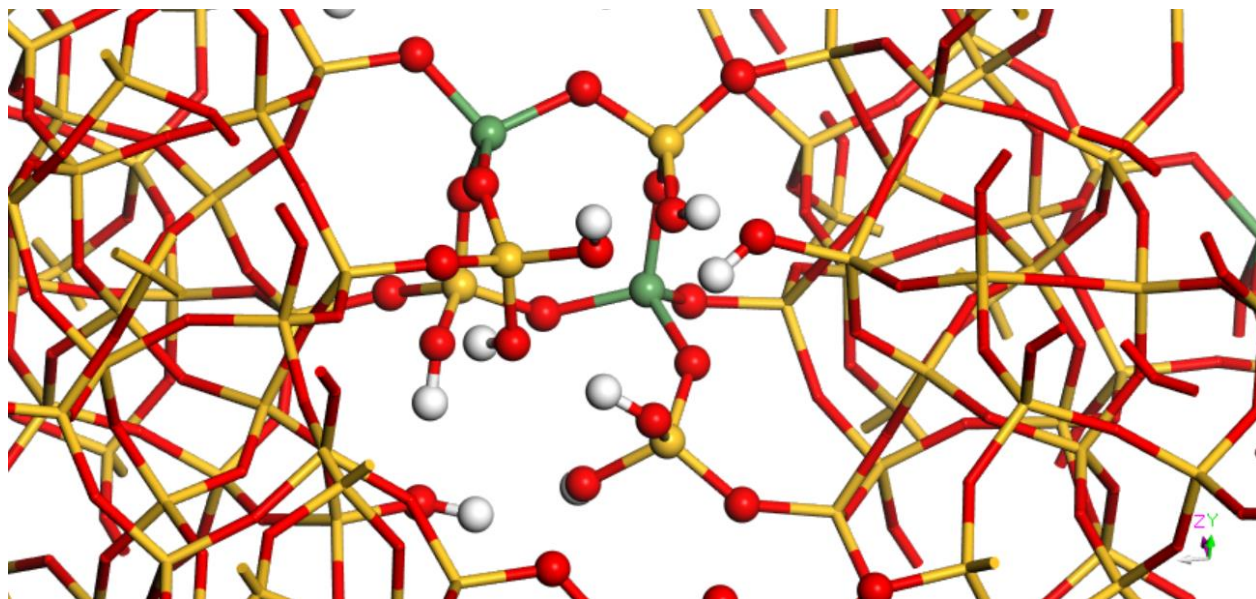


S5-Figure 10: deconvoluted ²⁷Al MAS NMR spectra of IM-12_Si₃Ge_6PAC_6HCl and Al quantification.

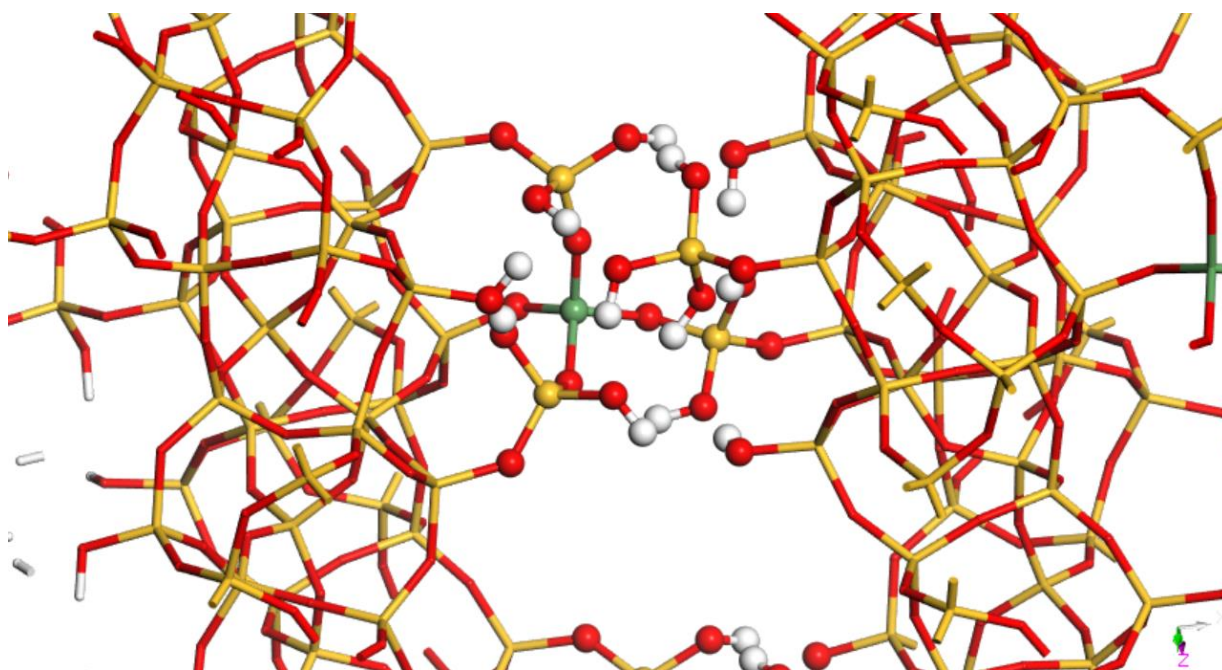
Appendix Chapter 6



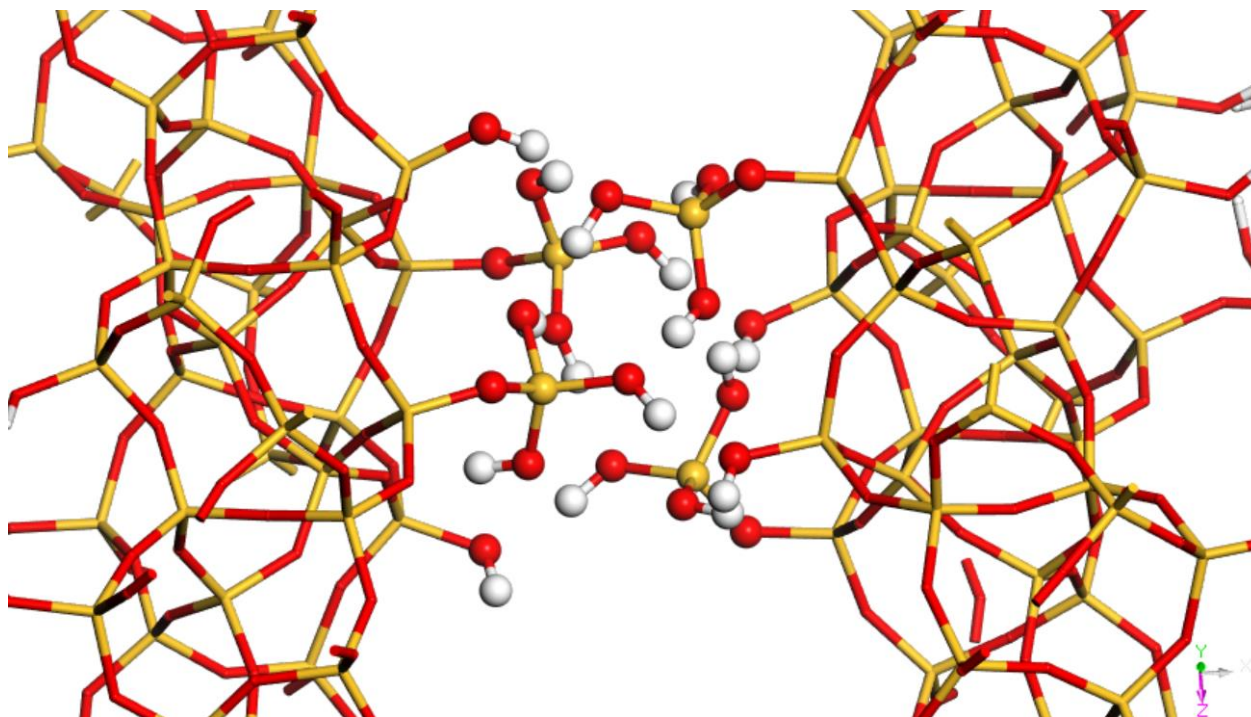
S6-Figure 1: IM-12 bulk model after removal of 2 Ge from different s4r from of bulk initially with Ge alternated between 2 s4r.



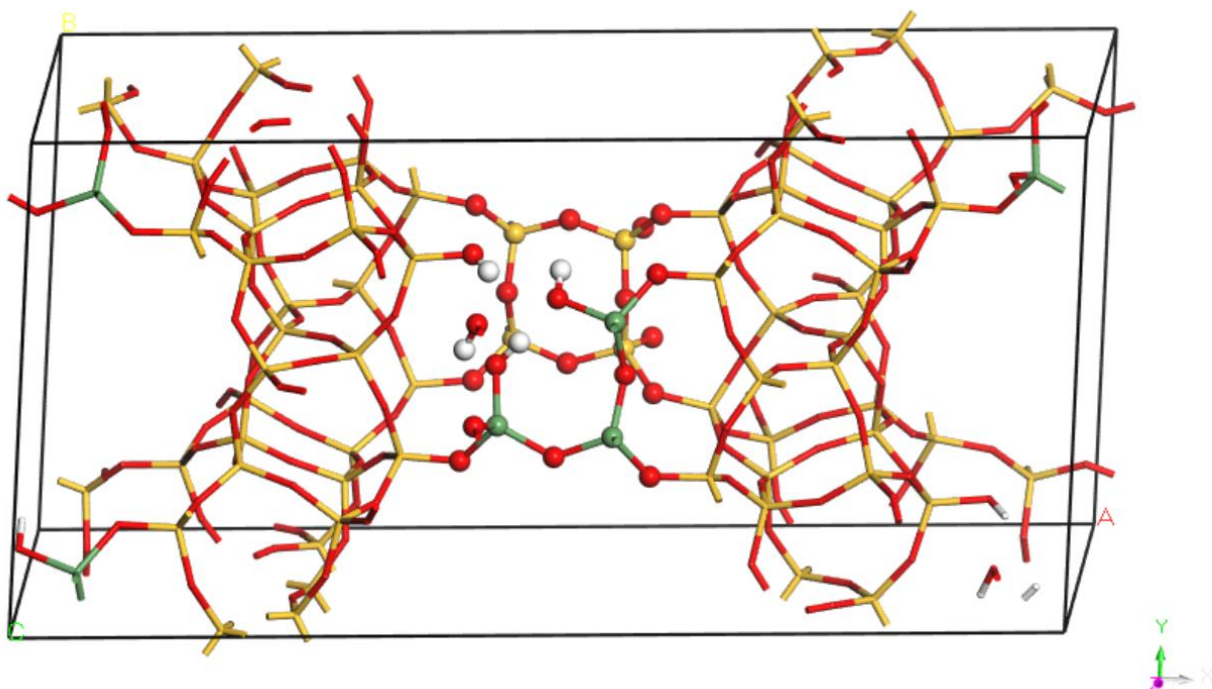
S6-Figure 2: IM-12 bulk model after removal of 2 Ge from same s4r from of bulk initially with Ge alternated between 2 s4r.



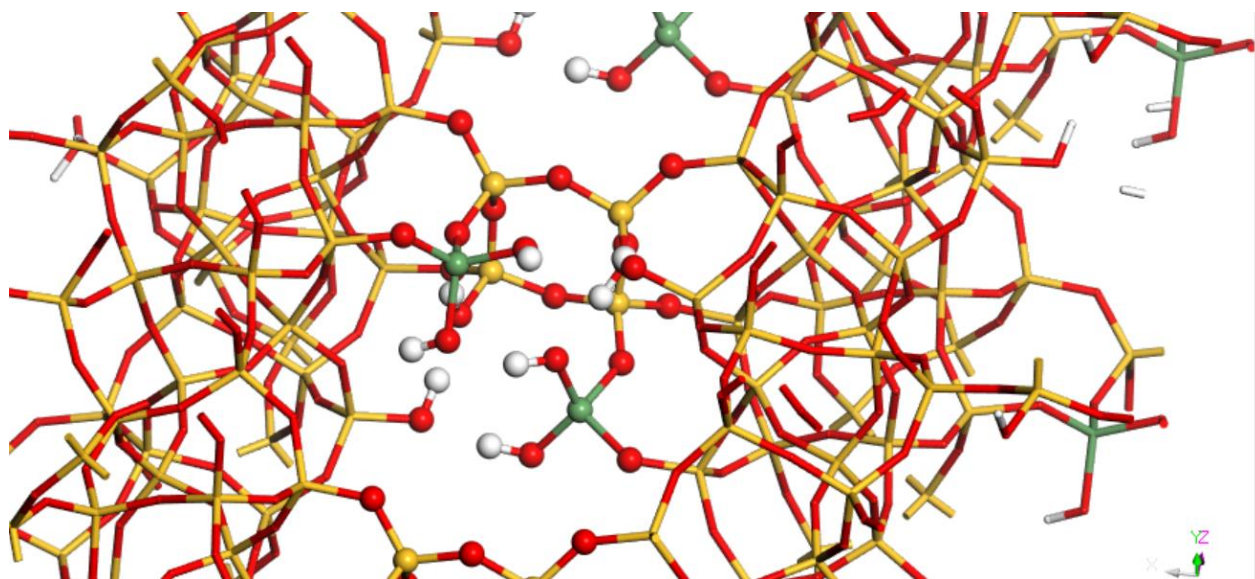
S6-Figure 3: IM-12 bulk model after removal of 3 Ge of bulk initially with Ge alternated between 2 s4r.



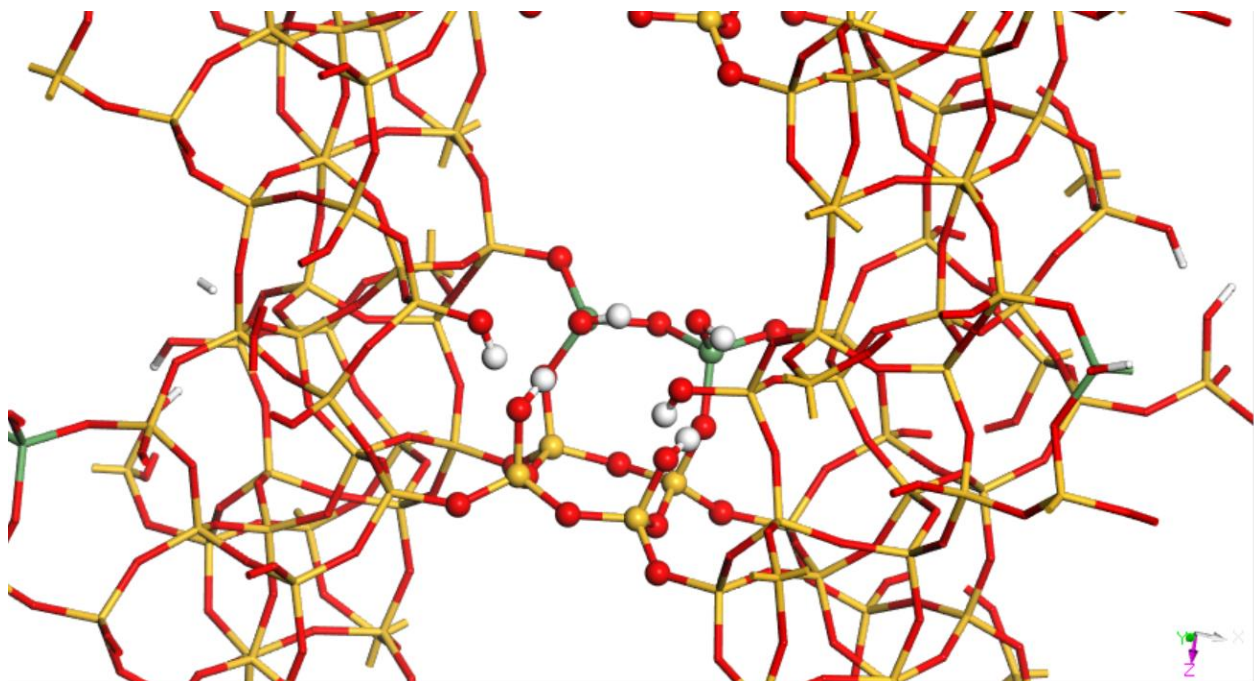
S6-Figure 4: IM-12 bulk model after removal of 4 Ge of bulk initially with Ge alternated between 2 s4r.



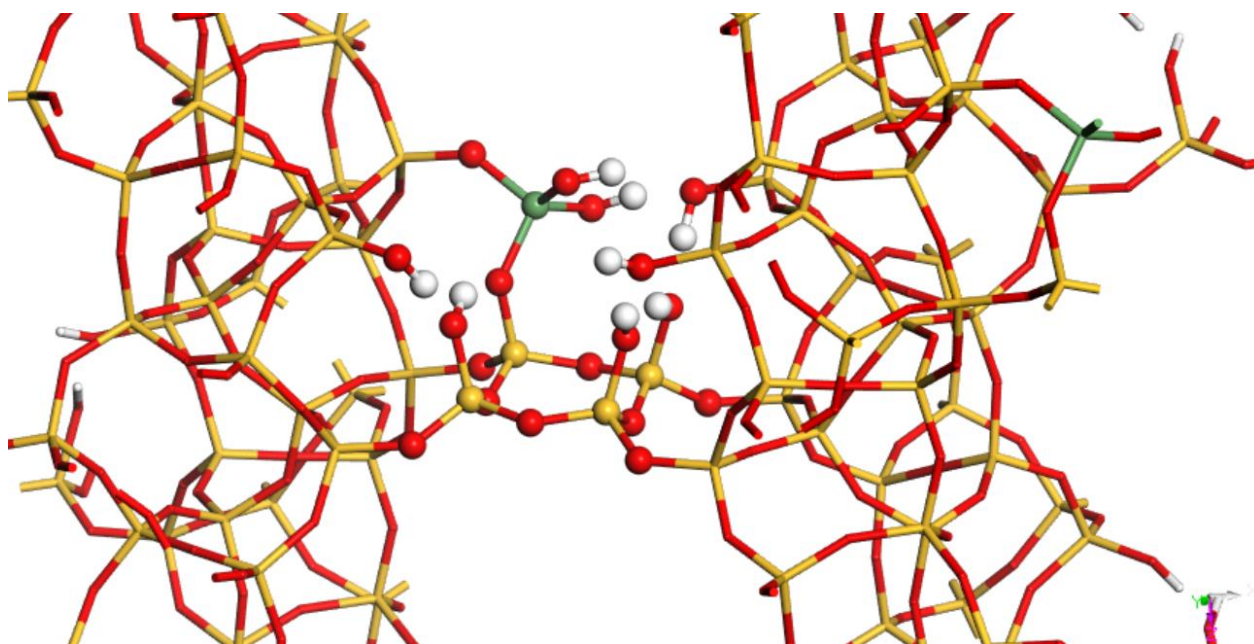
S6-Figure 5: IM-12 bulk model after removal of 1 Ge of bulk initially with Ge in the same s4r of the d4r.



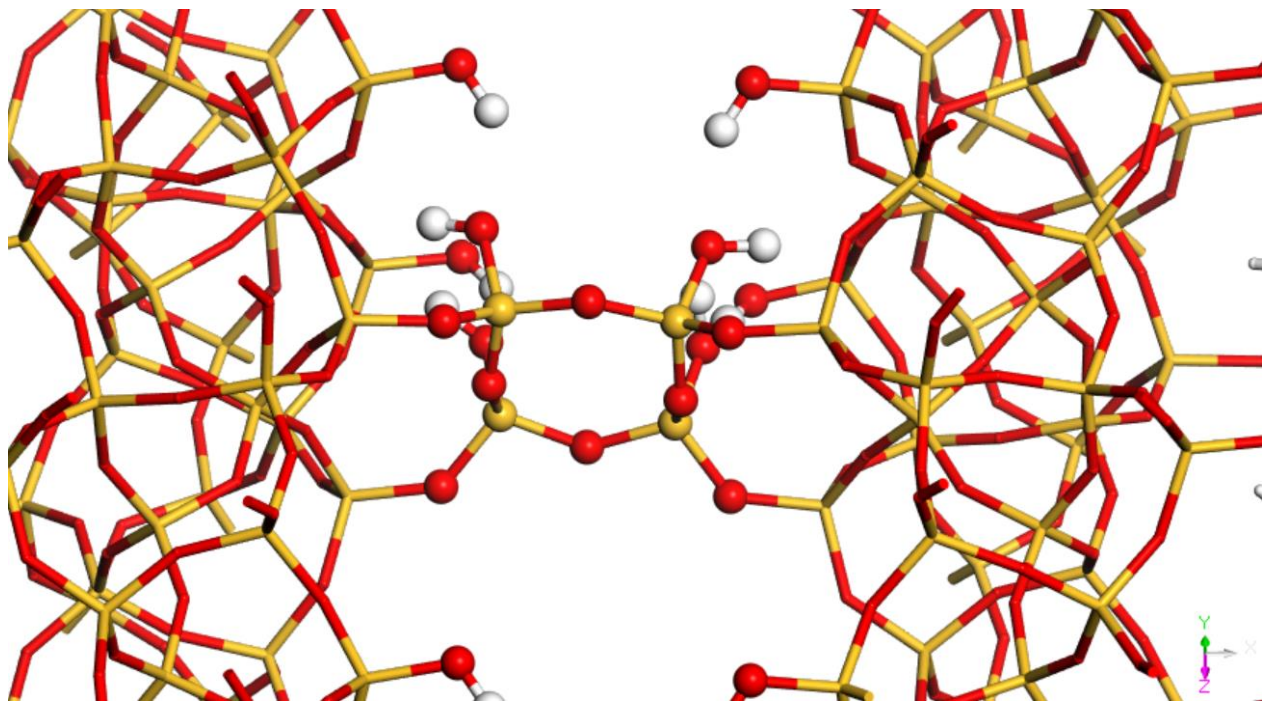
S6-Figure 6: IM-12 bulk model after removal of 2 separated Ge of bulk initially with Ge in the same s4r of the d4r.



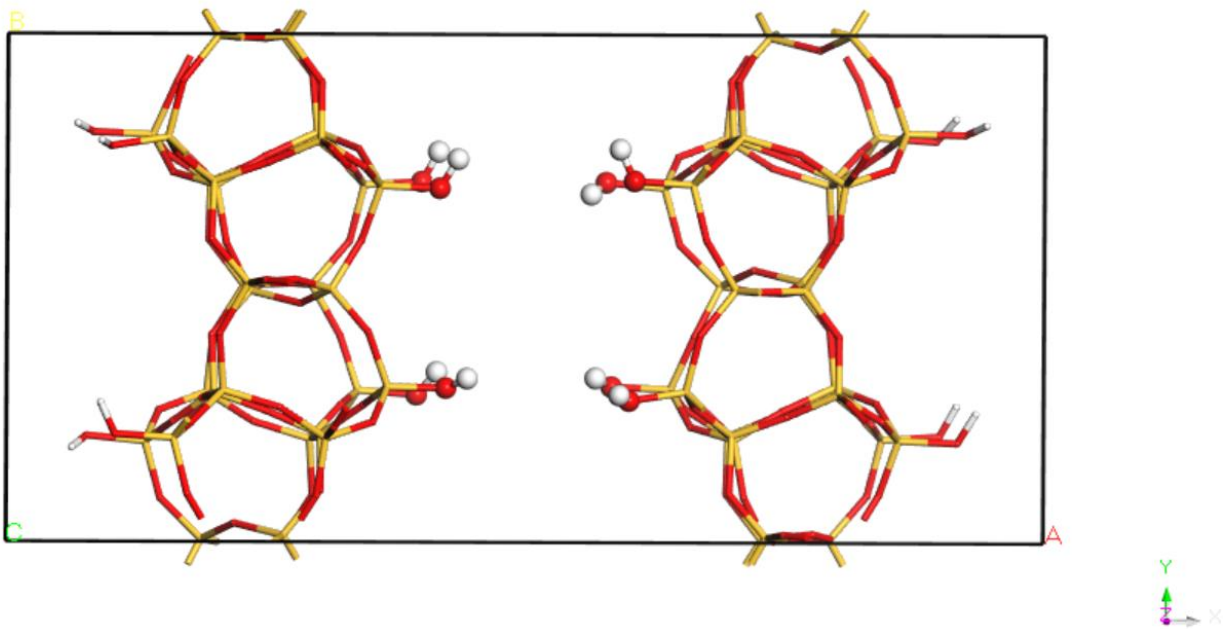
S6-Figure 7: IM-12 bulk model after removal of 2 consecutive Ge of bulk initially with Ge in the same s4r of the d4r.



S6-Figure 8: IM-12 bulk model after removal of 3 Ge of bulk initially with Ge in the same s4r of the d4r.



S6-Figure 9: IM-12 bulk model after removal of 4 Ge of bulk initially with Ge in the same s4r of the d4r.



S6-Figure 10: IM-12 bulk model after removal of the d4r units.

Appendix Chapter 7

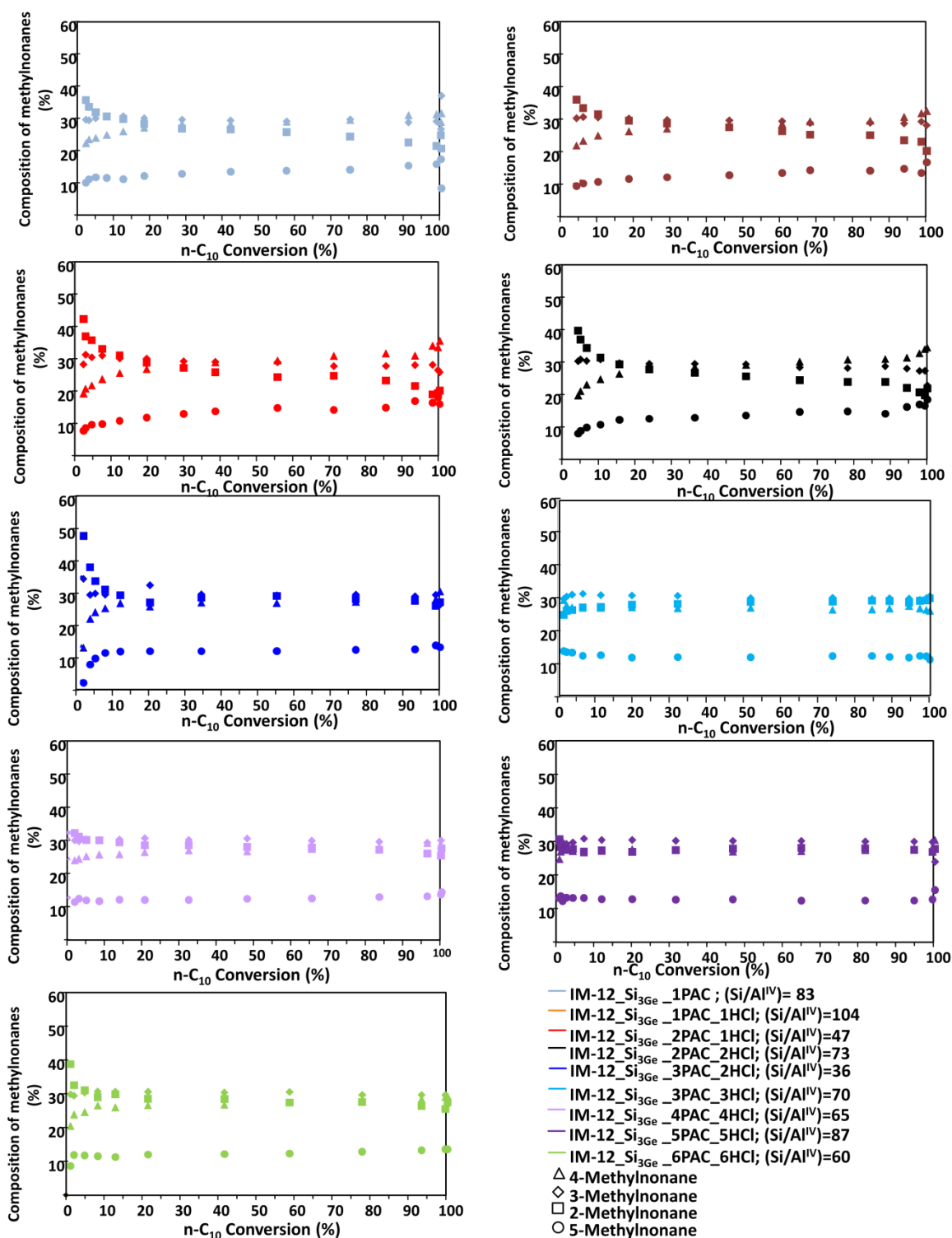


Figure S7- 1 Distribution of the four methylnonane isomers obtained from n-decane hydroconversion on bi-functional 0.3 wt.% Pt/IM-12 bi-functional catalysts with IM-12 treated with PAC.

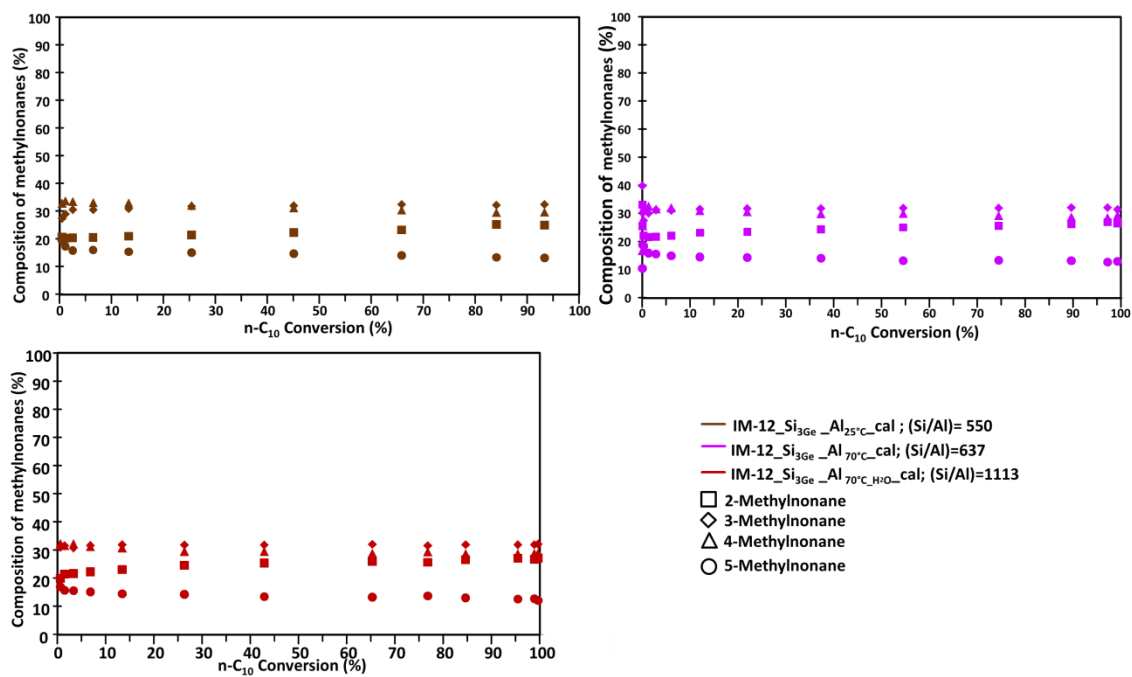


Figure S7- 2 Distribution of the four methylnonane isomers obtained from n-decane hydroconversion on bi-functional 0.3 wt.% Pt/IM-12 bi-functional catalysts with IM-12 treated with AlCl₃.

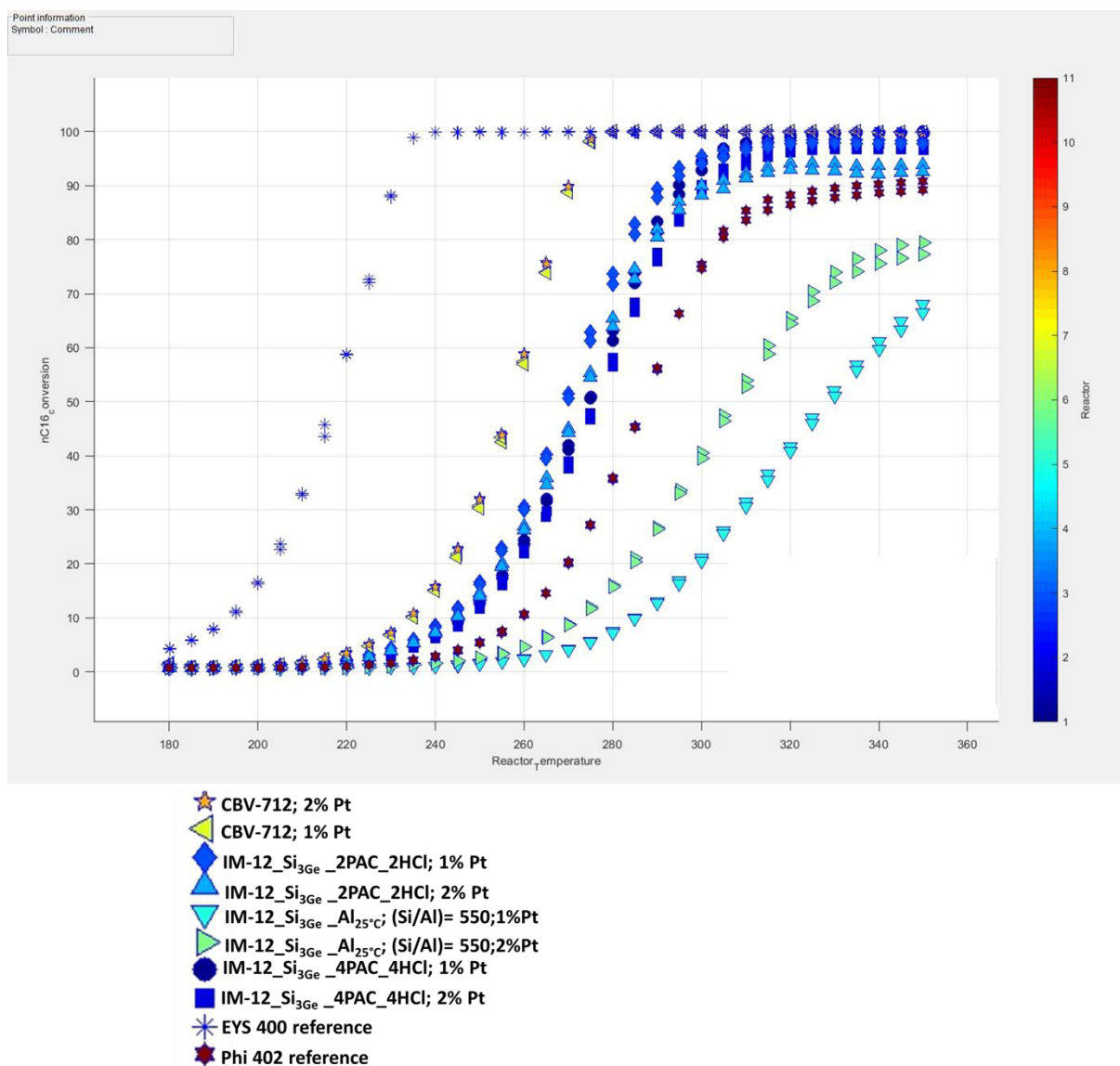


Figure S7- 3: Evolution of hexadecane conversion over time reflected via the two successive measured conversions for a given temperature of samples treated with PAC, AlCl₃, CBV-712 and a 2 calibration samples. For a given set of data, the point appearing at slightly lower conversion corresponds to the second measurement. The time gap between the two measurements is 4 hours.

References of Appendices

- [1] L. Q. Tang, M. S. Dadachov, X. D. Zou, Synthesis and Structures of New Silicogermanates, *Studies in Surface Science and Catalysis Elsevier*, 2004, **154**, 739-745.
- [2] A. Corma, M. T. Navarro, F. Rey, J. Rius, S. Valencia, Pure Polymorph C of Zeolite Beta Synthesized by Using Framework Isomorphous Substitution as a Structure-Directing Mechanism, *Angew. Chem. Int. Ed.*, 2001, **40**, 2277-2280.
- [3] A. Corma; M. T. Navarro; F. Rey; S. Valencia, Synthesis of Pure Polymorph C of Beta Zeolite in a Fluoride-Free System, *Chem. Commun.*, 2001, **0**, 1486-1487.
- [4] L. Shi; Y. Yuan; N. Zhang; S. Lin; T. Yu; J. Wang, Synthesis and Characterization of BEC-Zeotype Germanosilicates and B-Substituted Zeolitic Materials, *J. Porous. Mater.*, 2016, **23**, 647-654.
- [5] K. Jiao; Z. Zhang; X. Xu; Z. Lv; J. Song; C. Lin; J. Sun; M. He; H. Gies, Synthesis and Characterization of Germanosilicate Molecular Sieves: GeO₂/SiO₂ Ratio, H₂O/TO₂ Ratio and Temperature, *Dalton Trans.*, 2017, **46**, 2270-2280.
- [6] M. Hernández-Rodríguez; J. L. Jordá; F. Rey; A. Corma, Synthesis and Structure Determination of a New Microporous Zeolite with Large Cavities Connected by Small Pores, *J. Am. Chem. Soc.*, 2012, **134**, 13232-13235.
- [7] J. Jiang; J. L. Jorda; M. J. Diaz-Cabanas; J. Yu; A. Corma, The Synthesis of an Extra-Large-Pore Zeolite with Double Three-Ring Building Units and a Low Framework Density, *Angew. Chem. Int. Ed.*, 2010, **49**, 4986-4988.
- [8] J. Jiang; Y. Xu; P. Cheng; Q. Sun; J. Yu; A. Corma; R. Xu, Investigation of Extra-Large Pore Zeolite Synthesis by a High-Throughput Approach, *Chem. Mater.*, 2011, **23**, 4709-4715.
- [9] K. Qian; Y. Wang; Z. Liang; J. Li, Germanosilicate Zeolite ITQ-44 with Extra-Large 18-Rings Synthesized Using a Commercial Quaternary Ammonium as a Structure-Directing Agent, *RSC Adv.*, 2015, **5**, 63209-63214.
- [10] R. Bai; Q. Sun; N. Wang; Y. Zou; G. Guo; S. Iborra; A. Corma; J. Yu, Simple Quaternary Ammonium Cations-Templated Syntheses of Extra-Large Pore Germanosilicate Zeolites, *Chem. Mater.*, 2016, **28**, 6455-6458.
- [11] M. Moliner, T. Willhammar, W. Wan, J. González, F. Rey, J. L. Jorda, X. Zou, A. Corma, Synthesis Design and Structure of a Multipore Zeolite with Interconnected 12- and 10-MR Channels, *J. Am. Chem. Soc.*, 2012, **134**, 6473-6478.
- [12] A. Corma; M. J. Diaz-Cabanas; J. L. Jorda; F. Rey; G. Sastre; K. G. Strohmaier, A Zeolitic Structure (ITQ-34) with Connected 9- and 10-Ring Channels Obtained with Phosphonium Cations as Structure Directing Agents, *J. Am. Chem. Soc.*, 2008, **130**, 16482-16483.

- [13] A. Corma; M. J. Diaz-Cabanas; J. L. Jorda; F. Rey; K. Boulahya; J. M. Gonzalez-Calbet, High-Resolution Transmission Electron Microscopy (HRTEM) and X-Ray Diffraction (XRD) Study of the Intergrowth in Zeolites ITQ-13/ITQ-34, *J. Phys. Chem. C*, 2009, **113**, 9305-9308.
- [14] A. Corma, M. J. Diaz-Cabanas, J. L. Jorda, C. Martinez; M. Moliner, High-Throughput Synthesis and Catalytic Properties of a Molecular Sieve with 18- and 10-Member Rings, *Nature*, 2006, **443**, 842-845.
- [15] A. Corma; M. Moliner; M. J. Diaz-Cabanas; J. M. Serra Alfaro; R. Castañeda, Microporous Crystalline Material, Zeolite ITQ-33, Preparation Method Thereof and Use of Same, *European Patent 1847510A1*, 2006.
- [16] M. Bjørgen; A. H. Grave; Saepurahman; A. Volynkin; K. Mathisen; K. P. Lillerud; U. Olsbye; S. Svelle, Spectroscopic and Catalytic Characterization of Extra Large Pore Zeotype H-ITQ-33, *Microporous Mesoporous Mater.*, 2012, **151**, 424-433.
- [17] Q. Kun; S. Xiao-Wei; X. Da; L. Ji-Yang, Synthesis and Characterization of Extra-large 18-Ring Zeolite ITQ-33 Using Phosphonium as Structure-directing Agent, *Chem. J. Chinese U.*, 2012, **33**, 2141-2145.
- [18] L. Liu; Z.-B. Yu; H. Chen; Y. Deng; B.-L. Lee; J. Sun, Disorder in Extra-Large Pore Zeolite ITQ-33 Revealed by Single Crystal XRD, *Cryst. Growth Des.*, 2013, **13**, 4168-4171.
- [19] L. Wu; J. Hughes; M. Moliner; A. Navrotsky; A. Corma, Experimental Energetics of Large and Extra-Large Pore Zeolites: Pure Silica Beta Polymorph C (BEC) and Ge-Containing ITQ-33, *Microporous Mesoporous Mater.*, 2014, **187**, 77-81.
- [20] Z. Zhang; Y. Guo; X. Liu, Solid State NMR Techniques Study the Structural Characteristics of as-Synthesized ITQ-33, *J. Phys. Chem. C*, 2017, **121**, 11568-11575.
- [21] R. Castañeda; A. Corma; V. Fornés; F. Rey; J. Rius, Synthesis of a New Zeolite Structure ITQ-24, with Intersecting 10- and 12-Membered Ring Pores, *J. Am. Chem. Soc.*, 2003, **125**, 7820-7821.
- [22] A. Cantín, A. Corma, M. J. Diaz-Cabanas, J. L. Jordá, M. Moliner, Rational Design and HT Techniques Allow the Synthesis of New IWR Zeolite Polymorphs, *J. Am. Chem. Soc.*, 2006, **128**, 4216-4217.
- [23] W. H. Fu, Z. Yuan, Z. Wang, Y. Wang, W. Yang, M. Y. He, Direct Synthesis of Hydrothermally Stable Ge-IWR Zeolites, *Dalton Trans.*, 2017, **46**, 6692-6699.
- [24] D. L. Dorset; K. G. Strohmaier; C. E. Kliewer; A. Corma; M. J. Díaz-Cabañas; F. Rey; C. J. Gilmore, Crystal Structure of ITQ-26, a 3D Framework with Extra-Large Pores, *Chem. Mater.*, 2008, **20**, 5325-5331.
- [25] A. Corma; F. Rey; S. Valencia; J. L. Jordá; J. Rius, A Zeolite with Interconnected 8-, 10- and 12-Ring Pores and Its Unique Catalytic Selectivity, *Nat. Mater.*, 2003, **2**, 493-497.
- [26] G. Sastre; A. Pulido; R. Castañeda; A. Corma, Effect of the Germanium Incorporation in the Synthesis of EU-1, ITQ-13, ITQ-22, and ITQ-24 Zeolites, *J. Phys. Chem. B*, 2004, **108**, 8830-8835.

- [27] X. Liu; U. Ravon; F. Bosselet; G. Bergeret; A. Tuel, Probing Ge Distribution in Zeolite Frameworks by Post-Synthesis Introduction of Fluoride in as-Made Materials, *Chem. Mater.*, 2012, **24**, 3016-3022.
- [28] R. Yuan; N. Claes; E. Verheyen; A. Tuel; S. Bals; E. Breynaert; J. A. Martens; C. E. A. Kirschhock, Synthesis of an IWW-Type Germanosilicate Zeolite Using 5-Azonia-Spiro[4,4]Nonane as a Structure Directing Agent, *New J. Chem.*, 2016, **40**, 4319-4324.
- [29] W. Hua; H. Chen; Z.-B. Yu; X. Zou; J. Lin; J. Sun, A Germanosilicate Structure with 11×11×12-Ring Channels Solved by Electron Crystallography, *Angew. Chem. Int. Ed.*, 2014, **53**, 5868-5871.
- [30] L. Tang; L. Shi; C. Bonneau; J. Sun; H. Yue; A. Ojuva; B.-L. Lee; M. Kritikos; R. G. Bell; Z. Bacsik; J. Mink; X. Zou, A Zeolite Family with Chiral and Achiral Structures Built from the Same Building Layer, *Nat. Mater.*, 2008, **7**, 381-385.
- [31] Y. Luo; S. Smeets; F. Peng; A. S. Etman; Z. Wang; J. Sun; W. Yang, Synthesis and Structure Determination of Large-Pore Zeolite SCM-14, *Chem. Eur. J.*, 2017, **23**, 16829-16834.
- [32] L. Bieseki; R. Simancas; J. L. Jordá; P. J. Bereciartua; Á. Cantín; J. Simancas; S. B. Pergher; S. Valencia; F. Rey; A. Corma, Synthesis and Structure Determination via Ultra-Fast Electron Diffraction of the New Microporous Zeolitic Germanosilicate ITQ-62, *Chem. Commun.*, 2018, **54**, 2122-2125.
- [33] Y. Luo; S. Smeets; Z. Wang; J. Sun; W. Yang, Synthesis and Structure Determination of SCM-15, *Chemistry (Weinheim an der Bergstrasse, Germany)*, 2019, **25**, 2184-2188.
- [34] N. Zhang; L. Shi; T. Yu; T. Li; W. Hua; C. Lin, Synthesis and Characterization of Pure STW-Zeotype Germanosilicate, Cu- and Co-Substituted STW-Zeotype Materials, *J. Solid State Chem.*, 2015, **225**, 271-277.
- [35] D. J. Earl; A. W. Burton; T. Rea; K. Ong; M. W. Deem; S.-J. Hwang; S. I. Zones, Synthesis and Monte Carlo Structure Determination of SSZ-77: A New Zeolite Topology, *J. Phys. Chem. C*, 2008, **112**, 9099-9105.
- [36] L. B. McCusker; C. Baerlocher; A. W. Burton; S. I. Zones, A Re-Examination of the Structure of the Germanosilicate Zeolite SSZ-77, *Solid State Sci.*, 2011, **13**, 800-805.
- [37] Y. Lorgouilloux; M. Dodin; J.-L. Paillaud; P. Caullet; L. Michelin; L. Josien; O. Ersen; N. Bats, IM-16: A New Microporous Germanosilicate with a Novel Framework Topology Containing D4r and Mtw Composite Building Units, *J. Solid State Chem.*, 2009, **182**, 622-629.
- [38] Y. Lorgouilloux; M. Dodin; E. Mugnaioli; C. Marichal; P. Caullet; N. Bats; U. Kolb; J.-L. Paillaud, IM-17: A New Zeolitic Material, Synthesis and Structure Elucidation from Electron Diffraction ADT Data and Rietveld Analysis, *RSC Adv.*, 2014, **4**, 19440-19449.
- [39] Y. Mathieu; J.-L. Paillaud; P. Caullet; N. Bats, Synthesis and Characterization of IM-10, *Microporous Mesoporous Mater.*, 2004, **75**, 13-22.

- [40] J.-L. Paillaud; B. Harbuzaru; J. Patarin; N. Bats, Extra-Large-Pore Zeolites with Two-Dimensional Channels Formed by 14 and 12 Rings, *Science*, 2004, **304**, 990-992.
- [41] O. V. Shvets; A. Zukal; N. Kasian; N. Zilková; J. Čejka, The Role of Crystallization Parameters for the Synthesis of Germanosilicate with UTL Topology, *Chem. Eur. J.*, 2008, **14**, 10134-10140.
- [42] O. V. Shvets; N. Kasian; A. Zukal; J. Pinkas; J. Čejka, The Role of Template Structure and Synergism Between Inorganic and Organic Structure Directing Agents in the Synthesis of UTL Zeolite, *Chem. Mater.*, 2010, **22**, 3482-3495.
- [43] A. Corma; M. J. Diaz-Cabanas; F. Rey; S. Nicolopoulos; K. Boulahya, ITQ-15: The First Ultralarge Pore Zeolite with a Bi-Directional Pore System Formed by Intersecting 14- and 12-Ring Channels, and Its Catalytic Implications, *Chem. Commun.*, 2004, 1356-1357.
- [44] M. Dodin; J.-L. Paillaud; Y. Lorgouilloux; P. Caullet; E. Elkaïm; N. Bats, A Zeolitic Material with a Three-Dimensional Pore System Formed by Straight 12- and 10-Ring Channels Synthesized with an Imidazolium Derivative as Structure-Directing Agent, *J. Am. Chem. Soc.*, 2010, **132**, 10221-10223.
- [45] Y. Yun; M. Hernandez; W. Wan; X. Zou; J. L. Jorda; A. Cantin; F. Rey; A. Corma, The First Zeolite with a Tri-Directional Extra-Large 14-Ring Pore System Derived Using a Phosphonium-Based Organic Molecule, *Chem. Commun.*, 2015, **51**, 7602-7605.
- [46] J. Jiang; Y. Yun; X. Zou; J. L. Jorda; A. Corma, ITQ-54: A Multi-Dimensional Extra-Large Pore Zeolite with $20 \times 14 \times 12$ -Ring Channels, *Chem. Sci.*, 2015, **6**, 480-485.
- [47] A. Corma; M. J. Diaz-Cabanas; J. Jiand; D. L. Dorset; S. L. Soled; K. G. Strohmaier, Extra-Large Pore Zeolite (ITQ-40) with the Lowest Framework Density Containing Double Four- and Double Three-Rings, *PNAS*, 2010, **107**, 13997-14002.
- [48] J. Sun; C. Bonneau; A. Cantin; A. Corma; M. J. Díaz-Cabañas; M. Moliner; D. Zhang; M. Li; X. Zou, The ITQ-37 Mesoporous Chiral Zeolite, *Nature*, 2009, **458**, 1154-1157.
- [49] K. Qian; J. Li; J. Jiang; Z. Liang; J. Yu; R. Xu, Synthesis and Characterization of Chiral Zeolite ITQ-37 by Using Achiral Organic Structure-Directing Agent, *Microporous Mesoporous Mater.*, 2012, **164**, 88-92.
- [50] F.-J. Chen; Z.-H. Gao; L.-L. Liang; J. Zhang; H.-B. Du, Facile Preparation of Extra-Large Pore Zeolite ITQ-37 Based on Supramolecular Assemblies as Structure-Directing Agents, *CrystEngComm*, 2016, **18**, 2735-2741.
- [51] J. H. Kang; D. Xie; S. I. Zones; S. Smeets; L. B. McCusker; M. E. Davis, Synthesis and Characterization of CIT-13, a Germanosilicate Molecular Sieve with Extra-Large Pore Openings, *Chem. Mater.*, 2016, **28**, 6250-6259.
- [52] B. W. Boal; M. W. Deem; D. Xie; J. H. Kang; M. E. Davis; S. I. Zones, Synthesis of Germanosilicate Molecular Sieves from Mono- and Di-Quaternary Ammonium OSDAs Constructed from Benzyl Imidazolium Derivatives: Stabilization of Large Micropore Volumes Including New Molecular Sieve CIT-13, *Chem. Mater.*, 2016, **28**, 2158-2164.

- [53] Z.-H. Gao; F.-J. Chen; L. Xu; L. Sun; Y. Xu; H.-B. Du, A Stable Extra-Large-Pore Zeolite with Intersecting 14- and 10-Membered-Ring Channels, *Chem. Eur. J.*, 2016, **22**, 14367-14372.
- [54] D. S. Firth; S. A. Morris; P. S. Wheatley; S. E. Russell; A. M. Z. Slawin; D. M. Dawson; A. Mayoral; M. Opanasenko; M. Položij; J. Čejka; P. Nachtigall; R. E. Morris, Assembly–Disassembly–Organization–Reassembly Synthesis of Zeolites Based on Cfi -Type Layers, *Chem. Mater.*, 2017, **29**, 5605-5611.
- [55] M. O. Cichocka; Y. Lorgouilloux; S. Smeets; J. Su; W. Wan; P. Caullet; N. Bats; L. B. McCusker; J.-L. Paillaud; X. Zou, Multidimensional Disorder in Zeolite IM-18 Revealed by Combining Transmission Electron Microscopy and X-Ray Powder Diffraction Analyses, *Cryst. Growth Des.*, 2018, **18**, 2441-2451.